SUBSYSTEM ARCHITECTURE SIZING AND ANALYSIS FOR AIRCRAFT CONCEPTUAL DESIGN

A Thesis
Presented to
The Academic Faculty

by

Imon Chakraborty

In Partial Fulfillment
of the Requirements for the Degree
Doctor of Philosophy in the
Daniel Guggenheim School of Aerospace Engineering

Georgia Institute of Technology
December 2015

SUBSYSTEM ARCHITECTURE SIZING AND ANALYSIS FOR AIRCRAFT CONCEPTUAL DESIGN

Approved by:

Professor Dimitri N. Mavris, Advisor
Daniel Guggenheim School of
Aerospace Engineering
Georgia Institute of Technology

Professor Brian J. German
Daniel Guggenheim School of
Aerospace Engineering
Georgia Institute of Technology

Dr. Elena Garcia
Daniel Guggenheim School of
Aerospace Engineering
Georgia Institute of Technology

Professor Daniel P. Schrage
Daniel Guggenheim School of
Aerospace Engineering
Georgia Institute of Technology

Dr. Ruben Del Rosario
Glenn Research Center
*National Aeronautics and
Space Administration*

Date Approved: Nov 13, 2015

To my parents

ACKNOWLEDGEMENTS

It would seem that yet another graduate student's Ph.D. journey has come to a completion through several challenging, laborious, and/or time-consuming activities: A research proposal was formulated, pitched, and approved, a research plan was painstakingly executed, a doctoral dissertation was compiled, and finally a defense was successfully mounted. At the end of it all, I gladly and gratefully acknowledge those who guided, assisted, and encouraged me along the way.

First and foremost, I would like to express my profound appreciation for the members of my defense committee. I must thank whole-heartedly my advisor Professor Dimitri Mavris for multiple things, among them the opportunity to be a part of the Aerospace Systems Design Laboratory (ASDL) and the freedom to explore a number of research areas and projects en route to identifying my dissertation focus. Along the way, he provided unwavering mentoring and encouragement, displayed admirably imperturbable patience, and shared many an enlightening insight into the inner workings of academia and industry. I must also thank Professor Brian German for finding time from his schedule on numerous occasions to review, critique, and provide advice on various intricate technical details of my analysis approach. It is difficult for me to express in words how grateful I am to Dr. Elena Garcia for her sustained patience, her ever-present willingness to review and critique my work, and her constant reminders that I should remain mindful of the larger picture when the engineer in me tended to dive at and strafe a pixel. Last but not least, I would like to thank Professor Daniel Schrage and Dr. Ruben Del Rosario, who despite joining the committee quite far along in the process, took time from their busy schedules to review my work and provide me valuable technical feedback.

The graduate school experience is not merely about one's research but also about one's interactions with colleagues, friends, and compatriots. I cannot possibly name everyone, but let me at least name a few in no particular order: Kalyana Gottiparthi, Daniel Garmendia and Burak Bagdatli (each of whom I've known since I started graduate school!), Matthew LeVine (synchronized promotions, proposal, and defense!), David Trawick (a fair bit of cross-country piloting together!), Michael Miller, Metin Ozcan, Charlie Potter, Mohammed Hassan, and of course Gokcin Cinar and Fatma Karagoz (continuous source of amusement!). To the few I mentioned and to many others as well, I have this to say: my graduate school experience was made all the richer through my interactions with all of you. I shall never forget the camaraderie and I wish all of you the very best in your professional careers and personal lives.

Last but most certainly not least, I would like to thank my parents for the continuous support, guidance, and encouragement that they provided throughout my life. This work is dedicated to both of you. My father, the most well-rounded and technically sound engineer that I have ever met, inspired me from a young age to pursue a career in aerospace engineering. My mother, despite the lack of an engineering or technical background, did (and continues to do) everything in her power to ensure that I am steadfast in that pursuit. Collectively, they taught me that there is no substitute for perseverance and no easy route to success, which in turn cannot endure unless established upon a solid foundation of honesty and integrity.

Imon Chakraborty

Atlanta, GA

November, 2015

TABLE OF CONTENTS

LIST OF TABLES

LIST OF FIGURES

List of Acronyms

AC   Alternating Current

ACM   Air Cycle Machine

AEA   All Electric Aircraft

AEE   All Electric Engine

AES   Aircraft Equipment Systems

APU   Auxiliary Power Unit

APUG   Auxiliary Power Unit Generator

ATRU   Auto-Transformer Rectifier Unit

BF   Block Fuel

CAC   Cabin Air Compressor

CBV   Cross-Bleed Valve

CG   Center of Gravity

CIPS   Cowl Ice Protection System

CMI   Continuous Maximum Icing

COPA   Center Of Protected Area

CSA   Conventional Subsystem Architecture

CSAD   Candidate Subsystem Architecture Descriptor

CSD   Constant Speed Drive

DC   Direct Current

DSE   Degree of Subsystem Electrification

EASA   European Aviation Safety Agency

EBHA   Electrical Backup Hydraulic Actuator

ECS   Environmental Control System

EDG   Engine Driven Generator

EDP   Engine Driven Pump

EDS	Environmental Design Space
EHA	Electrohydrostatic Actuator
EMA	Electromechanical Actuator
EMP	Electric Motor (Driven) Pump
EOP	Extent Of Protection
EPGDS	Electric Power Generation and Distribution System
ESA	Electric Subsystem Architecture
ETRAS	Electric Thrust Reverser Actuation System
ETS	Electric Taxiing System
FAR	Federal Aviation Regulations
FACV	Fan Air Control Valve
FBW	Fly By Wire
FCAS	Flight Controls Actuation System
FLOPS	FLight OPtimization System
FMEA	Failure Modes and Effects Analysis
FTA	Fault Tree Analysis
HLD	High Lift Devices
HPGDS	Hydraulic Power Generation and Distribution System
HT	Horizontal Tail
IFE	In-Flight Entertainment
IMI	Intermittent Maximum Icing
IPS	Ice Protection System
LE	Leading Edge
LED	Leading Edge Device
LGAS	Landing Gear Actuation System
LTA	Large Twin-aisle Aircraft
LWC	Liquid Water Content

MAC	Mean Aerodynamic Chord
MEA	More Electric Aircraft
MEI	More Electric Initiative
MLG	Main Landing Gear
MO	Mixed Off-take
MoA	Matrix of Alternatives
MOET	More Open Electrical Technologies
MPGDS	Mechanical Power Generation and Distribution System
MRM	Maximum Ramp Mass
MRW	Maximum Ramp Weight
MTOM	Maximum Take-Off Mass
MTOW	Maximum Take-Off Weight
NASA	National Aeronautics and Space Administration
NLG	Nose Landing Gear
NPSS	Numerical Propulsion System Simulation
NWS	Nose-Wheel Steering
NWSS	Nose-Wheel Steering System
OEI	One Engine Inoperative
OEW	Operating Empty Weight
PCU	Power Control Unit
PDU	Power Drive Unit
PGDS	Power Generation and Distribution System
PHX	Precooler Heat Exchanger
POA	Power Optimized Aircraft
PPGDS	Pneumatic Power Generation and Distribution System
RAT	Ram Air Turbine
RB	Reduced Bleed

RHS	Right Hand Side
RPM	Revolutions Per Minute
SFC	(Thrust)-Specific Fuel Consumption
SLS	Sea Level Static
SSA	Small Single-aisle Aircraft
SOTA	State-Of-The-Art
TCM	Technology Compatibility Matrix
TCV	Temperature Control Valve
TE	Trailing-Edge
TED	Trailing-Edge Device
TFI	Total Fuel Impact
THS	Trimmable Horizontal Stabilizer
THSA	Trimmable Horizontal Stabilizer Actuator
TRAS	Thrust Reverser Actuation System
TSFC	Thrust-Specific Fuel Consumption
TWI	Total Weight Impact
VAC	Volts Alternating Current
VDC	Volts Direct Current
VFSG	Variable Frequency Starter-Generator
VLA	Very Large Aircraft
VT	Vertical Tail
WBS	Wheel Braking System
WIPS	Wing Ice Protection System
ZB	Zero Bleed

SUMMARY

Traditional aircraft conceptual design focuses primarily on the sizing of the vehicle and its propulsion system. The effects of the vehicle subsystems are largely accounted for implicitly based on historical data and trends, and their detailed design is typically relegated to subsequent design phases. Thus far, this has been possible largely due to the limited interactions among conventional subsystems, and a wealth of historical data collected over decades of aeronautical experience and development.

There are limitations to such an approach, however, when novel subsystem solutions and architectures are considered, such as those proposed for future More Electric Aircraft or All Electric Aircraft. Historical data regarding such subsystems and their effect on the aircraft as a whole is either limited or non-existent. Moreover, hitherto non-existent or limited interactions among vehicle subsystems may become much more significant for such novel subsystems. In such cases, the incorporation of a more thorough and explicit consideration of the aircraft subsystems into the conceptual design phase is warranted.

The first objective of this dissertation, therefore, is to integrate subsystem sizing and analysis methods that are suitable for the early design phases with the traditional aircraft sizing methodology. Suitable methods for early design phases are those that are computationally inexpensive and do not require detailed aircraft definition. The goal is to determine subsystem characteristics in sufficient detail to permit the aircraft-level and mission-level impacts of subsystem architectures to be ascertained.

The second objective is to investigate the relative performances of a large number of subsystem architectures and any variations of these with aircraft size. This

objective is motivated by the observation that the progressive electrification of subsystem architectures within the aerospace industry is occurring through More Electric Aircraft, in which only some of the subsystems are electrified while others retain a conventional architecture.

The third and final objective is to assess the sensitivity of the predicted performance for novel subsystem architectures to epistemic and technological uncertainty. This objective is motivated by the observation that the performance predicted for any subsystem architecture is affected by the uncertainty that stems from modeling limitations, modeling assumptions, and tool fidelity on one hand and assumptions regarding current or projected technological state-of-the-art on the other.

These objectives are pursued through the development of an integrated modeling, simulation, and sizing environment that links aircraft-level and subsystem-level parameters to allow simultaneous sizing of the aircraft and its subsystems. The subsystems are sized and evaluated using models that are computationally inexpensive and require only limited input information that is either available or easily estimable during early design. The connectivities among the different subsystem architecture elements are determined automatically by a heuristic algorithm. The heuristics are based on criticality of subsystem functions as evaluated from typical redundancies in existing conventional and More Electric subsystem architectures. The effects of subsystem mass, secondary power requirements, and drag increments on the aircraft's mission performance are used to simultaneously re-size the aircraft and its subsystems.

The performance and functionality of different modules within the integrated environment are evaluated by (i) assessing the aircraft-level and mission-level impacts of electrification of a single power consuming subsystem and electrification of all subsystems, (ii) verifying the ability of the architecting algorithm to generate subsystem architectures that are equivalent to existing architectures in terms of redundancy, (iii) verifying the feasibility of incorporating information regarding

off-take sensitivities generated using a higher-fidelity propulsion tool without direct integration of the tool, and (iv) verifying that a subsystem architecture's overall impact can be decomposed into contributions from constituent subsystems, and further decomposed into contributions stemming from each subsystem's mass, secondary power requirements, and drag. Subsequently, the impact of epistemic and technological uncertainty on the predicted performance of a number of subsystem architectures is ascertained. Finally, a large number of architectural combinations is evaluated for three aircraft of differing sizes to analyze the relative performance of the subsystem architectures for each.

The completion of the research effort yielded a modular environment linking subsystem sizing and analysis with traditional aircraft sizing, with a focus on novel subsystem architectures for which historical information is unavailable. The application of this environment to the investigation of subsystem architectures for a range of aircraft sizes yielded insight regarding combinations of subsystem solutions that provided the highest payoffs for each vehicle size. Further, it facilitated the investigation of the effect of epistemic and technological uncertainty on the predicted performance of several subsystem architectures. Information of this nature is valuable for the design of More Electric Aircraft which have already appeared in service and also All Electric Aircraft which may become a future reality.

CHAPTER I

BACKGROUND AND MOTIVATION

This chapter provides a brief overview of aircraft subsystem functions, the use of different forms of non-propulsive power for subsystem operation, historical and modern trends for subsystem architectures, and the effect of subsystems on aircraft conceptual design. A summary of notable industry research programs and relevant academic research is presented, followed by observations that influenced the technical approach pursued in this dissertation.

1.1 Aircraft Subsystems and Their Functions

Aircraft subsystems, also known as Aircraft Equipment Systems (AES) [1], may be defined as systems of the aircraft that are essential to performance, safety, controllability, and comfort [2]. These include the Environmental Control System (ECS), the Ice Protection Systems (IPS), the actuation systems for flight controls, landing gear, thrust reversers, brakes, and nose-wheel steering, in addition to the avionics systems, cabin loads (galley loads, In-Flight Entertainment), etc.

The subsystems are designed to provide certain essential or desirable functionalities to the aircraft during the course of its flight or mission. For example, the ECS is responsible for maintaining the cabin at levels of pressure, temperature, and humidity that ensure sufficient human comfort despite possibly severe ambient conditions. The IPS is designed to prevent or eliminate ice formation from external surfaces of the aircraft that are at risk of suffering in-flight icing (such as leading edges of the wings and engine nacelles). The flight control surface actuation subsystem is responsible for ensuring the correct and precise movement or deployment of the flight control surfaces as required to ensure positive aircraft controllability, and

the maneuverability and flight characteristics necessary for a given condition or mode of flight. This subsystem comprises primary control surfaces that are active throughout the duration of the flight and secondary control surfaces which are used in particular flight modes or to obtain certain desired flight characteristics. Similarly, the landing gear actuation subsystem must ensure the positive deployment, retraction, and locking of the landing gear, while the thrust reverser actuation, brake actuation, and nose-wheel steering subsystems are responsible for ensuring adequate deceleration and control of the aircraft on the ground.

1.2   Non-propulsive / Secondary Power for Subsystems

The primary function of the aircraft engines is to generate the thrust (power) required to propel the vehicle in flight. This power is therefore often referred to as *primary* or *propulsive* power. However, an additional function typically performed by the main engines[1] is to provide the power required by the subsystems to carry out their designated functions. This power, which may be consumed in different forms, is termed *secondary* or *non-propulsive* power. When obtained from a gas turbine engine, secondary power may be of the following forms:

1. **Pneumatic power:** Also referred to simply as "bleed", this is obtained by extracting or *bleeding* pressurized air from one or more compressor stages of the gas turbine engine. The pressure and temperature of the air thus obtained is dependent on the compressor stage used and the engine throttle setting. After suitable conditioning to down-regulate the pressure and temperature to acceptable levels, the bleed air may be used for subsystems such as the ECS, the IPS, hydraulic reservoir pressurization, etc.

---

[1]On the ground, secondary power may also be provided by an Auxiliary Power Unit (APU). In certain cases, the APU design may also permit it to supply secondary power in flight. Depending on the magnitude of secondary power required, energy storage devices such as batteries (and perhaps in future super-capacitors and fuel cells) may also be used.

2. **Mechanical power:** Also known as *shaft-power off-take*, mechanical power may be extracted from the engine by driving a gearbox off the engine shaft. Certain loads such as engine fuel and oil pumps may be driven by such an arrangement. Using an accessory gearbox, mechanical power may also be converted to two additional forms of power for use by the aircraft subsystems:

   (a) **Hydraulic power:** This is obtained by driving a hydraulic pump off the engine accessory gearbox to pressurize hydraulic fluid to high pressures for supplying downstream hydraulic users. Nominal system pressures of 3,000 psi and 4,000 psi are common for commercial and military applications respectively, with newer commercial aircraft (e.g., Boeing 787) and military aircraft (e.g., V-22 Osprey) making use of 5,000 psi systems [3].

   (b) **Electric power:** This is obtained by running one or more electric generators off the engine gearbox, whose speed varies with engine operation. Depending on the presence or absence of a Constant Speed Drive (CSD), which can produce a constant speed output shaft from a variable speed input shaft, the power generated by the generators is respectively *constant frequency* or *variable frequency alternating current* (AC). The AC power thus produced may be rectified to *direct current* (DC), if required for use by downstream electric loads. Both AC and DC loads are found in aircraft today, and both types of power (and the associated transmission voltages) have advantages and disadvantages [4].

Secondary power for the subsystems is therefore available in four forms: pneumatic, mechanical, hydraulic, and electric. Since secondary power (in any form) is extracted from the engine, there is an increase in the rate of fuel consumption of the engine or, for the same engine thrust output, an increase in the *thrust-specific fuel consumption* (TSFC) in order to supply this power.

1.3 Gravitation Towards Conventional Subsystem Architectures

Secondary power requirements for aircraft grew steadily from the Second World War onwards, but even at that time, there was considerable debate regarding the optimal means of providing secondary power for aircraft subsystems [5]. Some wartime aircraft such as the British Short Stirling and the German Focke-Wulf Fw 190 made use of electrical power for onboard functions [3], even though these aircraft did not have powered flying controls. The British V-bombers of the 1950s (the Avro Vulcan, the Vickers Valiant, and the Handley Page Victor), which had powered flying controls, used electric power for actuation functions. The Vickers VC-10 of the 1960s also used electric power for most flight controls. However, during this period, the power densities of electric drive technologies did not develop at the same pace as those of hydraulic systems, which were soon able to produce nominal system pressures of 3,000 psi. As this provided a simpler and lighter solution to the actuation problem at the time, hydraulics became the mainstay for aircraft actuation functions for several decades, and continue to have a significant presence on modern aircraft even today.

At the same time, pressurization and air-conditioning functions (ECS) and ice protection functions (IPS) began to gravitate towards the use of pneumatic systems. While the bleed air mass flow requirements increased with increasing aircraft size, this was not considered a major problem for the turbojet engines or low bypass ratio turbofan engines powering aircraft at the time, since sufficient core flow was available to supply such pneumatic systems, albeit inefficiently.

Thus, the pattern of secondary power usage, i.e. the association of the aircraft subsystems to secondary power types, gravitated towards an industry-accepted conventional standard. Such conventional architectures (Fig. 1, left), which feature the use of (i) electric power for avionics, electronics, lighting, etc., (ii) pneumatic power for ECS and IPS functions, and (iii) hydraulic power for actuation functions [6],

4
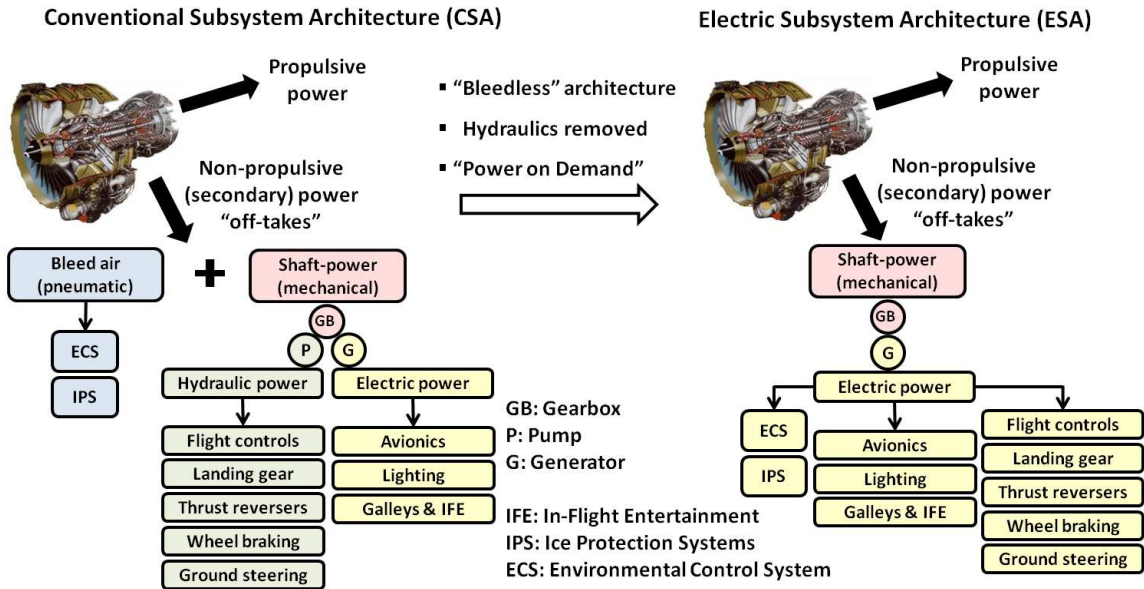
Figure 1: The transition from conventional subsystem architecture to electric subsystem architecture

have persisted for several decades. While the gravitation towards the conventional architectures was precipitated by the lack of feasible alternative solutions for subsystems [7], the persistence of such architectures has also been influenced by the "better-the-devil-you-know" philosophy of aircraft designers [8]. As a result, developments have largely been limited to the improvement of component efficiencies, the use of higher hydraulic system pressures (5,000 psi instead of 3,000 psi), and some attempts at localized energy management of pneumatic systems.

1.4   The Drive for More Electric Subsystem Architectures

The conventional subsystem architectures featuring largely mechanical, hydraulic, and pneumatic power (and relatively smaller amounts of electric power) have matured over decades of aeronautical experience, but have now reached a so-called "technology saturation", a point of diminishing returns whereafter further increases in efficiency are progressively more difficult to attain. This, coupled with rapid developments in power electronics and electric drives [3, 8], has led to a renewed interest in electric

subsystem solutions as part of the *More Electric Initiative* [9]. The end goal is to develop what has come to be called the *All Electric Aircraft* (AEA) [10, 11, 12], in which secondary (non-propulsive) power requirements are solely electric in nature (Fig. 1, right). Since the technological risks involved with a direct single-step transition to an AEA were unacceptably high, a step-wise transition approach was preferred by the industry. This resulted in attempts to develop *More Electric Aircraft* (MEA), intermediate steps in the possible transition to AEA that contained some (but not all) electric subsystems. While it was acknowledged that this step-by-step approach would initially obscure the true potential benefits of electric architectures, it did agree with the aerospace industry's preferred approach of risk mitigation and accumulation of flight experience [6]. The perceived benefits of AEA/MEA include improvements in aircraft empty weight, ownership cost, fuel consumption, installation and maintenance costs, turnaround times, range, and system reliability [4].

A major motivating factor for the MEI has been the recognition of the inefficiencies inherent in the conventional subsystem architectures. Pneumatic systems, for example, represent significant energy wastage due to the need to reduce the temperature and pressure of the extracted bleed air prior to supplying it to the downstream pneumatic system, a process called *down-regulation*. This is necessary because despite the implementation of port selection logic, the bleed air temperature and pressure are typically too high to be directly used downstream. The temperature is typically above the auto-ignition temperature of fuel in fuel lines which may be in close proximity to pneumatic ducts. Also, the high pressure presents challenges for sealing and containment [13]. This gross mismatch between the available and required (or usable) pneumatic energy [8] necessitates the use of a precooler and a pressure regulating valve to reduce respectively the temperature and pressure, which essentially amounts to simply rejecting extracted energy overboard. The progressive trend towards higher bypass ratio engines also presents additional challenges as the

available core flow is reduced. With regard to this aspect, pneumatic IPS is a more difficult problem to contend with, as the bleed requirements may equal or exceed those for pneumatic ECS, but are not continuous (like for ECS) since the IPS can be turned off at high altitudes [3]. As a result, electric power has been proposed for the ECS and IPS in lieu of pneumatic power. Quite significantly, such a predominantly "no-bleed" or "bleedless" architecture has already been achieved in the Boeing 787 Dreamliner, in which electric power is used for the ECS and the wing IPS. Rather than using bleed air from the engines, the Boeing 787 uses dedicated Cabin Air Compressors (CACs) to pressurize the necessary quantity of external ram air to the required pressure for supply to the cabin. Similarly, instead of using bleed air, the wing IPS uses electric heating mats (or pads) bonded to the inner skin of the protected leading edge to provide the necessary ice protection [14]. Since the ECS is the largest consumer of non-propulsive power, a potential advantage arising out of the use of electric ECS is the fact that the higher rating generators that are required can typically be motored to perform the engine starting function [15]. This additionally eliminates the traditional use of pneumatic power for engine starting.

The inefficiencies inherent in centralized hydraulic systems have also been recognized. In addition to technology saturation, centralized hydraulic systems have the disadvantage of being heavy (e.g., hydraulic pipework on an Airbus A300 sized airplane weighs in excess of 800 kg [3]), use flammable and corrosive hydraulic fluid, and are not necessarily immune to common cause failures despite triple redundancy [16]. System flow capacity is typically sized by actuation requirements in the landing approach phase, where high flow demands from the primary flight controls, high-lift system, and landing gear must be supplied at low engine speeds [17]. At other more benign flight conditions such as during cruise, when hydraulic flow requirements are lower while engine speeds are higher, the pumps are under-utilized and operate at a lower hydraulic efficiency [8]. Further, a constant power input is required to

maintain pressurization in centralized hydraulic systems due to leakage flow. These factors resulted in a renewed interest in the use of electric power for the actuation functions, using electric actuators which would consume power only when the control surface moves or overcomes a load, a concept called "Power on Demand".

Electric actuation of flight control surfaces was given particular attention on the military side [9]. The technology was especially attractive since the elimination of a centralized hydraulic power source would reduce the vulnerability of the aircraft in combat [18]. Actuation test programs were conducted on the C-141 Starlifter and C-130 Hercules aircraft [19]. In the late nineties, NASA's F-18 Systems Research Aircraft (SRA) was used to test the performance of two types of electric actuation, Electrohydrostatic Actuators (EHA)[20] and Electromechanical Actuators (EMA)[21]. Further technology maturation occurred during the USAF's J/IST program [22] culminating in the F-35, the first production fighter to use electric actuation for all flight control surfaces [23]. Commercial aviation has been more cautious, but Airbus, after conducting technology maturation programs on the A320 and A330 aircraft, introduced two types of electric actuators in the Airbus A380 in parallel to conventional hydraulics for several flight control surfaces [24]. For this aircraft, a weight savings of 450 kg (1,000 lb) has been attributed to the shift from a conventional three-hydraulic system (3H) architecture to a two-hydraulic/two-electric (2H/2E) architecture [25]. Electric actuation has also been considered for less flight-critical controls such as spoilers [26, 27] and the high-lift system [28, 29].

Electric power for the remaining actuation functions has also been considered. For example, the Airbus A380 features an Electric Thrust Reverser Actuation System (ETRAS), while the Boeing 787 uses electromechanically actuated brakes [30]. Electric actuation for the landing gear extension/retraction and nose-wheel steering functions was investigated as part of a research program [31], but is not found in any commercial aircraft in service at the time of writing.

A novel concept known as "Electric Green Taxiing System" (EGTS), where the aircraft is taxied using APU-powered electric motors fitted to the main gear axles, has also been tested successfully on the Airbus A320 aircraft through a collaborative project between Airbus, Honeywell, and Safran [32]. This allows the aircraft to taxi without the use of the main engines, and has been predicted to offer reasonable fuel savings for aircraft operating mainly on short-haul routes. Other auxiliary benefits of such a concept include the elimination of tugs and other ground personnel associated with the push-back from the gate and a reduction in airport emissions.

Parallel to the proposed concept of the All Electric Aircraft is that of the All Electric Engine (AEE) [6], where the only non-propulsive power off-take is in the form of electrical power. The AEE is not a new concept either, and as early as 1972 Secunde et al. [33] proposed an Integrated Engine-Generator (IEG) concept, which *"consists of locating an electric generator inside a turbojet or turbofan engine concentric with, and driven by, one of the main engine shafts"*. The IEG was presented as a technically feasible approach to aircraft secondary power generation. Provided a certain minimum rating was met, the generator could also be motored to start the engine. Electric engine starting has been realized in the design of the Boeing 787, which uses Variable Frequency Starter-Generators (VFSGs) that can be motored (powered) to start the engine (starting mode) and then driven by the running engine to generate electricity (generator mode) [14]. Electrically powered engine accessories (fuel and oil pumps) were also proposed, which would provide benefits in efficiency, weight, size, and flexibility of speed control [34, 35]. An added benefit is a possible reduction in required nacelle diameter as there is no longer the need for an accessory gearbox, which has often caused an undesirable ballooning of the nacelle [15].

1.5 Subsystem Considerations during Conceptual Design

With some background regarding conventional and More Electric solutions for the major aircraft subsystems having been presented in the preceding sections, the effect of the subsystems on the aircraft sizing process is now addressed. While several definitions of aircraft sizing exist in literature, the following is used in this work [36]:

> *an analytical process that determines the best combination of two scales of a baseline configuration, a geometric scale that is dictated by the wing area and a propulsive scale that is dictated by the amount of engine thrust so that the resultant aircraft should satisfy three criteria: matching power, energy, and volume.*

These two scales, the wing area (S_w) and the required sea-level static engine thrust (T_{SL}) may be considered along with the vehicle's maximum takeoff weight (W_{TO}) as being the three primary outputs from the aircraft sizing process.

The effect of the aircraft subsystems on the sizing of the aircraft is shown overlaid on the refined sizing method of Raymer [37] in Fig. 2. As indicated in the figure, the aircraft subsystems affect the conceptual phase sizing process in three ways:

1. Empty weight fraction: Subsystem components and architectures affect the empty weight of the vehicle through changes in the *fixed equipment weight*

2. Engine fuel consumption: The extraction of secondary power (shaft-power or bleed air) increases engine thrust-specific fuel consumption (TSFC)

3. Vehicle drag: The subsystems may contribute to the overall vehicle drag due to the drag arising from ram air inlets or any necessary external modifications

To estimate the contribution of conventional subsystem architectures to the aircraft fixed equipment weight, the conceptual phase designer has access to a vast historical database of information that has been populated and updated over the
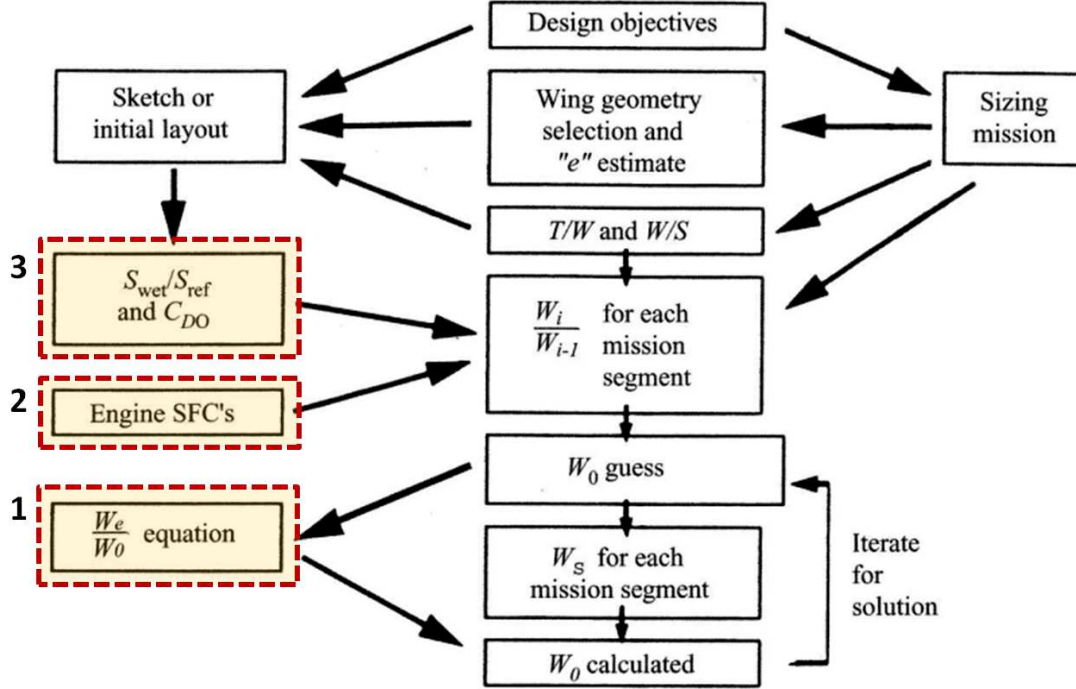
Figure 2: Effects of subsystems indicated on Raymer's refined sizing method [37]

course of several decades of aeronautical experience. This database has also allowed the regression of equations for the weights of various subsystems, which are quite often of the form $W = aX^b$. For example, the General Dynamics method [38] estimates the weight of the flight control system as

$$W_{fc} = 56.01 \; \{(W_{TO})(\bar{q}_D)/100,000\}^{0.576},$$ (1)

where $\bar{q}_D$ is the dynamic pressure corresponding to the aircraft's design dive speed. Similarly, Torenbeek suggests the following relationship for the combined weight of the hydraulic, pneumatic, and electrical systems[2] based on aircraft empty weight W_e:

$$W_{hps} + W_{els} = 0.0078 \; (W_e)^{1.2}$$ (2)

---

[2]It is seen from Eq. 2 that the equation gives the combined weight of a number of subsystems, and provides no means by which the individual masses of the subsystems can be determined. Lammering [39] provides several additional examples of such inconsistent groupings in regressed equations for conventional architectures.

The conceptual designer of AEA/MEA concepts, however, does *not* have access to a similar historical database or regression equations for the weights of electric subsystems. Further, for conventional subsystem architectures, the interactions among different subsystems had either been mild or non-existent. However, this may not be the case for a fully or even predominantly electric subsystem architecture, where a larger number of subsystems share the same form of energy: electricity. The sizing cases for subsystem architecture components are also likely to be different in this case. Efficiency improvements for conventional subsystems have generally been attained through optimization of these subsystems in isolation. However, to attempt to do the same for electric subsystem architectures would likely result in a sub-optimal solution at the vehicle level. Thus, it would be fair to say that the conceptual designer of AEA/MEA is faced with significant challenges, such as (i) the lack of a historical database to serve as a starting point during conceptual design, (ii) potentially significant interactions among subsystems, and (iii) likely vehicle level sub-optimality that will result from optimizing individual subsystems in isolation.

Further, it is clear from the Boeing 787 and the Airbus A380 aircraft that the transition from conventional subsystem architectures to electric subsystem architectures will be a gradual one, likely featuring a range of More Electric Aircraft (MEA) in between. This is largely necessitated by the need to mitigate technological uncertainty and risk, and it is unlikely that any abrupt steps towards an AEA will be taken by the major aircraft manufacturers. This then leaves the MEA conceptual designers with the additional task of determining which subsystems to target for electrification. From the fact that the Boeing 787 and the Airbus A380 have different electric subsystems, it is clear that there is no unique "right" choice. Rather, the decision may very well vary with the aircraft category, and is of a multi-objective nature that must be tackled in the face of considerable uncertainty and risk.

1.6 Previous AEA/MEA Feasibility Studies and Programs

Since the concept of AEA/MEA is not a new one, there is a reasonable amount of literature investigating these concepts. In particular, several detailed feasibility studies have been conducted, notably by NASA, Boeing, and Lockheed. In addition to these, some notable independent efforts were undertaken in the Europe. A summary of some of the notable studies (by no means exhaustive) is provided below.

A 1980 study conducted by NASA, Lockheed, AIResearch, and Honeywell titled "Electric/Electronic Technology Study" [40] was aimed at evaluating the improvements in commercial aircraft that might be attained due to transfer of fly-by-wire and related flight control technologies from the Space Shuttle. One of the technology suites considered involved that related to the AEA, i.e., the elimination of hydraulic and pneumatic systems and a transition to a completely electric secondary power system. Weight and cost data were obtained using the Lockheed-developed Advanced Systems Synthesis and Evaluation Technique (ASSET) program. For studying technology tradeoffs, the payload and missions were held fixed but the airplane was re-sized in response to estimated equipment and fuel weight changes. The alternative approach, taking advantage of the greater payload/range capability arising out of reduced systems weight, was avoided as the resulting designs would end up with dissimilar payload/range capabilities. This tradeoff study considered the incorporation of the various technology suites (including AEA technologies) into three aircraft - a tri-jet high bypass turbofan 500-passenger subsonic airliner (based on the L-1011-500 aircraft), and two short-haul twin-turboprop airplanes of 50-passenger and 30-passenger capacities. To circumvent the combinatorial problem arising out of multiple feasible technology combinations, a sequential approach was taken during the tradeoffs. In other words, to evaluate the effect of incorporating technologies A, B, C, etc. into the baseline, comparisons were made as follows: baseline vs. baseline + A, A vs. A + B, B vs. B + C, etc. All three aircraft considered were seen to benefit

from the AEA concept, but the effect on the 500-passenger aircraft was the most substantial. The use of an all-electric secondary power system exhibited the most impressive weight and cost payoffs. A major economic benefit was identified from the elimination of bleed air for the ECS. The overall benefits comprised component and system weight savings, significant reduction in complexity, and significant reduction in block fuel.

Building on the results of this study, a subsequent study conducted by Lockheed in 1982 [41] analyzed the benefits of incorporating 135 total technologies into three selected baseline configurations: a twin-engined 150-PAX aircraft, a three-engined 350-PAX aircraft (based on the 350-PAX, 5,000 NM Lockheed L-1011 aircraft), and a four-engined 700-PAX aircraft. Two representative stage lengths were considered for each aircraft to evaluate mission fuel burn performance. The technologies were grouped by functional similarity into eight main packages, two of which involved flight control technologies and secondary power systems (both near-term and far-term). Notably, the near-term secondary power system considered resulted in the elimination of bleed air, while the far-term secondary power system also saw the removal of centralized hydraulics. The study, which made use of the Lockheed-developed ASSET tool, started with the establishment of the three baseline designs. Consultation with in-house and vendor specialists was employed to obtain estimates of weights of actuators, lengths and weights of wiring runs, etc. Weight deletions from the baseline were based on known weights of similar items on contemporary aircraft scaled to the baseline configuration. In this study, each tradeoff was performed by comparing the tradeoff configuration to the original baseline that did not contain any of the technologies. The claim was made that while in theory, benefits could not be added together to ascertain combined benefits, in practice this could be done with negligible error incurred. Like the 1980 Lockheed study preceding it, this study also noted the fuel penalties incurred through the use of engine bleed air. However, it also recognized

efforts within the aerospace industry to pursue the reduction of bleed air requirements, due to which the projected fuel savings of bleedless architectures would not be as significant. While advanced secondary power technology showed large payoffs, it was recognized that strong coordination would be needed in the development phase among aircraft, engine, actuator, and avionics manufacturers. Like the preceding study, this study also concluded that the payoffs (in terms of weight and cost savings) grew with aircraft size.

In 1985, one of the two most prominent studies of the time was conducted by NASA and Boeing [42]. Titled "Systems Study for an Integrated Digital/Electric Aircraft (IDEA)", this was a nine-month long investigation of concepts related to advanced electrical and digital systems for aircraft. The configuration selected for use as a reference baseline was a modified Boeing 767 airplane powered by two high bypass ratio E^3 engines. This study noted the fact that the design of an AEA would require the modification or selection of an engine for higher mechanical power extraction. The engine considered in this study was meant to deliver high shaft-power extraction (via the electrical generator) at low engine power with a low extraction penalty compared to other existing turbofan engines. However, its bleed air penalty was significantly higher than most other turbofan engines. Despite this, the same engine was used to supply bleed air for the baseline aircraft customer bleed requirements, even though it was clearly at an unfair disadvantage in doing so [3]. Certain updated technologies were assumed for the baseline to represent a 1990 new airplane go-ahead. The baseline configuration was compared to the IDEA configuration in terms of economic performance, fuel efficiency, and significant system and airplane configuration characteristics. The IDEA configuration was developed by incorporating an "optimal combination" of IDEA concepts into the baseline configuration through a system of parallel and coordinated system trade studies to assure system compatibility. For each subsystem, system options were evaluated

using trade studies, analysis, and equipment supplier consultation, to narrow down the range of options to a finally-selected configuration. The IDEA configuration was predicted to offer a 3 % reduction in fuel and a 1.8 % reduction in DOC assessed over a 1,000 NM segment relative to the baseline for the same payload/range conditions. The system advances that were considered included all-electric secondary power extraction (via generators only, with no bleed air and no direct shaft-power), electric engine starting, and actuation using electromechanical actuators.

The other prominent study was conducted by NASA and Lockheed [43], and was titled "Integrated Digital/Electric Aircraft Concepts Study". It also considered an Integrated Digital/Electric Aircraft (IDEA) concept that employed advanced electrical power generation and engine starting, power distribution and management, electromechanical actuation systems, electrical deicing, and electrically driven ECS in addition to advanced data distribution and a digital flight control system. The baseline for this study was a stretched-fuselage Lockheed L-1011 derivative carrying 350 passengers over 4,600 NM, with performance benefits evaluated at an average stage length of 2,500 NM. Following the incorporation of electric technologies into the aircraft and subsequent re-sizing, the study predicted large benefits that included a 11.3 % reduction in block fuel and a 7.9 % reduction in direct operating cost. The study utilized the Lockheed Advanced Systems Synthesis and Evaluation Technique (ASSET). The IDEA concept featured the complete elimination of the hydraulic and pneumatic systems. The E^3 engine that was used for this analysis was based on a bleed configured design, and was not cycle-optimized for shaft-power extraction. In the absence of a specific cycle-optimized design, the authors stated that the physical differences in the IDEA engines were computed parametrically from the baseline E^3 design. It is noteworthy that while the summary of this study states that the block fuel reduction was 11.3 % overall, only half of this was attributed to the incorporation of all-electric secondary power systems. The remainder of the fuel burn benefit was

achieved through the assumption that an advanced computer-augmented fly-by-wire flight control system could be incorporated that would allow relaxed static stability and a reduction in the required tail volume ratio.

A separate study titled "Advanced Secondary Power System for Transport Aircraft" was conducted by the NASA Lewis Research Center in 1985 [44]. This study attempted to fill the gap left by two previous studies [40, 41] by analyzing electrification of a 200-PAX twin-engine transport, similar to the Boeing 767 aircraft. It considered a direct one-to-one replacement of hydraulic actuators with electromechanical ones for the flight control surfaces, landing gear, brakes, and thrust reversers, and the removal of the centralized hydraulic system. Similarly, the baseline pneumatic ECS was replaced with an electric motor-driven vapor cycle system for temperature regulation and an engine gearbox-driven compressor for cabin pressurization. The baseline anti-icing system was replaced with an electroimpulse de-icing system, thus allowing removal of the conventional pneumatic system. In this study the existing specifications of the Boeing 767 aircraft were used with no attempt made to adjust these figures for 1990s technology. The NASA/General Electric Energy Efficient Engine (E^3) was selected as the engine for the baseline aircraft. The General Aviation Synthesis Program (GASP) was used for weight sizing and mission performance analysis. This tool featured an integrated approach in which changes in wing loading (for example) were propagated to connected design parameters such as wing area, tail size, aerodynamics, etc. The study predicted an uncycled weight saving of 2,950 kg (6,500 lb) through an empty weight reduction of 10 %, and following re-sizing of the aircraft in response to this system weight reduction and the elimination of bleed air, a cycled weight saving in excess of 7,700 kg (17,000 lb), with a 9 % reduction in mission fuel burn. The most significant weight reduction was reported to be from the electrification of the secondary power system (i.e., removal of hydraulics and pneumatics), which allowed better load-sharing and

system utilization. The most significant fuel burn reduction was reported to be due to the removal of engine bleed air for ECS functions.

In the United Kingdom, the *Collaborative Research Initiative into Secondary Power Systems (CRISPS)* study, which began in 1988, aimed to take a broader look at future systems possibilities for a range of civil aircraft [3]. It involved a total of 14 organizations spanning industry, academia, and government. Among the three baselines considered in this study was an Airbus A320 aircraft. The results of the investigation are documented in an overall summary report [45] and an additional short executive summary report [46]. In the latter, the estimated benefits were presented along with their development risks (technical and financial). For the Airbus A320 baseline, an AEA version was seen to offer approximately 4 % fuel burn savings, which increased to almost 5 % when coupled with an AEE. It was predicted that an AEE could result in significant benefits by eliminating the drag caused by the accessory gearbox. However, both AEA and AEE were considered to be on the high-end as far as risk was concerned. Electrification of individual subsystems such as the IPS and actuation functions were considered to entail lower risks, but also lower benefits whose magnitudes could be matched by advanced versions of conventional secondary power systems.

In Europe, the *Power Optimized Aircraft (POA)* program was commissioned through the European Union's 5th framework program for Research and Technology Development (2002-2006), and was tasked with exploring the way forward for aircraft equipment systems [47]. It was led by Liebherr-Aerospace, and major participants included Airbus, Alenia Aeronautica, DLR (German Aerospace Center), Hispano-Suiza, Rolls-Royce, Snecma, Thales Avionics Electrical Systems, and Goodrich Actuation Systems. The project's goal was to identify, optimize, and validate innovative aircraft equipment aimed at reducing non-propulsive power consumption. The focus was on four main domains - engine systems, electrical power

systems, actuation systems, and pneumatic systems. The More Electrical Engine featuring the embedding of electrical generators within the engine as the sole source of secondary power (and removal of the accessory gearbox) was investigated. This necessitated the electrification of the engine fuel/oil systems. The load analysis, architecture, cabling mass, and stability for high voltage DC networks were studied. To avoid the large losses associated with pneumatic ECS due to the down-regulation requirement, a set of solutions ranging from the reduction of engine bleed air pressure to the complete removal of the bleed system and a transition to electric ECS and IPS were investigated. Electrification of actuation functions such as flight controls, thrust reversers, landing gear extension, and wheel braking was evaluated. It was observed that the benefits arising out of removal of hydraulics would be largest if multiple actuation functions such as flight controls *and* landing gear were electrified [48]. Another significant aspect of the POA program was the use of three interacting validation platforms: (1) an Engine Systems Validation Rig (ESVR) for demonstrating the integration of electrical power generation and accessory subsystems and the removal of the accessory gearbox, (2) Aircraft Systems Validation Rig (ASVR), an electrical characterization test rig for validating electrical power generation and distribution systems, actuation systems, and pneumatic systems, and (3) Virtual Iron Bird (VIB), an integrated software environment for aircraft level evaluation and optimization. This was linked with the ASVR in order to verify and tune component models. Some of the conclusions from the program were that electric technologies had potential for superior performance, but that when implemented within conventional architectures, electric technologies yielded only a fraction of their potential benefit. The forum recognized that many new technologies were at demonstration level and that many challenges and issues still needed to be addressed. The increased weights of electrified systems were identified as a major challenge. However, it was observed that these could be acceptable provided there was a net fuel

savings [48]. Finally, it recognized that functional thinking and cross-ATA expertise was needed for true integration at the aircraft level [48, 47]. The POA program focused more on in-depth optimization of a pre-defined/pre-determined architecture, and the architectural design space was rather limited. The detail of analysis that was performed required that the systems architecture be well-defined a priori.

The *More Open Electrical Technologies (MOET)* project was a 36-month research effort (2006-2009) undertaken under the European Commission's 6th Framework Program [49]. The overall goal was to develop the "Power By Wire" (PBW) or "More Electric Aircraft" (MEA) concept, in particular through the deletion of centralized hydraulics and all engine air off-takes. In line with the Advisory Council for Aeronautics Research in Europe (ACARE) vision for 2020, MOET aimed at establishing the new industrial standard for commercial aircraft electrical system design. The target applications for technology infusion were the Airbus A320 short-range airliner, the Dassault Falcon 2000 business jet, the Alenia ATR-72 short-haul regional airliner, and also the Eurocopter Super Puma helicopter. The project involved both the development of simulation models and also the development and testing of hardware components using a variety of test rigs. The study concluded that the More Electric technologies pursued demonstrated satisfactory performance when fully integrated at vendor and airframer facilities. Conceptual design studies concluded that airplane level benefits in terms of maintenance, operational flexibility, and technology growth potential were possible, without any fuel-burn performance penalty. However, system weight was identified as a challenge particularly for smaller short-range aircraft. The study found that the MEA short-range aircraft was heavier than the reference (conventional) aircraft for the systems (control volumes) considered. The MEA was also predicted to suffer a drag penalty due to the incorporation of additional ram air inlets for the ECS. Due to the elimination of customer bleed off-takes, an improvement in engine TSFC was predicted. However,

the study predicted no net effect on fuel burn for the short-range MEA, likely due to a mutual off-set between beneficial (reduced TSFC) and adverse (higher weight, drag) effects. Certain specific topics were recommended for future projects, including only one high voltage network (230 VAC or $\pm$ 270 VDC but not both), smart management of the overload capability of generators, deletion of conventional hydraulics and EMA-driven flight control surfaces and landing gear (specifically for regional jets). One of the salient features of this effort was that a large volume of test data was published and thereby made available in the public domain.

On the military side, the United States Air Force (USAF) led a program called *Integrated Vehicle and Energy Technology (INVENT)* whose main focus was to make the aircraft and vehicle systems more energy efficient by maximizing overall system energy efficiency in lieu of sub-optimized components and subsystems [50]. This program coined the term *Energy Optimized Aircraft* (EOA). Its efforts were aimed at creation of a tip-to-tail thermal model for military aircraft, featuring Air Vehicle System (AVS), Fuel Thermal Management System (FTMS), and Power Thermal Management System (PTMS). Design space trades were explored by exercising the PTMS model. The program noted that typical thermal, power, propulsion, and vehicle systems had been designed and optimized at a subsystem level with little consideration given to design of the thermal management system. However, the increase in heat loads and the increased usage of composite skins with high thermal resistance had made convective cooling difficult. One of the INVENT objectives was to make extensive use of Modeling and Simulation of integrated systems to investigate aircraft system design space prior to validation work being attempted, with the requirement that subsystem models (and their validity) be scalable over a reasonable size/capability range, with the target being set at +/- 25 % with respect to the design operating point. In particular, the ability of the model to simulate different timescales to address dynamics occurring at different rates was stressed

upon. The difficulties arising out of proprietary tools and simulation environments used by different subsystem manufacturers, which prevent aircraft-level integration studies, was recognized [51]. An approach to address this issue that was developed by the Air Force Research Laboratory (AFRL) and others is Distributed Heterogeneous Simulation (DHS). This allowed subsystem models to remain within their native simulation environment while being integrated within a dynamic system simulation.

1.7 Relevant Prior Theses/Dissertations

Several recent dissertations and archival papers related to aircraft subsystems have addressed different aspects of the problem in differing levels of detail. Some of the relevant works are briefly described below, along with a discussion of their advantages, distinguishing features, and limitations. Certain attributes that are common to most approaches (including this dissertation) are then identified, followed by a brief statement regarding how this dissertation differs from others preceding it.

Jackson [52] attempted to demonstrate robust subsystems architecting by considering the case of the flight control surface actuation subsystem for a small single-aisle aircraft with fixed configuration and design mission. A comparison was made between a conventional hydraulic actuation architecture and a hybrid architecture featuring both electrohydrostatic actuators (EHAs) and hydraulic actuators. The characteristics of the remaining aircraft subsystems were set to baseline values and their architecture was not considered further in greater detail. Comparisons were made with regard to secondary power extraction and subsystem weight. Jackson attempted to find a robust solution by considering the effect of epistemic uncertainty.

De Tenorio [53] addressed the conceptual design of aircraft power architectures, using the SysML language as a visual means of defining architectures. Optimization of subsystems was addressed using a multi-level Coordinated Optimization technique.

In this work, the aircraft size was assumed to be fixed, and the effect of changing subsystem architectures was captured through an increase in the aircraft range. The effect of subsystem architecture on the sizing of the aircraft and its integration with the latter were not considered.

Armstrong [54] attempted to identify emergent off-nominal operational requirements for defining the conceptual architecture of MEA. The thrust of this work was on providing the required reliability/availability of architecture components and optimized load-shedding strategies, and the subsystem models and their requirements-driven sizing were addressed in less detail. Only a fixed vehicle test-case was considered, and the work did not attempt to consider the effects of subsystem architecture on the sizing of the aircraft. Prior to this, Armstrong had addressed the definition and modeling of architectures [55], including the generation of alternatives, through an object-oriented program called the Architecture Design Environment (ADEN). The objective was to produce architectures in an automated manner, with functional and alternative definition, alternative selection, configuration definition, an interface for installation definition, and a method to defining the operating space for the architecture. Spatial orientation and installation of components was taken into account in this work. Armstrong considered limiting the alternative design space through the tacit incorporation of compatibility knowledge in an Interactive Reconfigurable Matrix of Alternatives (IRMA), which uses incompatibilities, or an Adaptive Reconfigurable Matrix of Alternatives (ARM), which uses induced functions instead of incompatibilities.

Liscouet-Hanke demonstrated an attempt to integrate subsystem architecture considerations with the early design phases through a doctoral dissertation and additional archival publications [56, 57, 58]. The author proposed generalized "power system modules" which shared common interfaces for receiving global and local parameters and propagating parameters such as mass and drag. While several

subsystem models were integrated by the author into the Airbus Mission and Performance Tool (AMPT), an internal Airbus tool, the dissertation [56] provides focus and insight on sizing and simulation for (i) wing ice protection, (ii) commercial cabin systems, (iii) pneumatic power system, and (iv) electric power system. Further reference is made to the work of Liscouet-Hanke in these four areas in relevant sections of this dissertation. Two other salient features of Liscouet-Hanke's approach were (i) the development of a Graphical User Interface (GUI) to enable the analyst to interact with the analysis environment and (ii) a preliminary analysis of the effect of rejected heat loads from the aircraft systems using a global thermal model of the aircraft (developed separately for another Airbus project). Additionally, the traditional ATA-based classification of subsystem architectures was avoided in these works. However, the effect of re-sizing of the aircraft in response to subsystem impacts was not explored in [56], in which the geometry, structure, and propulsion parameters were kept fixed and only the impact of the subsystems (or power systems) architecture was assessed for a limited number of subsystem architectures. Liscouet-Hanke's work was done in conjunction with Airbus as part of an internal project, and some of the integrated models were developed by various systems departments at Airbus, presumably using proprietary data. Since this data is of a restricted nature, the models themselves are not documented fully in the open literature, and consequently the modeling approach in certain cases naturally lacks transparency. Likely due to the same reason, most of the results presented are in a normalized or percentage contribution form. While this is understandable given the industry affiliation, it is nevertheless difficult to develop a proper appreciation of the magnitudes of various subsystem impacts (weights, power requirements, etc.) from these works.

A more recent investigation of integrated subsystems analysis was presented in the doctoral dissertation of **Lammering** [39]. This work was influenced by the author's observation that several other works existed where the modeling

approach either required a high level of detail and was therefore suitable only for a specific architecture, or where the use of restricted models and data limited the applicability of the methodology. In addition to the estimation of subsystem masses, Lammering's approach included estimates of the center of gravity of each system, and the analysis of the spatial layout of the architecture components was based on a two-dimensional (2-D) coordinate system. The subsystems models were integrated into an already existing analysis environment called Multidisciplinary Integrated Conceptual Aircraft Design and Optimization (MICADO). He noted the limitations of simple regression-based relationships which provide a first estimate of engine fuel consumption penalties due to power off-takes but do not take into account the engine type, operating condition, or power extraction architecture. For his work he used instead multi-dimensional polynomial curve fits which were created based on engine performance analysis conducted using GasTurb. The predicted subsystem impacts were fed back into the aircraft sizing program in order to re-size the aircraft and ascertain the so-called "snowball" effects of subsystem architecture changes. The sensitivity of the model to variations/uncertainty in input parameters was also assessed. Some noteworthy trends included the effect of the following on predicted subsystems mass and secondary power requirements: (i) model-specific inputs such as ECS recirculation fraction and IPS extent of protection, (ii) aircraft design parameters such as number of passengers and cabin dimensions, and (iii) top-level aircraft requirements such as design range and payload. However, the comparisons and sensitivities that were assessed were limited to a relatively small number of architectural combinations, and a detailed investigation of the architectural design space was not attempted.

Seresinhe [59] presented an electrical load sizing methodology suitable for early design stages of large commercial aircraft, in which a generic baseline electrical load architecture could be modified and adapted for a MEA architecture. While the

electrical load analysis and sizing of the power generation system were considered with due diligence, the methodology was heavily dependent on valid estimates for the electrical loads imposed by MEA subsystems being available as input. In case of the electric ECS, the power requirement was computed from a simple thermodynamic relationship, while for other subsystems such as the IPS and flight control surface actuation, the required power was interpolated or scaled from the results of other prior studies. In a separate but related work by the same author in the context of a trajectory optimization problem [60], the effect of shaft-power and bleed air extraction on the fuel consumption of the engine was investigated. Penalty coefficients for each were determined as a function of flight altitude and Mach number. This work also focused more on estimating electrical power requirement and did not account for factors such as increased ram drag or weight for an ECS layout or increased weight of electrical components within a MEA. Thus, for comparing minimum fuel-burn trajectories, the assumption was made that the mass of the MEA would be the same as that of the conventional aircraft, and improving power-to-weight ratio of electric components was cited in order to justify this assumption. This work therefore did not consider all relevant aspects of a subsystems architecture transition assessment, since recent MEA investigations [49] have specifically identified the weights of added electrical components as a significant challenge for MEA.

1.8 Observations from Previous Studies and Characteristics of the Present Approach

Based on the conclusions and opinions expressed in the most notable studies which were described previously, the following pertinent observations may be made:

1. It is generally acknowledged that only the overall electrification of the subsystem architecture will allow the true benefits and potential of AEA to be realized. An incremental piece-by-piece approach will at best yield a fraction of the

net potential benefit [10, 47]. Several studies, therefore, have compared completely conventional subsystem architectures to all-electric architectures, as these represent two ends of the subsystem architecture spectrum.

2. However, the gradual electrification of subsystems seen in current MEA (e.g., Airbus A380 and Boeing 787) indicates that industry prefers a progressive transition from a practical standpoint of implementation and risk mitigation.

3. Since the architectural transition is occurring through the development of MEA, two questions immediately arise. First, which subsystems should be targeted for electrification? Second, for those subsystems so targeted, which of several competing electric subsystem solutions is the most suitable?

4. In general, the majority of plausible solutions for each subsystem are not incompatible with the majority of solutions for the other subsystems, even though certain combinations may be impractical. The presence of multiple vehicle subsystems with multiple possible solutions for each results in a large combinatorial space of feasible/compatible subsystem architectures, all of which are not necessarily viable/practical.

5. A thorough investigation of the effect of vehicle class (i.e., size and weight) on the merits/de-merits of electric subsystem architectures relative to their conventional counterparts would be of significant value to conceptual designers of MEA, who must determine a limited number of subsystems to target for electrification, keeping in mind both the payoffs (incentives) and the technological risks.

6. In order to perform a fair comparison between conventional and electric subsystem architectures, it should be ensured that the conventional design is not unfairly or overly penalized through the assumptions made. For example,

if electric actuation is being compared to centralized hydraulic actuation, a state-of-the-art nominal pressure of 5,000 psi (which is already seen in service) should be considered rather than the traditional 3,000 psi [3].

7. Architecture comparisons of this nature do not have a "right" or "wrong" answer as such. The results of such comparisons are strongly dependent on the assumed current state-of-the-art and its projected future evolution [61], especially with regard to the power densities of electric components. Additional variability may result from differences in the so-called "ground rules" for comparison. For example, the results of independent studies conducted by Boeing and Rockwell (comparing electric control surface actuation to hydraulic) showed appreciable differences as the former allowed a hydraulic actuator to be replaced by an electric actuator which was not necessarily of the same configuration, while the latter did not [11].

8. The need to optimize the engine cycle to maximize fuel economy following the substitution of bleed air requirement with shaft-power requirement has been acknowledged [41]. However, it has also been noted that not all studies have taken this into consideration [3]. In particular, mis-representation of engine fuel consumption and hence mission fuel requirement is likely if pure shaft-power extraction is considered from an engine designed for mixed power off-take (both shaft-power and bleed), or conversely if mixed power extraction is considered from an engine designed to provide only shaft-power off-take. At the same time it must be borne in mind that due to the considerable expense and development time of a new engine, it is unreasonable to expect a bespoke engine cycle design for each and every subsystem architecture variant.

9. In cases where subsystem architecture transitions result in reductions of vehicle gross weight, two different opportunities may be perceived. The first is a

possible increase in the utility of the vehicle through an augmentation of its payload-range capabilities. The second is a further down-sizing of the vehicle through re-sizing of the design, while maintaining the same payload-range and point performance capabilities. The latter approach may be more applicable for comparative evaluations of subsystem architecture effects, since in each case, the capabilities of the aircraft remain the same [40].

Due to the very nature of the subsystems analysis problem itself, certain commonalities exist with regard to the approach followed in prior work performed both by individual researchers and industry. In particular:

- The sizing of the subsystems is driven by the flow-down of top-level vehicle and mission requirements, and the flow-down of additional requirements from sized subsystem components to other subsystem components that are sized further downstream.

- A distinction is made between *power consuming elements*, *power distributing elements*, and *power generating elements* (with some differences in the terminology used), and they are addressed in this order.

- Once sized, the impact of subsystems mass, power off-takes, and drag penalties at the aircraft and mission levels are assessed by linking this information with a suitable aircraft sizing and mission performance analysis tool (which varies from organization to organization).

The above characteristics are also to be found in the approach described in this dissertation. However, what distinguishes this dissertation from other work is the fact that it addresses certain aspects of the problem that were either not addressed by other researchers, or addressed in insufficient detail. Some of the chief distinguishing features, which are elaborated on in subsequent chapters, are summarized below:

29

1. A parsimonious modeling approach is undertaken using parameters that are either available or reasonably estimated in the early design phase. Large-scale interpolation or scaling from the results of prior studies is avoided. The modeling approach is transparent in that no restricted data or models are used.

2. The combinatorial problem arising from multiple solutions for each subsystem is addressed explicitly. Starting from an initially large number of combinations, a subset of interest is identified based on pertinent physical and engineering constraints. The impact of the identified subset of subsystem architectures at the vehicle and mission levels is then systematically assessed.

3. To assess the impact of aircraft size on the performance of subsystem architectures, three baseline aircraft which collectively cover a wide range of gross weights are considered: (i) a twin-engined Small Single-aisle Aircraft (SSA), (ii) a twin-engined Large Twin-aisle Aircraft (LTA), and (iii) a four-engined Very Large Aircraft (VLA). A summary of relevant information regarding these three aircraft sizes is provided in Table 1.

4. To satisfy the necessary architecture redundancy requirements without performing a formal fault-tree analysis, the connectivity of the power sources, power systems, and power consumers is determined through the incorporation of a set of heuristic rules that were identified by inspection and extrapolation of current design practices.

5. The effect of subsystem secondary power requirements on the engine thermodynamic cycle is accounted for by sizing a number of engines that differ in the magnitudes of shaft-power and bleed air that they are designed to supply. The mission performance of each subsystem architecture is then assessed using an appropriate architecture-to-engine association logic.

Table 1: Data summary for Small Single-aisle Aircraft (SSA), Large Twin-aisle Aircraft (LTA), and Very Large Aircraft (VLA) baselines. In each case, tabulated data corresponds to an aircraft with conventional subsystem architecture (hydraulic actuation, pneumatic ECS and ice protection, and no Electric Taxiing System)

Aircraft data	Aircraft Identification		
	SSA	**LTA**	**VLA**
Passenger capacity	170	396	852
Design range (NM)	3,000	7,800	8,200
Cruise Mach number	0.785	0.84	0.85
Max. ramp weight (lb)	175,130	746,610	1,270,000
Sea-level static thrust (lbf)	2 x 26,244	2 x 114,220	4 x 69,872
Wing planform area (ft^2)	1,347	4,695	9,111
Wingspan (ft)	114.8	201.8	266.4
Wing taper ratio	0.24	0.15	0.21
Wing 1/4-chord sweep (deg)	25	31.6	30
HT planform area (ft^2)	305	1,089	2,212
HT aspect ratio	5.47	4.50	4.49
HT taper ratio	0.37	0.30	0.39
HT 1/4-chord sweep (deg)	30	35	35
VT planform area (ft^2)	231	562	1,316
VT aspect ratio	1.80	1.60	1.74
VT taper ratio	0.30	0.29	0.39
VT 1/4-chord sweep (deg)	30	35	37
Fuselage length (ft)	123.3	239.8	230.9
Fuselage max. width (ft)	12.9	20.3	23.4
Fuselage max. height (ft)	12.9	20.3	27.9

6. The net impact of each architecture is broken down into the individual impacts of each constituent subsystem, which are further decomposed into the individual contributions from subsystem mass, secondary power requirement, and drag. This can guide the focus of subsystem design refinement efforts by facilitating a very fundamental assessment of each architecture's performance relative to a conventional baseline.

7. The sensitivity of the performance of subsystem architectures is assessed with respect to (i) variations in parameters that represent modeling uncertainty and (ii) variations in the assumed technological state-of-the-art (SOTA), especially with regard to electrical and electronic components. Such an approach allows the elicitation of more insight than possible in some other works where only point-solutions were compared.

1.9   *Chapter Summary*

The aerospace industry is currently experiencing a gradual transition towards More Electric subsystem architectures, which is driven by the technology saturation of conventional architectures and the steadily increasing competitiveness of electrical and electronic components.   Such novel subsystem architectures present the conceptual designer with additional challenges due to the lack of historical information and the need to down-select a reasonable number of architectures for further consideration from a large number of combinatorial possibilities.

The goal of this dissertation is to respond to these challenges by developing and demonstrating an integrated methodology that facilitates an assessment of candidate subsystem architectures using only the limited information that is available during aircraft conceptual design. This will permit designers to seek out combinations of subsystem solutions that yield favorable benefits relative to a conventional baseline despite variations in uncertainty parameters. It will also permit the investigation of possible relationships between vehicle size and the most favorable subsystem architectures for that size. Further, in addition to allowing the designer to assess the impact of a novel architecture relative to a conventional one, it will provide traceability that permits the overall impact to be decomposed and attributed to its underlying causes.

CHAPTER II

RESEARCH OBJECTIVE, RESEARCH QUESTIONS, AND HYPOTHESES

In Chapter 1, it was established that the design of subsystems for commercial aircraft had largely gravitated towards a conventional architecture in which secondary power is consumed in pneumatic, mechanical, hydraulic, and electrical form. The decades-long persistence of such conventionalism had permitted conceptual designers to account for the effect of subsystems through heuristic rules and statistical regression equations based off historical data. However, equivalent information of this nature is not available for the electric subsystem architectures towards which the aerospace industry is currently progressing as part of the More Electric Initiative. This therefore creates significant challenges for designing aircraft with such subsystem architectures.

The over-arching research objective of this dissertation, which was formulated based on the observations listed above and those discussed previously, is presented in §2.1. The research questions that must be addressed in order to realize this objective are identified and presented in §2.2. The research questions, associated hypotheses, and experiments which collectively form the research approach undertaken in this dissertation are discussed further in §2.3 - §2.4.

2.1 Research Objective

The objective of this dissertation is to develop a methodology that is capable of:

1. Integrating the explicit sizing and analysis of aircraft subsystem architectures with traditional aircraft sizing using methods suitable for and information available during aircraft conceptual design

2. Providing a rapid evaluation of the gross effect of different subsystem architectures on vehicle-level and mission-level performance, and decomposing the overall effect into individual contributions from various subsystems

3. Identifying the best-performing subsystem architectures for a given aircraft size with respect to suitable figures of merit, and assessing their sensitivities to epistemic uncertainty and assumed or projected technological state-of-the-art

The first capability allows initial sizing of aircraft subsystems and subsystem architectures in parallel with aircraft and engine sizing during aircraft conceptual design. Suitable sizing methods are those which are computationally inexpensive and do not require detailed aircraft definition, thus facilitating rapid tradeoffs using only information that is typically available during aircraft conceptual design.

The second capability allows not only the identification of the overall effect of a particular subsystem architecture, but also the decomposition of the overall impact into the contributions stemming from individual subsystems. This in turn allows the relative magnitudes of each subsystem's impact to be identified.

The third capability allows the best-performing subsystem architectures with respect to a suitable metric and for a given aircraft size to be identified. In addition, since the predicted performance is influenced by the fidelity of the modeling approach and assumptions regarding technological state-of-the-art, it allows the sensitivity of subsystem architectures to the above uncertainties to be assessed.

2.2 Statement of Research Questions

The stated research objective may be realized by addressing three major research questions, which are summarized below:

- **Research Question 1:** *How can the performance of competing solutions for a particular subsystem or competing subsystem architectures be compared at the vehicle and mission level using computationally inexpensive sizing and analysis methods that require only limited information regarding the aircraft design?*

- **Research Question 2:** *Which are the best-performing subsystem architectures with respect to a suitably defined performance metric or figure of merit and what variation in their performance, if any, occurs with variation in the aircraft size?*

- **Research Question 3:** *What is the sensitivity of the predicted performance of subsystem architectures to (i) variations in model parameters chosen to reflect epistemic uncertainty and (ii) variations in assumptions regarding current or projected technological state-of-the-art (SOTA)?*

These research questions are addressed by formulating hypotheses and subsequently testing these hypotheses with sets of experiments. The remainder of this chapter contains discussions leading up to the research questions and hypotheses and overviews of the experiments that are addressed in greater detail in subsequent chapters. Motivating discussions precede the introduction of each research question. Hypothesis formulations are followed by a discussion of the statements of the hypotheses. An overview of the research plan showing the relationships among research questions, hypotheses, and experiments is provided in Fig. 3.
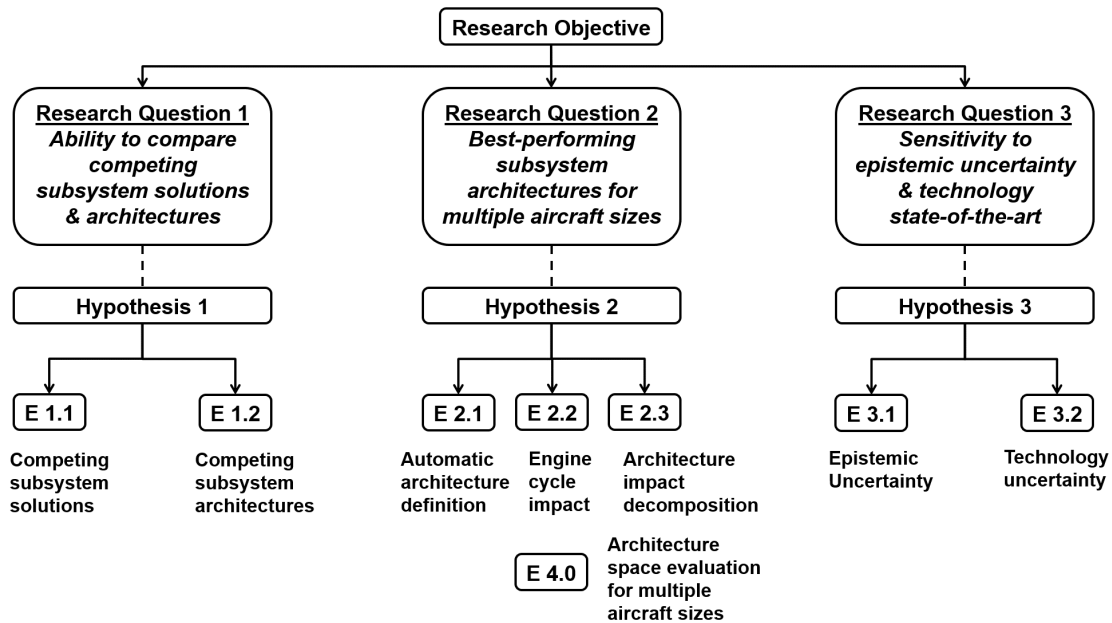
Figure 3: Summary of research questions, hypotheses, and experiments

2.3 Comparing Competing Subsystem Solutions and Competing Subsystem Architectures

Comparisons between novel or unconventional subsystem designs and conventional ones can be broken down into two major types:

1. Comparisons between competing solutions for a single subsystem

2. Comparisons between competing subsystem architectures

As an example of the first type of comparison, an Environmental Control System (ECS) solution that uses electric power may be compared against a conventional ECS solution that uses pneumatic power. In this case, the electric solution and the pneumatic solution are two competing solutions for the same subsystem: the ECS. The comparison may also be between two differing approaches to the same type of solution, e.g., electrothermal ice protection versus electroimpulse ice protection (both electric ice protection solutions), or electrohydrostatic actuation versus electromechanical actuation (both electric actuation solutions). The common

factor in these examples is that the focus is a single subsystem whose design is being varied, while the design of remaining subsystems is not altered unless necessary.

As an example of the second type of comparison, a design with electrified actuation, ECS, and ice protection systems may be compared to a design with hydraulic actuation, and pneumatic ECS/IPS. In this case, the comparison is between competing *subsystem architectures* - in this case between an All Electric subsystems architecture and a conventional subsystems architecture. This differs from the first type since the designs of multiple subsystems are being varied simultaneously.

For both the first and second comparison types, multiple choices exist regarding the metrics chosen for the comparison. A *subsystem-level metric* such as the net mass or weight of the subsystem ultimately feeds into a *vehicle-level metric* such as the aircraft's Operating Empty Weight (OEW). The OEW directly affects a *mission-level metric* such as required fuel, which in addition is also affected by subsystem secondary power requirements and drag increments. The OEW and the fuel requirement in turn affect other mission-level metrics such as Maximum Takeoff Weight (MTOW) or Maximum Ramp Weight (MRW). The intent and scope of the comparison determines the applicability of the subsystem-, vehicle-, and mission-level metrics.

The computational expense associated with subsystem sizing and evaluation methods is an important factor to consider, since the conceptual aircraft design phase is dominated by the need to perform rapid trade studies or comparisons between vehicle designs, or in this case, between subsystem architectures. Computationally burdensome methods would in such a scenario become a hindrance.

The success of the sizing and analysis methodology is also contingent on the input parameters required for the subsystem sizing methods remaining limited to those that are either available or easily estimated during conceptual aircraft design. For example, a method whose evaluation requires knowledge of wing planform area and sweep is acceptable, but one that requires detailed definition of the wing's airfoil or its

pressure distribution is not, since these latter parameters are finalized only through rigorous optimization occurring further downstream in the design process. These discussions motivate the first of the major research questions:

- **Research Question 1:** *How can the performance of competing solutions for a particular subsystem or competing subsystem architectures be compared at the vehicle and mission level using computationally inexpensive sizing and analysis methods that require only limited information regarding the aircraft design?*

In order to address the above research question, the following hypothesis, a discussion of which follows its formal statement, was formulated:

Hypothesis 1: *The differences between competing subsystem solutions or competing subsystem architectures with regard to suitable vehicle-level and mission-level metrics may be quantified within the framework of aircraft conceptual design by using an integrated sizing and analysis environment if it can be demonstrated that within said environment:*

(a) *the initial sizes and characteristics of major components in individual power consuming subsystems can be determined based on the definition of their functional requirements in conjunction with only the available or estimable aircraft and mission parameters and constraints*

(b) *the initial sizes and characteristics of additional components in power generation and distribution subsystems can be determined based on the identified requirements of the power consuming subsystems and the direct or heuristic identification of limiting, constraining, or off-nominal operating conditions*

(c) *the mission performance analysis reflects the direct and indirect effects of the subsystem architectures on the performance of the propulsion system*

(d) relevant dependencies can be established among subsystem-level and aircraft-level parameters to allow the simultaneous re-sizing of both parameter sets based on logically defined re-sizing rules

A brief description of the statements of the hypothesis is provided here as each statement will be addressed in greater detail in subsequent chapters. To give an example of the functional requirements mentioned in statement (a), the ECS may be considered. Its top-level functional requirements are to provide pressurization and adequate mass flow to specified compartments and, depending on the thermal loads experienced by the compartments, to remove or supply heat as required in order to maintain a desired temperature. The statement may be tested by verifying whether such top-level functional requirements, when viewed in conjunction with known or estimable attributes of the design (e.g., number of passengers, principal fuselage dimensions, pressurization schedule, etc.), allow quantities such as required mass flow rates, required range of cabin air inlet temperature and pressure, etc. to be computed. Successive flow-down of these derived requirements must in turn allow the determination of the necessary characteristics of ECS packs and their constituent components. Equivalent assessments applied to the other subsystems will complete the testing of this statement.

The additional architecture components referred to in statement (b) include distribution elements such as electric cables/wires for an electric system, pipes in a hydraulic system, and ducts in a pneumatic system. Further, they also refer to *source* elements such as electric generators and hydraulic pumps, which serve as the sources or producers of electric and hydraulic power respectively. The sizing conditions for these components are typically encountered only briefly during a normal flight, or in some cases they are encountered only during failure or degraded operating conditions. This statement may be tested by verifying whether such conditions can be identified and characterized using the information gained through (a) in addition to relevant

heuristic rules or guidelines available to the conceptual designer.

The *direct* and *indirect* effects of the subsystem architectures on the propulsion system performance (statement (c)) originate from the incremental fuel flow rate due to the incorporation of subsystems, which may be illustrated as follows:

$$\dot{w}_f = T_{req} \cdot SFC$$

$$\implies \Delta\dot{w}_f = T_{req} \cdot \Delta SFC + \Delta T_{req} \cdot SFC$$

$$= \underbrace{T_{req} \cdot (\Delta SFC_{spx} + \Delta SFC_{bx})}_{\textbf{Direct effect}} + \underbrace{(\Delta D_0 + \Delta D_i) \cdot SFC}_{\textbf{Indirect effect}} \qquad (3)$$

Here T_{req} and SFC are respectively the required thrust and the engine thrust-specific fuel consumption for a given flight condition, ΔSFC_{spx} and ΔSFC_{bx} are the degradations (increments) in TSFC due to shaft-power extraction and bleed extraction respectively, and $\Delta D_0 = \bar{q} S_w \Delta C_{D_0}$ and $\Delta D_i = \bar{q} S_w \Delta C_{D_i}$ are respectively the increments to zero-lift and induced drag components (or coefficients). To account for the direct effects of subsystem secondary power extraction on the engine (either as shaft-power or bleed), it must be possible to characterize the increase in engine SFC in terms of the shaft-power off-take P_{spx} and the bleed air off-take $\dot{m}_{bx}$, i.e., $\Delta SFC_{spx} = f(P_{spx}), \Delta SFC_{bx} = g(\dot{m}_{bx})$. The subsystems also indirectly affect the required fuel flow rate by affecting the required thrust through the addition of drag to the vehicle. The lift-independent drag component ΔD_0 captures the effect of external modifications to the aircraft through the incorporation of ram air inlets and the associated momentum drag of admitted ram air. The lift-dependent drag component ΔD_i accounts for the increase in induced drag that occurs due to the increased lift required to offset the added mass and fuel requirement of the subsystems.

The establishment of dependencies among subsystem requirements and the aircraft sizing parameters (such as S_w, T_{SL}, and W_{TO}) mentioned in statement (d) is necessary in order to allow the first group of parameters to respond to changes in the second group and vice versa. For example, let it be assumed that the change

from conventional to electric ECS architecture results in a reasonable change in the vehicle's OEW. In response to this change, the wing planform area S_w may need to be changed. This in turn may result in changes in the dimensions of the leading-edge and trailing-edge control surfaces. These may then cause changes in the weights of the wing IPS and control surface actuators. These latter two changes, triggered by changes in the architecture of an unrelated subsystem, will then feed back into the vehicle's OEW, thus creating a circular dependency. This necessitates a set of aircraft re-sizing rules for such scenarios, which will be discussed in a subsequent section. To test Hypothesis 1, two experiments are conducted:

- **Experiment 1.1 (§ 6.1):** Demonstrate that the developed sizing and analysis environment can be used to differentiate between two competing solutions for a single power consuming subsystem using relevant vehicle-level and mission-level metrics of interest, while assuming fixed vehicle size (no re-sizing of the vehicle) and invariant design for all unaffected subsystems.

  - **Overview:** The Environmental Control System (ECS) is considered. The two competing solutions are the conventional ECS and the electrified ECS. Based on the solution chosen, the ECS mass, secondary power requirements, and direct drag penalty change. The designs of all other power consuming subsystems are left unaffected. However, due to the change in the secondary power requirements of the ECS, there are concomitant changes to the Pneumatic Power Generation and Distribution System (PPGDS) and the Electric Power Generation and Distribution System (EPGDS). The two solutions are compared using suitable vehicle-level and mission-level metrics.

- **Experiment 1.2 (§ 6.2):** Demonstrate that the developed analysis environment can be used to differentiate between two competing subsystem

41

architectures using relevant vehicle-level and mission-level metrics of interest. Additionally, re-size the aircraft and demonstrate that the overall impact can be decomposed into the individual impacts stemming from various subsystems.

– **Overview:** Conventional and electrified solutions for the following subsystems are considered: Flight Controls Actuation System (FCAS), Landing Gear Actuation System (LGAS), Nose-wheel Steering System (NWSS), Wheel Braking System (WBS), Thrust Reverser Actuation System (TRAS), Environmental Control System (ECS), Wing Ice Protection System (WIPS), and Cowl Ice Protection System (CIPS). The secondary power requirements of the above determine the characteristics of the Hydraulic Power Generation and Distribution System (HPGDS), Pneumatic Power Generation and Distribution System (PPGDS), and Electric Power Generation and Distribution System (EPGDS). The above collectively constitute two subsystem architectures: a Conventional Subsystems Architecture (CSA) and an Electric Subsystems Architecture (ESA). For both cases, the aircraft are re-sized to meet the same point performance and mission performance requirements. The architectures are compared using suitable vehicle-level and mission-level metrics.

2.4 Evaluating Subsystem Architecture Space and the Effect of Aircraft Size

The two most notable commercial MEA in service today, the Airbus A380 and the Boeing 787, show important differences with respect to the subsystems that were targeted for electrification. On the Airbus A380, Electrohydrostatic Actuators (EHAs) and Electrical Backup Hydraulic Actuators (EBHAs) are incorporated on some flight control surfaces. An Electric Thrust Reverser Actuation System (ETRAS) is also present. However, other subsystems such as the ECS and the IPS retain a

conventional architecture. On the Boeing 787, the extent of electrification of the subsystem architecture (in terms of secondary power consumption) is greater. The most significant electrification is clearly that of the ECS, followed by the wing IPS. Electric engine starting is employed and electromechanically actuated wheel brakes are used. Additionally, a few of the wing spoilers and the Trimmable Horizontal Stabilizer (THS) are electrically actuated. There is more significant usage of localized hydraulic circuits that are pressurized by Electric Motor (Driven) Pumps (EMPs) rather than Engine Driven Pumps (EDPs). The immediate question that arises based on these observations is: *Why do these two More Electric Aircraft differ in both the nature and the extent of subsystem electrification?*

A possible and quite likely explanation for this particular case may be differences in organizational philosophy and the approach taken to limit technological risk. However, this observation raises interesting general questions regarding (i) combinations of solutions for different subsystems for which the overall subsystem architecture shows enhanced performance and (ii) variations in the performance with aircraft size. These therefore form the basis for the second major research question:

- **Research Question 2:** *Which are the best-performing subsystem architectures with respect to a suitably defined performance metric or figure of merit and what variation in their performance, if any, occurs with variation in the aircraft size?*

The following observations played a significant role in the formulation of a hypothesis associated with the above research question:

1. As there are multiple subsystems and multiple solutions for each, there is a large combinatorial space of subsystem architectures. A comparative assessment of the performance of architectures within this space, or at least a logically defined sub-space of it, is required

2. These architectures differ in the nature, number, and connectivity of the

elements present within them. Since these elements contribute directly to subsystem mass, a means to determine which elements are necessary and how they are connected to one another is required before the sizing of the elements themselves can commence

3. Gas turbine engines designed for a conventional subsystems architecture provide *mixed* secondary power in the form of both shaft-power and bleed air. If a subsystem architecture required pure shaft-power off-take, it is likely that this requirement would be factored into the sizing of the engine itself. Therefore, the ability to capture the effect that the subsystem architecture off-takes would have on the determination of the engine cycle characteristics is desirable

4. The selection of an aircraft-level or mission-level metric to measure subsystem architecture performance does not by itself provide sufficient information to guide the design of the individual subsystems themselves to enhance the performance. Thus, a method is required that allows the contributions of individual subsystem masses, secondary power requirements, and drag increments towards the top-level performance metric to be traced

Based on the above observations Hypothesis 2, whose stipulations correspond directly to the observations above, was formulated as follows:

Hypothesis 2: *Any variations of the preferred subsystem architectures (as measured with respect to a suitably defined figure of merit) with aircraft size may be ascertained through the integrated analysis if it can be demonstrated that:*

(a) *with knowledge of subsystem non-propulsive power requirements, it is possible to determine the number, nature, and connectivity of required subsystem architecture elements using heuristic rules that implicitly capture architecture redundancy requirements*

(b) with an estimate of the type and magnitude of non-propulsive power requirements, it is possible to capture the effect of changes in the engine cycle that would be driven by this information

(c) the relative magnitudes of the contributions of individual subsystems towards the top-level figure of merit can be identified and decomposed further into contributions from subsystem mass, secondary power requirements, and drag increments

With regard to statement (a), in some cases it is quite trivial to determine whether certain architecture elements are required or not. For example, if actuation functions use hydraulic power, then it is clear that hydraulic systems and pumps will be required. However, it is more challenging to determine *how many* hydraulic systems are required in order to satisfy redundancy requirements, which in turn would depend on how flight-critical the hydraulically actuated functions are. This determination typically occurs later in the design process using Failure Modes and Effects Analyses (FMEA) or Fault Tree Analyses (FTA). Statement (a) makes the claim that an equivalent determination that is suitable for the purpose of early subsystem architecture assessments may be made using heuristic rules or guidelines as opposed to formal FMEA/FTA methods. Experiment 2.1 (described subsequently) was formulated in order to test this statement.

The effect of subsystem secondary power requirements on the engine cycle parameters (statement (b)) can be analyzed using a higher-fidelity propulsion system analysis tool. It is also possible to integrate such a tool directly with the subsystems sizing and analysis environment. However, this may be infeasible from the point of view of computational expense. Instead, a higher-fidelity propulsion system analysis tool can be used to establish a *truth model*, which can be queried in order to determine the effect of secondary power off-takes on the engine's performance. Experiment 2.2 (described subsequently) was formulated in order to test this possibility.

Statement (c) is concerned with defining a suitable performance metric for each subsystem to be sized to based on its effects on vehicle level energy consumption. There is potentially a difference between this approach and designing each subsystem to optimize a single criterion such as subsystem mass or power consumption. For a fuel-consuming aircraft, the effect of the subsystems on the energy optimality of the vehicle may be regarded as the increment in fuel consumption due to their presence and operation. This was illustrated in Eq. 3, which is re-arranged below.

$$
\begin{aligned}
\Delta \dot{w}_f &= \underbrace{T_{req} \cdot (\Delta SFC_{spx} + \Delta SFC_{bx})}_{\textbf{Direct effect}} + \underbrace{(\Delta D_0 + \Delta D_i) \cdot SFC}_{\textbf{Indirect effect}} \\
&= \underbrace{T_{req} \cdot \Delta SFC_{spx}}_{\textbf{Shaft-power}} + \underbrace{T_{req} \cdot \Delta SFC_{bx}}_{\textbf{Bleed}} + \underbrace{\Delta D_0 \cdot SFC}_{\textbf{Drag}} + \underbrace{\Delta D_i \cdot SFC}_{\textbf{Weight}} \\
&= \Delta \dot{w}_{f,spx} \quad + \quad \Delta \dot{w}_{f,bx} \quad + \quad \Delta \dot{w}_{f,d} \quad + \quad \Delta \dot{w}_{f,w} \quad (4)
\end{aligned}
$$

Thus, each subsystem will penalize (increase) the vehicle's rate of fuel consumption (fuel flow rate) through its shaft-power requirement (if present), bleed air requirement (if present), direct drag increment (if present), and weight (always present). The absolute and relative magnitudes of these components will, of course, vary from subsystem to subsystem. However, the increment in fuel flow rate is representative of the additional *power* required to support (operate *and* carry) the subsystems. To obtain the additional *energy* required to support the subsystems, the evolution of the additional power requirement over the course of a mission must be considered:

$$
\begin{aligned}
\Delta w_f &= \int_{t_i}^{t_f} \Delta \dot{w}_{f,spx}(t)dt + \int_{t_i}^{t_f} \Delta \dot{w}_{f,bx}(t)dt + \int_{t_i}^{t_f} \Delta \dot{w}_{f,d}(t)dt + \int_{t_i}^{t_f} \Delta \dot{w}_{f,w}(t)dt \\
&= \Delta w_{f,spx} \quad + \quad \Delta w_{f,bx} \quad + \quad \Delta w_{f,d} \quad + \quad \Delta w_{f,w} \quad (5)
\end{aligned}
$$

The relative magnitudes of the four effects (shaft-power, bleed, drag increment, and weight) may be conveniently represented through the following ratios:

$$
\kappa_{spx} = \frac{\Delta w_{f,spx}}{\Delta w_f}, \qquad \kappa_{bx} = \frac{\Delta w_{f,bx}}{\Delta w_f}, \qquad \kappa_d = \frac{\Delta w_{f,d}}{\Delta w_f}, \qquad \kappa_w = \frac{\Delta w_{f,w}}{\Delta w_f} \qquad (6)
$$

The relative magnitudes of the four ratios κ_{spx}, κ_{bx}, κ_d, and κ_w provide a rational means of linking a mission-level metric such as fuel consumption to the design

characteristics of the subsystems. Considering for example the landing gear actuation subsystem, which may use either hydraulic or electric power, $P_{spx} \neq 0, \dot{m}_{bx} = 0$. Further, assuming that there is no substantial drag increment on account of the actuator alone, $\Delta D_0 \approx 0$. However, the landing gear actuator operates twice per flight, for about 20-30 seconds per occurrence, whereas its weight is borne within the aircraft for the entire flight. Considering the integration over time in Eq. 5 and then Eq. 6, it is clear that $\kappa_{spx} \ll \kappa_w$. In other words, based on the manner in which it impacts a mission-level metric such as fuel consumption, there is strong justification for concentrating design effort on minimizing the actuator weight. Similar arguments apply to subsystems which operate infrequently (i.e., do not consume secondary power continuously) and essentially serve as *dead-weight* for the majority of the flight.

Considering instead the ECS, depending on whether it is pneumatic or electric, $\dot{m}_{bx} \neq 0$ or $P_{spx} \neq 0$. In both cases $W_{sub} \neq 0, D_0 \neq 0$, the latter since the use of ram air as the heat sink adds drag to the vehicle. Since the ECS operates throughout the flight, it is much less clear *a priori* what the relative magnitudes of the factors κ_{spx}, κ_{bx}, κ_d, and κ_w are, and whether any of them is dominant. Further, considering a potential transition from conventional to electric ECS architecture, the bleed air requirement $\dot{m}_{bx}$ is replaced by shaft-power requirement P_{spx}, but the drag penalty ΔD_0 is also higher as the cabin air must now be admitted through a separate ram air inlet. It follows then that for an electric ECS, the magnitudes of the factors κ_{spx}, κ_{bx}, κ_d, and κ_w, and thus the focus of design efforts may be considerably different.

In the case of an *optional* subsystem, which may or may not be present within an architecture, a determination of whether it can "buy its way onto the airplane" must be made. For example, an Electric Taxiing System (ETS) permits the aircraft to be taxied without using main engine thrust. The practicality of such an optional subsystem may be evaluated through a modified form of Eq. 5,

$$\Delta w_f = \Delta w_{f,spx} + \Delta w_{f,b}^{\,0} + \Delta w_{f,d}^{\,0} + \Delta w_{f,w} - \Delta w_{f,mc}, \tag{7}$$

in which $\Delta w_{f,mc} > 0$ represents any fuel *saved* due to *mitigating circumstances*. In this case, this would be due to the fact that the electric motors are powered from the APU while the main engines are not turned on. The desired outcome from this optional subsystem is fuel savings: $\Delta w_f < 0$. It is clear that the sign of Δw_f is determined by the relative magnitudes of $\Delta w_{f,mc}$ (function of taxiing time), $\Delta w_{f,spx}$ (function of motor power draw), and $\Delta w_{f,w}$ (function of additional weight). Further, since electric taxi motors become dead-weight during non-taxiing phases of flight, it is clear that the longer the duration of the flight $\Delta t = t_f - t_i$, the less attractive this feature will become. In fact, if for very long-haul flights, $\Delta w_f > 0$ is obtained, then the inclusion of this technology may not be justifiable. Such conclusions were drawn by an Airbus trade study into the Electric Green Taxiing System (EGTS) [32].

Experiments 2.1, 2.2, and 2.3 are intended to test the statements of Hypothesis 2, while Experiment 4.0 is intended to address Research Question 2 directly. The formal statements of all the experiments are as follows:

- **Experiment 2.1 (§7.1):** Verify whether an architecting algorithm designed to determine the connectivity among subsystem architecture elements can reproduce the known subsystem architectures of existing commercial aircraft with acceptable accuracy and equivalent redundancy.

  - **Overview:** The architecting algorithm is provided inputs corresponding to the known subsystem architectures of existing aircraft, such as the number of engines, number of control surfaces, solutions employed for various subsystems (conventional or More Electric), etc. The subsystem architectures generated by the architecting algorithm with these inputs are compared to the existing aircrafts' actual subsystem architectures. For each such benchmarking case, a determination is made regarding whether the generated and actual architectures are equivalent in terms

of redundancy. This is done by inspecting and comparing the association of (i) power systems to power consumers, (ii) power systems to power sources, and (iii) power sources to prime movers.

- **Experiment 2.2 (§7.2):** Verify whether it is possible to capture the effects of secondary power extraction on the sizing and performance of a gas turbine engine sized to provide a certain combination of shaft-power and bleed air without directly integrating a higher-fidelity propulsion system sizing and analysis tool into the subsystems sizing and analysis environment.

  - **Overview:** A performance model for a gas turbine engine sized for a given secondary power extraction using a higher-fidelity propulsion system sizing and analysis tool is treated as the truth model. The truth model is queried in order to determine coefficients that represent the sensitivity of engine performance to shaft-power and bleed air extraction. The fuel consumption predicted using these coefficients is compared to that predicted using the truth model directly to verify the feasibility of incorporating the coefficients (as opposed to the truth model) into the mission performance analysis.

- **Experiment 2.3 (§7.3):** Verify whether the contribution of each individual subsystem's mass, secondary power requirements, and drag increments (if any) towards a top-level performance metric can be determined in order to guide subsequent design efforts for the subsystems. Further, verify whether this method allows a determination regarding the inclusion of a certain optional subsystem within a subsystem architecture to be made.

  - **Overview:** (i) A two-level decomposition of the impact of a particular subsystem architecture on a mission-level metric such as fuel burn is presented. The net impact is first decomposed into contributions from the individual subsystems, and then further decomposed into the contributions

from each subsystem's mass, secondary power requirements, and drag increments. (ii) The utility of the two-level decomposition in determining the focus of design refinement efforts for the subsystems is demonstrated using two major subsystems as examples. (iii) The necessary conditions which may justify the incorporation of an optional subsystem into the aircraft subsystem architecture are investigated.

- **Experiment 4.0 (§9.1, §9.2):** Identify the best-performing subsystem architectures or high-performance subsystem architectures with respect to a suitably defined performance metric for differing aircraft sizes.

  - **Overview:** A comparative assessment of the performance of subsystem architectures from within the architectural space with respect to suitable aircraft-level and mission-level performance metrics is presented. This assessment is made for aircraft of differing sizes in order to determine the effect of aircraft size on the performance of subsystem architectures.

2.5 Investigating Subsystem Architecture Sensitivities to Modeling and Technological Uncertainty

The discussion thus far has focused on (i) sizing the aircraft subsystems using the limited information that exists regarding the design in the conceptual design phase, and (ii) assessing the impacts of subsystem architectures on aircraft-level and mission-level metrics. However, the performance predicted for an architecture may be quite sensitive to uncertainties from various sources. For the purposes of this dissertation, uncertainties are classified as:

1. Epistemic uncertainty: This is uncertainty that exists due to a lack of knowledge or incomplete knowledge during the modeling of a system [62], or due to the limitations inherent in the modeling approach

2. Technology uncertainty: This exists due to the inability to predict with 100 % confidence the technological state-of-the-art (SOTA) at a future time

A few examples of epistemic uncertainty are provided as follows: (i) The actuation loads for certain control surfaces are determined based on their dimensions, the estimation of their hinge moment coefficients, and the identification of the flight condition that results in the maximum aerodynamic load. In conceptual design, only a preliminary estimate (at best) can be made for each of these, and therefore the computed actuation load is subject to epistemic uncertainty. (ii) The computed power (heat) requirement for the IPS depends on an estimate of the surface area to be protected and the net heat flux for a given set of atmospheric and flight conditions. Without detailed icing simulations, only a preliminary estimate can be made for the protected area, while the computation of the heat flux is subject to multiple simplifying assumptions. (iii) The computed total ECS thermal load depends on an estimate of the internal cabin heat loads and the rate of heat exchange between the cabin and the ambient. Without detailed cabin thermal simulations, only preliminary estimates for these heat loads (at best) can be obtained.

Technology uncertainty, on the other hand, arises as the rate of evolution of the state-of-the-art (SOTA) of a technology or field cannot be predicted with absolute certainty. Such predictions are often required for feasibility studies or due to the fact that the design process for a complex commercial aircraft may span over a decade, thus necessitating a projection of the technological SOTA to correspond to the time of fabrication. This is even more relevant for the case of More Electric subsystem architectures, whose predicted viability relative to conventional architectures is strongly influenced by the assumed technological SOTA for components such as electric motors, power electronics, etc., which are on reasonably steep development curves. The presence of these two forms of uncertainty motivated the third major research question, which is stated as follows:

- **Research Question 3:** *What is the sensitivity of the predicted performance of subsystem architectures to (i) variations in model parameters chosen to reflect epistemic uncertainty and (ii) variations in assumptions regarding current or projected technological state-of-the-art (SOTA)?*

A hypothesis corresponding to this research question and a set of experiments addressing both forms of uncertainty are described as follows:

Hypothesis 3: *The sensitivity of the predicted performance of an architecture to epistemic uncertainties and uncertainties regarding technological state-of-the-art can be assessed through a sensitivity analysis in which*

(a) *a parsimoniously selected set of model K-factors is varied in order to represent variations in internally computed model parameters that would occur due to inaccuracies or limitations of subsystem modeling approaches, or due to the presence of simplifying assumptions*

(b) *a parsimoniously selected set of technology K-factors is varied in order to represent the variations in technological state-of-the-art of architecture components such as electric motors, power electronics, and generators, which have a significant impact on electrified subsystem architectures, and for which there is currently a relatively steep development curve*

- **Experiment 3.1 (§8.1):** Determine the sensitivity of certain select subsystem architectures to deliberate variations in internal model parameters that may in reality occur due to the existing epistemic uncertainty.

  - **Overview:** A limited number of subsystem architectures is chosen which include the following: (i) conventional, (ii) All Electric, (iii) bleedless (with conventional actuation), and (iv) electric actuation (retaining pneumatics). The sensitivity of the performance of these architectures to the variation

of certain key internal model parameters is determined. A determination is also made regarding whether some architectures are more/less sensitive to certain parameter variations than others.

- **Experiment 3.2 (§8.2):** Determine the sensitivity of certain select subsystem architectures to variations in the technological state-of-the-art of certain key architecture components such as electric motors, power electronics, ECS compressors, and generators.

  - **Overview:** A limited number of subsystem architectures is chosen which include the following: (i) All Electric, (ii) bleedless (with conventional actuation), and (iii) electric actuation (retaining pneumatics). The overall sensitivity of the performance of these architectures to variations in technological state-of-the-art and the contributions of individual technology K-factors to the sensitivity are determimed.

2.6 Chapter Summary

This chapter introduced the research objective of this dissertation and identified the research questions to be pursued in order to meet the objective. A hypothesis associated with each major research question was formulated. Additionally, experiments were outlined whose intended purpose is to test the hypothesis statements or address the research question itself. The technical approach pursued in this dissertation is introduced and discussed in Chapter 3, with further technical details regarding the modeling of subsystem architecture elements presented in Chapters 4 and 5. The experiments aimed at verifying the capabilities of the developed approach and assessing the performance and sensitivities of subsystem architectures follow subsequently in Chapters 6 through 9. Finally, the conclusions and contributions of the research effort are discussed in Chapter 10 along with the identification of avenues for future work.

CHAPTER III

TECHNICAL APPROACH

During the traditional aircraft conceptual design process, only limited attention has been given to the aircraft subsystems, which instead are considered in more detail in subsequent design phases [37]. However, from the discussion in previous chapters, it is clear that this can no longer be the case for novel or unconventional subsystem architectures that may be used for future AEA or MEA. In fact, for the design of such AEA/MEA, the preliminary design of the aircraft subsystems must be considered in parallel with conceptual aircraft and engine sizing in an integrated approach. In Chapter 2, this was identified as one of the primary objectives of this dissertation. This chapter contains technical details regarding the approach taken to meet the research objectives. The relationship between *system* and *subsystem* within the context of this dissertation, a generalized representation of subsystem architectures, the subsystems considered within the scope of this work, a measure of subsystem electrification, and a means to decompose subsystem impacts within an architecture are first presented in §3.1. Following this, the developed integrated sizing and analysis approach is presented, and each of the modules is discussed in some detail in §3.2.

3.1 System, Subsystems, and Subsystem Architectures

A complex engineering system may be considered to be constituted by multiple subsystems, with the individual subsystem functionalities contributing to the net system functionality. Since the terms *system* and *subsystem* are ubiquitous within this dissertation, it is necessary therefore to define what constitutes the *system* and what constitutes *subsystems*. For the purpose of this dissertation, the *system* is the aircraft itself, with the Aircraft Equipment Systems (AES) constituting the *subsystems*.
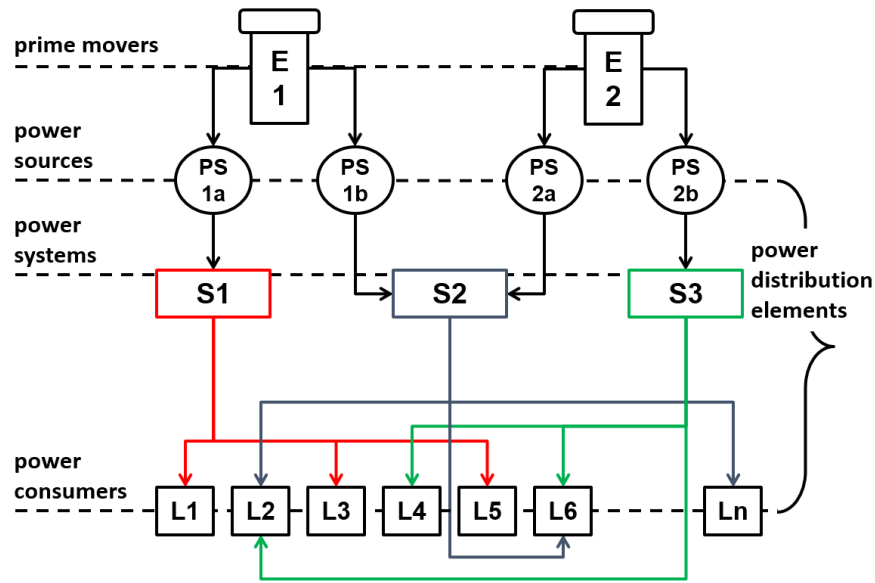
Figure 4: Generalized representation of subsystems architecture

3.1.1 Subsystem Architectures

While the term *subsystem* suggests a certain amount of physical and functional compartmentalization, it is also true that to provide the desired functionality, several subsystems must be linked together within an *architecture*. The subsystems, as discussed within the remainder of this dissertation, are assumed to fall within the generalized subsystem architecture shown in Fig. 4. This generalized representation comprises the following five elements:

1. **Prime movers:** These may be thought to be the origins of *all* types of secondary power. As discussed previously, the main engines generally satisfy this role, but an APU satisfies the definition as well

2. **Power sources:** These may be thought to be the origins of a *specific* type of secondary power. By this definition, the power sources include (i) electric generators, (ii) hydraulic pumps, and (iii) pneumatic bleed ports. In each case, these are the points within the subsystem architecture where the corresponding

55

form of secondary power first becomes available. Multiple power sources of the same type may be present (e.g., multiple pumps and generators)

3. **Power systems:** These are responsible for receiving secondary power, and regulating or transforming this power to meet the requirements of architecture elements located further downstream. They include (i) electric systems, within which power transformations across different voltage types and magnitudes may occur, (ii) hydraulic systems, within which hydraulic pressure may be regulated, and (iii) pneumatic systems, within which elements may be present that regulate the state of the pneumatic power received. Like the power sources, the subsystem architecture may feature multiple power systems of the same type

4. **Power distribution elements:** These link the power sources to the power systems and the power systems to the power consumers. They are responsible for physically conveying the appropriate secondary power from one point to another. They include (i) electrical cabling/wiring, (ii) hydraulic piping, and (iii) pneumatic ducting. Connecting elements may link multiple power sources to the same power system, and multiple power systems to the same power consumer

5. **Power consumers:** These are the end recipients or consumers of secondary power, which is used in order to provide some functionality to the aircraft. If the flow of secondary power within a subsystem architecture is considered, then the power consumers are effectively the *end loads*

The subsystem architecture components when presented in the order above also represent the actual flow of secondary power within the subsystem architecture. However, for sizing of the subsystem architecture components, a bottom-up approach is required. In other words, the power consumers must be addressed first, which involves the determination of their secondary power requirements, mass, and direct

drag contributions, if any. These are determined based on a flow-down of requirements from the aircraft level and their translation into corresponding subsystem-level requirements.

Within this dissertation, the power sources, power systems, and power distribution elements for a particular secondary power type are collectively referred to as the *Power Generation and Distribution Systems* (PGDS). The sizing of the PGDS elements follows that of the power consuming subsystems, and requires knowledge regarding not only the magnitudes of secondary power required by the power consuming subsystems, but also the connectivity of elements within the subsystem architecture. The connectivity for a conventional subsystems architecture is fairly well-established, while for a MEA architecture it is not necessarily obvious. However, it is essential to be cognizant of these associations while comparing conventional and MEA architectures as the presence of redundant architecture elements (multiple actuators, multiple hydraulic systems, etc.) contributes significantly to aircraft empty weight.

The power consuming subsystems and power generation and distribution subsystems that are addressed within the scope of this dissertation are summarized in Fig. 5. The power consuming subsystems considered include the (i) Flight Controls Actuation System (FCAS), (ii) Landing Gear Actuation System (LGAS), (iii) Nose-wheel Steering System (NWSS), (iv) Wheel Braking System (WBS), (v) Thrust Reverser Actuation System (TRAS), (vi) Electric Taxiing System (ETS)[1], (vii) Environmental Control System (ECS), (viii) Wing Ice Protection System (WIPS), and (ix) Cowl Ice Protection System (CIPS).

A PGDS was considered for each of the secondary power types. Further, since hydraulic and electric power are obtained from the conversion of mechanical power (shaft-power), four PGDS were considered in total: (i) the Electric Power

---

[1]Of the power consuming subsystems, the Electric Taxiing System (ETS) differs from the others in that it is an *optional* subsystem that need not necessarily exist within all subsystem architectures.

SPX:	shaft-power extraction
BX:	bleed (air) extraction
MPGDS:	Mechanical power generation & distribution (sub)system
HPGDS:	Hydraulic power generation & distribution (sub)system
EPGDS:	Electric power generation & distribution (sub)system
PPGDS:	pneumatic power generation & distribution (sub)system
FCAS:	Flight controls actuation (sub)system
LGAS:	Landing gear actuation (sub)system
NWSS:	Nose-wheel steering (sub)system
WBS:	Wheel braking (sub)system
TRAS:	Thrust reverser actuation (sub)system
ETS:	Electric taxiing system (sub)system (optional)
ECS:	Environmental control system (sub)system
WIPS:	Wing ice protection system (sub)system
CIPS:	Cowl ice protection system (sub)system
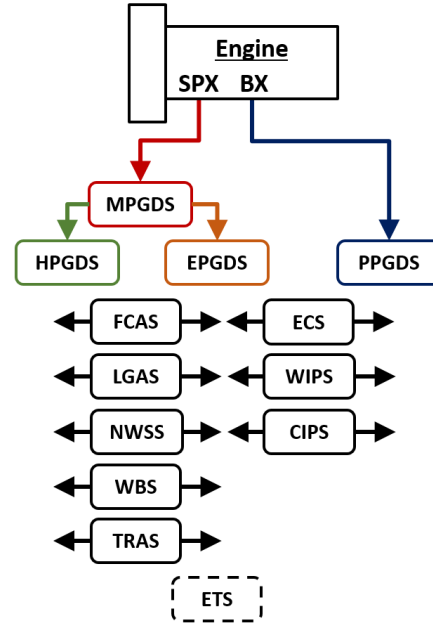
Figure 5: Summary of power consuming subsystems and power generation and distribution subsystems considered within the scope of the dissertation

Generation and Distribution System (EPGDS), (ii) the Hydraulic Power Generation and Distribution System (HPGDS), (iii) the Pneumatic Power Generation and Distribution System (PPGDS), and (iv) the Mechanical Power Generation and Distribution System (MPGDS).

Since the All Electric Engine (AEE) is not considered within the scope of this dissertation, the MPGDS and the EPGDS exist within all subsystem architectures considered. However, for architectures where no hydraulic and/or pneumatic power is consumed by any power consuming subsystems, the HPGDS and/or the PPGDS can be eliminated entirely from the aircraft.

Of the power consuming subsystems, the FCAS, LGAS, NWSS, WBS, and TRAS are frequently referred to within this dissertation as the *actuation functions* or the *actuation subsystems*, since they are involved in the actuation of movable components or *movables*. As discussed in Chapter 1, within a conventional subsystems architecture, the actuation functions use hydraulic power, while within an electrified

subsystems architecture, they would use electric power. These two possible secondary power types for the actuation functions are indicated by the arrows in Fig. 5. Similarly, the ECS, WIPS, and CIPS within a conventional architecture use pneumatic power, while within an electrified architecture, they too would use electric power.

The fact that multiple secondary power options exist for these subsystems is the basis for the existence of numerous combinatorial possibilities for the aircraft-level subsystems architecture. Further, multiple solutions may exist for each subsystem that make use of the same secondary power type, which results in a further combinatorial expansion of the architecture space.

3.1.2 Degree of Subsystem Electrification (DSE)

When evaluating multiple subsystem architectures, it is convenient to have a simple metric that indicates to what extent an architecture has been electrified.

1. It is insufficient to simply use the *number* of electrified subsystems as an indicator, since the aircraft-level or mission-level impact of the electrification of a particular system may differ considerably from that of another

2. Merely considering the installed electrical power generation capacity or its ratio to hydraulic and pneumatic capacities does not directly indicate the degree to which it is utilized over the course of a flight

3. The metric must account for the fact that certain subsystems operate throughout the flight while others are only active for brief durations

Based on the above considerations, the Degree of Subsystem Electrification (DSE) is proposed as a simple measure of the extent of electrification of a given architecture. The DSE is defined as the ratio of the electrical energy consumed by N power consuming subsystems over a mission duration $[0, T]$ to the total non-propulsive

59

energy consumed by them over the same duration in either electrical, hydraulic, or pneumatic form.

$$DSE = \frac{\sum_{i=1}^{N} \int_0^T P_{elec}(t).dt}{\sum_{i=1}^{N} \int_0^T \{P_{elec}(t) + P_{hyd}(t) + P_{pneu}(t)\} .dt} \tag{8}$$

The pneumatic power corresponding to bleed air extraction $\dot{m}_b$ is determined as $P_{pneu}(t) = \dot{m}_b(t) \ h(T_{ref})$, where $h(T_{ref})$ is the specific enthalpy of the bleed air at a reference bleed air temperature, taken here to be $T_{ref} = 500 \ K$ (based on typical bleed system temperatures given by Hunt [13]). From Eq. 8, it is clear that $DSE = 1$ indicates an AEA in which power consuming subsystems use only electric power.

The DSE considers directly the time-dependency of the power consumption of the subsystems. In that regard, it is superior to a metric that simply considers the maximum magnitudes of electric power (installed generator capacity), hydraulic power (installed pump capacity), and pneumatic power (maximum rate of bleed air extraction), since it is well-known that the installed capacity is not completely utilized throughout the mission.

3.1.3 Total Fuel Impact and Total Weight Impact of Subsystems

A subsystem penalizes the vehicle's fuel burn through weight, the extraction of secondary power from the engine in the form of shaft-power and/or bleed, and the direct generation of additional drag. The summation of these effects over a defined mission gives the subsystems Total Fuel Impact (TFI):

$$TFI^{(i)} = \Delta w_{f,w}^{(i)} + \Delta w_{f,spx}^{(i)} + \Delta w_{f,bx}^{(i)} + \Delta w_{f,d}^{(i)} \tag{9}$$

The Total Weight Impact (TWI) may additionally be assessed by adding the weight of the subsystem to the TFI obtained using Eq. 9:

$$TWI^{(i)} = w_{ss}^{(i)} + \Delta w_f^{(i)} = w_{ss}^{(i)} + \Delta w_{f,w}^{(i)} + \Delta w_{f,spx}^{(i)} + \Delta w_{f,bx}^{(i)} + \Delta w_{f,d}^{(i)} \tag{10}$$

The TFI of a subsystem essentially indicates its contribution to the aircraft's mission fuel burn, while the TWI essentially indicates its contribution to the ramp weight. Moir [63] states that when comparing systems, the overall system weight penalty (i.e., the TWI) should be used. However, in case of More Electric subsystem architectures, an increase in the empty weight of the aircraft is not necessarily unacceptable if there is a simultaneous reduction in fuel consumption [48]. There may be cases therefore where, relative to a conventional baseline, a More Electric subsystem solution has a favorable TFI but an unfavorable TWI. Since one of the stated goals of the More Electric Initiative is to reduce fuel consumption, it would be unfair to consider a MEA architecture as being *unfavorable* simply based on the unfavorable TWI. Therefore, while both TFI and TWI are computed for subsystem architectures, the TFI is analyzed in greater detail within this dissertation.

3.2 Integrated Sizing and Analysis Approach

A top-level overview of the implemented approach for the integrated sizing and analysis of the aircraft and its subsystem architecture is presented in Fig. 6. It involves the flow of necessary information to/from the following major modules, each of which is expanded upon further in the remainder of this chapter.

1. Definition of design requirements

2. Traditional aircraft and engine sizing

3. Generation of subsystem architecture combinations

4. Subsystem architecture sizing and evaluation

5. Evaluation and decomposition of subsystem impacts

6. Re-sizing of aircraft and subsystems

7. Post-processing analyses
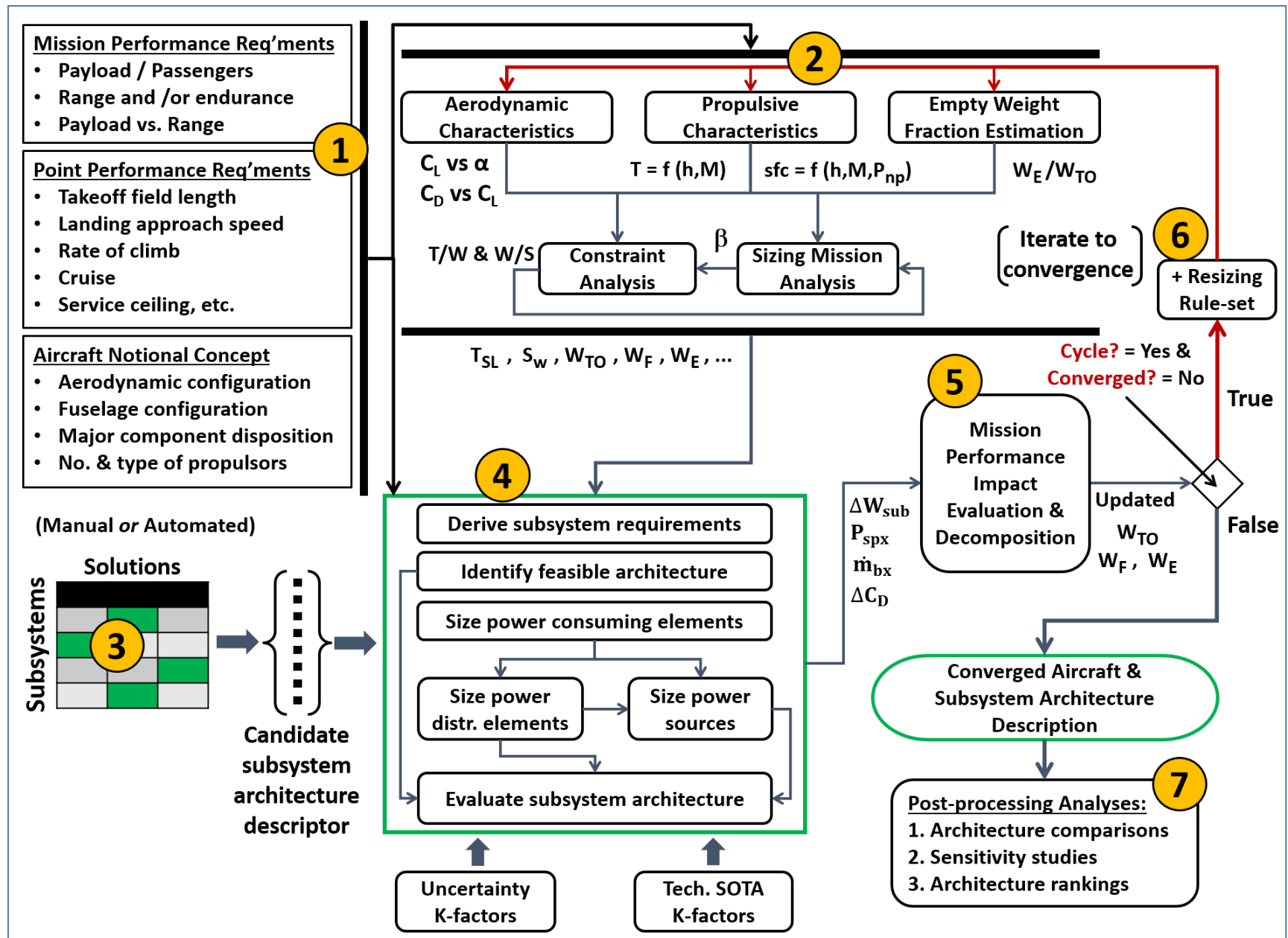
Figure 6: Integrated approach developed for aircraft and subsystem sizing
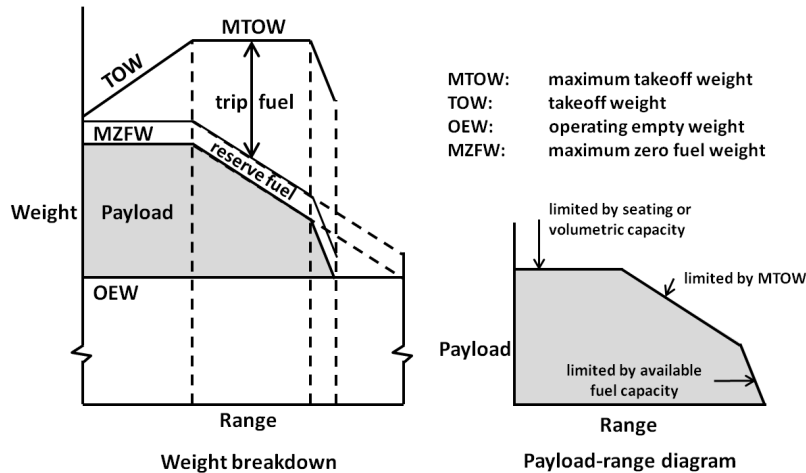
Figure 7: Notional payload-range characteristics

3.2.1 Definition of Design Requirements

These are the standard design requirements that apply to the design of commercial transport aircraft. They include:

1. Mission performance requirements: For a commercial transport, these are defined mainly through the vehicle's range and payload capabilities, which are typically specified using a payload-range diagram, a notional example of which is shown in Fig. 7

2. Point performance requirements: These are additional operational constraints which the vehicle must satisfy in order to ensure adequate operability. Commonly specified requirements include takeoff and landing field lengths (TOFL/LFL), landing approach speed, rate of climb, minimum climb gradient following engine-failure or go-around initiation, cruise requirements stated in terms of altitude/Mach number combinations, service ceiling, etc.

3. Aircraft notional concept: This provides general information such as the relative arrangement of lifting surfaces, fuselage cross-sectional shape and

63

integration with main lifting surfaces, the disposition of major components, empennage and landing gear configuration, etc. This dissertation is limited to the analysis of subsystem architectures for conventional aft-tail tube-and-wing configurations with under-wing turbofan engines. Further, the number of engines is constrained to either two (twin-jet or twin-engined aircraft) or four (quad-jet or four-engined aircraft). Tri-jets (three-engined aircraft), which are gradually being phased out, are not considered

The design requirements for the aircraft are assumed to be known. Further, it is assumed that (i) the design requirements are invariant to the choice of subsystem architecture for the aircraft, and (ii) there is no extra credit for a design whose performance capabilities are in excess of the design requirements. The latter assumption in particular will be shown subsequently to influence the approach to re-sizing the vehicle and its subsystems.

3.2.2 Traditional Aircraft and Engine Sizing Process

The mission and operational requirements and the notional air vehicle concept drive the traditional aircraft and engine sizing process. The objective of this process is to obtain a geometric scale for the vehicle in terms of the wing planform area S_w, a propulsive power scale in terms of the required sea-level static thrust T_{SL}, and the takeoff gross weight of the vehicle W_{TO}. It may also be thought of as an attempt to perform the following three activities [36]:

1. Power (or thrust) matching: balancing the available power (or thrust) against the required power (or thrust) to satisfy the point performance requirements

2. Energy (or fuel) matching: balancing the available energy (or fuel) against the required energy (or fuel) to satisfy the mission performance requirements

3. Volume balance: balancing available volume against required volume. For the

conventional aircraft configurations that are analyzed here, this is often satisfied implicitly. Therefore, the focus is on the first two items

The sizing process is heavily dominated by three disciplines: aerodynamics, propulsion, and weight estimation. On the aerodynamic side, the notional concept allows for an initial estimate of the lift and drag characteristics of the aircraft in terms of the lift curves (lift coefficient C_L versus angle of attack α) and drag polars (drag coefficient C_D versus lift coefficient C_L) for clean and flapped configurations. The propulsion side starts with an estimate of the engine specific fuel consumption (SFC), and variations of this quantity and the engine thrust with altitude and Mach number. In addition, there may be engine scaling laws that allow for a preliminary estimate of dry engine weight. The weight estimation side begins with an empirical estimate of the empty weight fraction of the aircraft (W_e/W_{TO}).

Since the weight of the aircraft W_{TO} is not known at this point, the thrust balance (ensuring that available thrust exceeds the thrust required to satisfy point performance requirements) may be performed through *constraint analysis*. Here the goal is to determine a *thrust-to-weight ratio* T_{SL}/W_{TO} and *wing loading* W_{TO}/S_w that is in the feasible region formed by the superposition of the point performance requirements in the form of constraint curves. Such curves may be represented as

$$\frac{T_{SL}}{W_{TO}} = \frac{\beta}{\alpha}\left\{\frac{\bar{q}S}{\beta W_{TO}}\left[K_1\left(\frac{n\beta}{\bar{q}}\frac{W_{TO}}{S}\right)^2 + K_2\left(\frac{n\beta}{\bar{q}}\frac{W_{TO}}{S}\right) + C_{D_0} + \frac{R}{\bar{q}S}\right] + \frac{1}{V}\frac{d}{dt}\left(h + \frac{V^2}{2g_0}\right)\right\}$$

(11)

in which $\beta = \frac{W}{W_{TO}}$ is the ratio of current vehicle weight to W_{TO}, $\alpha = \frac{T}{T_{SL}}$ relates the current minimum required thrust to the equivalent thrust at sea-level static (SLS) conditions, $\bar{q}$ is the dynamic pressure, $K_1, K_2,$ and C_{D_0} are the coefficients of the parabolic drag polar $C_D = K_1 C_L^2 + K_2 C_L + C_{D_0}$, and n is the load factor [64]. R captures additional resistive forces such as those due to ground friction. By making suitable substitutions and simplifications to Eq. 11, each point performance requirement may be represented by a constraint curve of the form $T_{SL}/W_{TO} =$
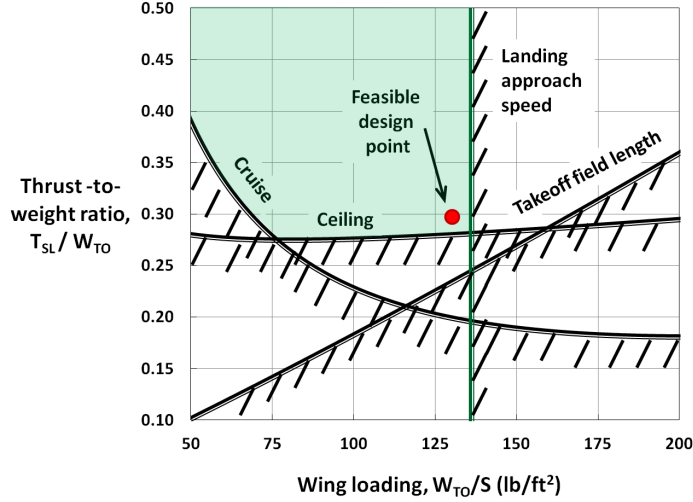
Figure 8: Securing power/thrust balance using constraint analysis to satisfy point performance requirements

$f(W_{TO}/S)$. Considering all such constraint curves simultaneously allows the feasible $T_{SL}/W_{TO} - W_{TO}/S$ design space to be identified, as shown notionally in Fig. 8.

The fuel balance (ensuring that the available fuel is greater than or equal to the required fuel to complete the mission requirements) may be secured through *mission performance analysis*. The fuel requirement for the sizing mission may be expressed as a mission fuel fraction W_f/W_{TO}, which in turn may be expressed as the product of fuel fractions of 'n' successive mission segments,

$$\frac{W_f}{W_{TO}} = 1 - \prod_{k=1}^{n} \left(\frac{W_f^{(k)}}{W_i^{(k)}} \right) \tag{12}$$

where the fuel fraction for segment 'k' is the ratio of aircraft final weight at the end of the segment $(W_f^{(k)})$ to initial weight at the beginning of the segment $(W_i^{(k)})$. Raymer [37] provides expressions for preliminary estimates of the segment fuel fractions that may be used to evaluate Eq. 12. With known weights for the payload (W_{pl}) and crew (W_{crew}), the takeoff weight W_{TO} may be obtained through an iterative convergence of

$$W_{TO} = \frac{W_{pl} + W_{crew}}{1 - W_e/W_{TO} - W_f/W_{TO}}, \tag{13}$$

66

where W_e/W_{TO} is the empty weight fraction of the vehicle. While a first estimate of this fraction may be made based on historical trends, a better estimate may be obtained by using a component weight buildup method [38].

Several aircraft sizing and performance analysis codes already exist that perform the activities described above (in Chapter 1, several such tools were mentioned that were used either by industry or by individual researchers in their respective analyses). This dissertation uses a tool developed by NASA Langley Research Center called Flight Optimization System (FLOPS) [65] for this purpose. If the design requirements are provided as inputs, then the tool is capable of determining the vehicle size, gross weight, and fuel necessary to satisfy these requirements. The weight buildup relationships within this tool (as with most other similar tools) are based on regressions of historical data, and therefore apply to conventional subsystem architectures. Therefore, it provides a conventional baseline which serves as a starting point for the remaining modules of the integrated environment.

3.2.3 Generation of Subsystem Architecture Combinations

For both conventional and More Electric subsystem architectures, there may be multiple methods of achieving the required subsystem functions. For example, the actuators used for the ailerons, elevators, rudders, and spoilers may be classified according to the type of power that they consume: conventional actuators consuming hydraulic power, electrohydrostatic or electromechanical actuators (EHA or EMA) consuming only electric power, or electrical backup hydraulic actuators (EBHAs) consuming both hydraulic and electric power. These actuators may be further classified based on the nature of the output motion: linear actuators or rotary (hinge-line) actuators. Similarly, the leading-edge and trailing-edge high-lift devices may be actuated using on-site hydraulic or electric actuators (which, depending on the kinematics of the flap mechanism, may be linear or rotary), or using centralized

Table 2: Matrix of Alternatives (MoA) based on some subsystem solutions

Subsystems		Options	#
Flt. Ctrl.	Ailerons	Lin-hyd, Rot-hyd, Lin-EHA, Lin-EMA, Rot-EMA	5
	Elevators	Lin-hyd, Rot-hyd, Lin-EHA, Lin-EMA, Rot-EMA	5
	Rudder	Lin-hyd, Rot-hyd, Lin-EHA, Lin-EMA, Rot-EMA	5
	Spoilers	Lin-hyd, Rot-hyd, Lin-EHA, Lin-EMA, Rot-EMA	5
	LE-flaps	Lin-hyd, Rot-hyd, Lin-elec, Rot-elec, H-PDU, E-PDU, H/E-PDU	7
	TE-flaps	Lin-hyd, Rot-hyd, Lin-elec, Rot-elec, H-PDU, E-PDU, H/E-PDU	7
	THS	H-jackscrew, E-jackscrew, H/E-jackscrew	3
Ice Prot.	Wing	P-Ev-AI, P-RW-AI, E-Ev-AI, E-RW-AI, P-DI, E-DI	6
	Cowl	P-Ev-AI, P-RW-AI, E-Ev-AI, E-RW-AI, P-DI, E-DI	6
Env. Ctrl. System		Pneumatic, electric	2
Elec. Taxi System		Present, absent	2
Total combinations: 13,230,000			

power drive units (PDUs), which in turn may be powered hydraulically, electrically, or with one hydraulic and one electric power source. The latter three options also exist for the Trimmable Horizontal Stabilizer (THS).

Similar actuation options also exist for the landing gear retraction/extension function. The conventional nose-wheel steering system is hydraulic in nature, but both push-pull (linear) mechanisms and rack-and-pinion (rotary) mechanisms are found on in-service aircraft. Electric nose-wheel steering system solutions may also feature similar linear or rotary actuation arrangements. The wheel-braking function may use either hydraulically or electrically powered wheel brakes.

Other than the actuation functions, multiple options also exist for other aircraft subsystems. For example, the Environmental Control System (ECS) may use pneumatic or electric power for cabin pressurization. Depending on the type of power

consumed, the Wing Ice Protection System (WIPS) and the Cowl Ice Protection System (CIPS) may be classified as being pneumatic (P) or electrothermal (E) in nature (other possibilities such as electroimpulse systems also exist, but are not considered in this dissertation). Depending on the amount of heat supplied to the protected surfaces, these systems may be further classified as *evaporative* (Ev), where sufficient heat is supplied to completely evaporate all impinging water, or *running-wet* (RW), where the heat supplied is only sufficient for maintaining the protected surface just above freezing. Yet another classification is possible based on the mode of operation, as the systems may be of the anti-icing (AI) type, which operate continuously to prevent any ice formation, or the de-icing (DI) type, which operate intermittently to dispatch accumulated ice.

In certain cases, a subsystem may be present within one architecture but absent from others. A classic example would be an Electric Taxiing System (ETS), where the aircraft is taxied on the ground using electric motors that drive the wheels. For the conventional solution, where the aircraft is taxied using the thrust of the main engines, this subsystems is absent entirely.

Based on the subsystem solutions discussed above, a Matrix of Alternatives (MoA) may be constructed, as shown in Table 2. Despite the fact that only some major aircraft subsystems and a limited number of options for each such subsystem were considered in the MoA, it is clear from the total number of combinations that a very large combinatorial problem has been developed. The number of combinations would be even greater if the Hydraulic Power Generation and Distribution System (HPGDS) and the Electric Power Generation and Distribution System (EPGDS) were considered as additional rows in the MoA, with nominal system pressures and voltages as their respective options.

Due to computational expense, the exploration of each and every combination within such a large combinatorial space quickly becomes infeasible. To put this

in perspective, assuming continuous computer operation and a highly optimistic evaluation time of five seconds per architecture, exhaustive exploration of even the partial MoA of Table 2 would take approximately 2.13 years. In such cases, it may often be possible to use a Technology Compatibility Matrix (TCM) to filter out combinations with incompatible technologies, thus reducing the size of the combinatorial space. The TCM is essentially a matrix representation of physical or technological incompatibilities that prevent two technologies from co-existing within an architecture. Depending on the number and nature of incompatibilities, the application of a TCM as a filter to a MoA may permit the extraction of a significantly smaller (and thus more tractable) subset of *feasible* combinations from the MoA. Actual evaluation may then be limited to only these feasible combinations.

Such a TCM is *not* readily applicable as a filter for the case of aircraft subsystem architectures. Inspection of the MoA of Table 2 does not reveal any obvious physical incompatibilities. For example, the presence of an Electric Taxiing System does not directly preclude the use of hydraulic actuation for any of the actuation functions. Further, even the use of a particular actuation technology for one actuation function (e.g., elevator actuation) does not directly preclude the use of an alternative actuation solution for a different actuation function (e.g., rudder actuation). For instance, each of the four elevator panels of the Airbus A380 is actuated using a conventional hydraulic actuator in parallel with an EHA, while each of the two rudder panels is actuated by two parallel EBHAs [24]. The use of electrothermal wing ice protection imposes no direct restriction on the solution used for nacelle ice protection, which may remain conventional (pneumatic) - an example of which is the Boeing 787 [14].

A first attempt to reduce the size of the combinatorial space may be made by selecting only one architecture that represents the conventional state-of-the-art (SOTA), thus eliminating multiple other elements within the MoA which are only minor variations of such a conventional architecture. Such an approach is justified

70

since the objective here is to compare More Electric architectures against the conventional SOTA.

Since the multiple actuation functions collectively contribute a large number of elements to the MoA, the attempt to reduce the size of the architectural space is first focused on these functions. On almost all commercial aircraft currently in service, linear hydraulic actuators are used to actuate the ailerons, elevators, rudders, and spoilers. Therefore, only this type of actuator may be considered for the conventional actuation architecture (giving no further consideration to architectures with rotary hydraulic actuators for these surfaces). Further, a study of commercial aircraft high-lift devices shows that the LE and TE devices of most commercial aircraft are centrally actuated using PDUs [66]. Similarly, while both rotary and linear steering gear mechanisms are found, the kinematics of the linear "push-pull" type systems are such that there are certain steering angles at which only one of the two linear actuators is able to provide a force, thus removing fault tolerance through actuator redundancy [67]. Thus, for the purposes of this investigation, it is sufficient to represent the conventional SOTA for actuation functions with a single actuation architecture in which

1. Linear hydraulic actuators actuate ailerons, elevators, rudders, and spoilers

2. Centralized hydraulic Power Drive Units (PDUs) actuate the high-lift devices

3. A rotary hydraulic rack-and-pinion steering mechanism steers the nose-wheel

Despite the fact that the MoA does not contain any obvious incompatibilities, there are however a large number of *impractical* combinations. In the context of this dissertation, *impractical* combinations are those which are unlikely to be pursued by an engineering team comprising subject-matter experts due to (i) unnecessarily high complexity of implementation or (ii) a high level of perceived technological risk. An example of (i) would be a proposed actuation architecture in which all

71

actuation functions are electrified with the exception of, say, nose-wheel steering, which remains hydraulic. From an engineering standpoint, this arrangement would likely be considered impractical since, in addition to the electrical equipment required for the electrified actuation functions, conventional hydraulic pumps and piping would need to be retained solely for the purpose of powering the hydraulic nose-wheel steering system. If presented with such an architecture, subject-matter experts may presumably recommend electrifying the nose-wheel steering function as well to enable the removal of the hydraulic system entirely.

An example of (ii) may be provided considering the actuation functions once more, for which one of the primary drivers is safety [24]. Since hydraulic actuation has been used in commercial aircraft for several decades, it is regarded as a reliable and proven concept which presents low technological risk. On the other hand, the industry experience with electric actuation concepts is much more limited, as a result of which considerable conservatism is seen regarding their use on commercial aircraft. Due to the consequences arising from adverse failures, the conservatism is naturally greatest where electrification of flight control surfaces is concerned. In view of this, it may be argued that the introduction of electric actuators is likely to occur in a staged approach where the actuation functions are progressively electrified starting from the less critical ones, in order to minimize the risk. In such an approach, electric actuation solutions that have already been proven in flight (e.g., electric thrust reverser actuation for Airbus A380, electric brake actuation for Boeing 787) represent the lowest risk. These are followed by actuation functions for which some hardware development and validation have already been undertaken (e.g., nose-wheel steering [68]). For the flight control surfaces, electrification may commence with surfaces whose operation is not critical for the continued safety of the flight (e.g. the high-lift system [69]), in which case the failure probability requirements in terms of failures per flight hour are less stringent. This may be followed by control surfaces

such as spoilers that have *surface redundancy* [27, 26], where the presence of multiple spoiler panels reduces the criticality of any one panel. There may also be a preference in terms of the type of electric actuator being used. For example, within the actuation community at present, there is great debate and no consensus regarding the relative applicability of electric actuators of the electrohydrostatic type (EHA) and electromechanical type (EMA) for the purpose of control surface actuation. It is generally accepted that the EMA will be lighter than the EHA designed to the same actuation requirements. However, the EMA also presents some risk of single-point jamming failures [70] which have caused many to question its suitability for actuating the primary flight control surfaces in particular. Even for EHAs, their introduction to primary flight control actuation is likely to be in parallel with conventional hydraulic actuators (e.g., Airbus A380 [24]). Given their flight criticality and the relatively low industry experience with electric actuators, the primary flight control surfaces may in fact be the last actuation functions on the aircraft to be transitioned fully to electrohydrostatic or electromechanical actuation.

Based on practical considerations such as the above, it is possible to propose certain actuation *packages* which exhibit the following characteristics:

1. Successive actuation packages feature progressively more electrification. An actuation function once electrified is never de-electrified in a higher package

2. No package features a combination where a more critical actuation function has been electrified while a less critical function remains conventional (hydraulic)

3. When competing actuation technologies (such as EHAs and EMAs) differ in the perceived level of technological risk, the technology perceived to be riskier is introduced to less critical actuation functions first

A packaged approach of this nature automatically eliminates a large number of actuation combinations existing within the MoA in which the above rules are

Table 3: Packaged electrification of actuation functions (Electrification is indicated either by ✓or by the name of the type of actuator(s) employed. Abbreviations - EHA: electrohydrostatic actuator, EMA: electromechanical actuator, H/EHA: hydraulic actuator & EHA in parallel, HLD: high-lift devices, THSA: trimmable horizontal stabilizer actuator, Sp.: spoilers, Prim.: primary flight control surfaces)

Actuation Function	Actuation Package #							
	P-0	P-1	P-2	P-3	P-4	P-5	P-6	P-7
TRAS		✓	✓	✓	✓	✓	✓	✓
WBS		✓	✓	✓	✓	✓	✓	✓
LGAS			✓	✓	✓	✓	✓	✓
NWSS			✓	✓	✓	✓	✓	✓
FCAS-HLD				✓	✓	✓	✓	✓
FCAS-Sp.				EHA	EMA	EMA	EMA	EMA
FCAS-THSA					✓	✓	✓	✓
FCAS-Prim.						H/EHA	EHA	EMA

violated. The packages considered in this dissertation which were obtained in this manner are summarized in Table 3. Package 0 is a conventional actuation architecture (all hydraulic). In Package 1, the thrust reversers (TRAS) and wheel brakes (WBS) are electrified, and in Package 2, the landing gear extension/retraction (LGAS) and nose-wheel steering (NWSS) functions follow. Subsequent packages involve progressively more electrification of the FCAS. For example, in Package 3, EHA-driven spoilers and electrically actuated flaps are added, while in Package 4, the spoilers are transitioned to EMAs and additionally the THS actuation function is electrified. In Package 5, EHAs are added in parallel to conventional hydraulic actuators for the primary flight control surfaces, while in Package 6, the conventional hydraulic actuators are removed completely, yielding an All Electric actuation architecture. Finally, in Package 7, EMAs are considered even for the primary flight control surfaces.

Moving next to the solutions considered for the ice protection systems, it may be noted that pneumatic de-icing systems (P-DI) are not commonly found on in-service commercial aircraft as the advantage of reduced bleed requirements may be negated

74

Table 4: Reduced combinatorial space due to the application of engineering judgment

Subsystem	Options	#
Actuation functions	Packages P0, ..., P7	8
Wing ice protection	P-Ev-AI, P-RW-AI, E-RW-AI, E-RW-DI	4
Cowl ice protection	P-Ev-AI, P-RW-AI, E-EV-AI, E-RW-AI	4
Environmental control system	Pneumatic, electric	2
Electric taxiing system	Present, absent	2
	Total combinations: 512	

by increased systems complexity and weight [71]. Further, the use of a de-icing system in general for nacelle ice protection raises concerns over ice being expelled into the engine [71]. Also, it has been established that electrical power requirements for fully evaporative wing anti-icing systems (E-Ev-AI) are prohibitive [71], especially when the surface area to be protected increases. Thus, the architectural design sub-space for ice protection systems may be reduced by considering only running-wet electrothermal systems for WIPS (E-RW-AI, E-RW-DI), and only anti-icing electrothermal systems for CIPS (E-Ev-AI, E-RW-AI), in addition to the conventional evaporative and running-wet pneumatic systems (P-Ev-AI, P-RW-AI).

The application of the filters described above reduces the size of the architectural design space significantly to the tractable sub-space shown in Table 4. The architectures within this sub-space were evaluated for this dissertation. A convenient and compact way to describe a subsystem architecture from within the possibilities shown in Table 4 is through a *candidate subsystem architecture descriptor*, which is explained completely in Fig. 9. This convention is used throughout the dissertation. Thus, the baseline architectures for the three vehicle sizes considered are as follows: SSA-00000 (Small Single-aisle Aircraft), LTA-00000 (Large Twin-aisle Aircraft), and VLA-00000 (Very Large Aircraft).
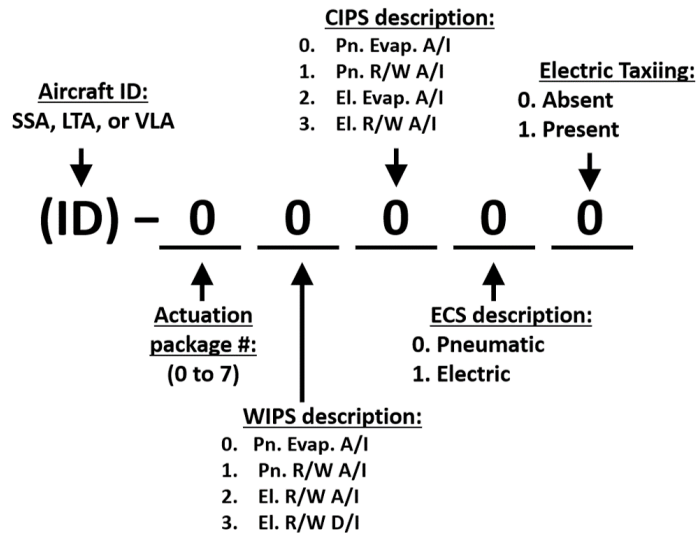
Figure 9: Definition of *Candidate Subsystem Architecture Descriptor*

3.2.4 Subsystem Architecture Sizing and Evaluation

The information input to the subsystem sizing and analysis module includes:

1. Aircraft design requirements definition (§3.2.1): Mission performance requirements, point performance requirements, and the notional aircraft concept

2. Aircraft sizing and performance evaluation module outputs (§3.2.2): Containing information about the aircraft mission profile, mass breakdown, and geometry

3. Candidate subsystem architecture descriptor (§3.2.3): Containing (for each subsystem) information about the subsystem solution to sized and evaluated

This information is used to first derive the requirements for each of the power consuming subsystems (the distinction between power consuming and power generation and distribution subsystems was made in §3.1), which are used to size major components within those subsystems. As far as propagation to subsequent analysis modules is concerned, the main parameters of interest are the subsystem mass, peak secondary power requirements, secondary power requirements over the course of a mission, and direct drag increments (if any). Detailed technical

76

descriptions of the sizing and analysis approach used for each power consuming subsystem considered are provided in Chapter 4.

Prior to the sizing of the major elements of the power generation and distribution subsystems, a feasible connectivity among different elements of the subsystem architecture is defined by an architecting algorithm based on a set of heuristic rules. The heuristic rules used by the algorithm are in turn derived from the inspection of subsystem architectures of existing commercial aircraft and suitable extrapolation of the observations to the case of MEA architectures. The goal is to develop feasible associations among the elements of a subsystem architecture that implicitly satisfy major redundancy requirements, but without the incorporation of a formal Fault Tree Analysis (FTA) or Failure Modes and Effects Analysis (FMEA). With the necessary connectivity of architecture elements defined in this manner, the lengths of the power distribution elements (pipes, ducts, and cables) required to physically establish those connections are estimated from a 3-dimensional geometric model of the aircraft. The mass per unit length for these distribution elements is determined based on the magnitude of the hydraulic fluid, pneumatic mass flow, or electrical current flowing through them. The required capacities of the power sources (e.g., hydraulic pumps and electric generators) are determined based on the evaluation of required secondary power in certain critical or off-nominal operating scenarios. Detailed descriptions of the architecting algorithm and the sizing and analysis approach for the PGDS are presented in Chapter 5. The major outputs of the subsystems sizing and evaluation module are the following parameters for each subsystem (including both power consuming subsystems and PGDS):

1. The mass of the subsystem, which comprises the mass of major components present within the defined control volume of the subsystem. For each subsystem, the computed mass is compared to the mass of the conventional subsystem solution to determine the change in mass relative to it

2. The shaft-power requirements of the subsystem (if any) as a function of time

3. The bleed air requirements of the subsystem (if any) as a function of time

4. The direct drag increments on account of the subsystem (if any) as a function of mission time

As described subsequently in §3.2.5, this information is reflected into the mission performance analysis to compute the updated mission fuel consumption and vehicle takeoff gross weight. This in turn sets the stage for the re-sizing of the vehicle in response to these changes, as discussed subsequently in §3.2.6.

The predicted performance of any subsystem architecture is subject to epistemic uncertainty that arises due to a combination of the following: (i) insufficient/incomplete knowledge of the input parameters that feed into the subsystem models, (ii) limitations in the modeling approaches themselves, (iii) simplifying assumptions that were made during modeling or analysis. Therefore, it is necessary to determine not merely the performance of a particular subsystem architecture, but also the sensitivity of that performance to sources of epistemic uncertainty. This is done by strategically associating a number of variation factors (commonly known as *K-factors*) to internal model parameters that would be significantly affected by the epistemic uncertainty, and then analyzing the variation in the predicted performance to variations in these K-factors (Chapter 8).

In a similar manner, the computed subsystems mass is strongly influenced by assumptions regarding the technological state-of-the-art (SOTA). This is more relevant for the case of the MEA architectures, since assumptions regarding the technological SOTA of electrical/electronic components have a direct impact on the predicted competitiveness of those architectures relative to a conventional one. Therefore, it is also necessary to determine the impact that changes in the assumed SOTA have on the performance of the MEA architectures. Since many of the

electrical/electronic components within a MEA architecture are currently on a steep development curve, an alternative way to view this is as an attempt to determine the projected performance of such MEA architectures under the assumption that technological SOTA progresses to a certain level. From the point of view of modeling, these two scenarios are however identical, and is done by strategically associating technology K-factors with the power-to-mass ratios of such electrical/electronic components. The sensitivity of the predicted performance of the MEA architectures to variations in the assigned K-factor values is then assessed (Chapter 8).

3.2.5 Evaluation and Decomposition of Subsystem Impacts

The subsystems affect a mission-level metric such as fuel consumption through their (i) mass, (ii) shaft-power requirement, (iii) bleed air requirement, and (iv) direct drag increments, as shown in Fig. 10. With the exception of the penalty due to mass, the remaining three penalties may or may not exist. Changes in subsystem mass and direct drag increments result in a change in the thrust required. On the other hand, changes in secondary power off-takes result in a change in engine TSFC. The cumulative result is a change in fuel flow, which may be represented as

$$\Delta \dot{w}_f(t) = \Delta \dot{w}_{f,w}(t) + \Delta \dot{w}_{f,spx}(t) + \Delta \dot{w}_{f,bx}(t) + \Delta \dot{w}_{f,d}(t), \tag{14}$$

in which the quantities on the RHS are respectively the incremental fuel flow rates due to the effect of weight (mass), shaft-power extraction, bleed air extraction, and direct drag increment. When the incremental fuel flow rate is integrated over the course of a mission, the incremental fuel consumption may be obtained as

$$
\begin{aligned}
\Delta w_f &= \int_{t_i}^{t_f} \Delta \dot{w}_{f,w}(t)dt + \int_{t_i}^{t_f} \Delta \dot{w}_{f,spx}(t)dt + \int_{t_i}^{t_f} \Delta \dot{w}_{f,bx}(t)dt + \int_{t_i}^{t_f} \Delta \dot{w}_{f,d}(t)dt \\
&= \quad \Delta w_{f,w} + \quad \Delta w_{f,spx} \quad + \quad \Delta w_{f,bx} \quad + \quad \Delta w_{f,d} \tag{15}
\end{aligned}
$$

in which the quantities on the RHS this time are respectively the incremental fuel consumption due to the effect of subsystem weight (mass), shaft-power extraction,
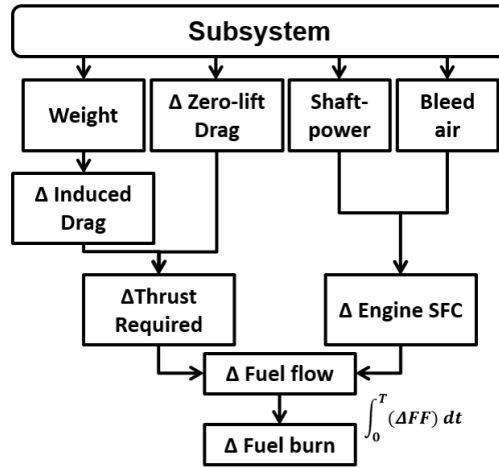
Figure 10: Contribution of subsystem effects towards mission fuel burn

bleed air extraction, and direct drag increment.

It is more convenient to address the incremental fuel burn $\Delta w_{f,w}$ due to the effect of the change in subsystems weight Δw_{ss} first, and then the remaining three components separately. To obtain some analytical insight on the effect of the overall change in subsystem mass on the fuel burn component $\Delta w_{f,w}$ for a single flight phase, a manipulation of the Breguet range equation yields

$$\Delta w_{f,w} = \Delta w_{ss} \left(e^{\frac{(TSFC)\ R}{VL/D}} - 1 \right), \tag{16}$$

in which R is the distance flown at speed V and lift-to-drag ratio L/D. It is possible to obtain the component $\Delta w_{f,w}$ by breaking up the entire mission into phases or segments and applying the above relationship successively to each segment, starting from the final one to the first one [63].

Fortunately, most aircraft sizing and performance analysis tools are able to directly estimate the effect of changing systems mass on mission fuel burn if the parameters of the mission and the magnitude of the change in mass are specified as input. If the flight performance analysis uses a point-mass approximation, then for the purpose of this estimation it makes no difference whether the total change in weight Δw_{ss} is input as a direct increment to the OEW of the aircraft, or whether the constituents

Table 5: Association of subsystem weights with FLOPS weight override parameters (namelist WTIN)

Subsystem Weight	Override Parameter
FCAS	WTIN.FRSC
Nose LGAS, NWSS	WTIN.FRLGN
Main LGAS, WBS, ETS	WTIN.FRLGM
TRAS	WTIN.WTHR
ECS	WTIN.WAC
WIPS, CIPS	WTIN.WAI
EPGDS	WTIN.WELEC
HPGDS	WTIN.WHYD
PPGDS ducting	WTIN.EWMARG
PPGDS precoolers	WTIN.WPMSC
MPGDS	WTIN.WPMSC

of Δw_{ss} (weight changes of individual subsystems) are separately factored into the weight breakdown of the aircraft. The latter approach is followed in this dissertation in order to retain resolution regarding the impact of subsystem architectures on the weight breakdown of the vehicle. To this end, the weights of individual subsystems as computed by the subsystems sizing module are associated with FLOPS weight override parameters, as summarized in Table 5.

A relatively simple approach to the computation of the remaining three effects (shaft-power extraction, bleed air extraction, and direct drag increments) is to divide the flight into main phases or segments (e.g., takeoff, climb, cruise, descent, landing), and assess these effects for each such segment, assuming no variation of shaft-power, bleed, drag, velocity, lift-to-drag ratio, and engine TSFC over the course of a segment [63]. However, certain limitations arise due to these assumptions, in particular the assumption that the off-takes do not vary over the course of a segment. For example, it is demonstrated subsequently that the power consumption of an electric ECS for pressurization increases with increasing altitude, which implies that it increases during the climb and decreases during the descent. Similarly, the IPS

may be active for only the parts of the climb/descent that are under approximately 22,000 ft altitude, even though those segments themselves may end at or begin from cruise altitudes that are much higher than that.

Such assumptions may be removed through an approach where the entire flight is divided into numerous small intervals, and the cumulative subsystem effects are assessed through a backward summation from landing to takeoff [72]. Since the power off-takes and drag increments are in general not constant over the course of a flight segment, such a backward-summation scheme is followed in this dissertation. The approach is to first compute the effect of the net subsystems weight change Δw_{ss} on fuel consumption (as described above), and then use the following update scheme to compute the additional fuel consumption due to power off-takes and drag:

$$\Delta C_L^{(k)} = \frac{\Delta W^{(k+1)}}{\left(\frac{1}{2}\rho V^2\right)^{(k)} S_w} = \frac{\Delta W_f^{(k+1)}}{\left(\frac{1}{2}\rho V^2\right)^{(k)} S_w} \tag{17a}$$

$$\Delta C_{D_i}^{(k)} = C_{D_i}(C_{L,0}^{(k)} + \Delta C_L^{(k)}) - C_{D_i}(C_{L,0}^{(k)}) \tag{17b}$$

$$\Delta D_{ddl}^{(k)} = \left(\frac{1}{2}\rho V^2\right)^{(k)} S_w \, \Delta C_{D_i}^{(k)} \tag{17c}$$

$$\Delta D_{dil}^{(k)} = \left(\frac{1}{2}\rho V^2\right)^{(k)} S_w \, \Delta C_{D_0}^{(k)} \tag{17d}$$

$$\Delta D^{(k)} = \Delta D_{ddl}^{(k)} + \Delta D_{dil}^{(k)} \tag{17e}$$

$$\Delta T^{(k)} = \Delta D^{(k)} + \Delta W^{(k+1)} \left(\frac{\dot{h}}{V} + \frac{\dot{V}}{g}\right)^{(k)} \tag{17f}$$

$$T^{(k)} = T_0^{(k)} + \Delta T^{(k)} \tag{17g}$$

$$\Delta \dot{w}_f^{(k)} = \dot{w}_f\left(T^{(k)}, h^{(k)}, M^{(k)}, P_{spx}^{(k)}, \dot{m}_{bx}^{(k)}\right) - \dot{w}_f\left(T_0^{(k)}, h^{(k)}, M^{(k)}, 0, 0\right) \tag{17h}$$

$$\Delta W^{(k)} = \Delta W^{(k+1)} + \Delta \dot{w}_f^{(k)} \, \Delta t^{(k)} \tag{17i}$$

$$k = k - 1, \qquad \text{and repeat sequence}$$

$$\text{Start point}: k = n - 1, \Delta W^{(n)} = 0$$

82

The Δ-quantities in this scheme are computed with respect to the corresponding quantities at the same instant in time for a mission in which the effect of subsystem weight changes has been accounted for (but not the effect of shaft-power and bleed requirements or drag increments). Henceforth, this is referred to as the *basic* mission, and parameters corresponding to it are marked with subscript $(\cdot)_0$. The flight profile for the basic mission may be obtained from the aircraft sizing and performance evaluation tool. While the flight profile may change due to the subsystem weight changes, it is assumed that there is no further change as a result of the effects of secondary power extraction and direct drag. Each sub-equation in the update scheme is described briefly, for an arbitrary time in the mission marked with time index superscript $(\cdot)^{(k)}$:

(a) Change in lift coefficient $\Delta C_L^{(k)}$: This is due to the change in vehicle weight ΔW relative to the same point in time of the basic mission. In this case, the change is simply due to the mass of additional fuel that will be consumed due to subsystem secondary power off-takes or direct drag between time index 'k' and the end of the mission

(b) Change in induced drag coefficient $\Delta C_{D_i}^{(k)}$: This is due to the change in the lift coefficient described above and can be obtained by querying the aerodynamic drag polar of the vehicle with the basic mission lift coefficient for the same time instant $C_{L,0}^{(k)}$ and the updated lift coefficient $C_{L,0}^{(k)} + \Delta C_L^{(k)}$

(c) Change in dimensional drag dependent on lift $\Delta D_{ddl}^{(k)}$: Corresponding to the change in induced drag coefficient computed above

(d) Change in dimensional drag independent of lift $\Delta D_{dil}^{(k)}$: This is due to the direct drag increments of the subsystems which may arise from the admission of ram air or the buildup of ice for an IPS of the de-icing type

(e) Change in dimensional drag $\Delta D^{(k)}$: Summation of the two dimensional drag components described above

(f) Change in required thrust $\Delta T^{(k)}$: In addition to the direct contribution due to the change in drag as computed above, there is an additional contribution due to the specific energy rate of the incremental weight $\Delta W^{(k)}$. The thrust change is obtained by perturbing the thrust balance equation $T = D + W\left(\frac{\dot{h}}{V} + \frac{\dot{V}}{g}\right)$, in which the specific energy rate $\left(\frac{\dot{h}}{V} + \frac{\dot{V}}{g}\right)$ is assumed to be the same as that for the basic mission at the same instant in time

(g) Updated thrust requirement $T^{(k)}$: Obtained by adding the thrust change $\Delta T^{(k)}$ computed above to the thrust $T_0^{(k)}$ of the basic mission at the same instant

(h) Change in fuel flow rate $\Delta \dot{w}_f^{(k)}$: Computed as the difference of the fuel flow rate obtained by accounting for the updated thrust, shaft-power, and bleed air off-takes and that obtained with the basic mission thrust and no off-takes. Two approaches to computing this quantity are discussed subsequently

(i) Change in vehicle weight $\Delta W^{(k)}$: Obtained by adding the fuel consumed in the time interval $\Delta t^{(k)}$ to the vehicle weight $W^{(k+1)}$ at time index 'k+1'

The time index is then decremented to 'k−1' and the system of equations is re-evaluated for that time index. The boundary condition is that the vehicle weight at the final time index 'n' is the same as that for the basic mission, i.e., $\Delta W^{(n)} = 0$. The fuel consumption due to the effect of shaft-power off-take, bleed air off-take, and direct drag increments is then the difference in vehicle weight at the first time index (k = 1) relative to that in the basic mission, i.e. $\Delta W^{(1)}$.

The above equation system can be used to determine the TFI (Eq. 9) of individual subsystems. As discussed above, it is relatively straightforward to determine the impact of the mass of subsystem 'i' on mission fuel burn, in other words $\Delta w_{f,w}^{(i)}$.

By feeding the time histories of the subsystem's shaft-power requirement, bleed air requirement, and direct drag increment one at a time through the system of Eq. 17, the impact of these on fuel burn can be determined as well, in other words $\Delta w_{f,spx}^{(i)}$, $\Delta w_{f,bx}^{(i)}$, and $\Delta w_{f,d}^{(i)}$. Due to the nonlinearities present in the update system of Eq. 17, the sum of the three individually-computed fuel penalties $\Delta w_{f,spx}^{(i)}$, $\Delta w_{f,bx}^{(i)}$, and $\Delta w_{f,d}^{(i)}$ will in general be (slightly) less than the penalty $\Delta w_{f,spx+bx+d}^{(i)}$ computed by considering the power off-takes and drag simultaneously. In this case, the residual quantity $\mathcal{R}^{(i)} = \Delta w_{f,spx+bx+d}^{(i)} - \Delta w_{f,spx}^{(i)} - \Delta w_{f,bx}^{(i)} - \Delta w_{f,d}^{(i)}$ is simply allocated (added) to the shaft-power, bleed, and drag fuel penalties in the ratio of their magnitudes. This guarantees that the equality shown in Eq. 9 is satisfied.

As shown in Eq. 17h, the fuel flow rate is a function of the flight condition (Mach number, altitude, and thrust setting) and the shaft-power and bleed air extraction:

$$\dot{w}_f = \dot{w}_f \left(T, h, M, P_{spx}, \dot{m}_{bx} \right) \tag{18}$$

The fuel flow rate may be obtained in the manner above by directly incorporating a higher-fidelity propulsion system analysis tool into the mission performance simulation. However, since the mission performance simulation may need to be run multiple times per subsystem architecture, this may not be feasible due to computational expense. Instead, the higher-fidelity tool may be evaluated off-line to determine coefficients that relate the fuel consumption penalty to the secondary power off-takes and the flight condition. Within the mission performance simulation (on-line), polynomial interpolation may be used to determine the fuel flow rate penalty corresponding to a given flight and operating condition [39]. In this dissertation, two differing approaches are used for the characterization of the fuel consumption penalty due to off-takes. The first uses simple empirical correlations that do not directly account for the effect of flight condition or engine cycle parameters. The second uses penalty coefficients obtained from off-line evaluation of a higher-fidelity propulsion system analysis tool. However, instead of polynomial interpolation, these coefficients

are scheduled with respect to normalized mission time (this is discussed subsequently in §7.2). In either case, it is convenient to represent the engine's fuel flow rate as the product of the thrust-specific fuel consumption (SFC) and the thrust, and account for changes to these quantities (as shown in Eq. 17) caused by secondary power off-takes and direct drag increments. Towards this end, the following three parameters are defined as the ratio of the change in the corresponding quantity brought about by off-takes and drag increments to the value of the quantity accounting for only propulsive power requirements:

$$\lambda_{ff} = \frac{\Delta \dot{w}_f}{\dot{w}_{f,0}}, \qquad \lambda_{sfc} = \frac{\Delta SFC}{SFC_0}, \qquad \lambda_T = \frac{\Delta T}{T_0} \tag{19}$$

Proceeding from the relationship between thrust, fuel flow rate, and thrust-specific fuel consumption, $\dot{w}_f = T \cdot SFC$, and noting that it yields for the basic mission $\dot{w}_{f,0} = T_0 \cdot SFC_0$, it is possible to relate the above quantities as follows:

$$
\begin{aligned}
\dot{w}_{f,0} + \Delta \dot{w}_f &= (T_0 + \Delta T)(SFC_0 + \Delta SFC) \\
\implies \cancel{\dot{w}_{f,0}} + \Delta \dot{w}_f &= \cancel{= T_0 \cdot SFC_0} + T_0 \cdot \Delta SFC + \Delta T \cdot SFC_0 + \Delta T \cdot \Delta SFC \\
\implies \frac{\Delta \dot{w}_f}{T_0 \cdot SFC_0} &= \frac{T_0 \cdot \Delta SFC}{T_0 \cdot SFC_0} + \frac{\Delta T \cdot SFC_0}{T_0 \cdot SFC_0} + \frac{\Delta T \cdot \Delta SFC}{T_0 \cdot SFC_0} \\
\implies \frac{\Delta \dot{w}_f}{\dot{w}_{f,0}} &= \frac{\Delta SFC}{SFC_0} + \frac{\Delta T}{T_0} + \left(\frac{\Delta T}{T_0}\right)\left(\frac{\Delta SFC}{SFC_0}\right) \\
\implies \lambda_{ff} &= \lambda_{sfc} + \lambda_T + \lambda_T \, \lambda_{sfc} \tag{20}
\end{aligned}
$$

Evaluation of the RHS quantities for each step in the backward-evaluation of Eq. 17 allows the increase in fuel flow rate relative to the basic mission to be obtained. The two approaches mentioned above differ in the method of evaluation of the quantity λ_{sfc}. The first method is introduced in Chapter 6 and the second in §7.2.

3.2.6 Re-sizing of Aircraft and Subsystems

In cases where a reduction in either the fuel consumption or the vehicle's empty weight (or both) are predicted for an alternate subsystems architecture, there may

be a reduction in the vehicle's takeoff gross weight (or ramp weight) for the design mission considered. There are two distinct ways in which designers may respond to such a scenario:

1. Increase the payload and/or range capability of the vehicle by adding payload or fuel in order to maintain the same gross weight as the baseline

2. Down-size the vehicle while maintaining the same payload-range capability as the baseline

It is clear that in the first case, the payload-range capabilities of the two vehicles are dissimilar, while in the second they are held constant. This dissertation assumes that the payload-range capabilities are specified as part of the design requirements of the airplane, and that there is no additional credit given to a design that exceeds those stated requirements. Therefore, the second option (re-sizing of the vehicle) is attempted through the implementation of certain re-sizing rules.

Based on the definition of wing loading W_{TO}/S_w, the following re-sizing rule is derived for the wing planform area S_w:

$$S_w = \frac{W_{TO}}{(W_{TO}/S_w)} \implies \Delta S_w = \frac{\Delta W_{TO}}{(W_{TO}/S_w)} - \frac{W_{TO}}{(W_{TO}/S_w)^2} \, \Delta \left(\frac{W_{TO}}{S_w} \right) \tag{21}$$

Similarly, based on the definition of thrust-to-weight ratio T_{SL}/W_{TO}, the following re-sizing rule is derived for the rated sea-level static thrust T_{SL}:

$$T_{SL} = \left(\frac{T_{SL}}{W_{TO}} \right) W_{TO} \implies \Delta T_{SL} = \left(\frac{T_{SL}}{W_{TO}} \right) \Delta W_{TO} + \Delta \left(\frac{T_{SL}}{W_{TO}} \right) W_{TO} \tag{22}$$

With the incorporation of a relaxation parameter $\alpha < 1$ into the thrust update equation for reasons of numerical stability, the two main re-sizing rules may be summarized as:

$$\begin{aligned} \Delta S_w &= \frac{\Delta W_{TO}}{(W_{TO}/S_w)} - \frac{W_{TO}}{(W_{TO}/S_w)^2} \, \Delta \left(\frac{W_{TO}}{S_w} \right) \\ \Delta T_{SL} &= \left(\frac{T_{SL}}{W_{TO}} \right) \Delta W_{TO} + \alpha \, \Delta \left(\frac{T_{SL}}{W_{TO}} \right) W_{TO} \end{aligned} \tag{23}$$

87

In addition to the main re-sizing rules presented above, additional rules are enforced for the planform areas of the horizontal and vertical stabilizers, so as to maintain the same horizontal tail volume ratio and vertical tail volume ratio as the baseline.

The iterations continue until the error terms ΔW_{TO}, $\Delta(W_{TO}/S_w)$, and $\Delta(T_{SL}/W_{TO})$ are all within a specified convergence tolerance. The second terms in the right-hand sides of each of the above expressions allow the wing area and thrust to be updated not just to guarantee convergence of the takeoff gross weight ($W_{TO} \rightarrow 0$), but also to guarantee that the mathematical system converges to the target wing loading ($\Delta(W_{TO}/S_w) \rightarrow 0$) and thrust-to-weight ratio ($\Delta(T_{SL}/W_{TO}) \rightarrow 0$). In general, the target wing loading and thrust-to-weight ratio may be updated in between iterations based on a re-evaluation of the constraint analysis (Eq. 11 and Fig. 8). The targets may change due to changes in the weight fractions β or the drag polar coefficients that are brought about by subsystem-induced effects. Within this dissertation, it is assumed that shifts in the constraint curves brought about by these effects would be small enough that the original feasible design point would continue to be feasible, with perhaps a slight alteration in the margin of the design point from the active constraints. Pursuant to this assumption, a constant wing loading and thrust-to-weight ratio are maintained during the re-sizing iterations.

The re-sizing establishes dependencies between aircraft-level and subsystem-level parameters and additionally among the subsystems themselves. For example, as seen from Fig. 11, changes in the mass of other subsystems due to changes in the design/architecture of those subsystems may result in a change in the mass of a subsystem whose architecture has not been altered (e.g., FCAS, as shown in Fig. 11).

An interesting decision arises regarding when to re-size the aircraft due to subsystems-induced changes. For instance, if a particular subsystems architecture results in a reduction in aircraft ramp weight, then it is clear from the re-sizing rules of Eq. 23 that this will precipitate a scaling down of the wing planform area
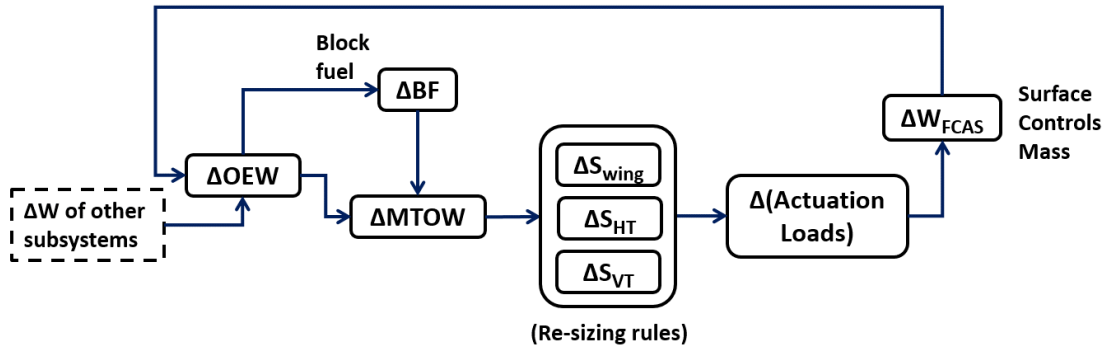
Figure 11: An example of establishment of dependencies among subsystem-, aircraft-, and mission-level parameters: Due to re-sizing, mass changes originating in other subsystems result in changes in lifting surface planform area, which change actuation loads and thus the mass of the surface controls sized to those loads. Thus, the surface controls mass may change even without architecture changes to the FCAS itself.

and the rated thrust, both of which will tend to reduce the ramp weight further (an amplifying effect). For the same reason, if a particular subsystems architecture results in the ramp weight of the aircraft increasing, then re-sizing will cause a scaling up of both the wing planform area and the rated thrust, which will in turn will tend to further increase the aircraft weight. It may be argued that it would be pointless to attempt re-sizing in this second case, given the amplifying effect. However, the counter-arguments to this may be stated as follows:

1. For the case of MEA architectures, it is quite possible that the empty weight of the aircraft increases while the fuel consumption reduces. The relative magnitudes of these effects could be such that overall, there is an increase in the vehicle's ramp weight. Despite this, the architecture is still of interest on account of its fuel-saving potential compared to a conventional baseline [48]

2. Such comparisons are more appropriate when the designs which have the same thrust-to-weight ratio and wing loading, since these essentially imply that they have the same point performance capabilities

Based on the above arguments, re-sizing of the aircraft is carried out regardless of whether the subsystems architecture results in an increase or decrease in the vehicle's ramp weight. Therefore, all comparisons between subsystem architectures that are presented within this dissertation are between aircraft that have both the same mission performance capabilities and point performance capabilities.

3.2.7 Post-processing Analyses

For each run of the integrated sizing and analysis environment, information generated regarding the sized aircraft's geometry, subsystem architecture, and mission performance analysis is stored. Therefore, a number of post-processing analyses can subsequently be run on the generated data. Those presented in this dissertation are mainly of the following types:

1. Architecture-to-architecture comparisons: the comparison of a particular subsystem architecture of interest relative to a conventional baseline architecture (Chapters 6 & 7)

2. Sensitivity analyses: For a limited number of pre-selected subsystem architectures, the determination of the effect of epistemic and technological uncertainty on the performance of these architectures (Chapter 8)

3. Results of architecture space exploration: Assessment of the performance of a larger number of subsystem architectures relative to a conventional baseline architecture (Chapter 9)

3.3 Chapter Summary

This chapter introduced the subsystems that are considered in this dissertation and the concept of the generalized subsystems architecture which is developed further subsequently. The major elements of the integrated subsystem sizing and analysis method such as the generation of candidate architectures, the evaluation and

decomposition of subsystem impacts on aircraft performance, and the simultaneous re-sizing of the aircraft and subsystems were presented and discussed. While the subsystems were classified as either power consuming subsystems or power generation and distribution subsystems, the sizing and analysis approach for subsystems falling within these two categories was not presented in this chapter to preserve continuity of presentation. Instead, these are deferred to Chapter 4 and Chapter 5 respectively, where the modeling approach for each of the subsystems is presented in detail.

CHAPTER IV

MODELING OF POWER CONSUMING SUBSYSTEMS

The power consuming subsystems are those that are the end-users or consumers of secondary power which is transmitted by the appropriate power generation and distribution systems (the latter are covered in Chapter 5). In the scope of this dissertation, the following subsystems are considered:

1. Flight Controls Actuation System (FCAS)

2. Landing Gear Actuation System (LGAS)

3. Nose-wheel Steering System (NWSS)

4. Wheel Braking System (WBS)

5. Electric Taxiing System (ETS) - optional

6. Thrust Reverser Actuation System (TRAS)

7. Environmental Control System (ECS)

8. Wing Ice Protection System (WIPS)

9. Cowl Ice Protection System (CIPS)

The remainder of this chapter is organized as follows: For each power consuming subsystem, the control volume for analysis is first defined. Subsequently a brief description of the function and major components is provided, followed by a discussion on applicable tradeoffs associated with novel solutions for the subsystem. The modeling and simulation approach for each subsystem, whose end goal is to estimate the mass, secondary power requirements, and drag increments, is then described.

4.1 Flight Controls Actuation System (FCAS)

The FCAS control volume includes the surface controls for all the control surfaces of the aircraft. Depending on the type of actuation being employed, the power input to this subsystem may be hydraulic, electric, or a combination of hydraulic and electric. The output power is always in mechanical form (movement of the control surfaces). Therefore, the power off-take from the engine in order to satisfy the requirements of this subsystem is always in the form of shaft-power. The subsystem does not utilize any bleed air and does not result in any direct drag increment since it is within the aircraft outer mold line.

In a conventional actuation architecture, the control surfaces are actuated using hydraulic actuators or power drive units (PDUs). However, there is a recent trend towards the use of electric actuators either in parallel with conventional hydraulic actuators and serving a backup role (e.g., Airbus A380 [24]) or for the actuation of control surfaces such as spoilers which have surface redundancy (e.g., Boeing 787). While electric actuators conform to the Power on Demand philosophy, challenges stem from the limited industry experience with them and the fact that with current technological state-of-the-art (SOTA), a hydraulic actuator still weighs less than an electric actuator designed for the same application [73]. Since the tradeoff must also account for weight reduction of the hydraulic system and weight addition to the electric system, it may not be necessary for the electric actuator to be lighter than the hydraulic actuator it is replacing for electric actuation as a whole to be beneficial. It should be noted that the possibility of the electric actuator being heavier than the hydraulic actuator it is replacing also exists for actuation functions other than flight control surface actuation. In each of these cases, the benefit has to be ascertained through an aircraft-level assessment.

4.1.1 Control Surface Descriptions and Layouts

The purpose of the flight control surfaces is to ensure adequate controllability and maneuverability for the aircraft and provide the required flight characteristics for a given mode of flight. While the number and layout of control surfaces varies greatly depending on the size and type of aircraft, the following characteristics are in general true for commercial transport aircraft:

- Primary flight control surfaces: The primary flight control surfaces are the ailerons, the elevators, and the rudder. These are hinged bi-directional trailing-edge control surfaces that are responsible for control of the aircraft in the roll, pitch, and yaw axes respectively. For small aircraft, it is common to employ two ailerons (one per wing), two elevators, and one rudder. Larger aircraft may employ four elevator panels, two rudder panels, and up to six aileron panels (three per wing). These control surfaces have high control authority, are considered flight-critical, and are provided the required redundancy by employing two or three actuators per panel (*actuator redundancy*).

- Spoilers: Multiple spoiler panels are located on the upper surface of the wing. *Flight* spoilers may be deflected symmetrically on both wings as *speed-brakes* in order to increase the aerodynamic drag, allowing for deceleration or a steeper descent. Further, on almost all modern commercial aircraft, the roll authority of the ailerons is augmented by deploying the flight spoilers only on the downward-moving wing. Flight spoilers may also be deployed following touch-down to aid in decelerating the aircraft. For this purpose, aircraft may also have dedicated *ground* spoilers, which are designed to only deploy upon touch-down but never in flight. In most cases, spoilers are uni-directional controls (deflecting upwards only), however some modern aircraft employ a spoiler droop function as well [74]. Due to the presence of multiple spoiler

panels, *surface redundancy* already exists, and no single spoiler panel is flight-critical. As a result, spoilers are actuated by only one actuator per panel.

- High-lift devices: The high-lift system system typically comprises an assortment of leading-edge and trailing-edge high-lift devices. These are required to satisfy the required approach speed and field performance constraints without compromising the aircraft's cruise performance through the use of an excessively large planform area wing. The types of high-lift devices used varies greatly between aircraft of different sizes and between manufacturers, and an excellent summary may be found in Rudolph [66]. In general, the wing leading-edge contains slats and/or Krueger flaps that cover nearly the entire wingspan except for the mounting positions of the engine pylons. Krueger flaps have high stowing loads and may also see actuation load reversals, and modern commercial airliners show a tendency toward the use of three-position slats which may be either constant-chord or tapered [66]. The trailing-edge typically contains an inboard and a midspan panel on each wing, made up of a single-slotted, double-slotted, or even triple-slotted flap. The latter entail significant complexity and weight penalties, and in modern aircraft are avoided in favor of better designed and lighter double-slotted flaps.

- Trimmable Horizontal Stabilizer (THS): In most commercial transport aircraft, the entire horizontal stabilizer can pivot about an axis. Due to its location and planform area, the THS has extremely high pitch control authority and is made a very slow-moving control by design. Typically, following changes in the aircraft trim caused by changes in airspeed or configuration (due to extension/retraction of flaps and/or landing gear), trim is re-established using the elevator. Following this, the THS may be moved to a new setting that allows the established trim to be maintained with the elevator returned to a faired position.

Table 6: Summary of control surfaces for SSA, LTA, and VLA baselines

Control	SSA	LTA	VLA
Aileron	2	4	6
Elevator	2	2	4
Rudder	1	1	2
Spoiler	10	14	16
L/E device	10	14	16
T/E device	2	2	2

The aerodynamic loads seen by the control surfaces are directly affected by their size (planform area), which can only be finalized after detailed dynamic analyses of control effectiveness, structural loads, and control system effects. Certain guidelines are nevertheless available for initial sizing [37]. The empennage surfaces (elevator and rudder) typically begin at the side of the fuselage and extend to the tip of the corresponding stabilizer (or at least to 90-95 % span). These control surfaces are typically tapered with the same chord ratio as the main lifting surface, allowing for a straight-tapered spar and yielding a constant chord fraction. For jet transports, Raymer [37] gives a chord fraction of 25 % for the elevators and 32 % for the rudders. For ailerons, Raymer [37] provides historical guidelines that relate the flap chord ratio of these surfaces to their spanwise extension. Depending on whether the slats are constant-chord or tapered, the chord ratio relative to the local wing chord may vary between 6.7 % to 16 % at the root and between 16.5 % to 33 % at the tip [66]. For trailing-edge devices, the ratio of flap chord to local wing chord in the stowed position may range between 20 % and 35 % [66].

The control surface sizes established using the above guidelines were cross-verified by reference to existing commercial aircraft similar to the SSA, LTA, and VLA. The control surface layouts and actuator positions are summarized in Table 6 and Fig. 12. The parametric definition of control surfaces with respect to parent lifting surfaces allows the former to re-size if aircraft re-sizing changes the geometry of the latter.
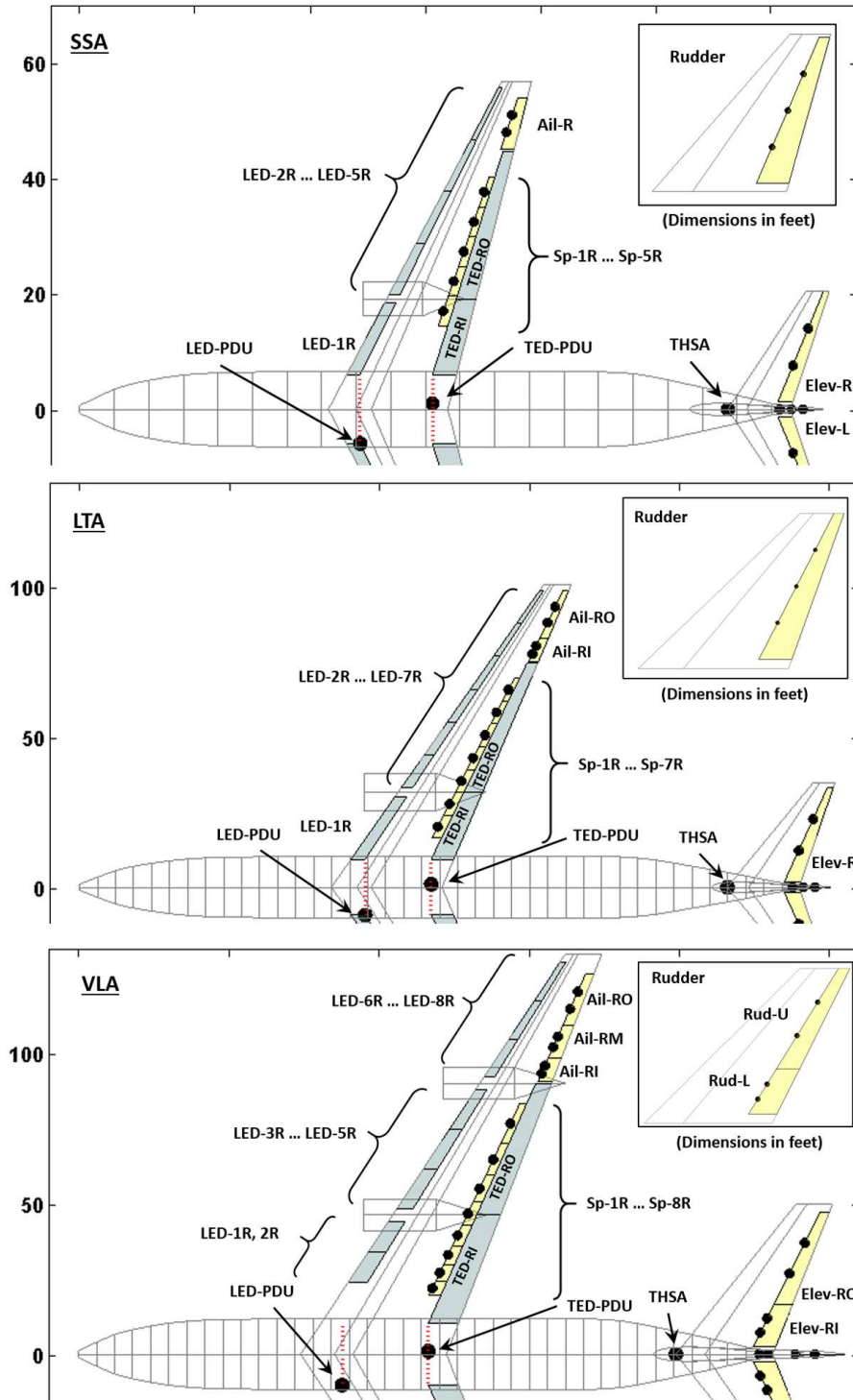
Figure 12: Control surface definitions for SSA, LTA, and VLA baselines

4.1.2 Actuation Loads for Ailerons, Elevators, and Rudders
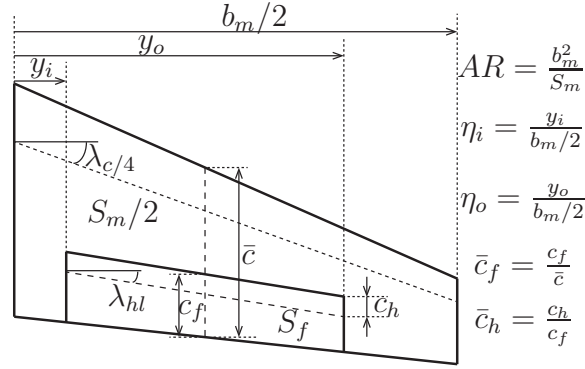
Figure 13: Control surface geometry for hinge moment coefficient estimation

For control surfaces hinged to the trailing edges of lifting surfaces (i.e, ailerons, elevators, and rudder), an overall hinge moment coefficient can be determined that comprises a baseline contribution due to control surface camber (if any), a contribution due to local effective incidence angle (α_{eff}), and a contribution due to control surface deflection (δ),

$$
\begin{aligned}
M_a &= \bar{q} S_f c_f C_h \\
C_h &= C_{h,0} + C_{h,\alpha}(M) \, \alpha_{eff} + C_{h,\delta}(M,\delta) \, \delta,
\end{aligned}
\tag{24}
$$

where $\bar{q}$ is the dynamic pressure, and S_f and c_f are respectively the planform area and the chord of the control surface. A slight manipulation of Eq. 24 yields the following:

$$
\begin{aligned}
M_a &= \bar{q} S_f c_f (C_{h,0} + C_{h,\alpha}(M) \, \alpha_{eff} + C_{h,\delta}(M,\delta) \, \delta) \\
&= [C_{h,0}, \ C_{h,\alpha}(M), \ C_{h,\delta}(M,\delta)] \quad . \quad [1, \ \alpha_{eff}, \ \delta]^T \bar{q} \quad . \quad S_f c_f
\end{aligned}
\tag{25}
$$

The first group of parameters consists of the dimensionless hinge moment coefficients which are estimated empirically using the methodology of Roskam [75]. This requires information such as the planform area (S_f), the mean chord of the control surface (c_f), flap chord ratio ($\bar{c}_f$), airfoil shape, hinge-line sweep (λ_{hl}), main surface sweep ($\lambda_{c/4}$), spanwise coordinates of the inboard and outboard extremities of

the surface (η_i, η_o), and distance between the hinge-line and the leading edge of the control surface ($\bar{c}_h$) (Fig. 13) to generate a 1-dimensional lookup table for $C_{h,\alpha}(M)$ and a 2-dimensional one for $C_{h,\delta}(M, \delta)$. This information is automatically extracted from the 3-D geometric model. In previous work [76], the hinge moment estimates obtained by this method were compared to published flight-test hinge moment measurements from the NASA F-18 SRA program [20], as shown in Fig. 14. The agreement between predicted and published hinge moments was found to be acceptable.

(a) Abrupt roll doublet - full stick (left): M = 0.72, h = 25 kft, q-bar = 13.60 kPa (284 lbf/sq.ft.)

(b) Abrupt aileron reversal - full stick (left): M = 0.84, h = 25 kft, q-bar = 18.29 kPa (382 lbf/sq.ft.)
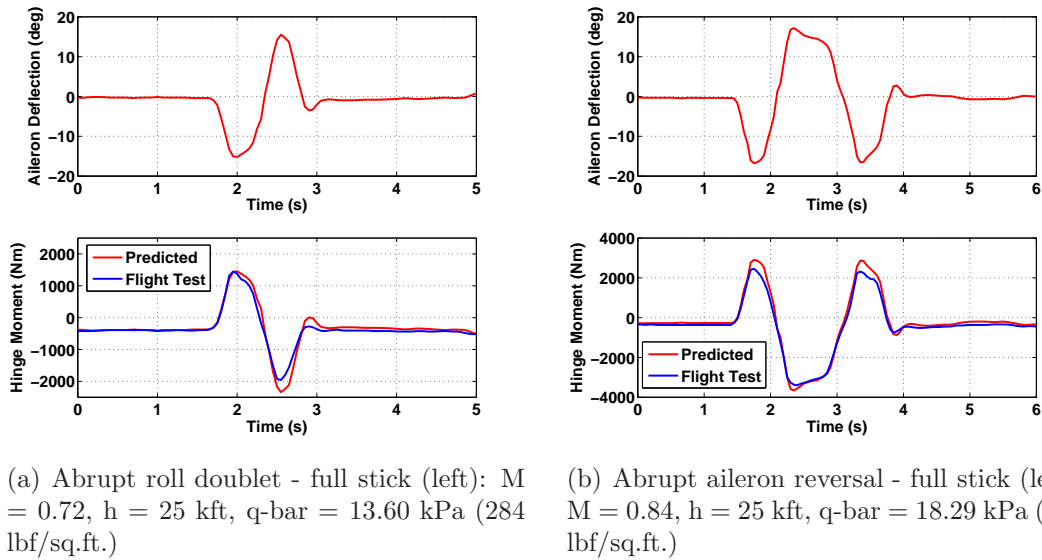
Figure 14: Comparison of predicted hinge moments with NASA F-18 SRA flight test data (same geometry, flight condition, and surface deflections as input)

The parameters in the second group of Eq. 25 collectively define a *flight condition*. The maximum hinge moment corresponds to a flight condition that maximizes the product of the first two groups. Given the Mach number and deflection angle dependencies of the coefficients of the first group, finding this critical flight condition requires the exploration of multiple points in the aircraft altitude-speed flight envelope in search of the peak hinge moment. The guidelines are provided in Part 25 of the Federal Aviation Regulations [77], and are further discussed in the works of Scholz [78, 79, 80]. Only a brief outline is provided here.
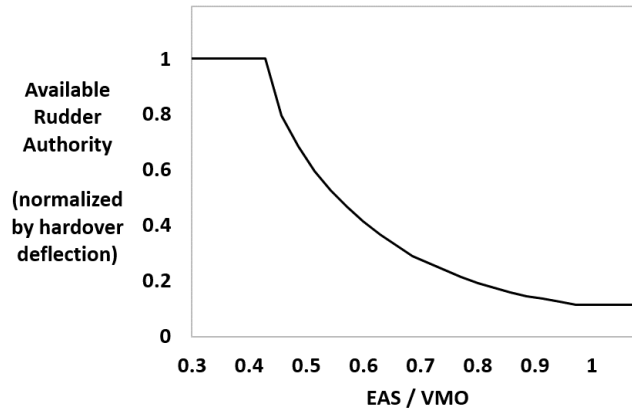
Figure 15: Rudder authority limiting relationship as function of airspeed

- Ailerons (FAR §25.349) - Three flight conditions are considered: (i) Full deflection at design maneuver speed (V_A), (ii) a deflection generating the same roll rate as (i) at design cruise speed (V_C), and (iii) a deflection generating 1/3 of this roll rate at design dive speed (V_D).

- Elevators (FAR §25.255) - The elevator deflections required to generate a specified recovery load factor in response to a runaway failure of the trim system in trailing-edge-up and trailing-edge-down directions are evaluated over the flight envelope.

- Rudder - The maximum hinge moment is determined by evaluating the moments arising from: (i) full rudder deflection in the One Engine Inoperative (OEI) condition at minimum controllable airspeed (FAR §25.149) and (ii) maximum available rudder deflection as a function of equivalent airspeed, with rudder travel limiting imposed as per Fig. 15 (FAR §25.351). The travel-limiting relationship shown in Fig. 15 was derived from [81].

4.1.3 Actuation Loads for Spoilers

In contrast to hinge moment estimation methods for hinged trailing-edge surfaces (shown above), there is not an abundance of handbook methods for the calculation

100

of spoiler hinge moments. Scholz [78] reviewed available data pertaining to spoilers from literature and also from aircraft manufacturers and suggested the following two relationships, applicable to extended and retracted spoiler panels respectively:

$$M_{ext} = \frac{1}{2}\rho V_l^2 \left(\frac{1}{2}C_D \sin^2 \delta_{sp}\right) S_{sp}c_{sp}$$

$$M_{ret} = K_{sp} \frac{c_{sp} S_{sp} W n_z}{c(y_{sp}) b \pi} \sqrt{1 - \left(\frac{2 y_{sp}}{b}\right)^2}, \tag{26}$$

where S_{sp} and c_{sp} are the spoiler planform area and chord, δ_{sp} its deflection, $c(y_{sp})$ the wing chord at spanwise location of spoiler, b the wingspan, W the aircraft weight, and n_z the load factor. The author recommended $C_D = 1.5 - 1.8$, $V_l = 1.14\ V_\infty$, and $K_{sp} = 1.5$, which gave a good match with available spoiler data.

In some aircraft, certain spoiler panels are dedicated to only the ground spoiler role and are not used in flight. Further, the deflection limits for all the spoilers are not necessarily identical. However, for simplicity, this dissertation assumes that:

1. All spoiler panels serve both flight spoiler and ground spoiler roles

2. For each spoiler panel, maximum physical deflection limit is 60° trailing-edge up, with maximum in-flight deflection limited to 38° (based on [82, 83])

With these assumptions, the following flight conditions are evaluated in order to estimate the maximum spoiler hinge moment:

1. Deployment in flight (flight spoiler role) - Extension to maximum permissible in-flight deflection during an emergency descent at the design dive speed (V_D)

2. Deployment on ground (ground spoiler role) - Extension to maximum physical deflection limit at maximum rated tire speed.

For all three baseline aircraft, extension in flight to the permissible limit generated the sizing hinge moments for the spoilers.

4.1.4 Actuation Loads for High-lift Devices

With only a few exceptions, the power required to actuate the high-lift systems of modern commercial aircraft comes from centrally located Power Drive Units[1] (PDU). In a conventional PDU, hydraulic motors (typically two) drive into a gearbox which converts hydraulic power to mechanical rotary output motion. This motion is transmitted through a system of torque tubes and reduction gearboxes to rotary or linear actuators which ultimately provide motion to the high lift devices. Such an arrangement ensures synchronization of the motion of the individual flap panels, which is further verified by position pick-up sensors. In case these sensors detect asymmetry that exceeds a defined threshold, brakes engage to immobilize the drive system completely to prevent further asymmetry from developing [28].

The actuation loads for the high-lift devices cannot be determined in as straightforward a manner as those for the hinged control surfaces described previously. The actuation loads are functions of not only the dimensions of the leading-edge devices (LED) and trailing-edge devices (TED), but also the kinematics of the associated mechanism. Rudolph [66] provides an excellent technical description of the high-lift systems of a large number of commercial aircraft, from which it is evident that there is significant variation in the flap design philosophy (including flap mechanisms) among aircraft and aircraft manufacturers.

Given the difficulty of assessing the actuation power of the high-lift system through a direct assessment of the aerodynamic loads, the actuation power is instead determined based on the power ratings of the PDUs. Based on PDU information collected from a number of sources [82, 84, 39] and the corresponding Maximum Takeoff Mass (MTOM) of each aircraft, the installed PDU power as a function of the MTOM is seen to follow the trend shown in Fig. 16. This power is typically supplied

---

[1]Power Drive Units (PDUs) are also often referred to as Power Control Units (PCUs)
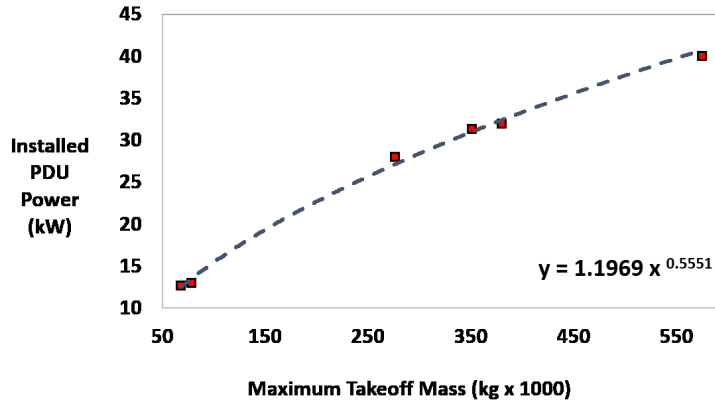
Figure 16: Variation of flap Power Drive Unit (PDU) rating with MTOM

by two power sources (e.g., hydraulic motors) which collectively supply the PDU. In the event of failure of one power source, the other power source can continue to drive the flap system, but at a reduced rate. For simplicity, it is assumed that both the TEDs and the LEDs are actuated by PDUs of identical design, upon verification that this is, in fact, the case for certain in-service aircraft [82, 84].

4.1.5 Actuation Loads for Trimmable Horizontal Stabilizer

The hinge moment estimation technique used for the aileron, elevator, and rudder is also applicable to the THS. However, while the hinge moment coefficients can be determined relatively easily, it is more difficult to determine the flight condition at which the THS will see the maximum hinge moment. For modern FBW aircraft, the THS under normal operating mode is automatically manipulated by the FBW system to allow the elevator to be offloaded and returned to a faired position following the establishment of pitch trim. This manipulation logic determines the amount of mis-trim that is permitted before the THS is actuated and therefore directly influences the magnitude of the hinge moments developed. Since this logic is determined much later in the design process, an alternative approach is taken to the determination of the actuation requirements of the THS and the subsequent mass estimation for the Trimmable Horizontal Stabilizer Actuator (THSA).

103
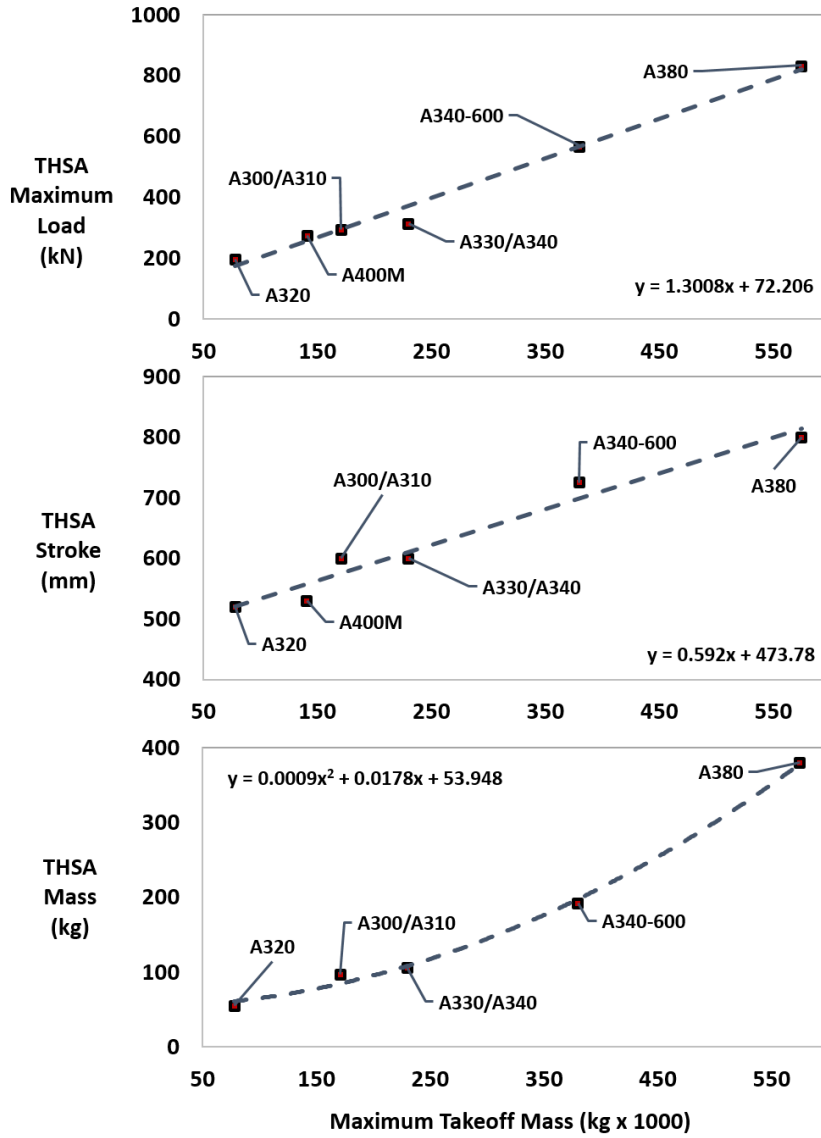
Figure 17: Variation of Trimmable Horizontal Stabilizer Actuator (THSA) characteristics with MTOM

Information regarding the THSA mass, maximum load $F_{0,thsa}$, and stroke s_{thsa} for a range of Airbus aircraft from 1970 to the present date was provided by Socheleau et al. [85]. Using this information and the publicly available information regarding the MTOM for each of these aircraft, the trends shown in Fig. 17 are obtained.

The stop-to-stop range of motion of the THSA is similar for most commercial aircraft, and is around $\Delta\delta_{max} = 17.5°$. As mentioned previously, the THS is a

slow-moving control by design, with a maximum rate around $\dot{\delta}_{max} = 1°/s$. This allows the maximum rate of the THSA to be estimated as

$$v_{max,thsa} = \frac{s_{thsa} \, \dot{\delta}_{max}}{\Delta \delta_{max}}. \tag{27}$$

The corner power of the THSA follows as

$$P_{thsa}^{cp} = F_{0,thsa} \, v_{max,thsa} \tag{28}$$

The mass of the THSA was determined as

$$M_{thsa} = M_{0,thsa} + M_{drive}, \tag{29}$$

where M_{drive} is the mass of the drive system, which for a conventional THSA typically comprises two hydraulic motors. However, in recent aircraft such as the Boeing 787 the THSA has been electrified [74], in which case electric motors are used. For either case, the component M_{drive} is estimated using the generic actuator mass estimation technique described in the following section.[2]

4.1.6 Actuator Mass Estimation

Mass estimation of electric actuators was addressed in Chakraborty et al. [86, 87] and Garmendia et al. [88, 89] using a component mass build-up approach, in which the masses of the major actuator components were evaluated based on the output requirements (load, force, and stroke) and subsequently summed to yield the actuator mass. A limited number of actuator and kinematic design variables was used to search for mass-optimal actuator designs. With regard to the current problem, one limitation of this approach is that explicit models are required for the main components of the actuator, thus necessitating the creation of a large number of component models to represent multiple actuator types. Since this dissertation

---

[2]Technically, the mass $M_{0,thsa}$ as obtained from Fig. 17 already accounts for the mass of the hydraulic motors. However, these motors account for only a very small fraction of the overall THSA mass. Thus, Eq. 29 provides a reasonable (and conservative) estimate of the THSA mass.

focuses more on the variation of actuator mass with technological SOTA than on mass-optimal actuator designs, a more generalized approach to mass estimation has been used. For simplicity, this is first developed for the case of a linear electric actuator and then further generalized to the case of any actuator and output motion.

For an electric actuator with linear output motion, let (F_0/M) define the ratio of the actuator's stall load to its mass (units: kN/kg or lbf/lbm). Further, let $(P/M)_{em}$ and $(P/M)_{pe}$ be the power-to-mass ratios of the electric motor and the power electronics (units: kW/kg or hp/lb) with current SOTA. These components are assumed to have overall efficiencies η_{em} and η_{pe} respectively. The overall efficiencies of actuator components downstream of the electric motor output shaft are collectively represented by η_m. Based on the actuator's load-speed envelope, let P_m^{max} be the maximum mechanical power output. The mass of the actuator is expressed as

$$M_{act} = \frac{F_0}{(F_0/M)} + \frac{P_m^{max}}{\eta_m} \left\{ \frac{1}{(P/M)_{em}} \left(\frac{1}{\kappa_{em}} - 1 \right) + \frac{1}{\eta_{em}\eta_{pe}(P/M)_{pe}} \left(\frac{1}{\kappa_{pe}} - 1 \right) \right\},$$
(30)

where $\kappa_{em} = 1$ and $\kappa_{pe} = 1$ indicate current SOTA as far as electric motor and power electronics technology are concerned. Improvements in the SOTA are represented by values of $\kappa_{em} > 1$ and $\kappa_{pe} > 1$, using which it is clear that a reduction in the actuator mass is predicted by Eq. 30.

The tacit assumption in this approach is that the design of mechanical components such as gearboxes and ballscrews (found in an EMA, for instance) or hydraulic components such as pumps and cylinders (found in an EHA, for instance) has already reached a high level of refinement. Thus, for these actuators, substantial mass reductions are unlikely to originate from enhancements to these components, but rather from improvements of electric motor and power electronics SOTA.

A more general form of Eq. 30 may be obtained as

$$M_{act} = \frac{\mathcal{X}_0}{(\mathcal{X}_0/M)} + \frac{P_m^{max}}{\eta_m} \left\{ \frac{1}{(P/M)_{em}} \left(\frac{1}{\kappa_{em}} - 1 \right) + \frac{1}{\eta_{em}\eta_{pe}(P/M)_{pe}} \left(\frac{1}{\kappa_{pe}} - 1 \right) \right\},$$
(31)

Table 7: Assumed figures of merit for actuator types and components

Actuator / Component	$(\mathcal{X}_0/M)$ or (P/M)	Source
Electrohydrostatic actuator (EHA)	2.2 kN/kg	Ref. [24]
Electromechanical actuator (EMA)	2.4 kN/kg	Ref. [90]
Hydraulic Power Control Unit (PCU)	3.8 kN/kg	Ref. [24]
Hydraulic Power Drive Unit (H-PDU)	4.5 kW/kg	Refs. [91, 82]
Stabilizer trim hydraulic motor	2.4 kW/kg	Ref. [92]
Electric motor	1.4 kW/kg	
Power electronics	2.0 kW/kg	Refs. [93, 94]

where $\mathcal{X}_0$ may represent the stall load F_0 for a linear actuator (Eq. 30), the maximum output moment $\mathcal{M}_0$ of a rotary hinge-line actuator, or the maximum shaft-power output of a PDU. The corresponding figure of merit $(\mathcal{X}_0/M)$ of the actuator may be identified by reference to product data sheets or other sources containing the specifications of existing actuators of that particular type (Table 7). Equation 31 may also be applied to the case of conventional hydraulic actuators or PDUs by simply ignoring the second term for the electric motor and power electronics.

4.1.7 Hydraulic Actuation Power Consumption

The power requirement of a hydraulic actuator is derived with reference to a linear actuator. Let it be assumed that an actuation function involves the generation of a peak stall load F_0. If Δp_{wk} is the maximum hydraulic pressure difference available at the site of the actuator, then the required actuator area may be estimated as

$$A_{req} = \frac{\kappa \ F_0}{\Delta p_{wk}}, \tag{32}$$

where $\kappa > 1$ provides an excess margin. Once the required hydraulic actuator area has been sized, it is clear that the required flow rate is directly proportional to the actuator's rate or output velocity. Thus, if the actuation function requires the

generation of an output velocity v, then the corresponding flow rate requirement is

$$Q = A_{req} \; v = \frac{\kappa \; F_0 \; v}{\Delta p_{wk}}.$$
(33)

This flow rate requirement becomes maximum when $v = v_{max}$, i.e., when the maximum output velocity is required. In other words,

$$Q_{max} = A_{req} \; v_{max} = \frac{\kappa \; F_0 \; v_{max}}{\Delta p_{wk}} = \frac{\kappa \; P_{cp}}{\Delta p_{wk}},$$
(34)

where $P_{cp} = F_0 \; v_{max}$ is the corner power of the actuator (product of maximum output force and maximum output velocity). From the above, the following two observations regarding hydraulic load flow requirements may be made:

1. From Eq. 33, it is seen that the flow rate required is directly proportional to the required output velocity. For the case of flight control surfaces, this implies that the maximum load (in terms of required flow rate) is imposed when the control surfaces move at high *rate* (angular velocity)

2. From Eq. 34, it is seen that for a given corner power P_{cp}, the maximum flow requirement is inversely proportional to the available working pressure P_{wk}. Thus, the same actuation load when served by a higher pressure system (e.g., 5,000 psi instead of 3,000 psi) will have a lower fluid flow rate requirement

4.1.8 Electric Actuation Power Consumption

The power requirement of an electric actuator is derived by first considering the air loads acting on a control surface. Let the control surface hinge moment M_h be expressed as a function of control surface position δ as

$$M_h = A + B\delta.$$
(35)

Further, let the mean gearing ratio (Fig. 18) between the control surface and the actuator be G_{kin} such that

$$G_{kin} = \frac{\Delta \delta}{\Delta x} = \frac{\dot{\delta}}{v}.$$
(36)
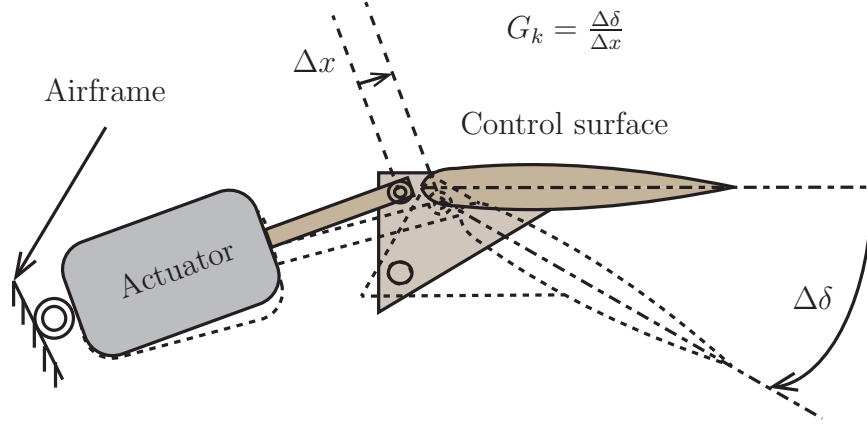
Figure 18: Kinematics of actuator to control surface linkage

Assuming a mechanism efficiency of η_{kin}, the actuator force corresponding to a given hinge moment is given by

$$F = \frac{M_h\ G_{kin}}{\eta_{kin}} \tag{37}$$

Let the overall actuator gearing be defined as the ratio of the maximum angular velocity of the electric motor and the maximum speed of the output ram, i.e.,

$$G_{act} = \frac{\omega_{max}}{v_{max}} = \frac{\omega}{v} \tag{38}$$

The following relationship exists between the two gearing ratios:

$$\frac{G_{kin}}{G_{act}} = \frac{\dot{\delta}/v}{\omega/v} = \frac{\dot{\delta}}{\omega} = G_{eff} \tag{39}$$

Assuming an actuator efficiency η_{act} that accounts for the motor windage losses and losses in components downstream of the electric motor, the required torque output of the motor may be given by

$$\tau_m = \frac{G_{eff}}{\eta_{kin}\eta_{act}}\ M_h = \kappa M_h \tag{40}$$

Considering only mechanical shaft-power output and heat losses, the required power input to the electric motor is given by

$$P_{in} = V\ I = (IR + K_m\omega)\ I \tag{41}$$

109

where K_m is the motor constant which also relates the torque and the current as $\tau_m = K_m\ I$. Using this, the power requirement becomes

$$P_{in} = I^2 R + K_m\ \omega\ I = \frac{R}{K_m^2}\tau_m^2 + \tau_m\ \omega = \lambda\ \tau_m^2 + \tau_m\ \omega \tag{42}$$

Using Eqs. 35, 39, and 40 in Eq. 42, the power requirement of the motor may be represented in terms of the control surface motion characteristics δ and $\dot{\delta}$ as

$$\begin{aligned} P_{in}(\delta, \dot{\delta}) &= \lambda\left\{\kappa(A+B\delta)\right\}^2 + \kappa(A+B\delta)\ \frac{\dot{\delta}}{G_{eff}} \\ &= \lambda\kappa^2 A^2 + (\lambda\kappa^2 B^2)\ \delta^2 + (2\lambda\kappa^2 AB)\delta + \left(\frac{\kappa A}{G_{eff}}\right)\dot{\delta} + \left(\frac{B}{\eta_{kin}\eta_{act}}\right)\delta\dot{\delta} \end{aligned} \tag{43}$$

Subject to the assumptions stated above, Eq. 43 is valid for any arbitrary control surface motion. Unlike hydraulic actuation, it is seen that for electric actuation the power requirement is a more complex function of both the instantaneous actuation load and the actuation rate.

4.1.9 Power Requirements for Prescribed Sinusoidal Motion

For evaluating the power requirements of control surface actuators during the course of the mission, the special case of prescribed sinusoidal excursions about $\delta = 0$ is considered. The prescribed motion may be represented as

$$\delta(t) = \delta_{peak}\sin(\Omega t), \qquad \dot{\delta}(t) = \delta_{peak}\ \Omega\cos(\Omega t), \tag{44}$$

where $\Omega = \dot{\delta}_{peak}/\delta_{peak}$ is the ratio of the peak control surface rate to the amplitude of excursion. The excursion amplitude is bounded by the deflection limits of the control surface, i.e. $0 \leq \delta_{peak} \leq \delta_{max}$. The peak rate is limited to the maximum permissible control surface angular rate, i.e., $0 \leq \dot{\delta}_{peak} \leq \dot{\delta}_{max}$.

If this sinusoidal motion of Eq. 44 is enforced in Eq. 43 for the electric actuator and the average power over one sinusoidal cycle period $T = 2\pi/\Omega$ is computed, then the following observations may be made:

- Term 1: This propagates unchanged, and represents the electrical power required to provide the holding load to maintain the surface at $\delta = 0$

- Term 2: The average value of this term is obtained by setting $\delta = \delta_{max}/\sqrt{2}$

- Term 3: The average value of this term over the time period is zero

- Term 4: The average value of this term over the time period is zero

- Term 5: If a simple integration is performed, then this term also evaluates to zero. Physically this is due to the fact that the power recovered (regenerated) during motion with aiding load ($M_h < 0, \dot{\delta} > 0$ and $M_h > 0, \dot{\delta} < 0$) is numerically equal to the power supplied by the actuator under antagonistic load ($M_h > 0, \dot{\delta} > 0$ and $M_h < 0, \dot{\delta} < 0$). However, if the re-introduction of regenerated power onto the electric bus is disallowed (by assuming that regenerated power is dissipated through a shunt resistor), then for this term the average value of the power *supplied* over the cycle may be obtained by setting $\delta\dot{\delta} = \delta_{max}\dot{\delta}_{max}/(2\pi)$

Incorporating these observations, the mean input power requirement of the motor for this prescribed motion is given by

$$\bar{P}_{in}(\delta_{max}, \dot{\delta}_{max}) = \lambda\kappa^2 A^2 + \left(\frac{\lambda\kappa^2 B^2}{2}\right)\delta_{max}^2 + \left(\frac{B}{2\pi\ \eta_{kin}\eta_{act}}\right)\delta_{max}\dot{\delta}_{max}, \qquad (45)$$

in which, as stated previously,

$$\lambda = \frac{R}{K_m^2}, \qquad \kappa = \frac{G_{eff}}{\eta_{kin}\eta_{act}}. \qquad (46)$$

Finally, if the prescribed motion only occurs for $\epsilon \in [0,1]$ fraction of the overall time, and if the efficiency of the actuator's power electronics is η_{pe}, then the mean bus power draw is given by

$$\bar{P}_{bus}(\delta_{max}, \dot{\delta}_{max}) = \frac{1}{\eta_{pe}}\left[\lambda\kappa^2 A^2 + \epsilon\left\{\left(\frac{\lambda\kappa^2 B^2}{2}\right)\delta_{max}^2 + \left(\frac{B}{2\pi\ \eta_{kin}\eta_{act}}\right)\delta_{max}\dot{\delta}_{max}\right\}\right]$$
$$(47)$$

111

Applying the prescribed sinusoidal motion for the case of the hydraulic actuator, the mean hydraulic power may be estimated as

$$\bar{P}_{hyd} = \frac{2}{\pi} \left(\frac{\epsilon}{\eta_{act}} \right) \left(\frac{\dot{\delta}_{peak}}{\dot{\delta}_{max}} \right) P_{cp}, \tag{48}$$

where η_{act} is the assumed overall efficiency of the hydraulic actuator. The quantity $2/\pi$ appears as the absolute value of the angular rate is integrated over a cycle.

4.2 Landing Gear Actuation System (LGAS)

Within the scope of this dissertation, the control volume of the LGAS includes only the retraction/extension actuator. Additional actuators such as the uplock and downlock actuators and door actuators are not modeled. Depending on the actuator type, hydraulic or electric power may be required. Therefore, this subsystem always uses shaft-power. It does not generate any direct drag penalty.

4.2.1 Landing Gear Actuation Requirements and System Sizing

During retraction/extension, the landing gear is subjected to gravitational, aerodynamic, frictional, and inertial forces which affect the magnitude of the actuation load. Of these, the effect of the gravitational load (due to the mass of the landing gear leg) is dominant [95]. An analysis of various aircraft showed that the total landing gear mass is approximately 3 % of the total mass of the airplane, with the nose gear accounting for 0.5 % [96] (in other words around 16.7 % of the total landing gear mass). However, a more detailed component mass breakdown for a number of transport aircraft of varying sizes [97] shows the contribution from the nose gear to be between 8 - 12 %. Based on this, a mean value of $\alpha_{nlg} = 0.1$ (i.e., 10 %) is used in this dissertation as representing the percentage contribution of the nose landing gear to the total landing gear mass. From the mass breakdown presented in [97], the relative location of the CG of the main landing gear $(\tilde{\ell}_{cg,mlg,0})$ and the nose landing gear $(\tilde{\ell}_{cg,nlg,0})$ were also computed. These are shown in Table 8 for the three

Table 8: Relative CG position of main landing gear leg ($\tilde{\ell}_{cg,mlg,0}$) and nose landing gear leg ($\tilde{\ell}_{cg,nlg,0}$) for SSA, LTA, and VLA baselines

Rel. CG	SSA	LTA	VLA
Main gear	0.72	0.69	0.69
Nose gear	0.79	0.68	0.68

baselines. The quantities are normalized using the total length of the gear legs (L_{mlg} and L_{nlg}) from the pivot point to the ground contact point, thus yielding a relative location of 0 for the pivot point and 1 for the ground contact point.

Since most aircraft sizing tools (including FLOPS) provide an estimate of the total landing gear group mass M_{lgg}, this is used with the percentage contributions discussed above to compute the mass of the nose and main landing gear legs as

$$
\begin{aligned}
M_{nlg,0} &= \alpha_{nlg}\, M_{lgg}, \\
M_{mlg,0} &= \frac{(1 - \alpha_{nlg})}{n_{mlg}}\, M_{lgg},
\end{aligned}
\tag{49}
$$

where n_{mlg} is the total number of main landing gear legs. Thus, the simplifying assumption was made that for aircraft with $n_{mlg} > 2$ (e.g., presence of two wing-mounted main gears and two body-mounted main gears), the masses of the main landing gear legs are identical. The approach to computing the landing gear actuation requirements is identical for nose and main landing gears, and subscripts 'nlg' and 'mlg' are not used subsequently.

The mass and relative CG location of the landing gear legs is affected by the mass and locations of subsystems such as the WBS, NWSS, and ETS (if installed). The subscripts '0' in Eq. 49 and Table 8 signify that the corresponding quantities apply to the baseline vehicle with conventional subsystem architecture (hydraulic WBS and NWSS, no ETS installed). Alternative actuation solutions for the WBS and NWSS may result in either an increase or decrease in the mass of the landing gear leg. The incorporation of ETS on the other hand always results in an increase of mass of the
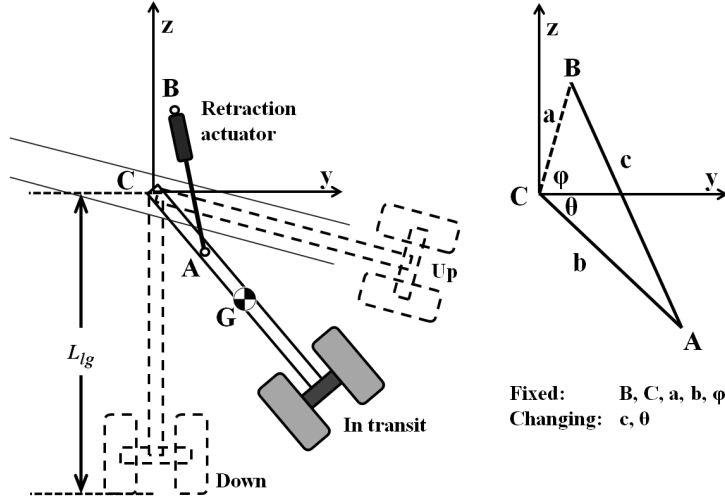
Figure 19: Landing gear retraction kinematics

leg. The net mass and effective CG position for the landing gear leg considering the NWSS, WBS, and ETS (if present) subsystem masses is computed as

$$
\begin{aligned}
M_{lg} &= M_{lg,0} + \sum_i^n \Delta M_{ss,i}, \\
\tilde{\ell}_{cg} &= \frac{M_{lg,0}\, \tilde{\ell}_{cg,0} + \sum_i^n \Delta M_{ss,i}\, \tilde{\ell}_{cg,ss,i}}{M_{lg,0} + \sum_i^n \Delta M_{ss,i}}
\end{aligned}
\tag{50}
$$

where $\Delta M_{ss,i}$ is the change in mass of the 'i'th subsystem relative to the conventional architecture, and $\tilde{\ell}_{cg,ss,i}$ is the relative location of subsystem 'i' on the gear leg.

To relate the mass properties of the landing gear to corresponding actuation requirements, it is assumed that the main landing gear legs pivot about an axis parallel to the aircraft's longitudinal axis, retracting into the main landing gear bay. Similarly, the nose gear is assumed to pivot about an axis parallel to the aircraft's lateral axis and retract forward into the nose landing gear bay [98]. The effect of friction in the mechanism is accounted for using an overall mechanism efficiency of η_m. Figure 19 shows the relevant kinematic parameters for the main landing gear mechanism. The same kinematic relationships are also valid for the nose gear. Point **A** is the actuator-strut attachment point, **B** the actuator-airframe attachment point, **C** the landing gear pivot point, and **G** the landing gear leg center of gravity.

114

Table 9: Main and nose landing gear retraction mechanism parameters

Parameter	Nose gear	Main Gear
BC (a)	$0.09\ L_{nlg}$	$0.09\ L_{mlg}$
CA (b)	$0.30\ L_{nlg}$	$0.30\ L_{mlg}$
ϕ	80°	80°
η_m	0.80	0.80
$\theta_{up},\ \theta_{dn}$	-20°, 90°	25°, 90°
Δt	20 sec	20 sec

Considering moments about the landing gear pivot point **C**, the length c (related to actuator ram position) and the required actuator force F may be computed as a function of landing gear leg angular position θ as follows:

$$
\begin{aligned}
c(\theta) &= \sqrt{a^2 + b^2 - 2ab\cos(\theta + \phi)}, \\
F(\theta) &= \frac{W_{lg}\ \ell_{cg}\cos\theta\ \sqrt{a^2 + b^2 - 2ab\cos(\theta + \phi)}}{\eta_m\ a\ b\ \sin(\theta + \phi)}
\end{aligned}
\tag{51}
$$

The actuator's stall load F_0, stroke s, and maximum ram speed v_{max} may then be computed as

$$
F_0 = \max_{\theta \in [\theta_{up}, \theta_{dn}]} F(\theta), \qquad s = c(\theta_{dn}) - c(\theta_{up}), \qquad v_{max} = \frac{s}{\Delta t\ (1 - \epsilon)},
\tag{52}
$$

where θ_{up} and θ_{dn} correspond to the retracted and extended positions of the gear respectively, and Δt is the retraction time. The mechanism is assumed to have angular acceleration/deceleration over equal time intervals $\epsilon \cdot \Delta t, \epsilon \in (0, 1)$. For the remaining time $\Delta t\ (1 - 2\epsilon)$, retraction at the maximum ram speed v_{max} is assumed.

The settings for the kinematic parameters appearing in Eq. 51 are summarized in Table 9. They are set based on the description of a commercial transport landing gear mechanism provided by Young [98]. The dimensions a and b are set as fractions of the landing gear length. The force-stroke characteristic that is obtained through Eq. 51 using the main landing gear parameters is shown in Fig. 20, and satisfies the preliminary requirement that the force be relatively uniform over the majority of the stroke without any pronounced peaks [99].
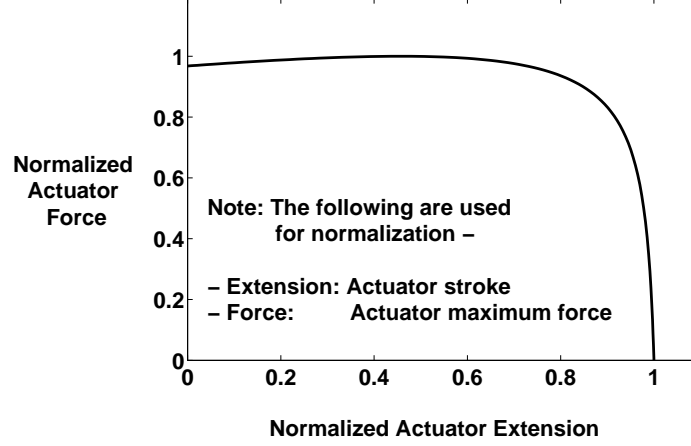
Figure 20: Force-stroke characteristic for landing gear retraction/extension

4.2.2 Power Requirements

Under the assumption that the landing gear is retracted with the actuator operating at its maximum rate v_{max}, the corner power and peak power corresponding to the retraction are given by

$$P_{lga}^{cp} = F_0 \ v_{max},$$

$$P_{lga}^{peak} = \max_{\theta=\theta_{dn}}^{\theta_{up}} F(\theta) \ v_{max}.$$

The maximum hydraulic and electric power requirements may be obtained as

$$P_{hyd}^{max} = \frac{P_{lga}^{cp}}{\eta_{ha}}$$

$$P_{elec}^{max} = \frac{P_{lga}^{peal}}{\eta_{ema}} \tag{53}$$

where η_{ha} and η_{ema} are the overall efficiencies of the hydraulic and electromechanical retraction actuators respectively.

4.2.3 Mass Estimation

For both hydraulic and electromechanical landing gear actuators, the mass is determined using the generic actuator mass relationship described in Section 4.1.6, using force-to-mass ratio (F/M) as the actuator figure of merit.

116

4.3 Nose-wheel Steering System (NWSS)

The control volume for the NWSS consists of the steering mechanism, which may use either hydraulic power or electric power. In either case therefore, the NWS imposes only a shaft-power requirement. No direct drag is attributed to this subsystem.

Electrification of the NWS function was considered as part of the ELGEAR and DRESS programs[3] [68, 67, 100], in part motivated by the interest in eliminating flammable hydraulic fluid from close proximity to heated brakes in landing gear bays. The optimized DRESS actuator was found to be heavier than the baseline hydraulic actuator and a global aircraft-level assessment was recommended [100].

4.3.1 Determination of Sizing Steering Moment

The sizing of the steering mechanism requires the estimation of the maximum required steering moment. The applied moment must overcome the opposing moment generated due to frictional forces between the tire and the ground. These frictional forces increase with the load being carried by the nose gear leg. The recommended range for nose gear static loading is 8-15 % [37, 96]. Below this range, nose-wheel steering authority may be compromised while above this range, takeoff rotation performance may be compromised. Thus, the following aircraft loading condition is used for NWSS sizing purposes: Maximum Ramp Weight (MRW) at forward CG limit. Under these conditions, the nose gear static load may be assumed to be $\epsilon_s = 15$ % of the total aircraft weight. The nose gear load may increase further under braking conditions due to the load transfer from the main gear to the nose gear. Therefore, in accordance with FAR §25.499, a dynamic load factor $\kappa = 1.33$ is applied to the static loading to obtain the maximum nose gear reaction to be used for NWSS

---

[3]ELGEAR: Electric Landing Gear Extend and Retract, DRESS: Distributed and Redundant Electromechanical nose wheel Steering System
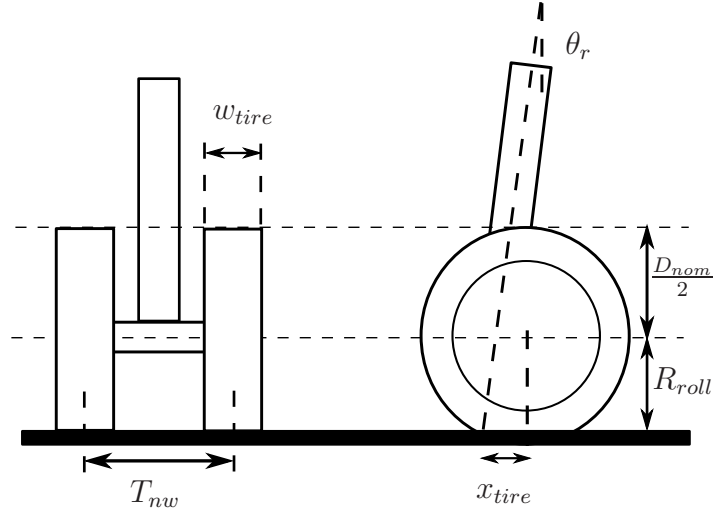
Figure 21: Nose-wheel steering geometry

sizing:

$$F_{z,nlg}^{max} = \kappa \ \epsilon_s \ (MRW) \tag{54}$$

Also in accordance with FAR §25.499, a critical horizontal (lateral) load at the tire-to-ground contact point of 0.8 times the normal reaction of Eq. 54 is considered, i.e., $\left(\frac{F_y^{nlg}}{F_z^{nlg}} \right) = 0.8$. The lateral load developed is thus given by

$$F_{y,nlg}^{max} = \left(\frac{F_y^{nlg}}{F_z^{nlg}} \right) \ F_{z,nlg}^{max} = \left(\frac{F_y^{nlg}}{F_z^{nlg}} \right) \ \kappa \ \epsilon_s \ (MRW). \tag{55}$$

The moment that is developed about the steering axis as a result of the lateral force $F_{y,nlg}^{max}$ may be determined based certain geometric parameters of the steering mechanism, which are shown in Fig. 21. The *rake angle* θ_r is simply the inclination of the steering axis to the vertical. This angle and the axle offset result in the generation of the *tire trail* x_{tire}, which is the distance between the theoretical ground contact point and the intersection of the steering axis with the ground, measured along the ground. The rake angle and trail are set as shown in Table 10 based on early design guidelines for this category of aircraft [37]. This geometry results in the creation of an effective moment arm

$$L_{eff} = x_{tire} \ \cos\theta_r, \tag{56}$$

118

Table 10: Nose landing gear and NWSS parameters

NLG parameters	Max. static load	ϵ_s	15 %
	Rake angle	θ_r	7°
	Tire trail	x_{tire}	16 % of tire radius
	Tire track	T_{nw}	2 x tire width
NWSS parameters	Deflection	$\delta_{max}, \delta_{min}$	± 75°
	Max. Rate	$\omega_{max}, \omega_{min}$	± 20°/s
	Rel. Posn.	$\tilde{\ell}_{nws}$	0.50
	Motor max RPM		2,000

using which the maximum steering moment for this case may be computed as

$$M_{steer}^{nws} = L_{eff} \ F_{y,nlg}^{max} = (x_{tire} \ \cos\theta_r) \ \left(\frac{F_y^{nlg}}{F_z^{nlg}}\right) \ (\kappa \ \epsilon_s \ MRW). \tag{57}$$

In addition to this, the steering moment required in order to steer the nose gear with the aircraft stationary must be computed. In this case, since there is no forward motion of the aircraft, a certain degree of tire scrubbing occurs. The friction forces generated as a result of this once more translate into a moment about the steering axis which must be overcome by the steering system. An empirical relationship for the scrubbing torque developed in this situation is given by

$$
\begin{aligned}
M_{scrub}^{nws} &= 0.24 \ F_{z,nlg}^{max} \ \frac{b^2}{T_{nw}/2} \qquad \text{(imperial units)}, \\
b &= 2w_{tire}\sqrt{\left(\frac{\delta}{w_{tire}}\right) - \left(\frac{\delta}{w_{tire}}\right)^2}, \\
\delta &= \frac{D_{nom}}{2} - R_{roll},
\end{aligned}
\tag{58}
$$

in which the wheel track T_{nw}, nominal tire diameter D_{nom}, rolling radius R_{roll}, and tire section width w_{tire} are in inches [101]. D_{nom}, R_{roll}, and w_{tire} are obtained by the process of tire selection, which is explained in Section 4.4. The sizing moment for the NWSS is taken to be the maximum of those predicted by Eq. 57 and Eq. 58. The steering moment for the SSA obtained using this approach was in good agreement with those published from the ELGEAR project [68] for the Airbus A320 aircraft.
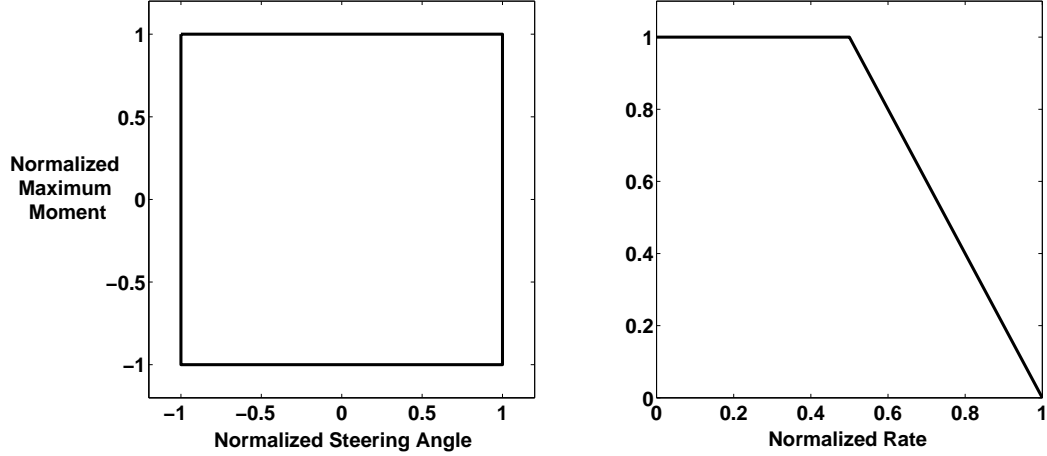
Figure 22: Load-angle and load-speed envelopes for nose-wheel steering system

4.3.2 Power Requirements

To determine the power requirements for the NWSS, the load-angle and load-rate envelopes shown in Fig. 22 are considered. The available moment is required to be independent of the steering angle. Above 50 % of the maximum angular rate, the available moment is permitted to decrease linearly to zero at the maximum angular rate. The peak power and corner power of the steering mechanism are then given by

$$
\begin{aligned}
P_{nws}^{peak} &= \max_{\dot{\delta}=0}^{\dot{\delta}_{max}} \left(\dot{\delta} \ M_{max}(\dot{\delta}) \right), \\
P_{nws}^{cp} &= M_{nws}^{max} \ \dot{\delta}_{max}.
\end{aligned}
\tag{59}
$$

Assuming an overall efficiency of η_{h-nws} and η_{e-nws} for hydraulic and electric steering mechanisms respectively, the maximum electrical and hydraulic power requirements for the nose-wheel steering function are given by

$$
\begin{aligned}
P_{hyd}^{max} &= \frac{P_{nws}^{cp}}{\eta_{h-nws}}, \\
P_{elec}^{max} &= \frac{P_{nws}^{peak}}{\eta_{e-nws}}.
\end{aligned}
\tag{60}
$$

4.3.3 Mass Estimation

For the electric NWSS, the mass of the gearbox is estimated using an empirical correlation developed at NASA using actual gearbox weight data [102], where gearbox mass is a function of the maximum delivered output power and the gear ratio:

$$
\begin{aligned}
W_{gb} \text{ [lb]} &= -37.4262 + 116.3297 \, \mathcal{K}_{gb}, \\
\mathcal{K}_{gb} &= \left(\frac{hp}{RPM_{out}}\right)^{0.75} \left(\frac{RPM_{in}}{RPM_{out}}\right)^{0.15}.
\end{aligned}
\tag{61}
$$

The horsepower (hp) in Eq. 61 is obtained from the peak power computed in Eq. 59. The input and output RPM correspond directly to the maximum angular rate of the NWSS and the maximum RPM of the electric motor (Table 10). The motor and power electronics mass are estimated as

$$
M_{em} + M_{pe} = \frac{P_{nws}^{peak}}{\eta_{gb}} \left(\frac{1}{(P/M)_{em}} + \frac{1}{\eta_{em} \, \eta_{pe} (P/M)_{pe}}\right),
\tag{62}
$$

where $(P/M)_{em}$ and $(P/M)_{pe}$ are the power-to-mass ratios of the electric motor and the power electronics. η_{gb}, η_{em} and η_{pe} are the overall efficiencies of the gearbox, motor, and power electronics respectively. The electric NWSS mass is summed as

$$
M_{e-nwss} = M_{gb} + M_{em} + M_{pe}.
\tag{63}
$$

No model of the hydraulic steering mechanism was created in the scope of this dissertation. Instead, the mass of the hydraulic steering system is estimated based on weight breakdown data presented by Currey [97] for the controls associated with the nose landing gear.

4.4 Wheel Braking System (WBS)

The function of the wheel braking system is to decelerate the aircraft on the ground. During the deceleration, the kinetic energy of the aircraft is converted to thermal (heat) energy which is dissipated through the brakes. In a conventional actuation

architecture, hydraulic brakes are used. However, as with landing gear actuation and nose-wheel steering functions, there is significant interest in electrifying brake actuation as well, since it would allow the elimination of flammable hydraulic fluid from the vicinity of heated brake disks. Electromechanical brakes are already in service on the Boeing 787 aircraft [30, 74]. Depending on the aircraft size, the weight of an electromechanical system may be slightly higher than the equivalent hydraulic system [103], once again necessitating an assessment at the aircraft-level.

4.4.1 Physical Modeling and Relationships

For the sizing of the brakes and brake actuation system, the aircraft deceleration requirements must be converted into brake actuation requirements. The total braking force F_b^{tot} between the tire and the ground required to generate a desired deceleration $\dot{V} < 0$ may be obtained through a force balance in the longitudinal direction:

$$
\begin{aligned}
M\dot{V} &= T - D - F_b^{tot} - F_f + Mg\sin\theta, \\
\implies F_b^{tot} &= T - D - F_f + Mg\sin\theta - M\dot{V}.
\end{aligned}
\tag{64}
$$

In Eq. 64, M is the aircraft mass, T the total thrust of all operating engines ($T < 0$ implies reverse thrust), D the aerodynamic drag, F_f the rolling friction force, and θ the surface gradient ($\theta > 0$ is the aircraft is moving down-hill).

If the total braking force F_b^{tot} is assumed to be generated by equal contributions from n_{brk} braked wheels, then the braking force per wheel is given by

$$
F_b = \frac{F_b^{tot}}{n_{brk}}.
\tag{65}
$$

The braking torque per wheel (torque applied by the braking system to the braked wheel) may be obtained from the braking force per wheel by considering the equation of motion of a braked wheel:

$$
\mathcal{I}_w\dot{\omega}_w = F_b R_{roll} - \tau_b \implies \tau_b = F_b R_{roll} - \mathcal{I}_w\dot{\omega}_w \approx F_b R_{roll}.
\tag{66}
$$
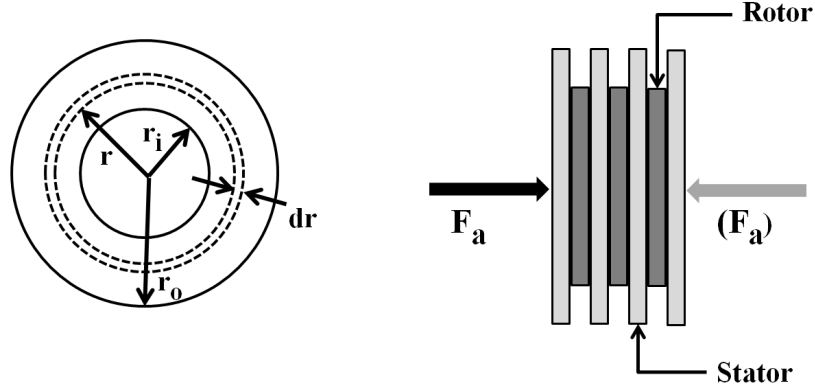
Figure 23: Geometry of brake rotors and stators

In Eq. 66, R_{roll} is the rolling radius of the braked tire, and the effect of wheel inertia $\mathcal{I}_w \dot{\omega}_w$ is neglected in comparison to the other term. Modern aircraft brakes consist of alternate "rotor" and "stator" elements that collectively form a "heat-stack" (Fig. 23). The rotors are keyed to the wheel and rotate with it, while the stators are keyed to the hub and are stationary. For N rotors, $2N$ total friction surfaces are formed. The braking torque τ_b and the required axial force F_a may be related as:

$$\tau_b = (2N) \int_{r_i}^{r_o} r.p(r).dA, \qquad F_a = \int_{r_i}^{r_o} p(r).dA, \quad dA = 2\pi r.dr, \quad A = \pi(r_o^2 - r_i^2)$$
(67)

To evaluate the relationships shown in Eq. 67, it is necessary to make an assumption regarding the radial pressure distribution $p(r)$. If uniform pressure ("u/p") distribution is assumed, then $p(r) = p = F_a/A$. On the other hand, if uniform wear ("u/w") is assumed, then $r.p(r) = \text{constant}$ (this case is assumed in this dissertation). With these assumptions, the torque and the axial force are related as follows:

$$\tau_b = C_{(.)}\, F_a, \quad \ldots \qquad C_{u/p} = (2N)\,\frac{2}{3}\mu\left(\frac{r_o^3 - r_i^3}{r_o^2 - r_i^2}\right), \qquad C_{u/w} = (2N)\,\mu\frac{r_o + r_i}{2}, \quad (68)$$

where r_o and r_i are respectively the outer and inner radii of the friction surfaces and μ is the friction coefficient between the friction surfaces.

Table 11: Static cases for establishing braking requirements

Case description	Full-throttle run-up	Parking on incline
Aircraft weight	MTOW	MRW
Thrust setting	Max. SLS	-
Ground speed	-	-
Deceleration	-	-
Opposing gradient	1.1°	1.1°

Table 12: Dynamic cases for establishing braking requirements

Case description	Accelerate-stop	Landing decel.
Aircraft weight	MTOW	MLW
Thrust setting	Idle	Idle
Ground speed	72 m/s (140 kts)	75 m/s (145 kts)
Deceleration	1.8 m/s^2(6.0 ft/s^2)	3.0 m/s^2(10 ft/s^2)
Opposing gradient	1.1°	1.1°

4.4.2   System Sizing

The brake actuation requirements are determined from the two static cases (aircraft stationary) and two dynamic cases (aircraft decelerating) shown in Tables 11 and 12 respectively. The static cases correspond to the ability of the brakes to hold the aircraft stationary during a full-throttle run-up and while parked on an incline of a specified gradient. The two dynamic cases are an accelerate-stop case corresponding to a rejected takeoff at maximum takeoff weight and a landing deceleration case at maximum landing weight (FAR 25.735 (f)(1) & (f)(2) [77]).

For each of the conditions listed in Tables 11 and 12, the total required braking force F_b^{tot} is evaluated using Eq. 64. For a conservative estimate, factors in this relationship that *reduce* the braking requirement, such as longitudinal load transfer, rolling friction, and the aerodynamic drag are neglected ($F_f \approx 0, D \approx 0$).

However, if the brakes are sized merely to these requirements, they will be under-sized and exhibit torque-limited operation under certain conditions, where the torque on the wheel due to the friction at the tire-ground interface exceeds the

Table 13: Number of main landing gear wheels and braked wheels

MRW (lb)	# of MLG wheels	# of braked MLG wheels
$[50,000 - 200,000)$	4	4
$[200,000 - 550,000)$	8	8
$[550000 - 820,000)$	12	12
$[820,000 - 1,100,000)$	16	16
$1,100,000 +$	20	16

available braking torque [104]. This is not typical of modern commercial aircraft, which are equipped with Anti-lock Braking Systems (ABS) to prevent the wheels from locking up under braking. ABS is designed to modulate braking pressure and keep the tires operating very close to the slip that yields maximum grip from the ground. Theoretically, this is equal to limiting static friction, which during braking at Maximum Ramp Weight (MRW) is given by

$$F_{b,lim}^{tot} = \mu_s \ (1 - \alpha_{nlg})(MRW), \tag{69}$$

where μ_s is the limiting static friction coefficient between tires and ground and α_{nlg} is the fraction of the total aircraft's weight supported by the nose landing gear under static conditions. The braking force obtained by evaluating Eq. 69 with $\mu_s = 0.8$ and $\alpha_{nlg} = 0.06$ is considered along with the forces obtained by evaluating Eq. 64 with the conditions of Tables 11 and 12.

For each of the above braking cases, the braking force per braked wheel is evaluated using Eq. 65 and assuming that all braked wheels contribute equally to the total braking force. The number of braked wheels is selected as a function of aircraft MRW according to Table 13 (created based on publicly available information), where the weight intervals are chosen to ensure that the landing gear characteristics match those of most existing Airbus and Boeing commercial aircraft.

The braking torque per braked wheel is computed through Eq. 66 using the rolling radius of the appropriate tire from Table 14 (data collected from [105]) whose

125

Table 14: Wheel / Tire Selection (data collected from [105])

Rated load (lbf)	Nom. diam. (in)	Nom. width (in)	Rim diam. (in)	Rolling radius (in)	Three-part name
9,650	27	7.75	15	11.8	27x7.75-15
13,700	30	9.5	14	12.65	30x9.5-14
17,200	31	13	12	12.7	31x13.0-12
21,525	36	12	18	15.2	36x12.0-18
24,100	37	14	15	15.25	37x14.0-15
30,100	40	14.5	19	16.65	40x14.5-19
36,800	40	14.5	19	16.65	40x14.5-19
41,100	44.5	16.5	21	18.55	44.5x16.5-21
44,200	46	18	20	18.85	46x18.0-20
51,100	46	18	20	18.85	46x18.0-20
56,600	49	19	22	20.2	49x19.0-22
68,500	54	21	23	22.5	54x21.0-23
72,200	54	21	24	22.2	54x21.0-24

Table 15: Heat sink dimensions vs. tire wheel diameter [97]

Rim diam. (in)	Face width. (in)	Rim diam. - OD (in)
14	2.312	2
15	2.437	2
16	2.5	2.25
17	2.625	2.25
18	2.812	2.25
19	2.875	2.5
20	3	2.5
21	3.125	2.5
22	3.312	2.5
23	3.312	2.625
24	3.5	2.625
25	3.625	2.625

rated load exceeds that computed for the aircraft's MRW. To find the required axial force per braked wheel through Eq. 68, the brake dimensions are first evaluated using the data in Table 15. With the rim diameter selected from Table 14, the brake outer diameter $OD = 2r_o$ is obtained from the third column of Table 15. The

126

inner diameter is then computed from the second column of Table 15 as $ID = 2r_i = OD - 2$ (face width). Evaluation of Eq. 68 with these dimensions yields the maximum end load F_0 that must be applied to actuate the brakes. The required maximum actuation rate v_{max} is computed based on the closure of a specified running clearance within a specified time interval [106].

4.4.3 Mass Estimation

The mass of the wheel braking system comprises the mass of the heat-stack M_{hs}, the mass of the brake actuation system M_{act}, and the mass of associated electronics M_{elec} for controlling the system:

$$M_{wbs} = M_{hs} + M_{act} + M_{elec} \tag{70}$$

A significant fraction of the mass of the braking system is comprised of the mass of the heat-stack M_{hs}, which is driven directly by the requirement that the necessary kinetic energy be absorbed without exceeding a permissible temperature rise ΔT_{max}.

$$\Delta K E_{max} = M_{hs} \; c_{hs} \; \Delta T_{max} \tag{71}$$

The recent industry trend has been towards the use of carbon brakes as opposed to steel brakes, since carbon brakes have a higher specific heat capacity c_{hs} which allows the same kinetic energy to be absorbed by a much smaller mass for the same temperature rise [107]. While it is clear that the use of carbon brakes may offer significant weight savings [108], these savings are applicable to conventional hydraulic braking systems as well. Therefore, no variation in heat-stack mass M_{hs} is considered with variation in braking system architecture, since both conventional and electric braking systems may make use of either carbon brakes or steel brakes.

Table 16 reproduces a comparative mass breakdown between electric and conventional hydraulic braking systems for an Airbus A330 baseline [109]. Inspection of the data provided by Chai and Mason [110] shows that for commercial aircraft,

Table 16: Projected mass savings of electric brakes relative to conventional Airbus A330 hydraulic brakes - reproduced from [109]

Electric Brakes		Hydraulic Brakes	
Torque plates	20 kg	Torque plates	78 kg
Electronics	21 kg	Electronics	39 kg
EMAs	207 kg	Hydraulics	86 kg
(Wiring)	34 kg	(Piping)	110 kg
Total	303 kg	Total	313 kg

the landing gear group weight may be taken to be approximately 4 % of the aircraft's MTOW. Inspection of percentage weight breakdowns of landing gear components shows that for small, medium, and large commercial aircraft, brakes account for a roughly constant 16 % of the total landing gear group weight [97]. With these percentages and the assumption of MTOW = 242,000 kg for the Airbus A330[4], the predicted weight of all wheel brakes is 1,549 kg.

As seen from Table 16, for the transition to electric brakes, a weight reduction of 162 kg or 10.46 % of the total brake weight was predicted for the torque plates and electronics and due to the removal of actuating hydraulics. At the same time, there is the added weight of the electromechanical actuators. Taking these into account, the net *change* in mass of the electric wheel braking system relative to the conventional hydraulic brakes may be written as

$$\Delta M_{wbs} = -\kappa_1 \; \kappa_2 \; \kappa_3 \; (MTOM) + n_{brk} \left\{ \frac{F_0}{(F/M)_{ema}} \right\}_{ema} \tag{72}$$

with $\kappa_1 = 4$ %, $\kappa_2 = 16$ %, $\kappa_3 = 10.46$ %, as per the preceding discussion. F_0 is the maximum end load required by the brake system, as evaluated from Eq. 68, and $(F/M)_{ema}$ is the force-to-mass ratio of the EMA. For the Airbus A330 case (Table 16), using the listed EMA mass and the end load computed using Eqs. 64-68 for this aircraft yields $(F/M)_{ema} = 7.57$ kN/kg. Collins [106] lists an EMA mass

---

[4]Online: `http://www.airbus.com/aircraftfamilies/passengeraircraft/a330family/a330-300/specifications/`, accessed July 12, 2015.

target for an Electrically Actuated Braking System (EABSys) of 18-20 kg for an end load of 150-160 kN, yielding a comparable $(F/M)_{ema}$ range of 7.50 - 8.89 kN/kg.

4.4.4 Power Requirements

For hydraulically actuated brakes, the effective piston area A_{eff} may be obtained from the maximum end load F_0 and the available working pressure P_{wk} as

$$A_{eff} = \frac{F_0}{P_{wk}}. \tag{73}$$

If the brake is to be applied at a rate v, then the required flow rate to the brake is given by

$$Q_{req} = A_{eff} \ v = \frac{F_0}{P_{wk}} \cdot v. \tag{74}$$

For the case of hydraulically actuated brakes, the maximum flow requirement occurs during the brake-fill period where the actuator moves at maximum rate $v = v_{max}$ to take up the running clearance.

In the case of electrically actuated brakes, the peak power requirement occurs during ABS operation [109] since combinations of large load and high rate occur. To obtain the power required from the bus, the *corner power* may first be obtained as

$$P_{cp} = \frac{F_0 \ v_{max}}{\eta_{pe} \ \eta_{em} \ \eta_{me}}, \tag{75}$$

where η_{pe}, η_{em}, and η_{me} are the efficiencies of the power electronics, electric motor, and mechanical drive of the EMA respectively. The corner power is the product of the maximum load and the maximum rate, which is an operating point that lies outside an actuator's operating envelope. Therefore, the peak power required may more realistically be estimated as $P_{req} = 0.7 \ P_{cp}$.

4.5 Thrust Reverser Actuation System (TRAS)

The Thrust Reverser Actuation System (TRAS) is responsible for the deployment and stowing of the thrust reverser mechanism. Typical deployment and stowing times

may be around 2-3 seconds. Under nominal conditions, the TRAS is energized only once per flight and only for these short durations. Therefore, the direct influence of its power requirements on engine fuel consumption is minimal. However, the power requirement, though brief, can be significant, and thus may affect the sizing and weight of components in the relevant Power Generation and Distribution System.

TRAS designs fall into two main categories [111]. In the *cascade type* design, movable translating sleeves translate aft to uncover cascades through which airflow (typically secondary airflow) is deflected by blocker doors. In the *pivoting type* design, the airflow is deflected through four pivoting doors which also act as the deflectors for the airflow. The cascade type design has lower actuation loads and is the more common of the two designs.

Among the subsystems, the TRAS is unique in that designs over the years have made use of each of the three secondary power types (pneumatic, hydraulic, and electric). Early cascade type TRAS designs used pneumatic power [85], where a pneumatic Power Drive Unit (PDU) provided pressure-regulated bleed air to an air motor which drove ballscrew actuators synchronized using flexible driveshafts [111]. The majority of TRAS designs use hydraulic power, and feature either separate linear hydraulic actuators [85] or separate ballscrews which are driven by a common hydraulic motor (or Power Drive Unit) [112]. More recently, an Electric Thrust Reverser Actuation System (ETRAS) of the cascade type has been used in the Airbus A380 [85], in which an electric PDU drives ballscrew actuators through a flex-shaft.

4.5.1 Power Requirements

Only very limited information on thrust reverser power requirements is found in the open literature. A flow rate for the CFM 56 engine is available from work by Scholz [113], and the electrical power rating (in kVA units) for the Airbus A380 ETRAS is available from [85]. Based on only these two data points, the power

requirement *per engine* for the TRAS is expressed as a linear function of the rated sea-level thrust of a single engine as

$$P_{tras} \text{ [kVA or kW]} = 0.047 \ T_{SL}\text{[kN]} + 10.782, \qquad \text{(per engine)} \qquad (76)$$

in which the power is assumed to be in kVA (kilo volt amperes) for electric TRAS and in equivalent kW for hydraulic TRAS. In the latter case, the equivalent kW figure is converted into a corresponding flow requirement using the hydraulic power equation.

4.5.2 Mass Estimation

Since both hydraulic and electric TRAS as considered in this dissertation comprise ballscrew actuators connected to the movable panels, the control volume for mass estimation is simplified to include only the hydraulic or electric PDU, whose mass is estimated as

$$M_{tras} = \frac{P_{tras}}{(P/M)_{pdu}}, \qquad \text{(per engine)} \qquad (77)$$

where $(P/M)_{pdu}$ is the power to mass ratio of the hydraulic or electric PDU. Without this simplifying assumption, the mass of the ballscrew actuators would have to be taken into account for both the hydraulic and electric TRAS. Since these actuators are common to both hydraulic and electromechanical TRAS designs, this would not affect the change in mass due to the electrification of the TRAS.

4.6 Electric Taxiing System (ETS)

The ETS concept involves using electric motors to drive the landing gear wheels of the aircraft in order to permit the aircraft to be taxied without use of the main engines. The power requirement of the motors is supplied by the APU. The motors may be integrated either in the nose gear or the main gear. Installation in the nose gear may be more convenient from an integration perspective, however the tractive force that can be generated is limited (especially under low grip conditions) by the relatively low fraction of the total aircraft weight supported by the nose gear (8-15 %).

The installation of an ETS always entails a weight penalty due to the incorporation of the required hardware - electric motors and their power electronics, reduction gearboxes, and electrical cabling. In addition to this, the APU generator may need to be up-sized in order to supply the system's power requirements, which imposes a further weight increment. The weight penalty results in additional fuel burn in flight, when the system is essentially dead-weight. However, the possibility of net fuel savings arises if the fuel saved through using the system on the ground exceeds the additional fuel burnt carrying the system in flight. The fuel savings increase with increased taxiing time, and deteriorate with increasing trip distance. Thus, the system is most attractive for smaller aircraft which typically fly shorter stage lengths and spend a proportionately larger percentage of time taxiing on the ground. Another advantage of the system is the possibility of installing it as a retrofit option on aircraft based on airline demand [32]. Sizing of an ETS and simulation of its power requirements during taxiing were addressed in greater detail in Chakraborty et al. [114]. Here, only a brief overview of estimation of system mass and power requirements is provided.

4.6.1 Estimation of System Power Requirement

The ETS operational requirements include the ability to produce the acceleration necessary to achieve a certain taxiing speed in a specified time, the ability to maintain a specified taxiing speed, and the ability to break away (commence motion from a stand-still) against a specified opposing gradient. The weight of the aircraft must also be specified as part of the definition of each requirement. These requirements drive the size and power consumption of the motors, reduction gearboxes, and associated power electronics.

The operational requirements shown in Table 17 are based on those identified by Airbus from the Airbus Electric Green Taxiing System (EGTS) test program [32]. A load condition is specified as part of each requirement.

Table 17: Electric taxiing system (ETS) requirements

	Scenario	Initial speed	Final speed	Time interval	Gradient	Loadout
1	Achieve breakaway	0 kt	-	-	1.5 %	MRW
2	Acc. for runway crossing	0 kt	10 kt	20 sec	-	MTOW
3	Acc. to max taxi speed	0 kt	18 kt	90 sec	-	MTOW
4	Maintain max taxi speed	-	20 kt	-	-	MTOW

To translate these operational requirements into design requirements of the ETS, the following generalized equation of motion for a taxiing aircraft was proposed in Chakraborty et al. [114]. It is applicable to aircraft being taxied using the main engines or an ETS or being towed, and expresses the acceleration $\dot{V}(t)$ of the aircraft and the instantaneous mass $M(t)$ during taxiing:

$$\dot{V}(t) = \frac{T(t) + F_{tow}(t) - D(V(t)) + \frac{2}{R_r}(\tau_d(t) - \tau_b(t)) - \mu_{rr}M(t)g - M(t)g\sin\theta}{M(t) + \frac{I_f}{R_f^2} + 2\,\frac{I_r}{R_r^2}}$$

$$M(t) = M_0 - \int_0^t (FF_{eng}(t) + FF_{apu}(t))\ dt \tag{78}$$

In Eq. 78, $FF_{eng}(t)$ and $FF_{apu}(t)$ are the fuel flow rates of the main engines and the APU respectively. The purpose of this equation is to simulate taxiing operation and certain simplifications may be made for the purpose of system sizing. For example, for ETS operation, the thrust of the main engines $T(t)$, the towing force $F_{tow}(t)$, and the braking torque $\tau_b(t)$ in Eq. 78 may be set to zero. Further, the contribution of the aerodynamic drag term $D(t)$ is typically negligible at taxiing speeds ($\approx$ 20 kt). Additionally, the inertia contributions of the aircraft wheels (I_f/R_f^2 and I_r/R_r^2) are small compared to the mass of the aircraft $M(t)$.

The rolling friction coefficient μ_{rr} may be accounted for through a commonly used break-away friction model in which the coefficient is expressed as a function of speed:

$$\mu_{rr} = \mu_{rr,0} + \Delta\mu_{rr}\left(1 - \frac{V}{V^*}\right), \qquad \dots V \leq V^*,$$

$$= \mu_{rr,0}, \qquad \dots V > V^*, \qquad V^* = 10\text{kt} \tag{79}$$

133

The incremental term $\Delta\mu_{rr}(1-V/V^*)$ models the so-called *break-away* friction. Thus, the effective friction coefficient that must be overcome to begin motion is $\mu_{b/a} = \mu_{rr,0} + \Delta\mu_{rr}$. In Chakraborty et al. [114], the coefficients $\mu_{rr,0}$ and $\Delta\mu_{rr}$ were estimated based on published data for taxiing and break-away thrust settings for a variety of aircraft taxiing at different percentages of their maximum takeoff weight (MTOW) [115]. The mean values were found to be $\mu_{rr,0} = 0.013$ and $\Delta\mu_{rr} = 0.009$, yielding a break-away friction coefficient $\mu_{b/a} = \mu_{rr,0} + \Delta\mu_{rr} = 0.022$.

In Chakraborty et al. [114], a simulation-based power-sizing approach was followed in order to determine the minimum overall motor power rating that would allow the performance requirements of Table 17 to be met. In addition to the dynamics of Eq. 78, the torque-speed envelope of the electric motor was considered, after accounting for maximum voltage, maximum current, and maximum power constraints. The minimum required peak power output was found to be related to the aircraft Maximum Takeoff Mass (MTOM) as

$$P_{mech}^{max} \text{ [kW]} = (4.10^{-10})(MTOM \text{ [kg]})^2 + 0.0016 \, (MTOM \text{ [kg]}) - 2.2971. \tag{80}$$

The Airbus Electric Green Taxiing System [32] used two 50 kW motors (i.e., 100 kW in total) for an Airbus A320 aircraft of MTOM = 78,000 kg. It is interesting to note that setting this MTOM in Eq. 80 yields a total output power requirement of 125 kW. The larger power predicted by Eq. 80 is due to the fact that all the taxiing requirements were defined at either MTOM/MTOW or MRM/MRW. In other words, no degradations in acceleration or top-speed performance were permitted with increasing aircraft loading and thus these requirements were more stringent.

The peak electrical power demand corresponding to the peak mechanical power demand is obtained by accounting for the efficiencies of the electric motors and the power electronics:

$$P_{ets}^{peak} = \frac{P_{mech}^{max}}{\eta_{em} \, \eta_{pe}} \tag{81}$$

This peak power requirement affects the sizing of power distribution elements and also the capacity of the APU generator (which is responsible for supplying the ETS power demand). These are discussed subsequently in Chapter 5.

4.6.2   Estimation of System Mass

The main hardware components within the control volume of the ETS are the electric motors, the power electronics, and the reduction gearboxes. The motor and power electronics mass are estimated as

$$M_{em} + M_{pe} = P_{mech}^{max} \left\{ \frac{1}{(P/M)_{em}} + \frac{1}{\eta_{em} \, \eta_{pe} (P/M)_{pe}} \right\}, \tag{82}$$

where $(P/M)_{em}$ and $(P/M)_{pe}$ are the power-to-mass ratios of the electric motor and the power electronics, and η_{em} and η_{pe} their respective component efficiencies.

To estimate the mass of the gearbox, the maximum output torque of the gearbox (required to achieve break-away) is first determined from the total break-away force using a force and moment balance as

$$\tau_{b/a} = R_{roll} \frac{F_{b/a}^{tot}}{N_{drive}} = R_{roll} \frac{(MRM) \, g \, \left(\mu_{b/a} + \sin \theta \right)}{N_{drive}}, \tag{83}$$

where R_{roll} is the rolling radius of the tire (determined after tire selection, Sec. 4.4) and N_{drive} is the total number of driven wheels. The gearbox mass is computed as

$$M_{gb} = \frac{\kappa_{gb} \, \tau_{b/a}}{(\tau/M)_{gb}}, \tag{84}$$

where $(\tau/M)_{gb}$ is the torque-to-mass ratio of the reduction gearbox and $\kappa_{gb} = 1.5$ represents a margin of safety for torque. The total ETS hardware mass is given by

$$M_{ets} = M_{em} + M_{pe} + M_{gb}. \tag{85}$$

In addition to this mass, there may be a further increase in mass due to the need to up-size the APU generator. The magnitude of the up-sizing is not determined by the presence of ETS alone, but also by the solution chosen for the ECS. Sizing of the APU
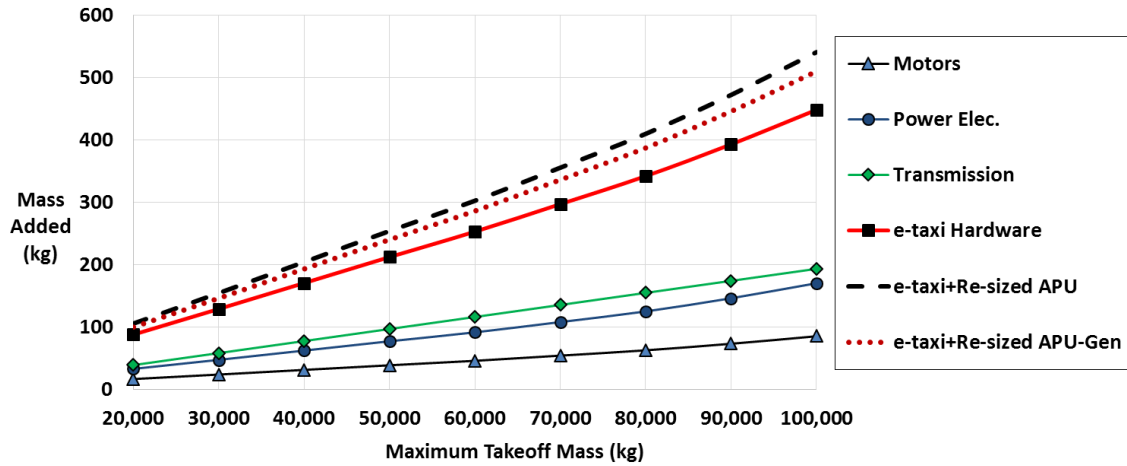
Figure 24: Estimated ETS mass addition as function of Maximum Takeoff Mass (MTOM). Technology assumptions: $(P/M)_{em}= 2$ kW/kg, $(P/M)_{pe} = 1.05$ kW/kg, $(\tau/M)_{gb} = 107$ Nm/kg, $\kappa_{gb} = 1.5$, APU generator $P/M = 2.76$ kW/kg, APU effective $P/M = 1.83$ kW/kg

generators, therefore, is deferred to Chapter 5. In the interim, Fig. 24 (from [114]) shows the estimated mass addition for an ETS as a function of the MTOM along with the relevant technology assumptions. It is interesting to note that with either assumption (generator re-sizing or APU re-sizing), the predicted total mass addition for an Airbus A320-sized aircraft (MTOM = 78,000 kg) is around 400 kg, which was the non-contractual figure cited by Airbus [32].

4.6.3 Estimation of Fuel Burn during Taxiing

In a full electric taxiing scheme [32], the ETS can be used to push back from the gate and taxi out to a point near the runway where the main engines are started. Up to this point, only the APU is active and burns fuel. The main engines must be run for a certain warm-up time before the aircraft can take the runway, during which time the APU may be turned off. Similarly, upon arrival, the engines must be run for a certain cooling-down time before they are turned off. Following this, the APU supplies power to the ETS to taxi to the gate. From this sequence of operations, the

fuel consumed during taxi-out and taxi-in may be readily computed as

$$M_{f,taxi-out} = (T_{taxi-out} - T_{warm-up})\ FF_{apu} + T_{warm-up}\ FF_{engs},$$

$$M_{f,taxi-in} = (T_{taxi-in} - T_{cool-down})\ FF_{apu} + T_{cool-down}\ FF_{engs}, \qquad (86)$$

where FF_{apu} and FF_{engs} are respectively the fuel flow rates of the APU and the main engines. For the A320 aircraft, these fuel flow rates were stated to be 12.5 kg/min for both main engines combined and 2 kg/min for the APU [32]. The fuel saved due to the use of ETS for taxi-out and taxi-in follows as

$$\Delta M_{f,taxi-out} = (FF_{engs} - FF_{apu})\ (T_{taxi-out} - T_{warm-up}),$$

$$\Delta M_{f,taxi-in} = (FF_{engs} - FF_{apu})\ (T_{taxi-in} - T_{cool-down}),$$

$$\implies \Delta M_{f,ground} = \Delta M_{f,taxi-out} + \Delta M_{f,taxi-in} = (FF_{engs} - FF_{apu})\ T_{ets}, \qquad (87)$$

from which it is clear that the fuel savings on the ground is directly proportional to the duration of use of ETS (T_{ets}), in other words on the total taxiing time.

The fuel penalty due to the ETS mass is computed directly during the mission performance analysis. However, some insight may also be gained from an analytical expression estimating this fuel penalty. A manipulation of the Breguet range equation yields the fuel penalty in flight due to the mass of the ETS for a flight distance R as

$$\Delta M_{f,flight} = M_{ets}\ \left(e^{\frac{(TSFC)\ R}{V\ (L/D)}} - 1\right), \qquad (88)$$

where $TSFC$ is the thrust-specific fuel consumption of the main engines, V the flight speed, and L/D the lift-to-drag ratio at a representative cruise condition. Thus, it is clear that the fuel penalty in-flight increases exponentially as the flight distance R increases. A simple estimate of the fuel savings then follows as

$$\Delta M_{f,savings,ets} = \Delta M_{f,ground} - \Delta M_{f,flight}$$

$$= (FF_{engs} - FF_{apu})\ T_{ets} - M_{ets}\ \left(e^{\frac{(TSFC)\ R}{V\ (L/D)}} - 1\right), \qquad (89)$$

which justifies the preference to use ETS for aircraft that fly frequent but short flights and spend significant amounts of time taxiing.

4.7 Environmental Control System (ECS)

The function of the ECS is to provide pressurization, thermal regulation, and ventilation for the aircraft cabin. It is the single biggest consumer of secondary power in commercial aircraft. The conventional ECS is pneumatic, and uses bleed air extracted from the engines for cabin pressurization and thermal regulation. An electric ECS design is found on the Boeing 787 aircraft [74], where it has facilitated a transition to a predominantly bleedless architecture for which the manufacturer has predicted a cruise fuel consumption improvement in the range of 1-2 % [116]. The power requirements of an electric ECS design are considerable, being in the range of 1.14 kW per passenger [117]. The incorporation of Cabin Air Compressors (CACs), motors to drive them, and the associated power electronics results in significant mass addition to the aircraft and requires considerable up-sizing of the electrical PGDS [118]. The development of light-weight power electronics (> 4 kW/kg) has been identified as one of the major challenges for electric ECS [118]. The tradeoff between electric and conventional ECS is thus a complex one since it features the counteracting effects of a reduction in bleed requirement, an increase in shaft-power requirement, an increase in system mass, and an increase in ram drag.

4.7.1 Cabin Temperature, Pressure, and Airflow Requirements

The aircraft cabin is typically divided into several zones, each of them having an independent zone temperature controller. A master cabin temperature is set for the entire cabin, which can be modified within certain limits for each cabin zone to set the target temperature for each zone temperature controller. The cabin zone with the lowest target temperature defines the temperature of conditioned air supplied to the cabin. The temperature target for the remaining zones is met by blending hotter *trim* air with the supply air to obtain the correct temperature. To explicitly account for the trim air requirements of individual cabin zones, a detailed thermal simulation
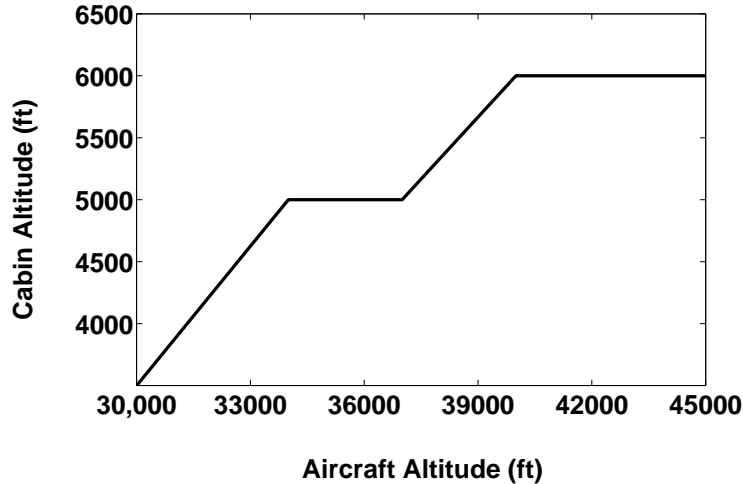
Figure 25: Cabin pressurization schedule (based on [74])

of the cabin is required [119]. However, a relatively large number of cabin-specific parameters enter into such an analysis, which are not necessarily available during early design phases. Therefore, a simpler analysis is implemented in this dissertation, in which a constant desired cabin temperature of $T_{cab} = 24$ °C [118] is assumed throughout the flight for each of the three baselines. A lumped thermal model analysis is performed by assuming this temperature to be uniform throughout the cabin.

To limit the difference between internal cabin pressure and external ambient pressure (which generates a radially outward stress on the fuselage), the cabin pressure P_{cab} is allowed to reduce with increasing altitude as per a pressurization schedule. As seen in the Boeing 787, the current trend is toward the use of higher minimum cabin pressures (lower maximum cabin altitudes, reduced from 8,000 ft to 6,000 ft) to facilitate increased passenger comfort. The pressurization schedule used in this dissertation is based on that given by Nelson [74] for the Boeing 787 aircraft (Fig. 25).

The nominal volume flow rate of air entering the cabin in modern commercial aircraft is approximately 20 cfm (cubic feet per minute) per occupant [13]. Thus, the

139

net volume flow rate of air entering the cabin is given by

$$\dot{\mathcal{V}}_{nom} = \dot{\mathcal{V}}_{\text{per occ.}} \ N_{occ}, \tag{90}$$

where N_{occ} is the number of cabin occupants. This volume flow rate may be converted to a nominal mass flow rate based on the cabin pressure and temperature as

$$\dot{m}_{nom} = \frac{P_{cab} \ \dot{\mathcal{V}}_{nom}}{R_{air} \ T_{cab}}, \tag{91}$$

where R_{air} is the gas constant for air. Since the cabin pressure P_{cab} reduces with aircraft altitude, the required mass flow rate for a given volume flow rate requirement reduces at higher altitudes.

4.7.2   Cabin Thermal Loads Analysis

Due to the temperature difference between the cabin temperature T_{cab} and the ambient temperature T_∞, heat transfer $\dot{Q}_{loss}$ occurs through the cabin wall (defined as positive if heat flows from the cabin to the ambient). This may be modeled as heat flow through three thermal resistors in series: convection between the cabin zone air at temperature T_{cab} and the inside wall, conduction to the outer skin of the aircraft, and convection to the ambient at temperature T_∞. The net thermal resistance R_{tot} is then given by

$$\begin{aligned} R_{tot} &= R_{conv,int} + R_{skin} + R_{conv,ext} \\ R_{conv,int} &= \frac{1}{h_{int} \ A_{int}}, \qquad R_{conv,ext} = \frac{1}{h_{ext} A_{ext}} \end{aligned} \tag{92}$$

where h_{int} and h_{ext} are the convection coefficients for the internal and external convection processes respectively, and A_{int} and A_{ext} are the corresponding heat exchange areas. A value of $h_{int} = 5 \ W.m^{-2}.K^{-1}$ is assumed for still air convection. The skin conduction resistance is set as $R_{skin} = 0.2 \ m^2.W^{-1}.K^{-1}$ based on representative material properties for paint, insulation, and metallic skin. The heat

transfer between the cabin and the ambient through the cabin wall is given by

$$\dot{Q}_{loss} = \frac{T_{cab} - T_{aw}}{R_{tot}}, \quad T_{aw} = T_\infty \left(1 + R_c \, \frac{\gamma - 1}{2} \, M_\infty^2 \right), \quad R_c = 1 - 0.99 \, (1 - Pr^{0.5}),$$
(93)

where T_{aw} is the adiabatic wall temperature corresponding to the freestream Mach number M_∞, R_c is the temperature recovery factor, and Pr the Prandtl number.

There are various sources of heat generation inside the cabin that collectively result in an internal heat load $\dot{Q}_{int}$. The metabolic heat load per passenger is assumed to be $\dot{Q}_{meta}/N_{pax} = 75 \ W$ [119]. The power consumption of In-Flight Entertainment (IFE) systems, $\dot{Q}_{ife}/N_{pax} = 50 \ W$ [120], is assumed to be dissipated entirely as heat. The same assumption is made for the galley loads, $\dot{Q}_{galley}/N_{pax} = 320 \ W$ [120]. Taking into account both $\dot{Q}_{loss}$ and $\dot{Q}_{int}$, the total ECS heat load is expressed as

$$\dot{Q}_{ecs} = \dot{Q}_{loss} - \dot{Q}_{int},$$
(94)

Clearly, if the ECS has to remove heat from the cabin, then $\dot{Q}_{ecs} < 0$.

To maintain the cabin at a desired temperature T_{cab} against the heat load $\dot{Q}_{ecs}$, air at temperature T_{in} must be supplied by the ECS to the cabin. The application of a steady-state heat balance to the cabin yields

$$\dot{Q}_{ecs} = \dot{m}_{nom} \, C_p (T_{in} - T_{cab}) \implies T_{in} = T_{cab} + \frac{\dot{Q}_{ecs}}{\dot{m}_{nom} \, C_p}.$$
(95)

Due to physical constraints, the permissible range of inlet temperatures is limited to $T_{in}^{min} \leq T_{in} \leq T_{in}^{max}$. In case the solution of Eq. 95 lies outside these bounds, then a higher mass flow rate must be introduced in order to service the heat load. To determine this mass flow rate, the inlet temperature in such cases is set to $T_{in} = T_{in}^{lim}$, where $T_{in}^{lim} = T_{in}^{max}$ or $T_{in}^{lim} = T_{in}^{min}$ depending on which bound was violated. The required cabin mass flow rate is then computed as

$$\dot{m}_{cab} = \frac{\dot{Q}_{ecs}}{C_p(T_{in}^{lim} - T_{cab})}.$$
(96)

Thus, it is clear that $\dot{m}_{cab} = \dot{m}_{nom}$ if the solution of Eq. 95 satisfies the temperature bounds, and $\dot{m}_{cab} > \dot{m}_{nom}$ otherwise.

For modern commercial aircraft using high bypass ratio turbofan engines, the fuel penalty associated with extracting engine bleed air to supply 100 % of the cabin airflow requirement would be severe [13]. Therefore, ECS designs employ *recirculation*, in which a certain fraction ϵ_{recirc} of the air supplied to the cabin is actually recirculated air which has previously been extracted from the forward section of the fuselage by recirculation fans located beneath the cabin floor [13]. The remaining $(1 - \epsilon_{recirc})$ fraction of the air is either extracted from the aft section of the cabin and exhausted overboard, or lost through a slight amount of leakage through the fuselage. Thus, taking recirculation into account, the required mass flow rate *per pack* for an ECS with N_{pack} packs[5] is computed as

$$\dot{m}_p = \frac{(1 - \epsilon_{recirc})}{N_{pack}} \, \dot{m}_{cab}. \tag{97}$$

To compute the required pack discharge temperature T_{pack} ($= T_6$ in the pack model of Fig. 26 which is discussed subsequently), an enthalpy balance is performed between recirculated air of mass flow rate $\epsilon_{recirc} \, \dot{m}_{cab}$ assumed to be at temperature T_{cab}, pack discharge air of net mass flow rate $(1 - \epsilon_{recirc}) \, \dot{m}_{cab}$ at temperature T_{pack}, and cabin supply air of mass flow rate $\dot{m}_{cab}$ and temperature T_{in}:

$$
\begin{aligned}
\dot{m}_{cab} \, C_p \, T_{in} &= \epsilon_{recirc} \, \dot{m}_{cab} \, C_p \, T_{cab} + (1 - \epsilon_{recirc}) \, \dot{m}_{cab} \, C_p \, T_{pack} \\
\implies T_{pack} &= T_6 = \frac{T_{in} - \epsilon_{recirc} \, T_{cab}}{1 - \epsilon_{recirc}}
\end{aligned} \tag{98}
$$

The total mass flow requirement of the ECS taking into account recirculation and the trim air requirement (expressed as a fraction λ_{trim} of $\dot{m}_{cab}$) is given by

$$
\begin{aligned}
\dot{m}_{ecs} &= N_{pack} \, \dot{m}_p + \dot{m}_{trim} = (1 - \epsilon_{recirc}) \, \dot{m}_{cab} + \lambda_{trim} \, \dot{m}_{cab} \\
&= (1 - \epsilon_{recirc} + \lambda_{trim}) \, \dot{m}_{cab}.
\end{aligned} \tag{99}
$$

---

[5]All analyses in this dissertation assume $N_{pack} = 2$, which was found to be applicable to most modern commercial aircraft of the sizes considered based on publicly available information.
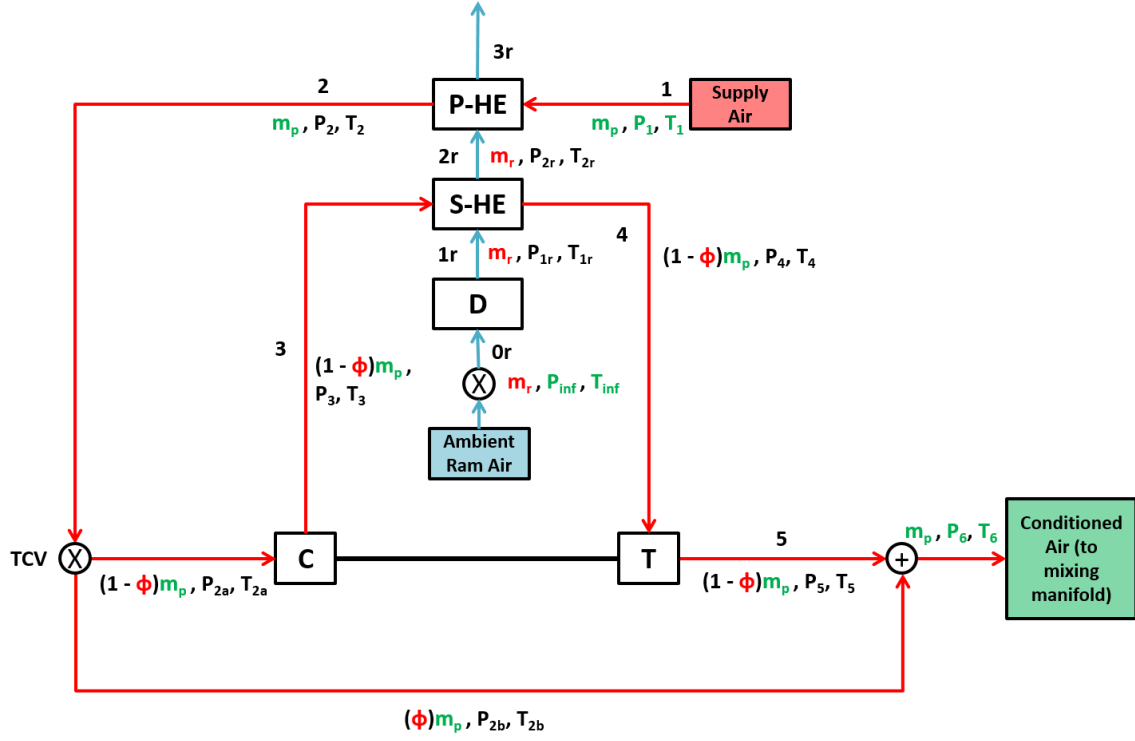
Figure 26: Component layout within thermodynamic model of ECS pack

In case of conventional (pneumatic) ECS, this mass flow rate is extracted from the engines as bleed air. Therefore, for $N_{op,eng}$ operating engines, the bleed air required per engine to supply the ECS is given by

$$\dot{m}_{bleed,ecs} = \frac{\dot{m}_{ecs}}{N_{op,eng}} = \frac{(1 - \epsilon_{recirc} + \lambda_{trim})\,\dot{m}_{cab}}{N_{op,eng}} \qquad \text{(per engine)} \qquad (100)$$

For an electric ECS, this mass flow rate is processed by all operating CACs combined.

$$\dot{m}_{cac,tot} = \dot{m}_{ecs} = (1 - \epsilon_{recirc} + \lambda_{trim})\,\dot{m}_{cab} \qquad (101)$$

Since this mass flow rate is admitted as ram air for an electric ECS design, it results in the generation of additional ram drag.

4.7.3   ECS Pack Model

The layout of components within the Environmental Control System (ECS) pack was determined based on inspection of Airbus and Boeing documents available in the

public domain [121, 122, 123, 124, 125, 126], and is shown in Fig. 26. While electric ECS solutions may feature customized ECS pack designs [49], conventional bootstrap units may also be considered within an electric ECS scheme [43]. Therefore, for simplicity the same pack architecture is assumed for both conventional and electric ECS solutions (a conservative assumption for the case of electric ECS).

The operation of the ECS pack involves the transfer of heat from a *supply stream* to a *cooling stream*. For both conventional and electric ECS architectures, ambient air admitted through ram air inlets serves as the cooling stream. In case of a conventional (pneumatic) ECS design, the supply stream (referred to as such since this air is ultimately supplied to the aircraft cabin) is obtained from engine bleed air. In an electric (bleedless) ECS design, ambient air admitted through additional dedicated ram air inlets constitutes the supply stream.

The supply stream of mass flow rate $\dot{m}_p$ enters the ECS pack at pressure P_1, and temperature T_1. It is cooled in the primary heat exchanger (P-HE) to temperature T_2, and due to the pressure drop in the P-HE, the pressure drops to P_2. Based on the setting $\phi \in [0, 1]$ of the temperature control valve (TCV), the supply stream is split into two streams: (i) the air cycle machine (ACM) stream of mass flow rate $(1-\phi)\dot{m}_p$, pressure P_{2a}, and temperature T_{2b}, and (ii) the bypass stream of mass flow rate $(\phi)\dot{m}_p$, pressure P_{2b}, and temperature T_{2b}. The ACM stream passes into the ACM compressor (C), where it is compressed to pressure P_3, resulting in a rise of temperature to T_3. At this elevated temperature, the supply stream rejects heat in the secondary heat exchanger (S-HE) and is cooled to temperature T_4. The pressure drop through the S-HE results in the pressure falling to P_4. The supply stream then passes through the ACM turbine (T) and is expanded to pressure P_5, resulting in a temperature drop to T_5. At this point, the ACM stream is mixed with the bypass stream, resulting in pack discharge temperature T_6 and pressure P_6. The work extracted from the supply stream during turbine expansion is used to drive the ACM compressor.

The cooling stream, initially at ambient pressure P_∞ and temperature T_∞ enters through a ram air door, with the position of the ram air door actuator (RADA) determining the admitted mass flow rate $\dot{m}_r$ (the RADA is marked as X in Fig. 26). The cooling stream passes through a diffuser, where its pressure and temperature rise to P_{1r} and T_{1r} respectively. After accepting heat from the supply stream in the S-HE, the cooling stream temperature rises to T_{2r} and due to the pressure drop through the S-HE, its pressure drops to P_{2r}. The cooling stream then accepts further heat from the supply stream in the P-HE, and is assumed to leave the control volume of the ECS pack thereafter.

Associated with each of the pack components, there are a set of well-known nonlinear thermodynamic relationships that relate the properties of the fluid stream(s) passing through the components. Collectively, these relationships constitute the thermodynamic model of the ECS pack. For solving this model, the following parameters (color-coded green in Fig. 26) are assumed to be known:

1. The state of the supply stream entering the pack, $\dot{m}_p, P_1, T_1$. The mass flow rate $\dot{m}_p$ is obtained from the cabin airflow requirements and the recirculation fraction. For conventional (pneumatic) ECS, the pressure P_1 and temperature T_1 are obtained from the precooler exit conditions. The pressure schedule P_1 used for electric ECS is described in Sec. 4.7.4.

2. The freestream pressure P_∞, temperature T_∞, and Mach number M_∞ for a particular flight condition

3. The required pack exit temperature T_6 and pressure P_6. Temperature T_6 is computed based on the cabin thermal analysis and the recirculation fraction employed. Pressure P_6 is set based on the cabin pressurization schedule and allowing for a certain percentage pressure drop in the mixing manifold and downstream distribution ducting.

The pack controller makes use of two controls (color-coded red in Fig. 26) for adjusting the pack discharge temperature T_6: (i) the ram air mass flow rate $\dot{m}_r$ and (ii) the TCV setting ϕ. To lower T_6, the RADA opens the ram air inlet more and the TCV closes more. The reverse occurs if the temperature T_6 must be raised [122]. The RADA also modulates ram air flow to regulate ACM compressor outlet temperature T_3 [126]. However, due to the thermal inertia of the heat exchangers, the effect of the RADA on T_6 is not immediate [127], and it may be regarded as a slow-acting control. On the other hand, the effect of the TCV setting on T_6 is immediate, and it can be used to quickly respond to temperature variations in the incoming supply air, or to variations in desired pack exit temperature T_6.

In general, to minimize the required amount of ram air (and thus ram drag), the TCV remains almost closed, except when the compressor exit temperature T_3 reaches an upper threshold. In such cases, the flow of ram air $\dot{m}_r$ is increased to regulate the compressor exit temperature T_3 while the TCV is opened as required to regulate the pack discharge temperature T_6. Thus, the pack thermodynamic model is initially solved as a root-finding problem for the ram air mass flow rate $\dot{m}_r$ for each flight condition. For solutions where the compressor exit temperature T_3 exceeds a maximum permissible threshold of $T_3^{max} = 230°C$ [121], the pack model is re-solved as an optimization problem: minimize ram air mass flow rate $\dot{m}_r$ while satisfying the maximum compressor exit temperature constraint T_3^{max} in addition to the pack exit temperature requirement T_6.

4.7.4 Power Requirements

As discussed previously, the supply air mass flow rate $\dot{m}_p$ is directly driven by the cabin airflow requirements. For the conventional (pneumatic) ECS, this mass flow rate is extracted as bleed air from the engines, which therefore imposes a fuel consumption penalty on the engine due to the extraction of pneumatic power.

For the electric ECS, the same mass flow rate $\dot{m}_p$ is admitted at pressure P_∞ and temperature T_∞ through dedicated ram air inlets and passes through a diffuser. The diffusion process results in diffuser exit temperature and pressure given by

$$
\begin{aligned}
T_{d,out} &= T_\infty \left(1 + \frac{\gamma-1}{2} M_\infty^2\right), \\
P_{d,out} &= \eta_d \, P_\infty \left(1 + \frac{\gamma-1}{2} M_\infty^2\right)^{\frac{\gamma}{\gamma-1}},
\end{aligned}
\tag{102}
$$

where η_d is the efficiency of the diffuser. This air is then compressed by the cabin air compressors (CAC). Assuming an exit pressure $P_{cac,out}$, the corresponding exit temperature is given by

$$
T_{cac,out} = T_{d,out} \left\{1 + \frac{1}{\eta_{cac}} \left(\Pi_{cac}^{\frac{\gamma-1}{\gamma}} - 1\right)\right\},
\tag{103}
$$

where η_{cac} is the CAC adiabatic efficiency and $\Pi_{cac} = P_{cac,out}/P_{d,out}$ is the CAC pressure ratio. The total electrical power requirement of the CACs is given by

$$
P_{elec} = N_{pack} \frac{\dot{m}_p C_p \left(T_{cac,out} - T_{d,out}\right)}{\eta_{em} \, \eta_{pe}},
\tag{104}
$$

where η_{em} and η_{pe} are the overall efficiencies of the electric motors and power electronics of the CACs.

The exit of the supply stream from the CAC essentially coincides with its entry into the ECS pack, and therefore from Fig. 26, $P_1 = P_{cac,out}, T_1 = T_{cac,out}$. It is clear that the electrical power requirement of the CACs depends on the CAC discharge temperature, which in turn depends on the CAC discharge pressure through Eq. 103. For a conventional ECS architecture, representative values for the pack entry pressure and temperature are $P_1 = 250\,\text{kPa}, T_1 = 180°\text{C}$. However, attempting to match either this pressure or temperature results in an excessively large CAC power requirement, especially at cruise conditions due to the high pressure ratio Π_{cac}. Instead, the CAC discharge pressure is scheduled such that a pressure differential with respect to the cabin pressure is maintained, which reduces linearly from 130 kPa at sea-level to 100

kPa at 45,000 ft cruise altitude. With the ECS model as described, the CAC power requirement at cruise conditions evaluates to approximately 1.25 kW/occupant. This compares reasonably well with the approximate figure of 400 kW for a 350 PAX aircraft, i.e., $\approx$ 1.14 kW/PAX, cited by Herzog [117].

4.7.5 Drag Generation

The operation of the ECS results in the generation of ram drag as external ram air is admitted into the aircraft. For both conventional and electric ECS solutions, ram air is used as the cooling stream. In case of electric ECS, the supply air is also external ram air. The ram drag penalties are estimated pessimistically by assuming complete momentum loss, in which case the ram drag penalty respectively for the pneumatic and electric ECS are given by

$$
\begin{aligned}
D_{ram,p-ecs}(\dot{m}_r, V_\infty) &= N_{pack}\ \dot{m}_r\ V_\infty, \\
D_{ram,e-ecs}(\dot{m}_r, \dot{m}_p, V_\infty) &= N_{pack}\ (\dot{m}_r + \dot{m}_p)\ V_\infty.
\end{aligned}
\tag{105}
$$

The assumption of complete momentum loss is a conservative one for the case of the cooling stream ram air, since after passing through the heat exchangers this air stream is typically re-accelerated prior to being discharged overboard. In addition to the drag due to momentum loss of the ram air, the incorporation of the ram air inlets themselves result in additional drag penalties, which is not modeled.

4.7.6 Mass Estimation

Since the same pack design is assumed for both the pneumatic and electric ECS solutions, there is no variation in the mass of the ECS packs between the two architectures. Aircraft sizing tools (including FLOPS) typically provide an estimate of the air conditioning system mass. This includes the mass of the ECS packs for the conventional architecture, which is therefore used directly. For the electric ECS, the

additional mass of the CACs, motors, and the power electronics was computed as

$$
\begin{aligned}
M_{cac} &= \frac{P_{cac}^{max}}{(P/M)_{cac}} = \frac{P_{elec}^{max}/N_{cac/pack}}{(P/M)_{cac}}, \\
M_{cac,em} + M_{cac,pe} &= P_{cac}^{max} \left(\frac{1}{(P/M)_{em}} + \frac{1}{\eta_{em}\ \eta_{pe}\ (P/M)_{pe}} \right), \\
\Delta M_{e-ecs} &= \kappa_{ecs}\ N_{pack}\ N_{cac/pack}\ (M_{cac} + M_{cac,em} + M_{cac,pe}), \quad (106)
\end{aligned}
$$

where $(P/M)_{cac}, (P/M)_{em}$, and $(P/M)_{pe}$ are the power-to-mass ratios of the CACs, motors, and power electronics respectively, with η_{em} and η_{pe} being the overall efficiencies of motors and power electronics. The factor κ_{ecs} accounts for the masses of other smaller pack components that are not explicitly estimated, and is assumed to be $\kappa_{ecs} = 1.25$ for all analyses. For component sizing, it is assumed that each ECS pack can satisfy the requirements of the whole aircraft in case of failure of the other pack. Each ECS pack is assumed to have two compressors ($N_{cac/pack} = 2$) [74], each with a dedicated motor and power electronics. Each motor-compressor is sized to be able to provide half of the pack's total mass flow capacity.

4.8 Wing Ice Protection Systems (WIPS)

Accretion of ice on aircraft surfaces in flight occurs due to the tendency of cloud droplets to remain in liquid state at below-freezing temperatures, a condition known as *supercooling*. This is an unstable state and the supercooled water may readily undergo a phase change from liquid to solid (i.e. ice) due to agitation by a passing aircraft. The effects of unmitigated icing on the aircraft may include loss of aerodynamic efficiency, engine power, adequate control authority, and even brake and landing gear operation, outside vision, flight instrument functions, and communication [128] Most commonly, the leading edges of the wings and engine nacelles of commercial aircraft are provided ice protection. In this dissertation, these are termed the Wing Ice Protection System (WIPS) and the Cowl Ice Protection System (CIPS). In certain aircraft, empennage surfaces may also require

ice protection, however this is not universal and is therefore not considered. Ice protection solutions for the cockpit windshield, drain masts, pitot probes, etc. is also not considered.

Only thermal ice protection solutions, in which thermal energy is used to prevent ice accretion, are considered in this dissertation, as they are almost universal on modern commercial aircraft. In conventional IPS designs, hot bleed air provides the necessary thermal energy. However, electrothermal IPS designs in which electric heating pads provide the required heat flux are also feasible, and most notably are found on the Boeing 787 [74, 116]. The IPS may be designed as an *anti-icing* system, where the build-up of ice is prevented completely, or a *de-icing* system, where ice is allowed to form and then subsequently dispatched [129]. Anti-icing designs may further be *evaporative*, where the supplied heat flux is sufficient to completely evaporate all impinging water and maintain a dry surface or (ii) running-wet, where the supplied heat flux is only sufficient to melt any ice, but not vaporize the resulting water. As discussed previously in Chapter 3, the following system types are down-selected for further consideration: (i) pneumatic evaporative anti-icing WIPS, (ii) pneumatic running-wet anti-icing WIPS, (iii) electrothermal running-wet anti-icing WIPS, and (iv) electrothermal running-wet de-icing WIPS.

The analysis assumes a technology level in which the supplied heat flux for all four IPS variants listed above can be modulated based on flight and icing conditions in order to maintain a desired surface temperature. It is noteworthy that such modulation is typically not possible in current commercial aircraft [57].

4.8.1 Determination of Protected Surface Area

The extent of protection (EOP) determines the dimensions of the protected area. It is defined by the spanwise and chordwise EOP and the spanwise Center of Protected Area (COPA) [56]. The relevant geometric parameters are defined in Fig. 27.
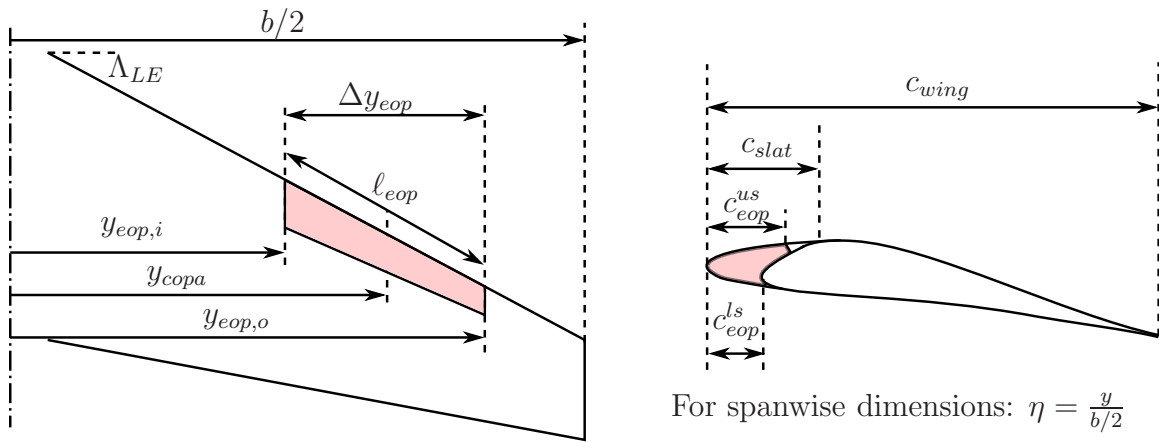
Figure 27: Geometric parameters for definition of spanwise and chordwise EOP

Typically a spanwise continuous section of the wing leading edge is provided protection. However, as shown in Fig. 28, the EOP varies from aircraft to aircraft. For example, on the Airbus A320, Airbus A330/A340, and Boeing 767, ice protection is provided to leading-edge slats located from approximately mid-wing to wingtip. On the Boeing 737, Boeing 757, Boeing 777, and Boeing 787, ice protection is provided to leading-edge slats outboard of the engine nacelle, but excluding the most outboard slat (two, in case of the Boeing 777). On the Airbus A380, ice protection is only provided to one slat per wing, located just inboard of the outboard engines. In all of these aircraft, the inboard leading-edge devices spanning from the side-of-body to the nacelle location are not provided ice protection.

The EOP must be estimated based on the wing profile and geometry, which have a significant influence on the rate of impingement of supercooled water while flying through icing conditions. In general, thinner profiles catch more water as they cause a greater diversion of the airstream prior to its incidence on the wing leading edge. Both spanwise and chordwise EOP are affected by the detailed geometry of the wing, which is not determined (or frozen) until much later in the design process [56].

Liscouet-Hanke [56] cited a study conducted by Airbus that established that the Mean Aerodynamic Chord (MAC) c_{mac} had the greatest influence on the spanwise
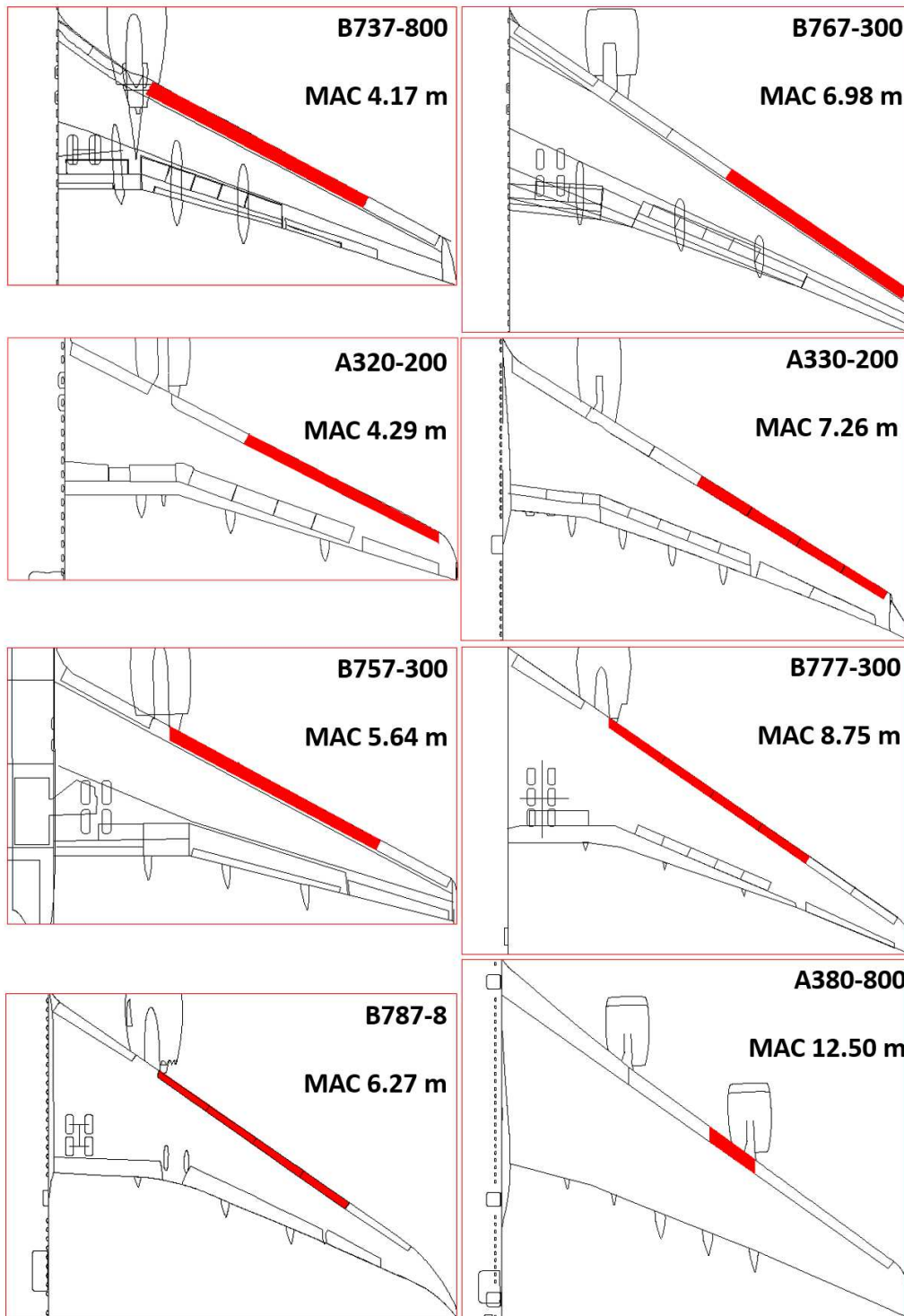
Figure 28: Wing leading-edge Extent of Protection (EOP) for some commercial aircraft. All spans equalized to illustrate relative spanwise EOP.
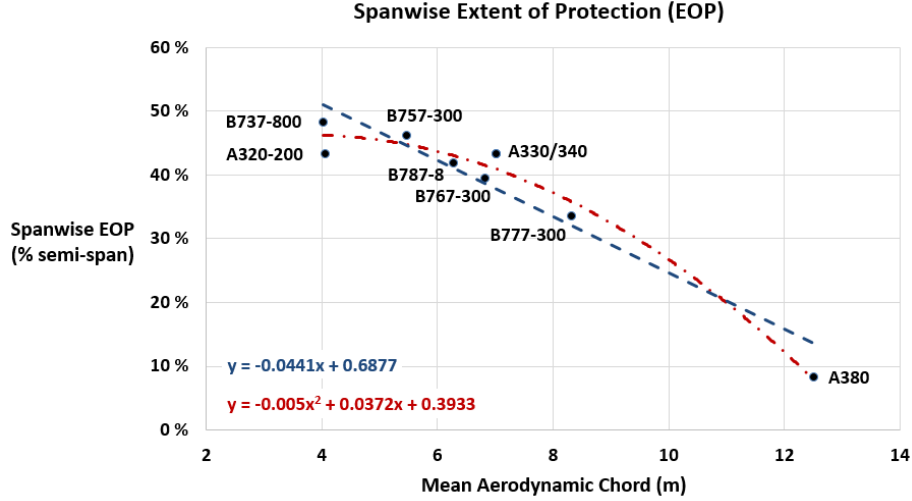
Figure 29: Spanwise EOP as a function of wing Mean Aerodynamic Chord (MAC) for a number of commercial aircraft

EOP, which decreased with increasing MAC. In that work, a linear relationship between the spanwise EOP and the MAC had been assumed. However, for this dissertation both a linear and a quadratic relationship were initially considered through the following general relationship:

$$\Delta \eta_{eop} = \kappa_0 + \kappa_1 \, c_{mac} + \kappa_2 \, c_{mac}^2. \tag{107}$$

Using the spanwise EOP of some common commercial aircraft as obtained from public domain information (Fig. 29), a linear regression yielded $\kappa_0 = 0.6877, \kappa_1 = -0.0441, \kappa_2 = 0$, with c_{mac} expressed in meters. The second-order polynomial regression yielded $\kappa_0 = 0.3933, \kappa_1 = 0.0372, \kappa_2 = -0.005$, with c_{mac} expressed in meters. The latter is used for all analyses in this dissertation given the better agreement with the data points seen in Fig. 29.

For locating the spanwise COPA η_{copa}, the trend-lines presented by Liscouet-Hanke [56] are used directly:

$$
\begin{aligned}
\eta_{copa} &= 0.554 \, \Delta \eta_{eop} + 0.428, && \Delta \eta_{eop} \le 0.5, \\
&= -0.607 \, \Delta \eta_{eop} + 0.708, && \Delta \eta_{eop} > 0.5 \tag{108}
\end{aligned}
$$

153

Respecting the wingtip constraint ($\eta_{eop,p} \leq 1.0$), the provisional inboard and outboard spanwise extremities of the protected area are then computed as

$$\begin{aligned}
\tilde{\eta}_{eop,o} &= \min\left(1.0, \eta_{copa} + \frac{\Delta\eta_{eop}}{2}\right) \\
\tilde{\eta}_{eop,i} &= \tilde{\eta}_{eop,o} - \Delta\eta_{eop}
\end{aligned} \tag{109}$$

Since the provisional interval $\eta \in [\tilde{\eta}_{eop,i}, \tilde{\eta}_{eop,o}]$ need not coincide with the spanwise extremities of the slats themselves, the following logic is applied: *a slat is considered to be provided ice protection if the intersection of the provisional interval $\eta \in [\tilde{\eta}_{eop,i}, \tilde{\eta}_{eop,o}]$ and the slat's spanwise interval $\eta \in [\eta_{slat,i}, \eta_{slat,o}]$ exceeds more than 40 % of the slat's length.* For the aircraft sizes considered, this logic results in ice protection requirement being deemed necessary for the following slats (referring to Fig. 12): (i) slats 3, 4, and 5 on each wing for the SSA (ii) slats 3, 4, and 5 on each wing for the LTA (iii) slat 4 on each wing for the VLA.

The actual inboard and outboard spanwise extremities of the protected area ($\eta_{eop,i}$ and $\eta_{eop,o}$) are set to coincide with the identified protected slats. The previously computed $\Delta\eta_{eop}$ (from Eq. 107) and η_{copa} (from Eq. 108) are then updated as

$$\begin{aligned}
\Delta\eta_{eop} &= \eta_{eop,o} - \eta_{eop,i}, \\
\eta_{copa} &= \frac{1}{2}(\eta_{eop,o} + \eta_{eop,i}).
\end{aligned} \tag{110}$$

The total protected leading edge length ℓ_{wips} for both wings combined is obtained by considering the wing's semispan $b/2$, leading-edge sweep Λ_{LE}, and dihedral Γ as

$$\ell_{wips} = 2\left(\frac{\Delta\eta_{eop}}{\cos\Lambda_{LE}\ \cos\Gamma}\right) \cdot \frac{b}{2}. \tag{111}$$

The upper and lower surface chordwise EOP c_{eop}^{us} and c_{eop}^{ls} are more sensitive to the

actual wing profile [56], and for this dissertation are expressed as follows:

$$c_{eop}^{us}(\eta) = \underbrace{\left(\frac{c_{eop}}{c_{slat}}\right)_{us}}_{=0.40} \cdot \left(\frac{c_{slat}}{c_{wing}}\right) \cdot c_{wing}(\eta),$$

$$c_{eop}^{ls}(\eta) = \underbrace{\left(\frac{c_{eop}}{c_{slat}}\right)_{ls}}_{=0.22} \cdot \left(\frac{c_{slat}}{c_{wing}}\right) \cdot c_{wing}(\eta). \tag{112}$$

For a slat with spanwise extent $[\eta_i, \eta_o]$ and slatwise length ℓ_{slat}, the protected surface area A_{prot} is computed as

$$A_{prot} = \frac{1}{2}\ell_{slat}\left\{\mathcal{P}\left(\eta_i, \frac{c_{eop}^{us}(\eta_i)}{c_{wing}(\eta_i)}, \frac{c_{eop}^{ls}(\eta_i)}{c_{wing}(\eta_i)}\right) + \mathcal{P}\left(\eta_o, \frac{c_{eop}^{us}(\eta_o)}{c_{wing}(\eta_o)}, \frac{c_{eop}^{ls}(\eta_o)}{c_{wing}(\eta_o)}\right)\right\}, \tag{113}$$

where $\mathcal{P}(\eta, \tilde{c}^{us}, \tilde{c}^{ls})$ is the perimeter of the wing airfoil at span station η and between upper surface and lower surface chordwise locations $\tilde{c}^{us}$ and $\tilde{c}^{ls}$ respectively. The total WIPS protected area A_{prot}^{wips} (both wings considered) is then obtained as the summation of the protected areas of all slats determined to require ice protection. It should be noted that this area has been determined using only information that is either available or estimable during conceptual design.

4.8.2 Modeling Assumptions and Technology Assumptions

To perform the IPS analysis using only limited information regarding the system geometry and characteristics, the following simplifying assumptions are made:

1. Only steady-state conditions are considered, in which the flight condition is constant and the surface temperature has stabilized

2. The temperature of impinging water droplets is assumed to be the same as the freestream temperature T_∞

3. The temperature of the runback water (if any) is assumed to be the same as the surface temperature [130]. To track these two temperatures separately, a more detailed analysis (e.g., [131]) is required which is beyond the present scope

Table 18: IPS thermodynamic modeling parameters

Parameter	Symbol	Comments
Freestream temp., press., Mach	$T_\infty, P_\infty, M_\infty$	
Reynolds number	Re_x	$Re = \rho_\infty V_\infty x / \mu$
Prandtl number	Pr	$Pr = \mu C_{p,a} / k_0$
Nusselt number	Nu	$Nu = 0.0296 \ Re^{4/5} \ Pr^{1/3}$
Temp. recovery factor	R_c	$R_c = 1 - 0.99(1 - Pr^{0.5})$
Adiabatic wall temp.	T_{aw}	$T_{aw} = T_\infty \left(1 + R_c \ \frac{\gamma-1}{2} \ M_\infty^2 \right)$
External convection coeff.	h_∞	$h_\infty = Nu \ k_0 / x$
Water heat of fusion	L_f	
Water heat of vaporization	L_v	
Water catch efficiency	β	
Impingement mass flux	$\dot{m}_{imp}$	Eq. 115
Evaporation mass flux	$\dot{m}_{evap}$	Eq. 121

4. The control volume at a given location is assumed to completely enclose both the heated area and the droplet impingement area. Thus, both the total supplied IPS heat flux and the total water catch enter this control volume in entirety

5. For running-wet systems, the separation of runback water into rivulets is captured through a *wetness factor* [131]. This rivulet effect is not considered

6. The effect of conduction through the metal skin in the flow-wise direction is not considered due to its relative magnitude in relation to other heat fluxes [131]

Electrothermal IPS solutions permit the modulation of the heat flux supplied to the protected surface. However, such modulation is typically not possible in the case of conventional pneumatic IPS, in which the system is either on or off [57]. This often results in the supply of heat which is in excess of that required to maintain an acceptable surface temperature for providing ice protection. For pneumatic IPS solutions, the possibility of using active control to modulate the rate of bleed air supplied to the protected areas (thus alleviating the associated bleed-induced fuel penalty) was investigated by Patricelli [132], who concluded that significant reductions in bleed air mass flow rate were possible in certain conditions. Therefore, flow

modulation for pneumatic IPS solutions was considered in this dissertation, under the assumption that pneumatic IPS designs of the future may employ such modulation. The estimation of IPS heating requirements subject to the above modeling and technology assumptions is described in the following sections.

4.8.3 Estimation of water impingement

The required heat flux for ice protection is affected by the rate of water impingement on the protected surface. The total rate of water impingement (dimension: $[M][T]^{-1}$) onto a surface with *projected* area A_{proj} normal to the flow direction at airspeed V_∞ is given by

$$\dot{m}_{imp} = E_m \; (LWC) \; V_\infty \; A_{proj}, \tag{114}$$

where $E_m \in [0, 1]$ is the water collection (or catch) efficiency and LWC is the Liquid Water Content of the air (explained further subsequently). The water impingement expressed as a mass flux per unit *protected* area (dimension: $[M][L]^{-2}[T]^{-1}$) is

$$\dot{m}''_{imp} = \frac{\dot{m}_{imp}}{A_{prot}} = E_m \; (LWC) \; V_\infty \; \frac{A_{proj}}{A_{prot}}. \tag{115}$$

In Eq. 115, the water collection efficiency E_m is defined as the ratio of the mass of water impinging on the surface to the total mass of water present in the theoretical volume swept out by the body:

$$E_m = \frac{\dot{m}_{imp}}{\dot{m}_{tot}} \tag{116}$$

It is a function of aircraft speed, droplet size, and the geometry of the surface of impingement. In general, higher velocities, larger droplet sizes, and thinner surfaces of impingement increase the collection efficiency. Detailed methods to compute E_m are available in AIR 1168/4, from which a simplified approximation was deduced by Krammer and Scholz [133]:

$$E_m = 0.00324 \; \left(\frac{V_\infty}{t}\right)^{0.613}, \tag{117}$$

where V_∞ is in meters per second and thickness t is in meters. This approximation is strictly true for a median droplet diameter of 20 microns and an altitude of 10,000 ft, but has less than 10 % error for other altitudes from sea level to 20,000 ft [133].

The LWC in Eq. 115 is expressed in FAR §25, Appendix C [77] as a function of mean effective droplet diameter and air temperature within the continuous and intermittent icing envelopes. The LWC for the two icing envelopes is discussed in greater detail in §4.8.5 and §4.9.3.

4.8.4 Estimation of Required Heat Flux

The total heat flux $\dot{q}_{tot}$ required to maintain the protected area at a given surface temperature T_s is made up of contributions from four heat transfer processes[6]: convection, sensible heating, evaporation, and kinetic heating:

$$\dot{q}_{tot} = \dot{q}_{conv} + \dot{q}_{sens} + \dot{q}_{evap} + \dot{q}_{kin} \tag{118}$$

Evaluating each of these contributions at a given flight condition allows the determination of the total required IPS heat flux $\dot{q}_{tot}$ for that flight condition. The convective heat flux $\dot{q}_{conv}$ may be expressed as

$$\dot{q}_{conv} = h_\infty (T_s - T_{aw}), \tag{119}$$

where h_∞ is the external convection coefficient and T_{aw} is the adiabatic wall temperature. These are in turn computed as

$$
\begin{aligned}
T_{aw} &= T_\infty \left(1 + R_c \frac{\gamma - 1}{2} M_\infty^2 \right), \quad R_c = 1 - 0.99 \left(1 - Pr^{0.5} \right), \quad Pr = \frac{\mu C_p}{k_0} \\
h_\infty &= \frac{Nu \, k_0}{x}, \quad Nu = 0.0296 \, Re^{4/5} \, Pr^{1/3}, \quad Re = \frac{\rho V_\infty x}{\mu},
\end{aligned}
\tag{120}
$$

---

[6]In some analyses, a fifth heat flux component called *aerodynamic heating* ($\dot{q}_{aero}$) is considered. However, in these analyses, the expression for convective heat flux uses the freestream static temperature T_∞. If instead the convective heat flux is computed using the adiabatic wall temperature T_{aw} (as in this dissertation), then it can be shown that the effect of aerodynamic heating is already accounted for and a separate aerodynamic heat flux term need not be considered.

with the characteristic length x taken to be the mean chord of each slat. The evaporation mass flux and heat flux $\dot{q}_{evap}$ may be expressed as

$$
\begin{aligned}
\dot{m}_{evap} &= \min\left(0.7\,\frac{h_\infty}{C_{p,a}\,P_\infty}(P_v(T_s) - R_h P_v(T_\infty)), \dot{m}_{imp}\right)\\
\dot{q}_{evap} &= \dot{m}_{evap}\,L_v,
\end{aligned}
\tag{121}
$$

where the relative humidity of a cloud is generally taken to be 100 % ($R_h = 1$) [131]. The saturated vapor pressure P_v at temperature T may be expressed as

$$
P_v[Pa] = 2337\ \exp\left\{6789\left(\frac{1}{293.15} - \frac{1}{T[K]}\right) - 5.031\ ln\left(\frac{T[K]}{293.15}\right)\right\}
\tag{122}
$$

The sensible heat flux $\dot{q}_{sens}$ and kinetic heat flux $\dot{q}_{kin} < 0$ may be expressed as

$$
\begin{aligned}
\dot{q}_{sens} &= \dot{m}_{imp}\,C_{p,w}\,(T_s - T_\infty)\\
\dot{q}_{kin} &= -\dot{m}_{imp}\frac{V_\infty^2}{2}
\end{aligned}
\tag{123}
\tag{124}
$$

The four heat flux components are estimated for a given flight condition to obtain the total required heat flux using Eq. 118. The heat flux multiplied by the protected surface area (obtained by applying Eq. 113 to each protected slat) yields the required rate of heat supply to provide ice protection for a given flight condition.

4.8.5   Determination of WIPS Sizing Flight Condition

Icing typically occurs at altitudes below 22,000 ft and in ambient temperatures between -30°C and 0°C. Requirements for the IPS may be derived from the airworthiness regulations for commercial transport category aircraft stated in FAR §25, Appendix C [77] or EASA CS-25, Appendix C [134], both of which contain very similar information with regard to icing conditions. Both make a distinction between two icing regimes: *Continuous Maximum Icing* (CMI) and *Intermittent Maximum Icing* (IMI). Both documents characterize these two icing regimes with three charts for each:

1. A chart with curves showing the probable maximum (99 %) LWC averaged over a standard distance (17.4 NM for CMI and 2.6 NM for IMI) for given temperature and droplet size [135]

2. A chart showing an icing envelope in terms of an ambient temperature range as a function of pressure altitude

3. A chart yielding correction factors for the LWC obtained (Item 1) for averaging distances other than the standard distances for CMI and IMI

Traditionally (since 1964), CMI conditions (stratiform clouds) have been applied to the design of airframe ice protection such as WIPS [135, 39]. The aircraft is considered to be exposed to relatively lower LWC, but for an extended period of time. The assumption is that wings are affected by flight through continuous icing, but more tolerant to encounters with more severe intermittent icing [39, 136].

Although there is no comprehensive guide to the use, interpretation, and application of FAR §25, Appendix C, designers have typically looked up the probable maximum LWC from it based on an appropriate temperature and a recommended droplet Median Volume Diameter (MVD)[7] [135]. This dissertation uses a 20 μm MVD, which is typically used for computation of ice accretion amounts [135, 137].

To find the WIPS sizing point, the heat flux estimation approach described in Sec. 4.8.4 is applied to a 3-dimensional search grid $\mathcal{G} : \{h, V_\infty, T_\infty\}$ where $h - V_\infty$ combinations are selected within the aircraft flight envelope and $h - T_\infty$ combinations are set based on the CMI icing envelope [77, 134]. The sizing point is identified as the flight condition yielding the maximum required total heat flux $\dot{q}_{tot}^{max}$. This corresponds to the maximum bleed air mass flow requirement in case of a pneumatic WIPS and the maximum electrical power requirement in case of electrothermal WIPS.

---

[7]Median Volume Diameter (MVD): A dimension such that 50 % of the mass volume of water in the cloud sample is contained in drops larger than the MVD, and the remaining 50 % in drops smaller than the MVD.

(a) Pneumatic ice protection system   (b) Electrothermal ice protection system
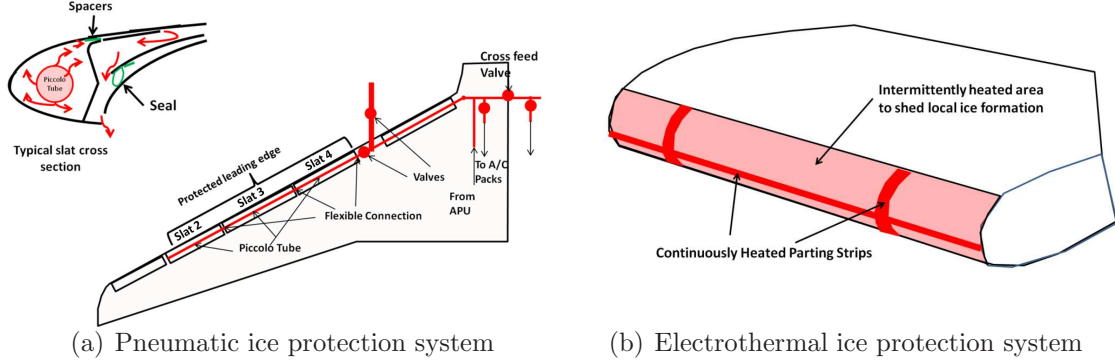
Figure 30: Pneumatic and electrothermal wing ice protection systems (WIPS).

4.8.6 Power Requirements

In a pneumatic IPS, hot bleed air extracted from the compressor stages of the engine is ducted to the surfaces to be protected and then discharged through piccolo tubes to transfer heat and maintain the desired surface temperature T_s (Fig. 30(a)). The hot supply air mixes with heated air in the bay, following which heat transfers to the inner wall through convection, and to the outer protected surface through subsequent conduction. Explicit modeling of the internal heat transfer process is impossible without considering the geometry in detail, especially since the internal convection coefficient has been shown to vary significantly based on the piccolo tube location and geometry [138]. Since such detailed geometric data may not be available during early design, a standard approach to modeling the efficiency of the internal heat transfer is to assume an overall heat transfer efficiency η_{p-wips} for the pneumatic WIPS [39, 56]. With this assumption, the required bleed air mass flow rate is computed as

$$\dot{m}_{p-wips,tot} = \frac{\dot{q}_{tot} \ A_{prot}^{wips}}{\eta_{p-wips} \ C_{p,a} \ (T_{supply} - T_s)},\tag{125}$$

where T_{supply} is the temperature of the bleed air supplied to the pneumatic WIPS. In analyses by other researchers, the value of the overall heat transfer efficiency has been assumed to be 65 % [39, 56]. The bleed air requirement per engine to supply

the WIPS for the case of $N_{op,eng}$ operating engines follows as

$$\dot{m}_{bleed,wips} = \frac{\dot{m}_{p-wips,tot}}{N_{op,eng}} \qquad \text{(per engine)} \qquad (126)$$

To estimate the power requirement of an electrothermal IPS (Fig. 30(b)), an elegant method presented by Krammer and Scholz [133] which is suitable for initial analysis without a priori knowledge of the detailed geometry is used. The authors demonstrated that this simplified approach predicted the power requirements of the Boeing 787 WIPS with reasonable accuracy. In this approach, the ratio of the total protected area that is covered by continuously heated parting strips is represented by $\kappa_{ps} \in (0,1)$. The parting strips are continuously heated with a heat flux $\dot{q}_{ps} = \dot{q}_{tot}$. The remaining area fraction $(1 - \kappa_{ps})$ is covered by cyclically heated surfaces which are supplied heat for a duration t_{heat} within a cycle of duration t_{cyc}, resulting in an effective activity ratio $\kappa_{cyc} = t_{heat}/t_{cyc}$. The heat flux provided to the cyclically heated areas is computed as

$$\dot{q}_{cyc} = \frac{\rho_{ice} \, \ell_{ice}}{t_{heat}} \left\{ c_{ice} \left(T_{ref} - T_\infty \right) + L_f \right\},$$

where ℓ_{ice} is the assumed minimum thickness of ice that must be melted during the heat-on portion of the cycle in order to allow aerodynamic forces to dispatch the ice buildup above it. Quantities ρ_{ice}, c_{ice}, and L_f are respectively the density, specific heat, and the latent heat of fusion of ice. $T_{ref} = 273 \ K$ is a reference temperature.

Considering both parting strips and cyclically heated areas, the required effective heat flux $\dot{q}_{e-wips}$ and corresponding electrical power requirement P_{e-wips} are given by

$$\begin{aligned}
\dot{q}_{e-wips} &= \dot{q}_{ps} \, \kappa_{ps} + \dot{q}_{cyc} \left(1 - \kappa_{ps} \right) \kappa_{cyc}, \\
P_{e-wips} &= \frac{A^{wips}_{prot} \, \dot{q}_{e-wips}}{\eta_{e-wips}},
\end{aligned} \qquad (127)$$

where η_{e-wips} is the overall efficiency of the electrothermal ice protection system. Assumed values for the geometric and operational parameters of the electrothermal IPS that appear in the above relationships are summarized in Table 19.

Table 19: Electrothermal IPS design parameters (based on [133])

Parameter	Symbol	Value
Parting strip area ratio	κ_{ps}	20 %
Cyclic heater activity ratio	κ_{cyc}	5 %
Heat "on" time	t_{heat}	9 sec
Ice thickness to melt	ℓ_{ice}	0.5 mm
Heater efficiency	η_{e-wips}	70 %

4.8.7 Mass Estimation

For a pneumatic IPS design, the subsystem mass includes the mass of the piccolo tubes in both wings. Instead of computing this mass explicitly, the estimated anti-icing system mass $M_{A/I}$ from the aircraft sizing program (FLOPS) is used to determine an effective mass per unit length for the piccolo tubes of both WIPS and CIPS:

$$(M/L)_{p-ips} = (M/L)_{p-wips} = (M/L)_{p-cips} = \left(\frac{M_{A/I}}{\ell_{wips} + \ell_{cips}} \right), \tag{128}$$

where ℓ_{wips} (from Eq. 111) and ℓ_{cips} are the total protected lengths for the WIPS and CIPS respectively. The mass of the pneumatic WIPS is then computed as

$$M_{p-wips} = (M/L)_{p-ips} \, \ell_{wips}. \tag{129}$$

For an electrothermal IPS design, data provided by Al-Khalil [139] which consisted of the densities and thicknesses of the materials forming the heated area is used to compute the effective mass per unit area of the heating pads $(M/A)_{e-ips}$. Using this, the total mass of the electrothermal IPS design is then estimated as

$$M_{e-wips} = (M/A)_{e-ips} \, A_{prot}. \tag{130}$$

4.8.8 Drag Penalty Estimation

A drag penalty is assessed only for the case of electrothermal de-icing, for which it is estimated using the following empirical correlation given by Gray [140]:

$$\Delta C_D \approx \left[8.7 \cdot 10^{-5} \frac{t_{icing} V_\infty}{c} \sqrt{(LWC)\bar{\beta}_m} (32 - T_{0,\infty})^{0.3} \right] \mathcal{T}_2$$

$$\mathcal{T}_2 = 1 + 6 \left[\{1 + 2\sin^4(12\alpha)\} \sin^2(\mathcal{T}_3) - 1.7 \sin^4(11\alpha) \right]$$

$$\mathcal{T}_3 = 543 \sqrt{(LWC)} \left(\frac{E_m}{32 - T_{0,\infty}} \right)^{1/3} - 81, \tag{131}$$

where t_{icing} is the icing time (in minutes, $= t_{heat}/\kappa_{cyc}$), V_∞ is the freestream velocity (in miles/h), c the chord (in inches), $T_{0,\infty}$ is the air total temperature (in Fahrenheit), and α is the angle of attack. For the maximum local impingement efficiency, $\bar{\beta}_m = 0.65$ is set based on inspection of the data presented in [140]. The above correlation is valid both for rime ice and glaze ice. The sectional drag increment computed through Eq. 131 is then converted to a dimensional drag increment as follows:

$$\Delta D_{D/I} = \bar{q} \, S_w \, \Delta C_D \left(\frac{S_{plan,prot}}{S_w} \right) \tag{132}$$

where $\bar{q}$ is the dynamic pressure, S_w is the wing planform area, and $S_{plan,prot}$ is the planform area corresponding to the protected span fraction.

The approach described above yields a scalable estimate for the power requirement and mass of the WIPS based only on quantities that are available during conceptual design. A similar approach is used for the Cowl Ice Protection System (CIPS), as described in the following section.

4.9 Cowl Ice Protection System (CIPS)

As discussed previously in Chapter 3, the following CIPS system types are down-selected for further consideration: (i) pneumatic evaporative anti-icing CIPS, (ii) pneumatic running-wet anti-icing CIPS, (iii) electrothermal evaporative anti-icing CIPS, and (iv) electrothermal running-wet anti-icing CIPS.

De-icing systems are not considered in this dissertation for the CIPS due to the risk of dislodged ice being ingested into the engines. Similar to the WIPS analysis, the CIPS analysis assumes a technology level in which the supplied heat flux for all four CIPS variants can be modulated based on flight and icing conditions in order to maintain a desired surface temperature. The sizing and analysis approach employed for the CIPS is very similar to that described in the previous sections for WIPS. Therefore, the following descriptions have been abbreviated, with references provided to the relevant WIPS sections where necessary.

4.9.1 Determination of Protected Surface Area

The total protected length ℓ_{cips} and total protected area A_{prot}^{cips} are determined as

$$
\begin{aligned}
\ell_{cips} &= N_{eng} \ \pi \ D_{nac,face} \\
A_{prot}^{cips} &= N_{eng} \ (\pi \ D_{nac,face}) \ (\pi \ \Delta x_{cips})
\end{aligned}
\tag{133}
$$

where $D_{nac,face}$ is the diameter of the front face of the engine nacelle and Δx_{cips} is the axial extent of protection measured along the longitudinal axis of the nacelle. The protected area is computed assuming a simplified nacelle geometry as shown in Fig. 31, where the perimeter of the protected area is approximated as being semi-circular.
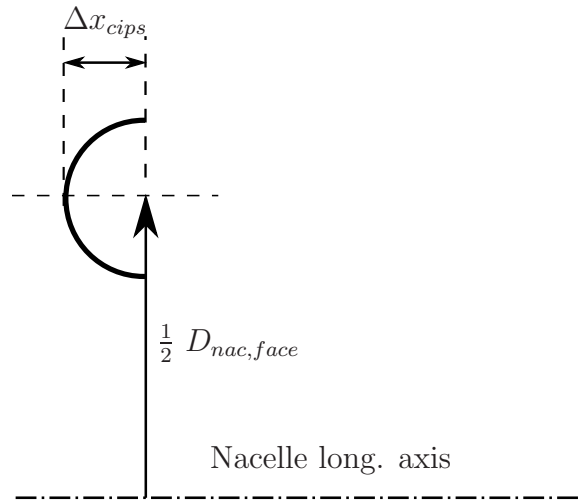
Figure 31: Simplified nacelle inlet geometry

4.9.2 Estimation of Required Heat Flux

The required CIPS heat flux is estimated for a given flight and atmospheric condition in the same manner as for WIPS in § 4.8.4, and is therefore not repeated.

4.9.3 Determination of CIPS Sizing Flight Condition

Traditionally, IMI conditions (cumuliform clouds) have been applied to the design of engine (cowl) ice protection systems [135, 39]. Here, the aircraft is considered to be exposed to relatively larger LWC, but for a relatively shorter period of time. The assumption in this case is that ice accretions of even short durations cannot be tolerated for engine inlets as they may overwhelm the CIPS and cause engine operating problems [39, 137]. Normal CIPS design practice is to design for at least a running-wet surface for intermittent maximum conditions if the ice formed during such an encounter compromises safe flight [137]. The approach taken to find the CIPS sizing point is similar to that for finding the WIPS sizing point. The heat flux estimation approach described in Sec. 4.8.4 is applied to a 3-dimensional search grid $\mathcal{G} : \{h, V_\infty, T_\infty\}$ where $h - V_\infty$ combinations aree selected within the aircraft flight envelope and $h - T_\infty$ combinations are set based on the IMI icing envelope [77, 134] (as opposed to the CMI envelope used for WIPS). The sizing point is identified as the flight condition yielding the maximum required total heat flux. Providing ice protection at this point requires the maximum bleed air mass flow in case of a pneumatic CIPS and the maximum electrical power in case of electrothermal CIPS.

4.9.4 Power Requirements

The CIPS power requirements are estimated in the same manner as the WIPS power requirements (described in §4.8.6). This is therefore not repeated.

4.9.5 Mass Estimation

The mass of the pneumatic CIPS is estimated as

$$M_{p-cips} = (M/L)_{p-ips} \; \ell_{cips}, \tag{134}$$

where $(M/L)_{p-ips}$ is the mass per unit length of the piccolo tubes (Eq. 128). In a similar manner, the mass of the electrothermal CIPS is computed as

$$M_{e-cips} = (M/A)_{e-ips} \; A_{prot}^{cips}. \tag{135}$$

where the mass per unit area $(M/A)_{e-ips}$ was discussed previously in § 4.8.7.

4.9.6 Drag Penalty Estimation

No drag penalties are assessed for any of the four CIPS designs considered, since none of them are of the de-icing type.

4.10 Chapter Summary

The modeling approaches for the power consuming subsystems (FCAS, LGAS, NWSS, WBS, ETS, TRAS, ECS, WIPS, and CIPS) were described in this chapter. For each of them, the control volume for analysis was first defined, following which approaches to estimate subsystem mass, secondary power requirements, and drag increments (if any) were presented for each technical solution considered. These quantities are ultimately fed back into the aircraft sizing and mission performance analysis to obtain the impact of a given subsystem architecture on aircraft-level and mission-level metrics of interest. Additionally, the secondary power requirements of the power consuming subsystems directly drive the sizing of the elements of the power generation and distribution subsystems, which are addressed in Chapter 5.

CHAPTER V

MODELING OF POWER GENERATION AND DISTRIBUTION SUBSYSTEMS

The power generation and distribution subsystems (PGDS) are responsible for generating the different types of secondary power and distributing it to the power consuming subsystems (described in Chapter 4). These include the following:

1. Hydraulic Power Generation and Distribution System (HPGDS): Responsible for the generation of hydraulic power through the conversion of mechanical power extracted from the engine and the distribution of hydraulic power to hydraulic power consuming subsystems

2. Electric Power Generation and Distribution System (EPGDS): Responsible for the generation of electrical power through the conversion of mechanical power extracted from the engine and the distribution of electric power in the appropriate form to electric power consuming subsystems

3. Pneumatic Power Generation and Distribution System (PPGDS): Responsible for the extraction of pneumatic power in the form of pressurized bleed air from the engine, the regulation of the required air as per requirements, and its distribution to pneumatic power consuming subsystems

4. Mechanical Power Generation and Distribution System (MPGDS): Responsible for the extraction of mechanical power (shaft-power) from the engine and the distribution of extracted shaft-power to direct users of mechanical power or for conversion to hydraulic and/or electric power

This chapter describes the modeling approach for each PGDS listed above. As discussed previously in Chapter 3, the determination of PGDS characteristics requires first the consideration of the component-to-component connectivity within the subsystem architecture, which is driven by redundancy requirements and which contributes to subsystem mass through the presence of redundant components. While fairly well-established for a fully conventional subsystems architecture, the connectivity of components becomes less obvious with the progressive electrification of subsystems due to the absence of existing architectures to serve as a reference. Therefore, the first part of this chapter (§5.1) describes how the component connectivity is explicitly accounted for within the modeling approach.

With the connectivities defined, the sizing of the distribution elements is in general driven by a combination of downstream consumer requirements and applicable physical constraints. Examples of the latter include the need to deliver a required flow rate to a hydraulic consumer without exceeding a maximum permissible pressure drop, or the need to deliver a required electric current to an electric consumer without exceeding a maximum permissible voltage drop. The capacities of the power sources are not obtained by simple summation of the peak power requirements of the connected consumers. They are instead sized by identifying constraining load cases where peak consumer demands or the unavailability of similar power sources (through engine or component failures) maximize the power demand. Further, even though the PGDS do not directly *consume* power like the power consuming subsystems, there is nevertheless power *dissipation* in these subsystems, which ultimately represents an increase in secondary power consumption at the aircraft level. The power dissipation occurs due to inefficiencies of system components (generators, pumps, etc.) and systemic inefficiencies caused by friction losses in piping and ducting or ohmic losses in electrical cables. The second part of this chapter addresses the modeling approach for the HPGDS (§5.2), EPGDS (§5.3), PPGDS (§5.4), and MPGDS (§5.5).

5.1 Heuristic Determination of Connectivity Among Subsystem Architecture Elements

Subsystem architecture definition refers to the determination of the associations or connectivity among the elements of the architecture, such as those between prime movers and power sources, power sources and power systems, and power systems and power consumers.

Certain similarities were assumed in the associations among hydraulic and electric power systems and the various actuation functions. Therefore, the definition of the actuation architecture is covered first (§5.1.1), followed by descriptions of the electric system architecture (§5.1.2), the hydraulic system architecture (5.1.3), and the pneumatic system architecture (§5.1.4).

5.1.1 Actuation Architecture (Hydraulic and/or Electric)

The actuation functions for the FCAS, LGAS, NWSS, WBS, and TRAS can use both hydraulic (conventional) and electric power (More Electric). For these subsystems, the layout of actuators and the power systems supplying the actuators is driven by redundancy requirements and the criticality of the actuation functions. In general, actuation functions that are highly critical (e.g., actuation of the primary flight control surfaces) are provided the highest degree of redundancy in the form of multiple actuators that are supplied by different power systems. Additional redundancy is provided by associating multiple power sources with each power system. These associations may be determined formally by methods such as Fault Tree Analysis (FTA) or Failure Modes and Effects Analysis (FMEA). However, these are typically performed much later in the design process. At the same time the redundancy requirements cannot be totally overlooked in early analyses, since the presence of multiple redundant power systems and associated distribution elements contributes significantly to the mass of the vehicle. The solution adopted in this dissertation for

determining the associations of power systems to the actuation subsystems involves the identification and subsequent application of a set of heuristic rules whose validity for electric actuation architectures revolves around a central technology assumption:

- For electrification of conventionally hydraulic actuation functions to be considered feasible,

    i. the overall reliability of a single electric power system must be at least comparable to that of a single conventional hydraulic power system

    ii. the overall reliability of a single electric actuator must be at least comparable to that of a conventional hydraulic actuator

The inherent reconfigurability of electric power systems and results from investigations into the reliability of electric actuators [141, 29, 31] support the possibility that these conditions may be realizable. Subject to the central assumption, it follows that an actuation function which was served by m hydraulic actuators powered by n hydraulic power systems may now be served by m electric actuators powered by n electric power systems. From this in turn, it follows that heuristic rules identified from inspection of existing conventional hydraulic actuation architectures[1] may be extendable to partially or completely electrified actuation architectures as well. A brief summary of the heuristic rules identified by inspection of such actuation architectures is provided for each of the actuation subsystems:

1. Ailerons and elevators (FCAS): Control surfaces such as ailerons and elevators, which are flight-critical, are provided with two actuators per panel. This is also true if multiple aileron panels exist per wing, and if multiple elevator panels

---

[1] Information regarding fully conventional hydraulic actuation in existing aircraft was determined from a number of public domain documents available from the website www.smartcockpit.com. This resource contains freely accessible PDF documents describing various systems of different aircraft from different manufacturers. For the purpose of identifying heuristic rules, the most relevant were documents dealing with ATA 27: Flight Controls and ATA 29: Hydraulic Power. Information regarding MEA architectures was obtained in particular from Refs. [116, 74, 24].

exist per horizontal stabilizer. Each actuator is supplied by a single power system. Let the terms *aileron group* and *elevator group* refer to all ailerons taken together and all elevators taken together respectively. Then,

a. If the aileron group and/or the elevator group is powered by the same *type* of power (i.e., either hydraulic *or* electric but *not* both), then three such power systems are required (i.e., either 3H architecture or 3E architecture)

b. If the aileron group and/or the elevator group is powered by both types of power (i.e., both hydraulic and electric), then two power systems of each type are required (i.e., 2H/2E architecture, provisionally)

2. Rudder (FCAS): If a single rudder panel is present, it is provided with two actuators. If the rudder is partitioned into two panels, then each panel is provided with three actuators. Each actuator is supplied by a single power system. Let the term *rudder group* refer to all rudder panels taken collectively.

a. If a single rudder panel is present and is powered by a single type of power (i.e., either hydraulic *or* electric), then there must be three such power systems of that type

b. If a single rudder panel is present and is supplied by both types of power (i.e, both hydraulic and electric), then it may be supplied by two hydraulic systems and one electric system

c. If two rudder panels are present and the rudder group is powered by a single type of power (i.e., either hydraulic *or* electric), then collectively the rudder group requires three systems providing that type of power

d. If two rudder panels are present and the rudder group is powered by both types of power (i.e. both hydraulic and electric), then two power systems of each type are required. Each panel must be supplied by one hydraulic

system and one electric system. The same hydraulic system cannot supply both panels. The same electric system cannot supply both panels

3. Spoilers (FCAS): Since the presence of multiple spoiler panels provides *surface redundancy*, each spoiler panel is driven by only one actuator. Each actuator is supplied by a single power source. Association of power systems to spoiler panels must always preserve left wing / right wing symmetry, i.e., equivalent spoilers on both wings must be powered by the same power system. Let the term *spoiler group* collectively refer to all spoilers.

    a. If the spoiler group is supplied by one type of power (i.e. either hydraulic *or* electric), then two such power systems are required (if not initialized already). These may be associated with the spoiler panels respecting the symmetry condition mentioned above, and minimizing occurrences where adjacent spoiler panels are supplied by the same power source

    b. If the spoiler group is supplied by one type of power (i.e. either hydraulic *or* electric) and three systems supplying that type of power are *already* initialized, then these may be associated with the spoiler panels respecting the symmetry condition mentioned above

    c. If the spoiler group is supplied by both types of power (i.e., both hydraulic and electric), then two power systems of each type are required. These may be associated with spoiler panels respecting the symmetry condition mentioned above, and in a manner that allocates approximately equal number of panels to electric and hydraulic power sources

4. Trimmable Horizontal Stabilizer (FCAS): The THS is actuated by a single Trimmable Horizontal Stabilizer Actuator (THSA).

    a. If the THSA is supplied by only one type of power (i.e., either hydraulic *or*

electric), then two such power systems must supply the THSA

b. If the THSA is supplied by both types of power (i.e., both hydraulic and electric), then two such hydraulic systems and one electric system must supply the THSA

5. Leading-edge high-lift devices (FCAS): The leading-edge high-lift system is powered centrally by a dedicated Power Drive Unit (PDU). Each PDU is supplied by two power systems. These may be two hydraulic systems, two electric systems, or a combination of one hydraulic and one electric system.

6. Trailing-edge high-lift devices (FCAS): Same logic as leading-edge devices.

7. Landing gear retraction/extension (LGAS): The retraction/extension function of each landing gear leg is served by a single retraction actuator. The actuator is supplied by a single power system. In case of three landing gear legs (one nose gear and two main gears), the same power system supplies the retraction actuator for each leg. In case body-mounted landing gears are also present, a separate power system supplies the retraction actuator for these additional landing gears.

8. Nose-wheel steering function (NWSS): The nose-wheel steering actuator is powered by a single power system, which is the same power system that supplies the landing gear actuators for the nose and wing-mounted landing gears.

9. Wheel brakes (WBS): The wheel brakes on each wing-mounted and body-mounted main gear are supplied by two power systems (one primary system and one alternate system). If body-mounted gears are present, then the primary system for the wing-mounted gears is the alternate system for the body-mounted gears. The alternate system for the wing-mounted gears is the primary system for the body-mounted gears.

174

10. Thrust reverser actuation (TRAS): Each thrust reverser is powered by a single power system. If by this point there are less than or equal to two power systems of the type supplying the TRAS, then (i) for a total of two thrust reversers, a single power system may supply both reversers, (ii) for a total of four thrust reversers, a total of two power systems may supply the reversers. Left wing / right wing symmetry must be maintained in this case. However, if by this point there are already three power systems of the type supplying the TRAS, then (i) for a total of two thrust reversers, each may be powered by a different power system, (ii) for a total of four thrust reversers, the two outboard reversers may be powered by the same power system, while the two inboard ones are each powered by one of the two remaining power systems.

The application of the above heuristics in the order in which they are stated allows the following to be identified:

1. the overall actuation architecture, i.e., the number of independent electric and/or hydraulic systems supplying actuation functions (3H, 3E, 2H/2E, etc.)

2. the association of each end actuation load (an individual actuator) with either a hydraulic or an electric power system

The associations established using these heuristics are used subsequently for the sizing of the power distribution elements (electric cables and/or hydraulic pipes) during the evaluation of the EPGDS and HPGDS respectively.

5.1.2 Electric System Architecture

Before the elements of the EPGDS can be sized, its architecture must be defined. Unlike the HPGDS and the PPGDS, which follow reasonably well-defined architectures that do not vary substantially between aircraft, a large number of architecture possibilities exist for the EPGDS. In particular, several options exist

with regard to the choice of voltage type used by major electrified loads (AC vs. DC) and also voltage magnitude. For MEA, due to the significantly higher electric load, higher voltage levels are often considered in order to reduce the magnitude of transmitted currents and thus the cable weight. Thus, while voltage levels of 115 VAC and $\pm$ 135 VDC were common in prior aircraft [142], higher voltage levels such as 230 VAC and $\pm$ 270 VDC have already appeared in service [116]. There is also a recent trend towards the use of *variable frequency power generation*, in which a generator is connected directly to the engine. It therefore generates AC power at a variable frequency that can range between 360-800 Hz [116]. This allows the elimination of a heavy and complex component called a *constant-speed drive*, which has traditionally been used for constant frequency power generation [142]. Further, recent aircraft feature *starter-generators* which can be used in generator mode to generate power off a running engine, or in motor mode using another electric power source to start the engines, thus eliminating the traditional air turbine starter [116]. The electrical system *template* shown in Fig. 32 is developed based on these observations and used as the basis of the EPGDS for the MEA architectures. Some of its important characteristics are as follows:

1. Electric power is generated by variable frequency starter-generators generating 230 VAC. Each such starter-generator is connected to its own variable frequency AC bus in order to avoid paralleling of generators, with the provision of tie-switches (not shown in Fig. 32) to avoid the loss of a bus owing to failure of one single power source [143]

2. 230 VAC power is directly supplied to large loads such as WIPS and CIPS (if electrified) that are insensitive to the frequency of supplied power [74]. This also helps to reduce the magnitude of converted power, and thereby the mass of power conversion equipment and power conversion losses [87]

176
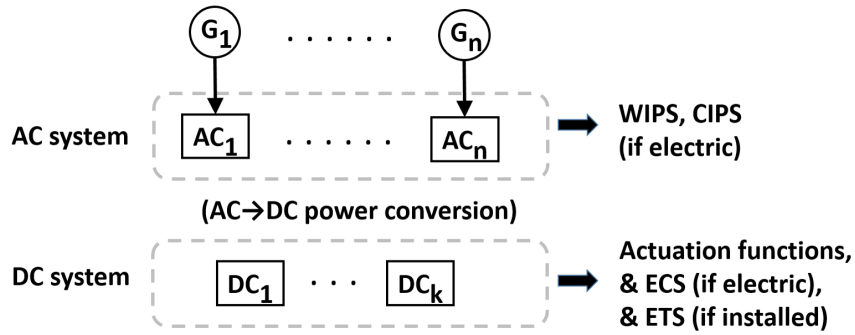
Figure 32: Electric system template - the basis for EPGDS architecture

3. 230 VAC power is converted to $\pm$ 270 VDC power using AC-to-DC power transformation equipment called *Auto-Transformer Rectifier Units* (ATRUs) in order to supply large loads such as the ECS, electrified actuation functions, and ETS (if installed)

The DC power systems $DC_1, \ldots DC_k$ shown in Fig. 32 are in fact the electric power systems described in §5.1.1 for the actuation functions. The association of the DC power systems to the electrified actuation functions has thus already been described. Each ECS pack is assumed to be supplied by a single DC system, a different system being used for each pack. The ETS, if installed, is assumed to be powered only by a single DC system. This is a valid assumption, since the ETS is neither flight-critical nor ground-critical, and in the event of its failure, there is always the provision to taxi conventionally using main engine thrust.

Due to the assumptions stated above, the number of AC buses equals the number of engine-driven generators (EDGs). The number of EDGs attached to each engine is actually determined taking into account several factors other than merely the magnitude of the electrical power requirement, such as a nonlinear relationship between generator capacity and weight [56] or the tendency of the nacelle diameter to balloon undesirably if a single high-rating generator is used [42]. In the approach presented, the number of EDGs per engine $N_{edg/eng}$ is set according to the following

simple rules based on the number of engines N_{eng} and the subsystems electrified:

1. If ECS is electrified, then $N_{edg/eng} = 2$

2. If both WIPS and CIPS are electrified and $N_{eng} = 2$, then $N_{edg/eng} = 2$

3. If primary flight control surfaces are electrified and $N_{eng} = 2$, then $N_{edg/eng} = 2$

4. In all other cases, $N_{edg/eng} = 1$

The above rules take into account both the relative magnitudes of electrical loads arising from electrification of different subsystems and the number of engines in order to determine $N_{edg/eng}$. All EDGs are assumed to be identical in terms of rated power generation capacity.

5.1.3 Hydraulic System Architecture

The heuristic logic for determining the connectivity of the hydraulic power systems with the hydraulic loads has already been described in §5.1.1. The same logic also allows the determination of the number of hydraulic systems required for any actuation architecture, ranging from fully conventional (3) to fully electric (0).

Heuristic rules for the association of hydraulic power sources (pumps) with the hydraulic power systems were also derived based on the inspection of existing aircraft hydraulic systems. In general each hydraulic system is supplied by at least two pumps. Typically, one of these is an Engine Driven Pump (EDP) while the other may in some cases be an Electric Motor (Driven) Pump (EMP). In such cases, the capacity of the EMP is considerably less than that of the EDP. In more recent designs however, the role of EMPs is increasing, and it is possible for a hydraulic system to be pressurized using two EMPs and no EDP (e.g., Boeing 787 Center System [74]). If hydraulics are present, then there may be one, two, or three hydraulic systems. Since the aircraft considered have either two or four engines, a total of six combinatorial possibilities

Table 20: Association of hydraulic power sources with hydraulic power systems (EDP: Engine Driven Pump. EMP: Electric Motor Pump. RAT: Ram Air Turbine. EDP-E1 means EDP driven off Engine # 1. EMPs are simply numbered sequentially.)

Engines	3 Hyd. Sys.			2 Hyd. Sys.		1 Hyd. Sys.
	H1	H2	H3	H1	H2	H1
2	EDP-E1	EMP-3	EDP-E2	EDP-E1	EDP-E2	EDP-E1
	EMP-1	EMP-4	EMP-2	EMP-1	EMP-2	EDP-E2
		(RAT)			(RAT)	(RAT)
4	EDP-E2	EDP-E1	EDP-E3	EDP-E1	EDP-E3	EDP-E3
	EMP-1	EDP-E4	EMP-2	EDP-E2	EDP-E4	EDP-E4
		(RAT)			(RAT)	(RAT)

arise, for which the associations of hydraulic power sources to hydraulic systems is summarized in Table 20.

The Ram Air Turbine (RAT) is able to pressurize one of the hydraulic systems in the event of failure of all engines. Inspection of existing hydraulic system architectures of Airbus and Boeing aircraft revealed that the hydraulic system supplied by the RAT

1. always supplies one actuator on the rudder, aileron, and elevator panels for aircraft that have only one rudder, two ailerons, and two elevators (to permit movement of primary flight controls in an all-engines inoperative scenario)

2. typically supplies one actuator on each outboard aileron for aircraft with multiple aileron panels per wing. In certain cases, one actuator on the inboard aileron panels may also be supplied (this latter logic is used for this work, and is further extended to also include multiple elevator panels)

3. is always one of the two systems that supply the leading-edge and trailing-edge flap PDUs (to permit flap operation at reduced rate)

4. is typically (but not always) one of the two systems that supply the THSA (for the exceptions, a manual reversion mode exists for the stabilizer)

179

5. is the system that powers gear actuation, wheel braking, and steering functions (to permit these functions following failure of all engines)

6. does *not* supply thrust reversers in the case of twin-engined aircraft (presumably as thrust reversers are ineffective in an all-engines inoperative scenario)

These heuristics and the ones identified previously allow for the heuristic definition of the connectivities within the hydraulic system architecture.

5.1.4 Pneumatic System Architecture
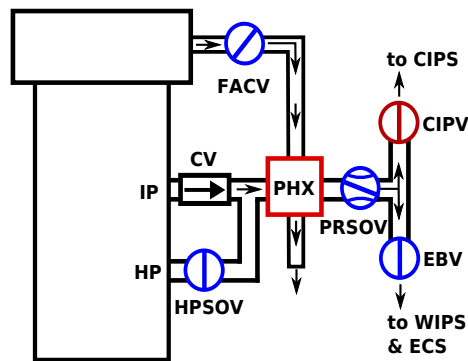
Figure 33: Schematic of conventional bleed system for turbofan engine

The architecture of the pneumatic system is fairly constant over current commercial aircraft in which pneumatic power is used for ECS and IPS functions. As shown in Fig. 33, bleed air (often referred to by engine manufacturers as *customer bleed*) is extracted from a turbofan engine through bleed ports. In most cases, the bleed can be tapped from at least two ports. Under high throttle settings that are commonly used for takeoff, climb, and cruise, an *Intermediate Pressure port* (IP) is used, as it provides bleed air at sufficient temperature and pressure. However, at low throttle settings that are used for descent, the IP temperature and pressure are insufficient, and air is instead extracted from a *High Pressure port* (HP). In this case, the *High Pressure Shutoff Valve* (HPSOV) opens and a *Check Valve* (CV) prevents backflow of the HP air into the IP. The port selection logic is an attempt

at localized energy management as it attempts to extract air from the least wasteful bleed port. Even so, under most operating conditions, the temperature and pressure of the extracted bleed air are too high for direct use by downstream consumers. Passing such high-temperature air through the wing ducts presents a problem since these are often in close proximity to fuel lines, and the bleed air temperature it typically above the auto-ignition temperature of fuel. Excessively high pressure can also cause sealing and containment problems. Therefore, the temperature of the extracted bleed air is reduced by passing it through a *Precooler Heat Exchanger* (PHX), which is an air-to-air heat exchanger in which the bleed air is cooled against a stream of cooler air extracted from the fan. The flow of fan air is modulated by a *Fan Air Control Valve* (FACV) based on temperature feedback from the bleed air exiting the PHX in order to attain a target temperature between 180-200°C. The pressure of the bleed air is down-regulated to around 300 kPa [118] by a *Pressure Regulating Shut Off Valve* (PRSOV), which can also be completely closed to prevent any bleed extraction.

The down-regulated air, which is now at acceptable temperature and pressure can be supplied to the pneumatic users. If the CIPS is activated, then the bleed air can pass through the *Cowl Ice Protection Valve* (CIPV) from where it is ducted to the nacelle front face. A review of the pneumatic system designs of existing commercial aircraft showed that in certain cases, bleed air for nacelle ice protection (CIPS) is tapped prior to the PHX and therefore is hotter than the air supplied to other pneumatic users such as the WIPS and the ECS. However, in certain other cases, the air used for the CIPS also passes through the PHX. For all results presented in this dissertation, the latter design is assumed. A logic switch exists in the PPGDS analysis module which can be set to enforce the first design, in which case electrification of the ECS and WIPS results in elimination of the PHX of each engine.

In order to supply the ECS and WIPS, the bleed air passes through the *Engine Bleed Valve* (EBV) and is ducted through wing ducts into a pneumatic manifold in the
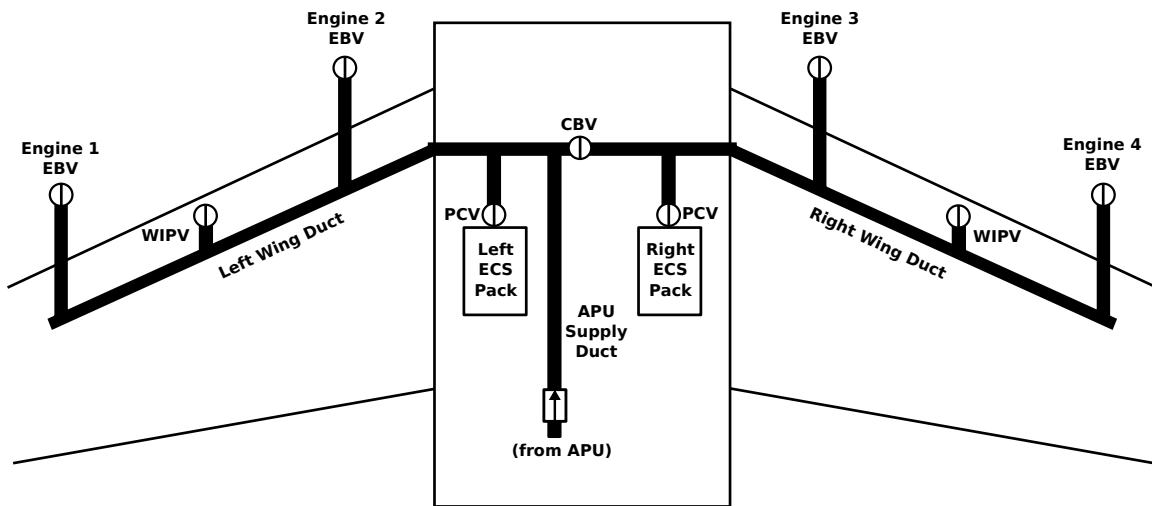
Figure 34: Schematic of conventional pneumatic system

fuselage area (Fig. 34). The pneumatic system is divided into left and right halves, which are interconnected through a *Cross-Bleed Valve* (CBV) so that one system can supply users on the other side in case of a failure in the other system. Under nominal operating conditions, the left system supplies the left WIPS and the left ECS pack, while the right system supplies the right WIPS and right ECS pack. Bleed air flow to the WIPS is controlled by the *Wing Ice Protection Valves* (WIPV), while flow into the ECS packs is controlled by *Pack Control Valves* (PCVs). In addition, since the APU must be able to support ECS operation on the ground, an APU supply duct runs from the aft fuselage to the central pneumatic manifold, through which the APU can supply air for ECS operation on the ground. The APU supply duct is also used to supply pressurized air that is used by the conventional pneumatic starters to start the main engines. Engine starting has not been considered in this dissertation. However, in previous studies which considered ECS electrification, the increased power rating of the main engine generators was found to be sufficient for these to be used as motors to start the main engines [42, 43]. Based on this finding, the electrification of the ECS is deemed to be a sufficient condition for elimination of the APU supply duct, as described subsequently.

Of the subsystems considered, the ECS, WIPS, and CIPS are pneumatic power users in a conventional architecture. Within the MEA architecture space, electrification may affect none, some, or all of these subsystems. This results in $2^3 = 8$ possibilities that must be accounted for in determining the layout of the pneumatic system and the sizing of its components. The logic rules that are applied for these cases are as follows:

- Case 1 - ECS, WIPS, and CIPS are pneumatic: The layout of the PPGDS is as described above and shown in Fig. 33 and Fig. 34

- Case 2 - Only ECS is electrified: The APU supply duct is eliminated. Remaining ducts and precoolers are down-sized based on the reduction in the mass flow rates that they process

- Case 3 - Only CIPS is electrified: Nacelle ducts running from bleed port to nacelle front face are eliminated. PHX is down-sized based on reduction in mass flow rate due to CIPS electrification

- Case 4 - Only WIPS is electrified: Wing ducts and central ducts are down-sized based on reduction in mass flow rate due to WIPS electrification. PHX is down-sized due to the same reason

- Case 5 - ECS, WIPS, and CIPS are all electrified: Entire PPGDS is removed

- Cases 6, 7, 8 - Any two among ECS, WIPS, and CIPS are electrified: The actions are based on the logic rules described in (1) - (5)

The sizing approach for the pneumatic ducts and the PHX based on the mass flow rates that they process is described subsequently in this chapter (§5.4).

183

5.1.5   Translation of Logical Connections to Physical Equivalents

The architecting heuristics described in the preceding sections allow the logical connectivities among subsystem architecture components such as power sources, power systems, and power consumers to be established. However, these by themselves do not provide any information regarding either the locations of the power sources, power systems, and power consumers, or the physical paths taken by the power distribution elements connecting them.

The locations of the power consumers, systems, and sources are fairly well-established for both conventional and MEA architectures, and thus may be specified with reference to the geometry of the *parent* body that they are contained in or associated with. A few examples will suffice to illustrate this point:

1. The position of control surface actuators is defined parametrically with respect to the control surfaces, which in turn are defined parametrically on the lifting surface (using spanwise and chordwise coordinates)

2. Components which are located on the outer periphery of the engine nacelles (or may be approximated as being so) are conveniently defined using their clockface position and distance aft of the nacelle front face (normalized by nacelle length). This allows the positions of engine-driven pumps and generators, the CIPS piccolo tube or heating elements, the thrust reverser actuators, and the exit point of bleed air from the PHX to be defined

3. Loads such as landing gear actuators, nose-wheel steering mechanism, wheel brakes, and electric taxi motors are defined by their normalized position on the landing gear legs, which themselves are defined by their attachment points to the fuselage or wing

The ultimate goal in creating such definitions is to be able to compute the Cartesian coordinates of each of these components, since they define the extremities (start

and end points) of the power distribution elements connecting them. However, simply knowing the extremities of the distribution elements is not sufficient, since in many cases physical constraints prohibit a straight-line connection between the start and end points. Even in such cases, through inspection of subsystem layouts of existing aircraft, it is possible to develop and program rules for the paths taken by the distribution elements to get to the so-called "four corners" of the aircraft. Such rules allow the parametric definition of one or more intermediate points in between the starting and ending points which collectively determine the route taken by the distribution element. For each PGDS, such rules may be defined for paths connecting an assumed point of origin to all other relevant points. For example, for a hydraulic system, assuming the point of origin to be a hydraulic manifold located in the center fuselage area, parametric routing rules are defined for distribution elements starting from the origin and ending at the locations of each hydraulic load. Additional rules are defined for paths leading from the power sources (pumps) to the system origin. Since no more than three hydraulic systems are envisioned, a set of rules for each such system may be developed and saved, thus creating a *template* for that hydraulic system. If the architecting algorithm (§5.1.1) determines that only two hydraulic systems are sufficient, then two of these three templates are activated. Since no one hydraulic system supplies all hydraulic loads, only the system-to-load connections determined through logical architecting to exist need be developed. This allows a one-to-one correspondence between each logical connection developed and its equivalent physical connection within the aircraft, as shown in Fig. 35.

Within this geometric model, each power distribution element $\mathcal{S}_{A \rightarrow B}$ connecting start point A to end point B is represented by a set of n points in Cartesian space, the first and n^{th} points by definition coinciding with A and B respectively. The curvilinear

185
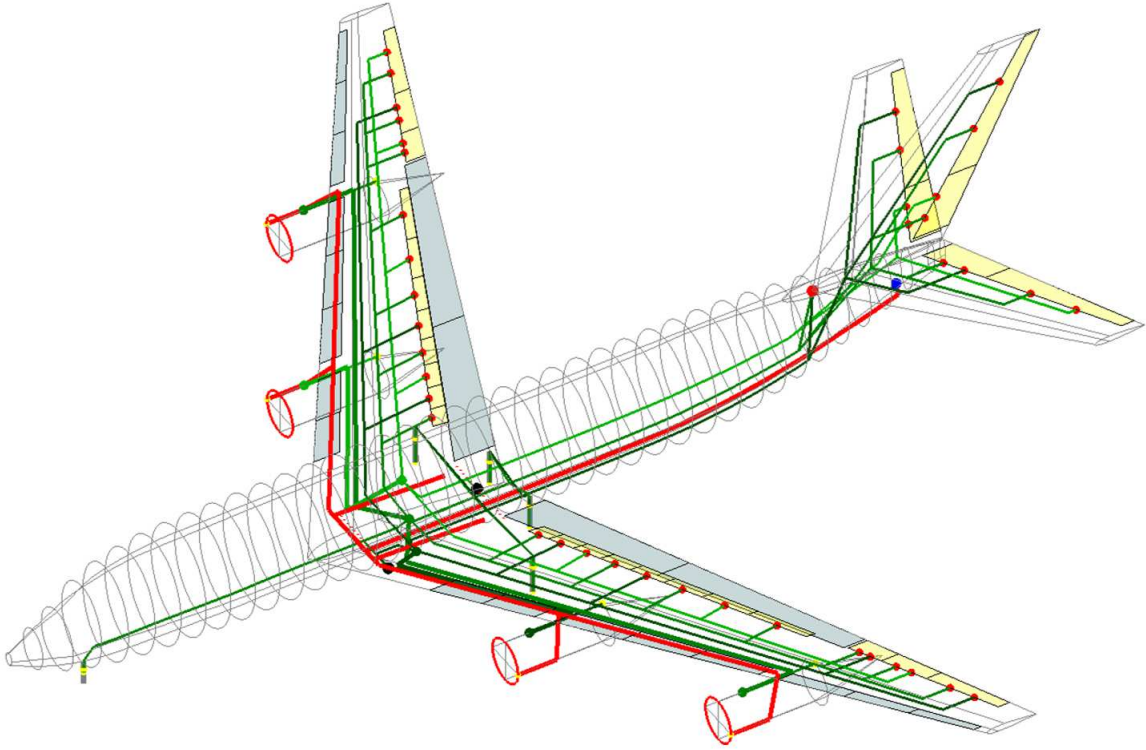
Figure 35: Translation of logical subsystem connections to physical/geometric equivalents - VLA-00000 (fully conventional subsystems architecture) is shown. Red lines indicate the PPGDS. Shades of green represent the three hydraulic systems of the HPGDS

length $\ell_{A \to B}$ of such an element now follows as

$$
\begin{aligned}
\mathcal{S}_{A \to B} &= \{P_1, \ldots, P_n\}, \qquad P_i = [x_i, y_i, z_i], \\
\ell_{A \to B} &= \sum_{i=2}^{n} \sqrt{(x_i - x_{i-1})^2 + (y_i - y_{i-1})^2 + (z_i - z_{i-1})^2}.
\end{aligned}
\tag{136}
$$

The masses of the power distribution elements are obtained using the computed lengths and the elements' mass per unit length (discussed in subsequent sections).

5.2 Hydraulic Power Generation and Distribution System (HPGDS)

The power generation elements of the HPGDS are the hydraulic pumps, which suck fluid from a hydraulic reservoir through suction lines and pressurize it to a high pressure, essentially transforming mechanical input power to hydraulic output power

(pressurized fluid flow). Systems with nominal pressures of 3,000 psi were the norm prior to the Boeing 787 and Airbus A380 aircraft, which have 5,000 psi hydraulic systems. Due to their successful use in these aircraft and beneficial impact on weight, it is foreseeable that future hydraulic systems would employ such higher pressures. Therefore, only 5,000 psi hydraulic systems were considered in this dissertation.

The pressurized fluid is then conveyed through the distribution elements, which are the hydraulic lines/pipes, to the hydraulic power consumers. In the conventional architecture (as addressed in this dissertation), these power consumers are the FCAS, LGAS, WBS, NWSS, and TRAS. Additional components of the HPGDS include accumulators, numerous regulating and check valves, and associated fittings, couplings, and brackets. The hydraulic pumps and piping (including associated fittings and valves) contribute to the mass of the HPGDS. The subsystem dissipates power due to component inefficiencies and leakage flow. The estimation of HPGDS mass and power dissipation are discussed in the following sections.

5.2.1 Mass Estimation

Since hydraulic systems have been in use for several decades, regression equations for their overall mass exist. For instance, the FLOPS-generated mass breakdown includes estimated mass of hydraulics, and takes into account the system pressure. Banel-Caule [144] presented the weight breakdown shown in Table 21 for the weights of the major HPGDS components based on a study of existing Airbus aircraft.

Table 21: Percentage weight breakdown of hydraulic system components [144]

Components	Weight percentage
Hydraulic pipes + fluid	45 %
Couplings + brackets	24 %
Manifolds + filters + valves	12 %
Ram air turbine	10 %
Miscellaneous equipment	8 %

However, the net hydraulic system mass or even the relative weight percentages of Table 21 are not sufficient for estimating the mass of hydraulic piping in all MEA architectures. This is due to the fact that in many of these MEA architectures, only *some* of the actuation functions are electrified. Among the actuation packages considered (Table 3), in packages other than Packages 0, 6, and 7, there is a *partial* removal of the conventional hydraulic system. The mass of the remaining (residual) hydraulic system must therefore be estimated.

For these cases, it is difficult to estimate the mass of the residual HPGDS through a component build-up approach. In particular, the masses of the hydraulic pipes are proportional to their lengths, which are not known with certainty in the early design phases. In fact, the final routing of these pipes may be quite complex and can often be affected by the need to avoid other equipment [144]. However Airbus, based on a study of data from Airbus aircraft [144], established the following in connection with hydraulic piping:

1. Dedicated pipes do *not* run from the central high-pressure manifold of a hydraulic system to each and every hydraulic consumer. Instead, there are common pipes which go from the generation point to a defined meeting point. There, they split (branch) to form dedicated lines which then run to the location of the different consumers

2. For a given material and nominal system pressure, the weight per unit length (W/L) of a filled hydraulic pipe is proportional to the filled pipe's cross-sectional area A_{cs}. Therefore, $(W/L) \propto A_{cs}$

3. The fluid speed v in high-pressure and low-pressure hydraulic lines is constant on all Airbus aircraft, and is specified by regulations and hydraulic system performance objectives. Since the continuity equation relates cross-sectional area A_{cs}, flow velocity v, and flow rate Q as $Q = A_{cs}v$, this implies that for a

given pipe, the cross-sectional area is proportional to the required flow through the pipe. This yields $A_{cs} \propto Q \implies (W/L) \propto Q \implies W \propto Q\,L$

4. The weight of hydraulic piping is proportional to the product of the flow rate, the pipe length, and the number of actuators - summed over all hydraulic consumers. This was verified by calibrating against real data for members of the Airbus family of aircraft that included the A320-family, A330-300, A340-300, A340-500, and A340-600 [144]. Thus, $W_{piping} \propto \sum_i n_{act,i}\,Q_i\,L_i$

Performing the summation of Item (4) over all of 'j' hydraulic *connections* rather than over all hydraulic *consumers* (a consumer may be served by multiple connections, such as a rudder served by three hydraulic connections to three actuators) removes the number of actuators and yields

$$W_{piping} \propto \sum_j Q_j\,L_j \implies W_{piping} = \mathcal{K}_{pws} \sum_j Q_j\,L_j. \tag{137}$$

As stated previously, aircraft sizing tools (such as FLOPS) typically provide a mass estimate W_{hyd}^{conv} for the hydraulic system which is based on historical data. This estimate, therefore, applies to a conventional actuation architecture where all actuation subsystems use hydraulics. Assuming such a conventional hydraulic architecture, a piping weight sensitivity factor $\mathcal{K}_{pws}$ may be determined as

$$\mathcal{K}_{pws} = \frac{W_{piping}^{conv}}{\left(\sum_j Q_j\,L_j\right)_{conv}} = \frac{\alpha\,W_{hyd}^{conv}}{\left(\sum_j Q_j\,L_j\right)_{conv}}, \tag{138}$$

where the parameter α is the ratio of piping mass to the total hydraulic system mass. From the percentage weight breakdown shown in Table 21, this parameter is set as $\alpha = 0.45 + 0.24 + 0.12 = 0.81$. The underlying assumption is that the weights of couplings, brackets, manifolds, filters, and valves associated with piping varies proportional to the weight of the piping itself. For each hydraulic consumer considered, the maximum required flow rate Q_j is determined based on the actuation requirements (described

in Chapter 4) and using the hydraulic power equation. Regarding the lengths L_j in the above formulation, a question arises regarding how the common piping segments prior to the branching out to different consumers factor into the summation, if at all. This is verified as follows:

A pipe is considered that runs for a length ℓ_0 from a source to a common distribution point. It then splits into two branches that run lengths ℓ_1 and ℓ_2 to two consumers with maximum flow rate requirements Q_1 and Q_2. Further, $L_1 = \ell_0 + \ell_1$ and $L_2 = \ell_0 + \ell_2$ are considered to denote the total length of piping from the source to the two consumers, including the common length. The continuity equation yields the flow through the common segment as being $Q_0 = Q_1 + Q_2$. The weight W of this simple piping layout may be computed as

$$
\begin{aligned}
W &= \mathcal{K}_{pws}\, Q_0\, \ell_0 + \mathcal{K}_{pws}\, Q_1\, \ell_1 + \mathcal{K}_{pws}\, Q_2\, \ell_2 \\
&= \mathcal{K}_{pws}\left\{(Q_1 + Q_2)\, \ell_0 + Q_1\, \ell_1 + Q_2\, \ell_2\right\} \\
&= \mathcal{K}_{pws}\left\{Q_1(\ell_0 + \ell_1) + Q_2(\ell_0 + \ell_2)\right\} \\
&= \mathcal{K}_{pws}\, Q_1 L_1 + \mathcal{K}_{pws}\, Q_2 L_2
\end{aligned}
\tag{139}
$$

Equation 139 establishes that even though dedicated (exclusive) piping runs do not exist from the source to each hydraulic consumer, for the purpose of the summation of Eq. 138, it is sufficient to consider the direct (non-exclusive) length from the source to each hydraulic consumer. This result presents a significant advantage since these direct lengths are readily computed from the 3-D geometric model of the aircraft (using Eq. 136) following the architecting of the HPGDS (§ 5.1.1 and § 5.1.3).

The piping weight sensitivity factors $\mathcal{K}_{pws}$ for the SSA, LTA, and VLA are computed using Eq. 138 by considering a conventional hydraulic actuation architecture for each. For each aircraft, the computed $\mathcal{K}_{pws}$ is assumed to be an invariant characteristic. Subject to that assumption, the residual piping weight of all

MEA architectures for that aircraft is evaluated as

$$W_{piping}^{MEA} = \mathcal{K}_{pws} \left(\sum_j Q_j \, L_j \right)_{MEA}. \tag{140}$$

This approach is superior to one that makes a simple assumption that the residual piping weight is proportional to either the residual piping length or the residual flow rate requirement. This is because it is clear from the proportionality relationships established previously that the weights of two pipes of equal length carrying different flow rates or that of two pipes of unequal length carrying identical flow rates will not be equal. If actuation is completely electrified, the predicted piping weight is zero.

The estimation of the weight of the hydraulic pumps (EDPs and EMPs) necessitates the estimation of their required flow capacities. These capacities are determined using a hydraulic load analysis [113] that includes both nominal and failure scenarios. In the scope of this dissertation, only a limited number of load cases are considered, which are summarized in Table 22. Each column represents a different load case, for which the load demands of each of the conventional hydraulic

Table 22: Hydraulic load cases considered for pump sizing (Abbreviations - G: ground, TO: takeoff, F-U: flaps up/retract, LG-U: landing gear up/retract, CR: cruise, DE: descent, F-D: flaps down/extend, LG-D: landing gear down/extend, S/B: spoilers extend + braking, B/TR: braking + thrust reverser deployment)

Load	G	TO	F-U	LG-U	CR	DE	F-D	LG-D	S/B	B/TR
Aileron	0.0	0.5	0.2	0.2	0.5	0.5	0.2	0.2	0.2	0.2
Elevator	0.0	0.5	0.2	0.2	0.5	0.5	0.2	0.2	0.2	0.2
Rudder	0.0	0.7	0.2	0.2	0.7	0.7	0.2	0.2	0.7	0.7
Spoilers	0.0	0.5	0.2	0.2	0.5	0.5	0.2	0.2	0.9	0.0
THS	0.0	1.0	1.0	1.0	1.0	1.0	1.0	1.0	0.0	0.0
Flaps	0.0	0.0	1.0	0.0	0.0	0.0	1.0	0.0	0.0	0.0
Gear	0.0	0.0	0.0	1.0	0.0	0.0	0.0	1.0	0.0	0.0
Brakes	0.5	0.0	0.0	0.0	0.0	0.0	0.0	0.0	1.0	1.0
Steering	0.8	0.0	0.0	0.0	0.0	0.0	0.0	0.0	0.0	0.0
Thr.Rev.	0.0	0.0	0.0	0.0	0.0	0.0	0.0	0.0	0.0	1.0
Engine % N2	54.0	105.0	100.0	100.0	100.0	54.0	54.0	54.0	59.4	59.4

consumers is specified as a fraction of its maximum flow (therefore, 1.0 implies the consumer's maximum flow demand). Since EDPs are geared to the accessory gearbox, the available flow varies with the engine N2 speed. Considering $i = 1 \ldots n$ hydraulic consumers and $j = 1 \ldots N$ load cases, the required pump capacity is given by

$$Q_{EDP} = \max_{j=1}^{N} \left(\frac{\sum_{i=1}^{n} Q_i}{\%N2/100 + \epsilon} \right)_j, \tag{141}$$

where ϵ is the ratio of the flow capacity of the EMP to that of the EDP for hydraulic systems that are pressurized by one pump of each type. The flow availability of the EMP does not vary with engine speed. For systems pressurized by two EDPs, the factor ϵ may simply be omitted in Eq. 141. For systems pressurized by two EMPs, the denominator can neglected entirely.

Though basic, this pump sizing approach can account for the fact that the constraining load case may change depending on which actuation functions are electrified. For example, in a conventional actuation architecture, given the dependence of the available pump flow on the engine speed, the sizing load case is typically one where high flow-demand loads such as landing gear, flaps, or thrust reversers must be actuated with the engine at or close to flight idle [17]. However, if these actuation functions are electrified, then the constraining load case for pump sizing may change. Such changes are captured in the approach described above.

Once the required pump capacity is determined, the masses of the pumps are determined based on power-to-mass ratios that were identified from various pump manufacturer product data-sheets. From inspection of these, EDPs were found to have a power-to-mass ratio in the range 3.20 - 3.80 kW/kg, while EMPs ranged from 0.70 - 0.76 kW/kg. Since hydraulics have reached technology saturation, the upper values from these ranges are taken to represent the SOTA in pump technology, and no scope for improvement is considered.

5.2.2 Power Dissipation

The power dissipation in the HPGDS may be represented as

$$P_{HPGDS} = \left(\frac{1}{\eta_{pump}} - 1 \right) \left(\sum_{i=1}^{N} P_{hyd}^{(i)} + \Delta p_{nom} Q_{lkg} \right) + \Delta p_{nom} Q_{lkg}, \qquad (142)$$

where the first term represents the power dissipation in the hydraulic pumps with overall efficiency $\eta_{pump} < 1$, and the second term represents the power dissipation due to the need to maintain nominal system pressurization Δp_{nom} against a leakage flow Q_{lkg}. For simplicity, the leakage flow is modeled as a fixed fraction of the installed hydraulic capacity based on the hydraulic load profile for the Airbus A320 [145]. The power dissipated within the HPGDS manifests itself at the architecture level as an increase in shaft-power extraction from the engines.

5.3 Electrical Power Generation and Distribution System (EPGDS)

An estimate of the mass of the EPGDS for conventional subsystem architectures is already provided by aircraft sizing tools (such as FLOPS). Since the electrification of subsystem architectures necessarily involves the expansion of the EPGDS, the mass of the EPGDS for a MEA architecture is computed by adding the subsystem's mass increment to the EPGDS mass for the baseline architecture.

With reference to the EPGDS template shown in Fig. 32, these major components are seen to be (i) Engine Driven Generators (EDGs) and APU Generators (APUG), which generate electrical power, (ii) ATRUs (power conversion equipment), which transform 230 VAC power to $\pm$ 270 VDC power, and (iii) electrical feeders and cables which transmit electrical power between EPGDS components and loads. Thus, the EPGDS mass in a MEA architecture is computed as

$$M_{EPGDS} = M_{0,EPGDS} + \Delta M_{gen} + \Delta M_{atru} + \Delta M_{cbl}, \qquad (143)$$

in which $M_{0,EPGDS}$ is the estimated mass of the EPGDS for the conventional

subsystem architecture. The following sections describe the estimation of the mass increments ΔM_{gen}, ΔM_{atru}, and ΔM_{cbl} due to increased generator capacity, additional power conversion equipment, and additional power distribution elements respectively.

5.3.1   APU Generator (APUG) Sizing

The required APU generator capacity is computed as

$$
\begin{aligned}
P_{apug} &= P_{apug,0} + P_{ets}^{max} + P_{eecs}^{gnd}, \\
\implies \Delta P_{apug} &= P_{apug} - P_{apug,0},
\end{aligned}
\tag{144}
$$

where $P_{apug,0}$ is the APU generator capacity of the conventional baseline architecture, P_{ets}^{max} is the maximum power demand for electric taxiing (if equipped), and P_{ecs}^{gnd} is the ground power requirement for electric ECS. If there is no ETS installed and the ECS is not electric, then the APU generator capacity remains at the baseline value.

5.3.2   Engine Driven Generator (EDG) Sizing

The required capacity of the Engine Driven Generators (EDGs) is computed using an approach that considers the following:

1. Due to the overload capacity of generators, they are able to supply power in excess of their nominal rated capacity for brief periods of time. Therefore, large loads which persist only for short durations (such as those due to the operation of electrified landing gear, high-lift devices, and thrust reversers), do not necessarily affect the sizing of the generator's nominal capacity provided that they fall within the overload capacity [42]

2. The sizing of the EDGs is not necessarily determined by nominal operating conditions, but by failure or off-nominal conditions in which the demand on a particular generator may be the most constraining. Such conditions, for example, may occur due to the failure of other generators within the EPGDS

194

3. Modern aircraft feature APUs with in-flight restart capability, often extending across the entire flight envelope. Factoring in the APU generator capacity would affect the sizing of the EDGs based on off-nominal/failure scenarios. However, doing so would require that the APU be operable in order to dispatch the aircraft, which is not the case for current commercial aircraft [56]

Based on the above considerations, the required EDG capacity for the whole aircraft (i.e., considering *all* EDGs together) is expressed as follows:

$$P_{edg} = P_{edg,0} + \Delta P_{edg,nst} + \Delta P_{edg,st} \tag{145}$$

In Eq. 145, $P_{edg,0}$ is the total generation capacity of all baseline EDGs. In other words, if the baseline aircraft has two EDGs each rated at 120 kVA, then $P_{edg,0}$= 240 kVA. $\Delta P_{edg,nst}$ is the required increment in total EDG capacity in order to support electrical loads within a MEA that are *not* short-term loads (*nst: non-short-term*). These are the loads that may persist for extended periods of time that are longer than the permitted overload duration of the EDGs. $\Delta P_{edg,st}$ is the required increment in total EDG capacity in order to support the short-term loads (*st: short-term*).

In off-nominal/failure scenarios, a certain fraction of the total EDG capacity of the aircraft may be lost. This is accounted for the *capacity ratio* κ, defined as the ratio of available EDG capacity to nominal EDG capacity:

$$\kappa = \frac{P_{edg,av}}{P_{edg}} \tag{146}$$

The overload ratio ϵ of a generator (EDG or APUG) is defined as the ratio of the power that it can deliver during temporary overload conditions to the rated nominal power output. Let $\lambda = 1$ and $\lambda = 0$ denote respectively the cases where the APU generator capacity is and is not factored into the EDG capacity determination.[2]

---

[2] A default setting of $\lambda = 0$ (no credit assumed for APU generator capacity) was used for all analyses presented in this dissertation, except some presented in Chapter 8 where the effect of $\lambda = 1$ (full APU credit) on EPGDS sizing was analyzed.

Considering the presence of non-short-term loads P_{nst} and short-term loads P_{st} over the course of the mission, the total electrical load may be expressed as

$$P_{tot}(t, \kappa) = P_{nst}(t, \kappa) + P_{st}(t, \kappa), \tag{147}$$

where the second argument κ indicates that the magnitudes of the loads may depend on the capacity ratio κ. This allows the modeling of degraded operation modes in which some non-essential loads may be shed. The required EDG capacity is determined by enforcing the following two conditions:

1. The available power generation capacity for a given capacity ratio must be sufficient to meet the maximum non-short-term loads corresponding to that capacity ratio *without* any generators working at overload conditions

2. The available power capacity for a given capacity ratio *with* generators working at overload conditions must be sufficient to meet the maximum total load (including both non-short-term and short-term loads) for that capacity ratio

Stated mathematically, the first condition is essentially a power balance between available electrical power and required electrical power considering only the non-short-term loads, which allows the increment $\Delta P_{edg,nst}$ to be determined as

$$\kappa(P_{edg,0} + \Delta P_{edg,nst}) + \lambda P_{apug} = \max\left(P_{nst}(t, \kappa)\right)$$
$$\implies \Delta P_{edg,nst} = \frac{\max\left(P_{nst}(t, \kappa)\right) - \kappa\, P_{edg,0} - \lambda P_{apug}}{\kappa}. \tag{148}$$

If the evaluation of Eq. 148 yields $\Delta P_{edg,nst} < 0$, then $\Delta P_{edg,nst} = 0$ is set. A similar subsequent power balance for the second condition yields the increment $\Delta P_{edg,st}$ as

$$\epsilon\, \kappa(P_{edg,0} + \Delta P_{edg,nst} + \Delta P_{edg,st}) + \epsilon\, \lambda P_{apug} = \max\left(P_{tot}(t, \kappa)\right)$$
$$\implies \Delta P_{edg,st} = \frac{\max\left(P_{tot}(t, \kappa)\right) - \epsilon\, \kappa\, (P_{edg,0} + P_{edg,nst}) - \epsilon\, \lambda P_{apug}}{\epsilon\, \kappa} \tag{149}$$

Here too, the condition $\Delta P_{edg,st} \geq 0$ is enforced. The required EDG capacity to satisfy both short-term and non-short-term loads corresponding to this capacity ratio κ is now computed as $P_{edg} = P_{edg,0} + \Delta P_{edg,nst} + \Delta P_{edg,st}$.

Repeating the above procedure for multiple failure scenarios with different capacity ratios κ and corresponding load profiles $P_{nst}(t, \kappa)$ and $P_{st}(t, \kappa)$ allows the identification of the most constraining sizing case for the generators. Within the scope of this dissertation, the following cases are considered:

1. Nominal flight condition: In this case, all EDGs are operational, and therefore $\kappa = 1$. Further, the APU is not being operated, and therefore $\lambda = 0$

2. Off-nominal flight condition: The failure of a single engine is considered. For the case of multiple generators per engine, it was shown in [57] that the engine failure scenario is more constraining than the failure of a single generator, since the latter removes the generating capacity of all generators on the failed engine. The capacity ratio in this case is given by $\kappa = 1 - 1/N_{eng}$

With the required increments in generator capacity known, the total increase in generator mass considering both EDGs and APUGs is computed as

$$\Delta M_{gen} = \frac{\Delta P_{edg} + \Delta P_{apug}}{(P/M)_{gen}}, \tag{150}$$

where $(P/M)_{gen}$ is the assumed power-to-mass ratio of generators. The nominal value of $(P/M)_{gen} = 2.8$ kVA/kg [146, 93] was varied in sensitivity analyses (Chapter 8).

5.3.3 AC-to-DC Power Conversion Equipment

The mass addition due to the incorporation of ATRUs, which are responsible for conversion of AC power to DC power, is estimated using the *peak* DC power and the power-to-mass ratio $(P/M)_{atru}$ for the ATRUs as follows:

$$\Delta M_{atru} = \frac{\sum_i P_{dc,i}^{peak}}{\eta_{atru} \, (P/M)_{atru}} \tag{151}$$

The peak DC power $\sum_i P_{dc,i}^{peak}$ is conservatively estimated by summing the peak power requirements of all electrified subsystems consuming DC power. Referring to the

EPGDS template of Fig. 32, these are seen to be electrified actuation functions, electrified ECS, and ETS (if installed). A fixed value of $\eta_{atru} = 0.97$ [147] is used for all analyses. The power-to-mass ratio, which is set to a nominal value of $(P/M)_{atru} = 1.54$ kW/kg [147], was varied during sensitivity analyses (Chapter 8).

5.3.4 Power Distribution Elements

In order to estimate the mass of power distribution elements, the dependency of the mass on nominal system voltage, voltage drops, power transmitted, and length is first analyzed. The current I flowing through a conductor is related to the voltage V_{nom} and power P_{in} (measured on the input side) by

$$P_{in} = V_{nom} \ I. \tag{152}$$

The voltage drop over a length L for this conductor is given by

$$\Delta V = IR = I\rho_e \frac{L}{A_{cs}}, \tag{153}$$

where R is the electrical resistance, ρ_e the electrical resistivity, and A_{cs} the cross-sectional area. Combining these two relationships, the cross-sectional area may be expressed as

$$A_{cs} = \frac{P_{in} \ \rho_e}{V_{nom} \ (\Delta V/L)}. \tag{154}$$

It follows that if ρ_m is the material density of the conducting cable, then its mass M_{cbl} is given by

$$M_{cbl}(P_{in}, L) = \rho_m \ A_{cs} \ L = \left[\frac{\rho_m \ \rho_e}{V_{nom} \ (\Delta V/L)} \right] P_{in} \ L = \mathcal{K}_{cbl} \ P_{in} \ L, \tag{155}$$

in which $(\Delta V/L)$ may be thought of as the maximum permissible voltage drop per unit length and the constant $\mathcal{K}_{cbl}$ can be shown to have units of kg/(VA.m) (kilogram per volt-ampere per meter). It is clear from Eq. 155 that the mass of a conductor carrying a given power over a given length can be reduced by (i) using a material of low

density and low electrical resistivity, (ii) using a high nominal transmission voltage[3], and (iii) allowing a higher permissible voltage drop per unit length. Further, replacing $P_i = V_{nom} I$ in Eq. 155 leads to the additional result

$$M_{cbl}(P_{in}, L) = \left[\frac{\rho_m \, \rho_e}{(\Delta V / L)} \right] I \, L = \mathcal{K}'_{cbl} \, I \, L. \tag{156}$$

Considering a conducting cable that runs for a length ℓ_0 from a source to a common distribution point and then splits into two cables that run lengths ℓ_1 and ℓ_2 to two consumers with maximum current requirements I_1 and I_2, application of Kirchoff's junction law yields that the current through the common length is $I_0 = I_1 + I_2$. Further, if $L_1 = \ell_0 + \ell_1$ and $L_2 = \ell_0 + \ell_2$ denote the total length of cabling from the source to the two consumers (including the common length), then using the relationship of Eq. 156, the total mass M of this cable layout may be computed as

$$
\begin{aligned}
M &= \mathcal{K}'_{cbl} \, I_0 \, \ell_0 + \mathcal{K}'_{cbl} \, I_1 \, \ell_1 + \mathcal{K}'_{cbl} \, I_2 \, \ell_2 \\
&= \mathcal{K}'_{cbl} \left\{ (I_1 + I_2) \, \ell_0 + I_1 \, \ell_1 + I_2 \, \ell_2 \right\} \\
&= \mathcal{K}'_{cbl} \left\{ I_1(\ell_0 + \ell_1) + I_2(\ell_0 + \ell_2) \right\} \\
&= \mathcal{K}'_{cbl} \, I_1 L_1 + \mathcal{K}'_{cbl} \, I_2 L_2
\end{aligned}
\tag{157}
$$

The above result (equivalent to that of Eq. 139 for HPGDS) establishes that even if dedicated cabling does not exist from a source to each consumer, it is sufficient to consider the direct (non-exclusive) length from a source to a consumer for the purpose of computing cable mass. The direct lengths of the power distribution elements are automatically computed from the 3-D geometric model of the aircraft (using Eq. 136) subsequent to the architecting of the EPGDS (described in § 5.1.1 and § 5.1.2).

It is possible to compute the parameters $\mathcal{K}_{cbl}$ or $\mathcal{K}'_{cbl}$ using information regarding the necessary mass and electrical properties of conducting materials, nominal system voltage, and permissible voltage drops. However, attempting to compute the mass

---

[3]Hence the recent trend towards the use of higher voltage networks for aircraft

of power distribution elements in this manner would be overly simplistic due to the following reasons:

1. This estimate would be valid for a single conducting wire, whereas in aircraft electrical networks bundles of wires are used. For example, a 3-phase AC system with a neutral would have four wires, a 3-phase AC system with no neutral would have three wires [148]

2. The estimate would not account for the weight of insulating material. In aircraft wiring, sufficient insulation has to be provided in order to prevent discharges due to high voltages. Further, the amount of insulation typically increases with the voltage level [148]

Christou et al. [148] investigated the choice of optimal voltages for MEA wiring systems, in which the effect of voltage level on the necessary insulation thickness and the multiplicity of wires within a bundle for different AC and DC systems were explicitly accounted for. The authors attempted to optimize a wiring system while considering maximum power transfer and wiring weight with constraints related to the occurrence of discharges at high voltages. As part of their results, they presented the power-to-weight ratio (power transfer capability of the wire per unit mass) as a function of the voltage rating. This has the units of kVA.m/kg (kilo volt-ampere meter per kg), the inverse of the units for $\mathcal{K}_{cbl}$. Based on their results, $1/\mathcal{K}_{cbl}^{230\text{VAC}} = 64.6$ kVA.m/kg and $1/\mathcal{K}_{cbl}^{\pm270\text{VDC}} = 86.8$ kVA.m/kg were identified for the 230 VAC and ±270 VDC networks considered. It is important to note that this method of selecting $\mathcal{K}_{cbl}$ *does* allow the effect of wire bundles and insulation to be accounted for in the effective power-to-mass (or power-to-weight) ratio of the cabling.

The actual wiring length is likely to be somewhat greater than the computed wiring length due to the need to avoid obstacles whose positions become defined only later in the design. Also, the mass estimation method does not directly account for

the mass of connectors and other fittings required in a wiring system. Therefore, an installation factor κ_{inst} is used to modify the cabling mass estimation:

$$M_{cbl}(P_{in}, L) = \kappa_{inst}\ \mathcal{K}_{cbl}\ P_{in}\ L. \tag{158}$$

It is clear from the above relationship that the mass of cabling is subject to uncertainty as a result of possible uncertainties associated with each of the four terms on the right-hand side. The impact of this at the architecture level is assessed subsequently through a sensitivity analysis (Chapter 8).

5.3.5 Power Dissipation

Although the EPGDS does not directly consume power, there is power *dissipation* as a result of component inefficiencies and losses in the distribution system. There is, therefore, a net aircraft-level shaft-power off-take on account of the dissipation. The magnitude of power dissipated will in general increase with the magnitude of power processed by the EPGDS, and therefore is likely to be more substantial as the degree of subsystem electrification increases.

The total power dissipation is essentially the difference between the shaft-power input to the EPGDS generators and the total power delivered to the power consuming subsystems in either AC or DC form, respectively $\sum P_{ac}(t)$ and $\sum P_{dc}(t)$. Assuming an overall efficiency of $\eta^{(i)}$ for a component, the following relationships exist between the power input, power output, and power dissipation (loss) of that component:

$$\eta^{(i)} = \frac{P_{out}^{(i)}}{P_{in}^{(i)}}, \qquad P_{loss}^{(i)} = P_{in}^{(i)} - P_{out}^{(i)} = P_{out}^{(i)}\left(\frac{1}{\eta^{(i)}} - 1\right) \tag{159}$$

As per the assumed template for the EPGDS (Fig. 32), shaft-power entering the EPGDS control volume encounters the following inefficiencies en route to the AC and DC power consumers:

1. Between generator input and AC power consumers: The generators with overall efficiency η_{gen}, the power feeders with overall efficiency η_{fdr}, and the AC

distribution system (cabling/wiring) with assumed overall efficiency η_{ac}

2. Between generator input and DC power consumers: The generators and feeders listed above, the ATRU with overall efficiency η_{atru}, and the DC distribution system with assumed overall efficiency η_{dc}

Through successive applications of the relationships of Eq. 159 to these lossy components starting from the power consumers and working upstream to the generator input, it is easy to see that the total dissipation of the EPGDS is given by

$$P_{EPGDS}(t) = \left(\frac{1}{\eta_{gen} \ \eta_{fdr} \ \eta_{ac}} - 1 \right) \sum P_{ac}(t) + \left(\frac{1}{\eta_{gen} \ \eta_{fdr} \ \eta_{atru} \ \eta_{dc}} - 1 \right) \sum P_{dc}(t)$$

(160)

The component efficiencies in the above relationship are summarized in Table 23 and were identified from [147] and the permissible voltage drops listed in [149]. For a distribution system with nominal source voltage V_{ns} and a permissible voltage drop ΔV, the overall efficiency is approximated as $\eta = 1 - \Delta V / V_{ns}$. This relationship is used to obtain the AC and DC distribution system efficiencies η_{ac} and η_{dc}.

Table 23: Summary of EPGDS component efficiencies

Component	Efficiency	Symbol	Source/Comments
VF Generator	0.92	η_{gen}	[147]
Power feeders	0.98	η_{fdr}	based on [149]
ATRU	0.97	η_{atru}	[147]
AC distribution	0.95	η_{ac}	based on [149]
DC distribution	0.98	η_{dc}	based on [149]

5.4 Pneumatic Power Generation and Distribution System (PPGDS)

With reference to the PPGDS architecture shown in Fig. 33 and Fig. 34, the analysis control volume of the PPGDS is considered to include the *Precooler Heat Exchangers* (PHXs) and all pneumatic ducting originating at either the PHX exit or

the engine bleed ports and terminating at the locations of the pneumatic consumers. In case a subsystem architecture contains no pneumatic users, the PPGDS is deleted entirely. The mass estimation for the PHXs and pneumatic ducting is addressed in the subsequent sections.

5.4.1 Precooler Heat Exchanger (PHX)

There may be significant variation in the temperature of the engine bleed air depending on the engine throttle setting, the stages from which the bleed air is extracted, and the port selection logic employed. The function of the PHX is to down-regulate the bleed air to a pre-defined target temperature. The PHX is typically an air-to-air cross-flow heat exchanger that is integrated into the engine nacelle and uses air extracted from the fan stage as the cooling stream. The mass flow rate of the fan air is modulated by the FACV (Fig. 33) in response to feedback from a sensor that measures the temperature of the down-regulated air exiting the PHX. The exit temperature is typically limited to 200 °C, with high temperature and low temperature warnings annunciated if the detected temperature is above or below around 250 °C and 150 °C respectively [150, 151].

The sizing condition for the PHX is the case where the maximum amount of thermal energy has to be removed from the hot (bleed) stream. Therefore, it may be hypothesized that this would occur during a combination of the following: (i) high throttle settings that lead to high temperatures for bleed air entering the PHX, (ii) high bleed air demands from consuming subsystems, and (iii) additional demands imposed by failures of other pneumatic channels (either engine or bleed system failures). This hypothesis is substantiated by detailed simulations of PHX performance that were presented in [56], in which the takeoff condition with failure was identified as the constraining sizing case. Based on the above, a simple relationship for estimating PHX mass is used for twin-engines and four-engined

aircraft, subject to the assumption that the following remain invariant with aircraft size: (i) the heat exchanger technology level, (ii) the inlet temperatures of the hot and cold streams in the sizing case, and (iii) the target exit temperature of bleed air from the PHX. Subject to these, the PHX mass is estimated as

$$M_{phx} = \kappa_{phx} \frac{\max\left(\sum_i \dot{m}_b\right)}{\left(\frac{n_{eng}}{2}\right)}, \qquad \Longrightarrow M_{phx,tot} = n_{eng} \, M_{phx}, \qquad (161)$$

in which the summation is applied to all consumers of precooled bleed air, and the denominator $n_{eng}/2$ ensures that the consumers' bleed requirements can be satisfied with only half of the total pneumatic generation capacity available subsequent to failures. The constant κ_{phx} was identified by solving Eq. 161 for κ_{phx} for the case of a known precooler weight [152]. This yielded a value of $\kappa_{phx} = 17.33$ kg/(kg/s).

Due to the nature of the relationship shown in Eq. 161, the estimated PHX mass automatically reduces if the maximum bleed air demanded by consumers of precooled air reduces. This may occur if a consumer's bleed air requirement reduces (e.g., if pneumatic *running-wet* ice protection is used instead of pneumatic *evaporative*), or if the requirement is eliminated completely through electrification.

In addition to the fuel consumption penalty imposed by the extraction of bleed air from the compressor stages, an additional penalty is imposed due to the extraction of fan air for the purpose of down-regulating the temperature of this bleed air. Both these effects may be taken into consideration while computing the overall fuel consumption penalty due to bleed air extraction, as described subsequently in §7.2.

5.4.2 Pneumatic Ducting

The mass of pneumatic ducting is proportional to the duct length, but is also influenced by the mass flow rate of air through the duct, which influences the duct internal diameter. In addition to this, the fact that the air flowing through the duct is at an elevated temperature and pressure has to be taken into account. To capture these dependencies but also allow an estimate of the duct mass with knowledge of

only a limited number of parameters, the approach described subsequently is taken.

From simple geometry considerations, the mass per unit length M/L of a thin-walled pneumatic duct of inner diameter D_i and wall thickness t_w which is made of a material of density ρ is given by

$$\frac{M}{L} = \rho \frac{\pi}{4} \left\{ (D_i + t_w)^2 - D_i^2 \right\} = \rho \frac{\pi}{4} \, t_w \, (t_w + 2D_i). \tag{162}$$

Using the continuity equation and the equation of state, the duct internal diameter D_i can be related to the mass flow rate of air $\dot{m}$ of air flowing through the duct as

$$\dot{m} = \rho_a \, A_{cs} \, v_{max} = \left(\frac{p_{nom}}{R_a T_{nom}} \right) \left(\frac{\pi}{4} D_i^2 \right) v_{max},$$

$$\implies D_i = \sqrt{\frac{4}{\pi} \left(\frac{R_a T_{nom}}{p_{nom} v_{max}} \right) \dot{m}} \tag{163}$$

where R_a is the gas constant for air, T_{nom} is the nominal temperature of the air flowing through the duct, p_{nom} the nominal internal pressure, and v_{max} is the maximum permissible velocity of air flow based on considerations of allowable pressure drop.

The wall thickness t_w may be determined based on the permissible tensile stress σ_t corresponding to the operating temperature and the maximum pressure p_{max} as

$$t_w = \frac{p_{max} \, D_i}{2 \left\{ \sigma_t - p_{max}(1 - Y) \right\}} = \frac{p_{max} \, D_i}{2\sigma_{eff}}, \tag{164}$$

where a value of $Y = 0.4$ is used for non-ferrous metals [153]. The wall thickness relationship above originally uses the outer diameter D_o, but here it has been modified to use the internal diameter D_i through the relationship $D_o = D_i + 2t_w$.

Substituting Eq. 163 and Eq. 164 into Eq. 162 yields the mass of a duct of length L carrying a mass flow rate $\dot{m}$ as being

$$M_{duct}(\dot{m}, L) = \kappa_{inst} \left[\rho \left(\frac{p_{max}}{2\sigma_{eff}} \right) \left(\frac{p_{max}}{2\sigma_{eff}} + 2 \right) \left(\frac{R_a T_{nom}}{p_{nom} v_{max}} \right) \right] \dot{m} \, L$$

$$= \kappa_{inst} \, \kappa_{duct} \, \dot{m} \, L, \tag{165}$$

where κ_{inst} is an installation factor that accounts for (i) the weight of fittings and attachments that were not explicitly accounted for and (ii) for the fact that the

Table 24: Summary of constant parameters for duct mass estimation

Parameter	Value	Source/Comments
p_{nom}	330 kPa	Refs. [151, 150]
p_{max}	3.0 P_{nom}	FAR §25.1438 [77]
T_{nom}	200 °C	Ref. [151]
v_{max}	30 m/s	Ref. [155]
ρ	4,510 kg/m^3	Ti Gr.2/Gr.3, Ref. [153]
σ_t	49.5 MPa	mean for Ti Gr.2 & Gr.3 at T_{nom} [153]

actual ducting length is likely to be longer than the computed one due to installation issues. This work utilizes a conservative value of $\kappa_{inst} = 1.5$. A summary of parameters occurring in Eq. 165 is shown in Table 24. While the actual pressure and temperature of bleed air flowing through the ducts varies with time and location, κ_{duct} is determined using nominal values [151]. The pressure p_{max} used for determining the wall thickness t_w is set in accordance with FAR §25.1438 which requires that the integrity of ductwork be verified at burst pressures equal to three times the normal working pressure. Both Grade 2 and Grade 3 titanium are found in aircraft pneumatic systems [154], and σ_t is set to the mean value of their permissible tensile stresses at a temperature of T_{nom} [153]. The effect of duct mass on subsystem architecture performance is tested subsequently through a sensitivity analysis (Chapter 8).

5.4.3 Power Dissipation

The fuel consumption penalty as a result of bleed air extraction depends on the mass flow rate of bleed air extracted and its thermodynamic state at the point of extraction. Since it is assumed that there is no leakage within the PPGDS, there is no direct bleed air consumption attributable to the PPGDS. The mass flow rate of bleed air entering the PPGDS analysis control volume also exits that control volume to supply the pneumatic power consumers. Thus, the bleed air fuel penalties are accounted for under the pneumatic power consuming subsystems and not the PPGDS.

5.5 Mechanical Power Generation and Distribution System (MPGDS)

The selected control volume for the MPGDS only contains the accessory gearbox. The modeling of this subsystem is limited to (i) the estimation of mass changes of the gearbox with shaft-power demand and (ii) accounting for the mechanical losses from power transmission through the gearbox. For the same technological SOTA, the increased shaft-power requirements that arise as a result of subsystem electrification will result in an increase in the mass of the gearbox as well as the magnitude of the power dissipated within the gearbox.

5.5.1 Mass Estimation

The mass of the gearbox is estimated using an empirical correlation developed at NASA using actual gearbox weight data [102], where the gearbox mass is a function of the maximum delivered output power and the gear ratio:

$$
\begin{aligned}
W_{gb} \ [\text{lb}] &= -37.4262 + 116.3297 \, \mathcal{K}_{gb}, \\
\mathcal{K}_{gb} &= \left(\frac{hp}{RPM_{out}} \right)^{0.75} \left(\frac{RPM_{in}}{RPM_{out}} \right)^{0.15}.
\end{aligned} \tag{166}
$$

The horsepower (hp) in Eq. 166 is determined based on the peak shaft-power requirement accounting for both electrical power and hydraulic power (if any). The input and output RPMs are set based on data provided in engine type certification data-sheets (e.g., [156]) and considering high shaft-power extraction at lower rotational speeds, which results in larger torques applied to the gearbox.

5.5.2 Power Dissipation

The power dissipation of the MPGDS due to mechanical losses within the gearbox is estimated as

$$
P_{MPGDS}(t) = \left(\frac{1}{\eta_{gb}} - 1 \right) \left(\sum P_{elec}(t) + \sum P_{hyd}(t) \right) \tag{167}
$$

in which the gearbox efficiency is assumed to be $\eta_{gb} = 0.97$ for a modern high-performance gearbox [147]. Since the summation of shaft-power requirements $P_{spx}(t)$ is performed over all subsystems consuming or dissipating hydraulic or electric power, the dissipation as computed above is for the entire MPGDS which includes multiple gearboxes.

5.6 *Chapter Summary*

The modeling approaches for the Hydraulic Power Generation and Distribution System (HPGDS), Electric Power Generation and Distribution System (EPGDS), Pneumatic Power Generation and Distribution System (PPGDS), and Mechanical Power Generation and Distribution System (MPGDS) were described in this chapter. For each, the sizes and masses of the major components are determined based on the secondary power requirements of the power consuming subsystems (addressed in Chapter 4) and relevant sizing scenarios. For the HPGDS, EPGDS, and MPGDS, the power dissipation occurring as a result of component inefficiencies and distribution losses is also accounted for. These quantities are fed back into the aircraft sizing and mission performance analysis to evaluate the impact of the subsystem architecture on aircraft-level and mission-level metrics of interest.

CHAPTER VI

COMPARISON BETWEEN COMPETING SUBSYSTEM SOLUTIONS AND ARCHITECTURES

This chapter addresses Research Question 1 and tests Hypothesis 1, both of which are re-stated below:

- **Research Question 1:** *How can the performance of competing solutions for a particular subsystem or competing subsystem architectures be compared at the vehicle and mission level using computationally inexpensive sizing and analysis methods that require only limited information regarding the aircraft design?*

Hypothesis 1: *The differences between competing subsystem solutions or competing subsystem architectures with regard to suitable vehicle-level and mission-level metrics may be quantified within the framework of aircraft conceptual design by using an integrated sizing and analysis environment if it can be demonstrated that within said environment:*

(a) *the initial sizes and characteristics of major components in individual power consuming subsystems can be determined based on the definition of their functional requirements in conjunction with only the available or estimable aircraft and mission parameters and constraints*

(b) *the initial sizes and characteristics of additional components in power generation and distribution subsystems can be determined based on the identified requirements of the power consuming subsystems and the direct or heuristic identification of limiting, constraining, or off-nominal operating conditions*

209

(c) *the mission performance analysis reflects the direct and indirect effects of the subsystem architectures on the performance of the propulsion system*

(d) *relevant dependencies can be established among subsystem-level and aircraft-level parameters to allow the simultaneous re-sizing of both parameter sets based on logically defined re-sizing rules*

Two scenarios are studied in this context. The first (§6.1) analyzes the aircraft-level and mission-level impact of two competing solutions for a single subsystem (chosen to be the ECS). The second (§6.2) analyzes the aircraft-level and mission-level impact of two competing subsystem architectures: conventional versus All Electric. The two scenarios are analyzed for the SSA, LTA, and VLA baselines.

For the purpose of conducting these two analyses, the impact of shaft-power and bleed air extraction on the engine fuel consumption (fuel flow rate) are modeled using simple relationships that provide first approximations of the magnitude of the off-take penalties. The incremental fuel flow $\Delta \dot{w}_{f,spx}$ due to total shaft-power extraction of P_{spx} is modeled based on the k_p^* approach of Scholz [157]:

$$\Delta \dot{w}_{f,spx} = \dot{w}_{f,0} \; k_p^* \; \frac{P_{spx}[kW]}{N_{op,eng} \; T_{SL}[kN]}, \qquad \text{(per engine)} \qquad (168)$$

in which $\dot{w}_{f,0}$ is the basic fuel flow rate (without shaft-power extraction) for each of $N_{op,eng}$ engines which are assumed to contribute equally to the total shaft-power P_{spx}. The constant k_p^* was given as $k_p^* = 0.0094$ N/W as an average of the penalties computed at flight altitudes of 0 ft, 10,000 ft, 20,000 ft, and 35,000 ft at Mach numbers of 0.30, 0.60, and 0.85 at maximum continuous thrust [157].

The incremental fuel flow penalty $\Delta \dot{w}_{f,bx}$ due to bleed air extraction $\dot{w}_{bld} = \dot{m}_{bld} \, g$ per engine is computed following the method of SAE AIR 1168/8 [136] as

$$\Delta \dot{w}_{f,bx} = 0.0335 \left(\frac{T_{tet}[{}^\circ R]}{2000} \frac{\dot{w}_{bld}}{N_{op,eng}} \right), \qquad \text{(per engine)} \qquad (169)$$

in which T_{tet} is the turbine entry temperature, for which this dissertation uses a representative value of 2,400°R.

Off-take penalty relationships such as Eq. 168 and Eq. 169 are useful since they require little additional information other than the time variation of the shaft-power and bleed air off-takes. On the other hand, the limitation of these relationships is that these are general ones that do not apply to any one engine in particular and do not explicitly account for the variation of the magnitude of off-take penalties with flight condition (altitude, Mach number, and engine power setting). Therefore, they are suitable for providing approximate indications of the fuel penalties due to off-takes, but are sufficient for pursuing the intent of this chapter.

6.1 Comparison of Two Competing Subsystem Solutions - Pneumatic vs. Conventional ECS

To verify whether the developed integrated sizing and analysis environment can be used to differentiate between two competing technologies within a single power consuming subsystem's architecture, the electrification of the Environmental Control System (ECS) is considered. The architectures of all other power consuming subsystems remain unaffected. However, electrification of the ECS also requires changes to the Pneumatic Power Generation and Distribution System (PPGDS) and the Electrical Power Generation and Distribution System (EPGDS).

As mentioned in Chapter 4, the electrification of the ECS involves substantial changes to the subsystems architecture and also to the nature of secondary power off-takes, which are summarized below:

1. Addition of mass: A significant addition of mass occurs due to the incorporation of Cabin Air Compressors (CACs), motors, and power electronics into the ECS. Further, EPGDS mass increases due to higher rating electrical generators and power transformation devices and through the addition of electrical cabling

2. Reduction of mass: The mass of the PPGDS reduces due to the elimination or down-sizing of pneumatic ducting.

3. Reduction in bleed air off-take: The bleed air off-takes from the engine are significantly reduced. Due to this, the engine TSFC reduces

4. Increase in shaft-power off-take: There is a significant increase in the shaft-power extraction from the engine, since the electric ECS must be provided substantial electric power. Due to this, the engine TSFC increases

5. Increase in ram drag: The air supplied to the cabin must be admitted through ram air inlets instead of being bled from the engine, which results in an increase in ram drag

The overall consequence of electrification of the ECS depends upon the relative magnitudes of the impacts listed above. The consequence may be assessed using (i) subsystem-level metrics such as the masses of the ECS, EPGDS, and PPGDS, (ii) aircraft-level metrics such as the Operating Empty Weight (OEW), and (iii) mission-level metrics such as the block fuel or the ramp weight.

Using the Total Fuel Impact (TFI), the net impact on mission fuel consumption may be further decomposed and attributed to the individual causal factors (system mass, secondary power requirements, and drag increments) of the subsystems affected (in this case ECS, EPGDS, and PPGDS). In the subsequent sections, these analyses are presented for the SSA, LTA, and VLA baselines.

6.1.1 ECS Electrification for SSA

The ECS, EPGDS, and PPGDS architectures are established within the *Subsystem Architecting* module based on the heuristic architecting rules described in Chapter 5. For SSA-00000, the conventional baseline with pneumatic ECS, the PPGDS architecture is shown in Fig. 36. Bleed air is extracted from both main engines and ducted through wing ducts into the pneumatic manifold in the fuselage area. The pneumatic system is divided into left and right systems, which are interconnected
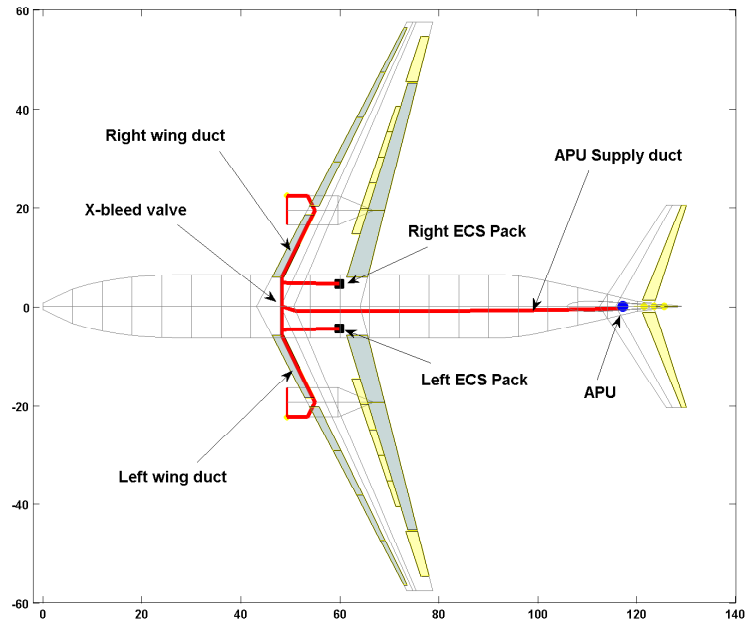
Figure 36: Conventional (pneumatic) ECS architecture (SSA-00000)
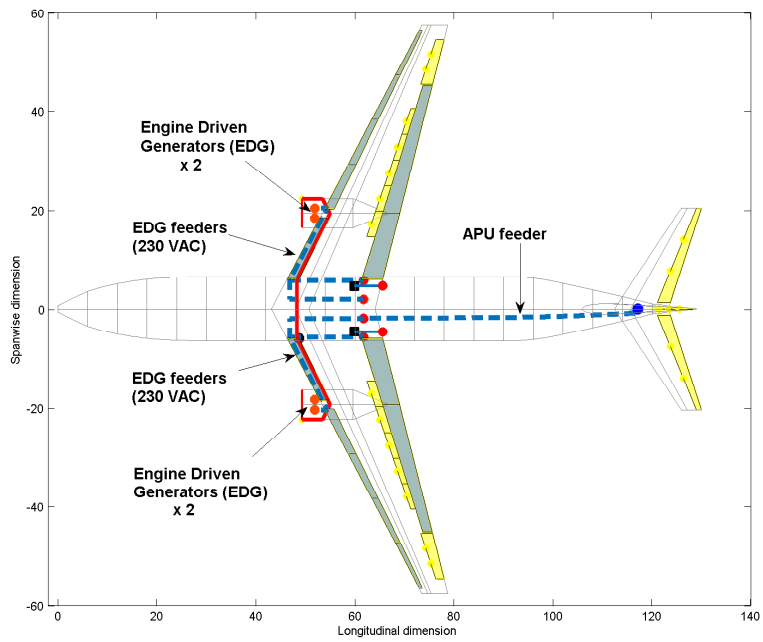
Figure 37: Electric ECS architecture (SSA-00010)
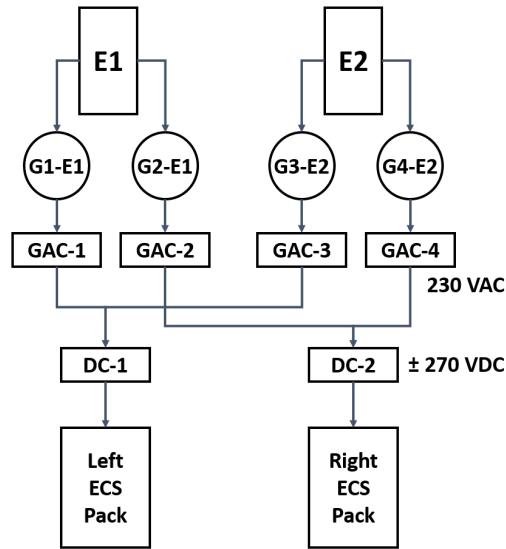
Figure 38: EPGDS architecture for electric ECS (SSA-00010)

through a cross-flow valve so that one system can supply users on the other side in case of a failure in the other system. Under nominal operating conditions, the left system supplies the left wing IPS and the left ECS pack. In addition, since the APU must be able to support ECS operation on the ground, an APU supply duct runs from the aft fuselage to the central pneumatic manifold[1].

For the electric ECS design, SSA-00010, the heuristic architecting rules initialize two electrical generators per engine due to the significantly higher electric load. For each generator, the generated AC power is received by a dedicated AC bus and subsequently transformed by ATRUs into DC power to supply the ECS. The resulting EPGDS architecture is shown in Fig. 37 and Fig. 38. Since the APU must still be able to power the ECS on the ground, an APU feeder runs from the aft fuselage to the main electrical/electronics bay to supply the AC system. Thus, it is clear that ECS electrification changes the EPGDS and PPGDS architectures considerably.

The overall analysis approach has already been described previously, and only

---

[1]Although the engine starting function is not covered within this dissertation, this same APU supply duct is used in a pneumatic starting arrangement for starting the first main engine.

a brief summary of relevant details for this particular case is presented. For both the architectures, the ECS, being the power consuming subsystem, is evaluated first. This results in computation of ECS mass, secondary power requirements (bleed or shaft-power), and ram air requirements over the course of the defined mission (§4.7).

The two affected power generation and distribution subsystems, the PPGDS and the EPGDS, are evaluated subsequently. In both cases, the lengths of the power distribution elements are established based on the architecting rules and the geometric model of the aircraft. The PPGDS sizing module uses ducting lengths and the mass flow rate requirements of the residual pneumatic power users to estimate the total mass of ducting and precoolers (§5.4). In a similar manner, the EPGDS sizing module determines the masses of the electrical cabling, generators, and power transformation devices based on the electrical power requirements of the ECS and consideration of relevant failure scenarios (§5.3).

The evaluation of the ECS, PPGDS, and EPGDS results in updates for the vehicle mass, secondary power requirements, and ram air requirements becoming available. This information is then used to re-evaluate the vehicle's mission performance (as described in §3.2.5). Finally, the computation of the TFI and TWI of individual subsystems completes the analysis.

Figure 39 summarizes how the electrification of ECS for the SSA affects subsystem-level metrics such as the masses of the ECS, PPGDS, and EPGDS, an aircraft-level metric such as the empty weight, and mission-level metrics such as ramp weight and block fuel. As evident from Fig. 39, as a result of electrification of the ECS, there is a 70 % increase in the mass of the ECS itself. This is due to the addition of the CACs, electric motors, and power electronics. The relative contributions of each of these is shown in Table 25. There is a significant reduction in the mass of the PPGDS. This is due to the elimination of the APU supply duct, the down-sizing of the wing pneumatic ducts, and the down-sizing of the precoolers. The

% Mass Δs for ECS Electrification - SSA

All %'s relative to corresponding baseline quantities
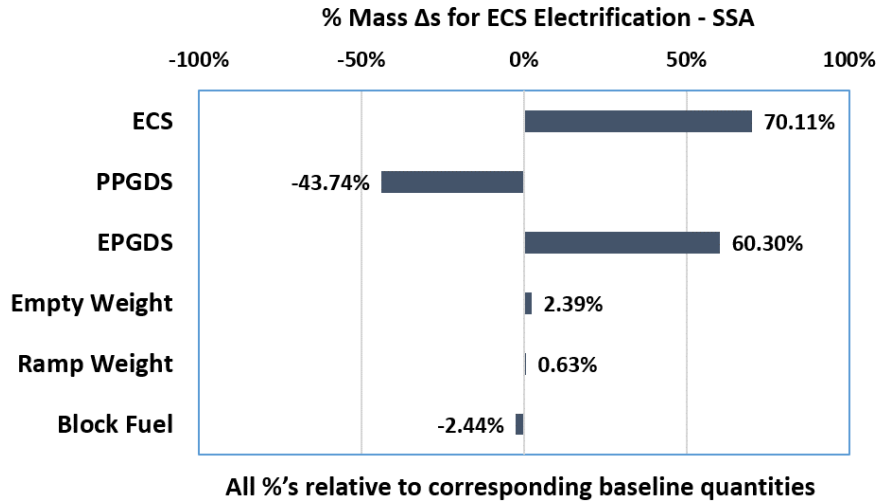
Figure 39: Summary of ECS electrification effects for SSA (SSA-00000 vs. SSA-00010)

Table 25: Detailed mass-Δ investigation for ECS, EPGDS, and PPGDS

ECS		EPGDS		PPGDS	
CACs	+ 18.4	Gen	+ 25.3	Ducting	-28.3
Motors	+ 24.9	Cables	+ 17.8	PHX	-15.4
Pwr. Elec.	+ 26.8	Pwr. Conv.	+ 17.2		
Total	+ 70.1	Total	+ 60.3	Total	- 43.7

relative contributions of ducting and precooler masses are shown in Table 25. There is considerable mass addition to the EPGDS, in order to support the large electrical demand of the ECS. The mass addition is due to higher higher-capacity generators, AC-to-DC power conversion equipment, and also feeders and cables. The relative contributions of the EPGDS components are also shown in Table 25.

The mass additions to the ECS and EPGDS exceed the mass reduction of the PPGDS, and thus overall there is a 2.39 % increase in the OEW of the aircraft. However, despite the overall increase in aircraft OEW, the electrification of the ECS results in a predicted fuel burn reduction of 2.44 %. To investigate the relative contribution of the subsystems to the overall fuel burn reduction, the Total Fuel

Table 26: Aircraft and mission-level impact of ECS electrification for SSA

Sub -system	%Δ Fuel due to				%Δ Total Fuel Imp.	%Δ Weight	%Δ Total Wt. Imp.
	Weight	SPX	BX	Drag			
ECS	10.8	13.4	-78.0	8.5	-45.3	70.1	-4.3
PPGDS	-43.7	0	0	0	-43.7	-43.7	-43.7
EPGDS	61.6	0	0	0	61.6	60.3	60.6
Aircraft/Mission-level impact					BF: -2.44	EW: 2.39	RW: 0.63

Impact (TFI) and Total Weight Impact (TWI) breakdown may be analyzed, as shown in Table 26. The quantities in this matrix are expressed in terms of percentage deltas (%-Δ) relative to the following base quantities: (i) The change in fuel penalty of the MEA due to weight, shaft-power, bleed air, and direct drag are all expressed as a %-Δ relative to the baseline architecture's TFI. Thus, for each row, the elements of the first four columns add up to the element in the fifth column. (ii) The change in each subsystem's mass is expressed as a %-Δ relative to the subsystem's mass in the conventional architecture. The figures in this column are identical to those in Fig. 39. (iii) The TWI is expressed as a %Δ relative to the baseline subsystems' TWI.

It is seen from Table 26 that the increase in mass of the ECS leads to a corresponding increase in the fuel penalty incurred over the course of the mission due to this extra mass. Since the cabin supply air is admitted through dedicated ram air inlets in case of electric ECS, this results in additional direct (ram) drag. However, the fuel burn reduction due to the elimination of bleed air off-take for the ECS is greater in magnitude than the fuel burn penalty due to the additional shaft-power required to supply its electrical requirement. This results in a significant reduction in the TFI of the electric ECS relative to the conventional (pneumatic) ECS. The predicted fuel savings is of sufficient magnitude to offset the increase in ECS mass and result in an overall favorable TWI. For the PPGDS and EPGDS, the TFI and TWI are driven directly by their respective mass deletion and addition.
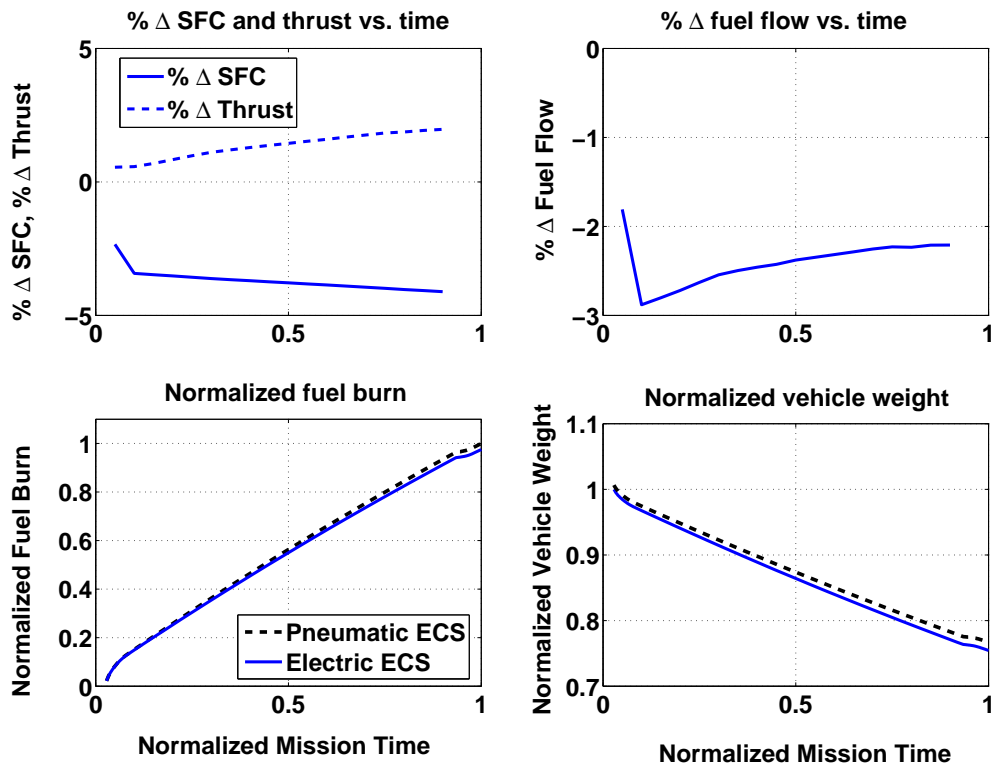
Figure 40: Comparison of thrust, TSFC, fuel flow, fuel burn, and vehicle weight over the course of the mission (SSA-00010 relative to SSA-00000)

Table 26 provides a gross summary of the performance of SSA-00010 versus SSA-00000 over the entire mission. To obtain more insight into the relative performance of one architecture against the other, the time evolution of these parameters over the mission must be examined. This is shown in Fig. 40, from which it can be seen that the replacement of ECS bleed air requirements with shaft-power requirement results in an improvement (reduction) in the TSFC. However, it can also be seen from the normalized vehicle weight comparison that SSA-00010 is heavier than SSA-00000 throughout the mission. As a result of this extra mass (the result of increased equipment weight) and additional ram drag for the ECS, the thrust requirement of SSA-00010 is higher than that of the baseline. The magnitudes of the increased thrust and the decreased fuel flow are such that overall there is a reduction in the required fuel flow rate of SSA-00010 which ultimately results in a mission

218
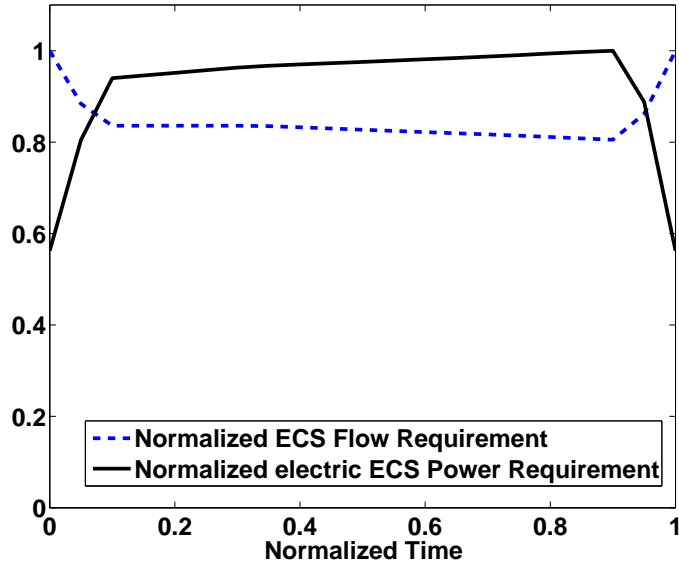
Figure 41: ECS mass flow and power requirements over mission

fuel burn reduction. An interesting observation regarding the power requirements for the ECS may be made from Fig. 41, from which it is seen that the mass flow rate requirement (for both pneumatic ECS and electric ECS) reduces with increasing altitude (due to the pressurization schedule). The mass flow rate is directly related to the bleed air penalty for the pneumatic ECS. Despite the reduction in the required mass flow rate, there is an increase in the electrical power consumed by the CACs with altitude, due to an increase in the required CAC pressure ratio to bring ambient air to the scheduled CAC discharge pressure.

6.1.2 ECS Electrification for LTA and VLA

The results for ECS electrification for the LTA and the VLA are presented in Fig. 42 and Fig. 43 respectively. In these cases, there is an even more significant addition of mass to the ECS. The total compression power requirement increases with the minimum required mass flow rate, which in turn is directly proportional to the number of cabin occupants. The higher compression power requirement results in correspondingly higher masses for CACs, drive motors, and power electronics.

% Mass Δs for ECS Electrification - LTA

ECS	65.09%
PPGDS	-50.68%
EPGDS	102.41%
Empty Weight	1.72%
Ramp Weight	-0.64%
Block Fuel	-3.08%

All %'s relative to corresponding baseline quantities
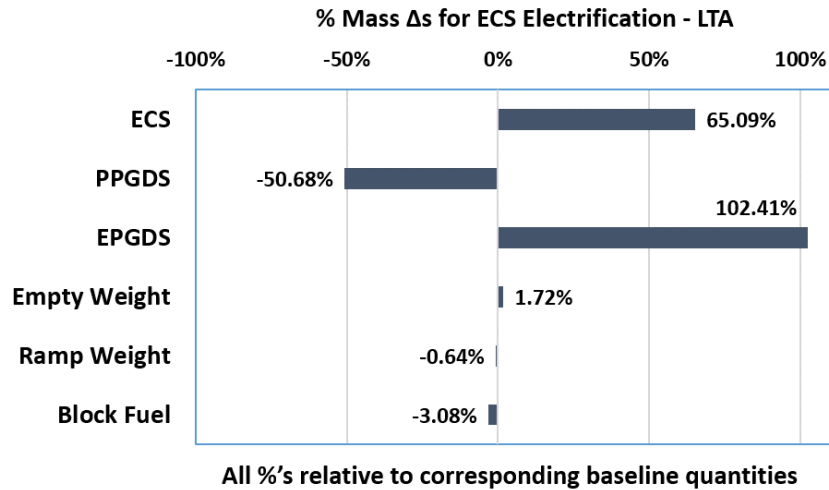
Figure 42: Summary of ECS electrification effects for LTA (LTA-00000 vs. LTA-00010)

% Mass Δs for ECS Electrification - VLA

ECS	91.28%
PPGDS	-79.37%
EPGDS	87.33%
Empty Weight	1.94%
Ramp Weight	-0.90%
Block Fuel	-4.01%

All %'s relative to corresponding baseline quantities
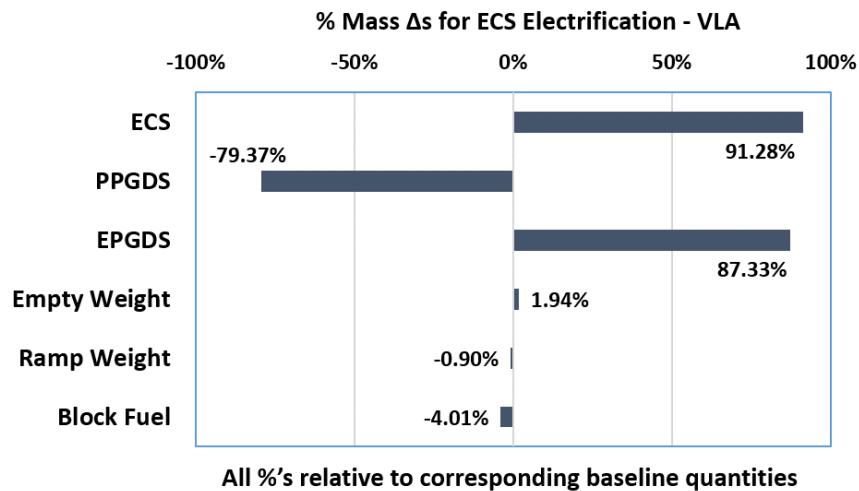
Figure 43: Summary of ECS electrification effects for VLA (VLA-00000 vs. VLA-00010)

A significantly larger percentage of the baseline PPGDS mass is eliminated for the LTA and the VLA compared to the SSA. It was established in Chapter 5, Sec. 5.4 that the mass of pneumatic ducting was approximately proportional to the product of mass flow rate and ducting length ($\dot{m}\,L$). In case of the VLA and LTA, the contribution of the ECS to the summation $\sum(\dot{m}\,L)$ is greater, due to the increasing ratio of ECS mass flow requirements to IPS mass flow requirements.

220

6.2 Comparison of Two Competing Subsystem Architectures - All Electric vs. Conventional

In §6.1, the case of electrification of one power consuming subsystem (ECS) was considered, along with the necessary changes to two power generation and distribution systems (PPGDS and EPGDS). In this section, a more comprehensive transition of the aircraft subsystem architecture is considered, in which all the subsystems are transitioned to electric solutions. Additionally, the aircraft is simultaneously re-sized in accordance with the following set of pre-defined re-sizing rules:

1. The wing planform area should be re-sized to maintain the same wing loading W_{TO}/S_w as the baseline (while maintaining the same planform shape)

2. The same thrust-to-weight ratio T_{SL}/W_{TO} as the baseline must be maintained

3. The horizontal and vertical stabilizers must be re-sized to maintain the same horizontal and vertical tail volume ratios as the baseline

For each of the three aircraft, a transition from a fully conventional subsystems architecture (SSA-00000, LTA-00000, and VLA-00000) to an All Electric subsystems architecture (SSA-73310, LTA-73310, and VLA-73310) is considered.

For the SSA, the effect of the SSA-00000→SSA-73310 transition is summarized in Fig. 44, in which all %-Δ quantities are expressed relative to the corresponding quantities for the baseline architecture. It is seen that for the majority of the actuation functions there is an increase in systems mass. This is due to the assumption that with the current technological state-of-the-art, electric actuators are heavier than the hydraulic actuators they replace. The significant increase in mass of the ECS was already observed in §6.1. For the WIPS and CIPS, electrification involves the removal of the piccolo tubes of the conventional architecture and the incorporation of heating elements and associated power electronics for the electrothermal IPS architecture. The electrification of the subsystem architecture leads to a significant expansion of

% Mass Δs for All Electric Subsystem Architecture - SSA

All %'s relative to corresponding baseline quantities
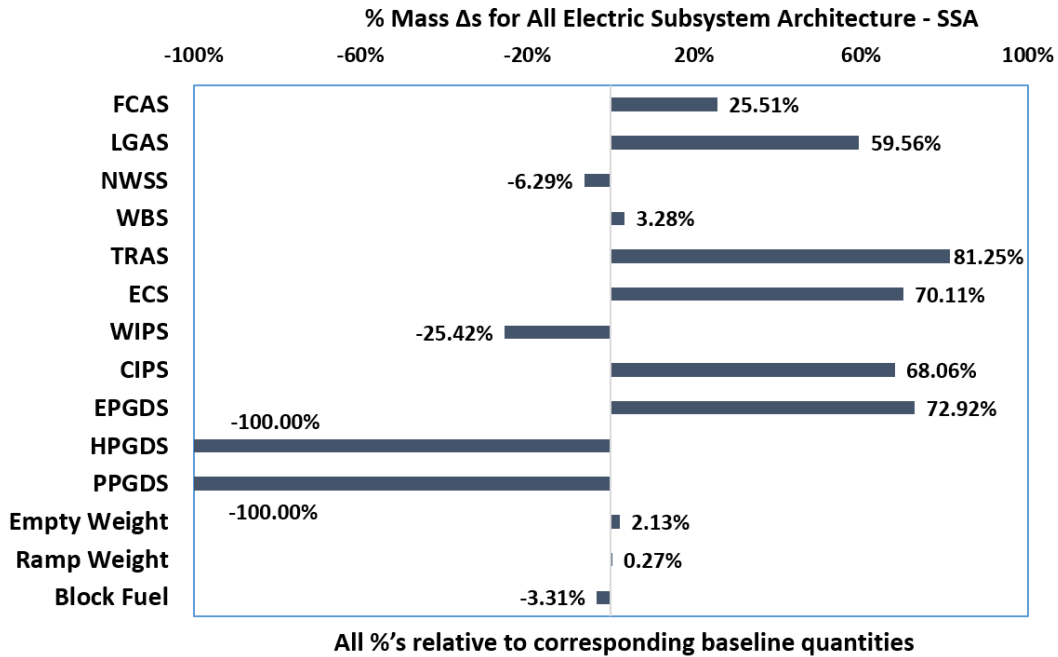
Figure 44: Summary of effects of conventional to All Electric subsystem architecture transition for SSA (SSA-73310 relative to SSA-00000)

Table 27: Subsystem-, aircraft-, and mission-level impact of All Electric subsystem architecture for SSA

Sub -system	%Δ Fuel due to				%Δ Total Fuel Imp.	%Δ Weight	%Δ Total Wt. Imp.
	Weight	SPX	BX	Drag			
FCAS	25.1	-2.8	0.0	0.0	22.3	25.5	24.8
LGAS	60.0	0.0	0.0	0.0	60.0	59.6	59.7
NWSS	-5.1	0.0	0.0	0.0	-5.1	-6.3	-6.0
WBS	3.7	0.0	0.0	0.0	3.7	3.3	3.4
TRAS	100.0	0.0	0.0	0.0	100.0	81.3	85.0
ECS	10.7	13.3	-78.0	8.5	-45.5	70.1	-4.4
WIPS	-4.5	0.6	-81.8	7.4	-77.8	-25.4	-56.8
CIPS	10.8	2.3	-84.6	0.0	-71.5	68.1	-21.8
EPGDS	73.7	0.0	0.0	0.0	73.7	72.9	73.1
HPGDS	-94.1	-5.9	0.0	0.0	-100.0	-100.0	-100.0
PPGDS	-100.0	0.0	0.0	0.0	-100.0	-100.0	-100.0
Aircraft/Mission-level impact					BF: -3.31	EW: 2.13	RW: 0.27

the EPGDS and a significant increase in its mass (in excess of what was observed in §6.1). At the same time, the PPGDS and HPGDS are eliminated completely from the aircraft, resulting in the elimination of significant mass. The net result is a 2.13 % increase in the empty weight of the aircraft. A similar increase in OEW of the aircraft was predicted in the MOET final report [49] for an electrified short-range reference aircraft similar to the SSA considered here. The TFI and TWI analyses for the subsystems architecture transition are shown in Table 27. For the actuation subsystems that show a net increase in systems mass, a corresponding increase in the fuel penalty due to systems mass is observed. For the case of the ECS, WIPS, and CIPS, a reduction in the total fuel penalty is seen due to the elimination of bleed air requirements, which results in a favorable TFI and TWI for these subsystems. At the mission-level, the resulting reduction in fuel consumption is seen to be 3.31 %. The increase in empty weight on the one hand and the reduction in mission fuel requirement on the other yield an increase in the ramp weight of the aircraft of 0.27 %. Due to the re-sizing rules described above, this implies that there is an increase in the wing area S_w and the thrust rating T_{SL} of the same magnitude.

Similar trends are observed for the electrification of the LTA and VLA subsystem architectures, which are presented in Appendix A (LTA: Fig. 63 and Table 36, VLA: Fig. 64 and Table 37). For these cases as well, there is an increase in the OEW of the aircraft due to the architecture transition and a reduction in fuel consumption driven primarily by the elimination of the bleed air requirement. In case of the LTA and the VLA, there is a net reduction in the ramp weight of the aircraft, by 0.65 % and 0.61 % respectively, which means that wing planform area S_w and sea-level rated thrust T_{SL} were reduced by the same percentage during the re-sizing.

6.3　Chapter Summary

The two architecture comparisons described in this chapter demonstrated that the developed integrated sizing and analysis environment is capable of quantifying the impact of competing subsystem solutions (e.g., conventional pneumatic ECS versus electrified ECS) and also competing subsystem architectures (e.g., conventional versus All Electric) on aircraft-level metrics such as empty weight and mission-level metrics such as fuel burn and ramp weight. This was verified for the three baseline aircraft considered (SSA, LTA, and VLA). In both cases, following the sub-statements of Hypothesis 1, the architectures were assessed by

(a) determining characteristics of the power consuming subsystems such as mass, secondary power requirements, and drag increments from an aircraft-level requirements flow-down and using information that either exists during early design phases or can be estimated relatively easily

(b) determining the impact of the subsystem solutions on the affected power generation and distribution subsystems based on the secondary power requirements of the power consuming subsystems

(c) propagating the effect of the masses, secondary power requirements, and drag increments for all affected subsystems to the mission performance analysis to obtain updated estimates of mission-level metrics such as fuel burn and vehicle weight, not just at the end-points of the mission but as a function of time over the course of the mission

Further, for the comparison between two competing subsystem architectures, each vehicle was re-sized in accordance with a set of re-sizing rules (statement (d) of Hypothesis 1). In addition to predicting gross fuel burn reductions, the TFI analysis for each subsystem allowed the relative contributions stemming from changes in

224

subsystem mass, secondary power extraction, and drag increments (associated with the subsystem or architecture transitions) to be identified. The results address Research Question 1 and support Hypothesis 1 by establishing that the developed integrated approach is capable of providing the required resolution at the subsystem, aircraft, and mission levels but without requiring detailed knowledge that would not necessarily be available during the early design phases.

CHAPTER VII

AUTOMATIC ARCHITECTURE DEFINITION AND DECOMPOSITION OF ARCHITECTURE IMPACTS

The purpose of this chapter is to describe Experiments 2.1, 2.2, and 2.3, which are aimed at verifying certain capabilities of the integrated sizing and analysis environment. The benchmarking of the automatic architecture definition algorithm (Experiment 2.1) is described in §7.1. The incorporation of propulsion system performance characteristics obtained from a high-fidelity propulsion tool into the integrated analysis (Experiment 2.2) is discussed in §7.2. The decomposition of the net architecture impact into contributions from masses, secondary power requirements, and drag increments of individual subsystems (Experiment 2.3) is addressed in §7.3.

7.1 Verification of Architecture Definition Algorithm

In §5.1, heuristics for the association of power sources, power systems, and power consumers were identified based on the inspection of subsystem architectures of existing aircraft. In addition, templates for the EPGDS and PPGDS were also presented and described. Based on the heuristics and templates, an algorithm was implemented to determine the associations among the subsystem architecture elements based on (i) the number of engines, (ii) the number of power consumers, i.e., the number of ailerons, spoilers, etc., (iii) the nature of the secondary power required by a consumer, i.e, pneumatic, electric, or hydraulic.

During subsystem architecture evaluations, the associations among prime movers, power sources, power systems, and power consumers determined by the algorithm

are passed to successive sizing and analysis modules. The algorithm also generates a diagrammatic representation of the architecture connectivity in the form of the subsystem architecture *snapshots* shown in Figs. 45-48. These snapshots serve to convey through a single diagram relevant top-level information regarding the architectures of the PPGDS, HPGDS, and EPGDS.

Considering the snapshot of Fig. 45 as an example, the top-left corner shows the nature of off-takes from the prime movers (engines E1, E2, etc. and the APU). If bleed air is extracted from the engines and APU, that bleed is marked B-E1, B-E2,..., and B-APU. Similarly, if EDPs and EDGs are run off the engine, these are marked EDP-E1, G1-E1, etc. To the right of this, the pneumatic system definition is shown. The left and right halves of the pneumatic system are marked P1 and P2, and are connected by the Cross-Bleed Valve (CBV). The bleed extracted from the engines and the APU supplies either system P1 or P2. Below the pneumatic system definition, the hydraulic system definition is shown. For each hydraulic system, the pumps that are involved in pressurizing it are shown above the system names H1, H2, and H3. Additionally, the RAT is shown marked above the system which it supplies in case of an emergency. The top-right corner of each snapshot shows a limited definition of the electrical system. As per the electrical system template described in §5.1.2, there is a separate AC bus for each main engine generator. In case of AC-to-DC power conversion, the connectivity of the AC systems to the DC systems is also shown (e.g., in Fig. 48). Thus, the top part of each snapshot shows the connectivity of prime movers to power sources, and power sources to power systems. The central part of each snapshot shows the association of power systems with the power consumers.

In order to test the performance of the heuristic architecture definition algorithm and the validity of the generated subsystem architectures (Experiment 2.1), the known subsystem architectures of some existing architectures are used as references. For each such case, the number of engines, number of power consumers (ailerons, leading-edge

and trailing-edge devices, spoilers, etc.), and the type of secondary power required by the power consumers is provided as an input. The subsystem architectures generated by the algorithm (Figs. 45-48) are then compared with the actual architectures. For cases where the association created by the algorithm differs from the actual association between the same two elements in the real architecture, the latter is indicated by red text in parentheses.

The first two benchmarking cases are the four-engined Airbus A340 and the twin-engined Boeing 777, for both of which the subsystems architecture is largely conventional. It is seen from Fig. 45 and Fig. 46 that in several cases there are differences between the hydraulic system to spoiler connectivity predicted by the algorithm and the actual connectivity existing in these two aircraft. However, this is to be expected since the heuristic for hydraulic system to spoiler association was a generalized one developed from the inspection of multiple hydraulic system architectures. Further, in several cases, hydraulic system H1 is predicted in place of H3 or vice versa. The hydraulic system definition shows that in terms of power source redundancy, these two systems are essentially equivalent. It is also noteworthy that the connectivity for the primary flight control surfaces, thrust reversers, and landing gear actuation functions is predicted correctly.

An architecture similar to the four-engined Airbus A380 (a MEA) is used as a third benchmarking case. Electrification includes the incorporation of electric actuators parallel to hydraulic ones for the ailerons, elevators, rudders, and spoilers, and the electrification of the TRAS. It differs from the actual A380 subsystems architecture in that the Airbus A380 uses Electrical Backup Hydraulic Actuators (EBHAs) for the rudder and some of the spoilers, whereas these are not considered within the scope of this dissertation[1]. It is noteworthy that for this case, the algorithm eliminates

---

[1] Within the scope of this dissertation, an actuator is supplied with either hydraulic power or electric power, but cannot receive both types of power (which is the case for EBHAs)

Validation Case - Airbus A340

2015-9-27 @ 18:25.56

Actuation architecture: 3H

Prime Movers

E1	E2	E3	E4	APU
B-E1	B-E2	B-E3	B-E4	B-APU
EDP-E1	EDP-E2	EDP-E3	EDP-E4	
G1-E1	G2-E2	G3-E3	G4-E4	G5-APU

Pneumatic Systems

B-E1	B-E2	B-APU		B-E3	B-E4
P1		CBV		P2	

Electric Systems

G1-E1	G2-E2	G3-E3	G4-E4
GAC-1	GAC-2	GAC-3	GAC-4

Hydraulic Systems

EMP_H1	(RAT) EDP_E4	EMP_H3
EDP_E2	EDP_E1	EDP_E3
H1	H2	H3
3000 psi	3000 psi	3000 psi

NWS	H2
NGA	H2

LED Actuatio	H1
	H2

L-WIPS

Slat_7L	Slat_6L	Slat_5L	Slat_4L	Slat_3L	Slat_2L	Slat_1L
P1	P1	P1	P1	P1		

R-WIPS

Slat_1R	Slat_2R	Slat_3R	Slat_4R	Slat_5R	Slat_6R	Slat_7R
		P2	P2	P2	P2	P2

		Sp_6L	Sp_5L	Sp_4L	Sp_3L	Sp_2L	Sp_1L
		H2	H1	H1	H3	H2	H3
		(H3)	(H2)	(H3)	(H1)	(H1)	(H2)

L-ECS Pack	R-ECS Pack
P1	P2

Sp_1R	Sp_2R	Sp_3R	Sp_4R	Sp_5R	Sp_6R
H3	H2	H3	H1	H1	H2
(H2)	(H1)	(H1)	(H3)	(H2)	(H3)

Left OB Aileron: H2 | H3

Left IB Aileron: H2 | H1

Right IB Aileron: H2 | H3 (H1)

Right OB Aileron: H2 | H1 (H3)

CIPS-E1	CIPS-E2
B-E1	B-E2
TR-E1	TR-E2
H2	H1

CIPS-E3	CIPS-E4
B-E3	B-E4
TR-E3	TR-E4
H3	H2

L-WGA	H2	TED Actuatio	H2	H2	R-WGA
L-WGB	H2		H3	H2	R-WGB
	H1			H1	

THS: H1 | H2 (H3)

Left Elevator: H2 | H1

Right Elevator: H2 | H3

Rudder: H1 | H2 | H3

Figure 45: Subsystem architecture snapshot generated by heuristic algorithm for Airbus A340 (for cases where the algorithm predicted a connection different from the actually existing connection, the latter is indicated using red text within parentheses)

Figure 46: Subsystem architecture snapshot generated by heuristic algorithm for Boeing 777 (for cases where the algorithm predicted a connection different from the actually existing connection, the latter is indicated using red text within parentheses)

one of the three hydraulic systems and generates a 2H/2E actuation architecture, as found on the Airbus A380. Hydraulic supply is removed from the TRAS and replaced with electric supply. For the ailerons, elevators, and rudders, one hydraulic supply is removed and replaced with one electric supply. Since this aircraft has a split rudder, each panel is provided with two actuators, one hydraulic and one electric.

As a final benchmarking case, inputs corresponding to the Boeing 787 (another MEA) are provided to the architecture definition algorithm. With regard to the association of hydraulic systems with spoilers and some of the ailerons, the same observations that were made for the Airbus A340 and Boeing 777 benchmarking cases are applicable to this case as well. Due to the greater electrical power demand caused by the electrification of the ECS, the algorithm initializes two generators per engine (and also for the APU) instead of the usual one. Due to the electrification of the ECS and WIPS functions, the pneumatic systems P1 and P2 are deleted. The conventional hydraulic supplies are removed from the brake and THS actuation functions and replaced with equivalent electric supplies. Finally, three spoilers per wing are electrified (in reality, the Boeing 787 has two electrified spoilers per wing).

It is clear from the benchmarking cases that while the algorithm does not precisely match each and every system-to-load connection within the subsystem architectures, it does provide *equivalent* connectivity from the perspective of required redundancy (subject to the central modeling assumption listed in §5.1.1). Further, for the case of the two MEA architectures, the algorithm replaces conventional hydraulic or pneumatic supplies with equivalent electric supplies in a manner corresponding to what is seen in reality for these two aircraft. The conclusion from these observations is that this algorithm can be used in lieu of a formal FTA/FMEA in order to rapidly determine (i) the required number of power sources and systems and (ii) feasible connectivity among subsystem architecture elements based on the subsystem solutions employed, while giving due consideration to reliability/redundancy requirements.

Extrapolation Case - A380-type Architecture

2015-9-27 @ 19:44.45

Actuation architecture: 2H/2E

Prime Movers

E1	E2	E3	E4	APU
B-E1	B-E2	B-E3	B-E4	B-APU
EDP-E1	EDP-E2	EDP-E3	EDP-E4	
G1-E1	G2-E2	G3-E3	G4-E4	G5-APU

Pneumatic Systems

B-E1	B-E2	B-APU		B-E3	B-E4
P1			CBV	P2	

Electric Systems

	G1-E1	G2-E2	G3-E3	G4-E4
	GAC-1	GAC-2	GAC-3	GAC-4
DC-1	x		x	
DC-2		x		x

Hydraulic Systems

	(RAT)	
EDP_E2	EDP_E4	
EDP_E1	EDP_E3	
H1	H2	
5000 psi	5000 psi	

NWS	H2
NGA	H2

LED	H1
Actuation	H2

L-ECS Pack	R-ECS Pack
P1	P2

L-WIPS

Slat_8L	Slat_7L	Slat_6L	Slat_5L	Slat_4L	Slat_3L	Slat_2L	Slat_1L
			P1				

Sp_8L	Sp_7L	Sp_6L	Sp_5L	Sp_4L	Sp_3L	Sp_2L	Sp_1L
H1	H2	DC-1	DC-2	DC-1	DC-2	H1	H2

R-WIPS

Slat_1R	Slat_2R	Slat_3R	Slat_4R	Slat_5R	Slat_6R	Slat_7R	Slat_8R
				P2			

Sp_1R	Sp_2R	Sp_3R	Sp_4R	Sp_5R	Sp_6R	Sp_7R	Sp_8R
H2	H1	DC-2	DC-1	DC-2	DC-1	H2	H1

Left OB Aileron / **Left MB Aileron** / **Left IB Aileron**

H2	DC-1	H1	DC-2	H2	DC-1

Right IB Aileron / **Right MB Aileron** / **Right OB Aileron**

H1	DC-2	H2	DC-1	H1	DC-2

CIPS-E1	CIPS-E2
B-E1	B-E2
TR-E1	TR-E2
DC-2	DC-1

CIPS-E3	CIPS-E4
B-E3	B-E4
TR-E3	TR-E4
DC-1	DC-2

L-WGA	H2	TED	H1	H2	R-WGA
L-WGB	H2	Actuation	H2	H2	R-WGB
	H1			H1	
L-BGA		H1	H1		R-BGA
L-BGB		H1	H1		R-BGB
		H2	H2		
L-BGS		H1	H1		R-BGS

THSA	H1
	H2
	DC-2

Left OB Elevator / **Left IB Elevator**

H1	DC-2	H2	DC-1

Right IB Elevator / **Right OB Elevator**

H1	DC-2	H2	DC-1

Lower Rudder	H1
	DC-2

Upper Rudder	H2
	DC-1

Figure 47: Subsystem architecture snapshot generated by heuristic algorithm for Airbus A380

Figure 48: Subsystem architecture snapshot generated by heuristic algorithm for Boeing 787 (for cases where the algorithm predicted a connection different from the actually existing connection, the latter is indicated using red text within parentheses)

7.2 Capturing Effect of Subsystem Architecture on Propulsion System Sizing and Performance

First approximations for the impact of shaft-power and bleed air extraction on the engine fuel consumption (fuel flow rate) were presented in Chapter 6. It was pointed out that relationships of this nature are convenient as they require little additional information other than the instantaneous shaft-power and bleed air off-takes. However, these relationships do not account for the fact that the engine's sensitivity to shaft-power and bleed air extraction depends on the engine cycle parameters, which vary from engine to engine even within the same thrust class. Such dependencies can be captured using a higher-fidelity propulsion system analysis tool. However, as mentioned previously, the direct integration of such a tool into the integrated sizing and analysis environment may be infeasible from the point of view of required computational time. Instead, the higher-fidelity propulsion system analysis tool is used to create a *truth model* for a gas turbine designed to provide a certain combination of maximum shaft-power and maximum bleed. The truth model is then queried in order to find the incremental fuel flow rate as a result of shaft-power and bleed air off-takes for a given flight condition. The coefficients thus obtained are incorporated into the integrated environment and used for architecture assessments. Within the scope of this dissertation, this method is employed only for the SSA (Experiments 3.1, 3.2, and Experiment 4.0 with architecture-to-engine association logic enforced). Therefore, a clarifying statement to this effect is included where SSA results for these experiments are presented. For the LTA and VLA, the basic relationships presented in Chapter 6 are used throughout. The creation of the propulsion system truth model and the determination of the fuel flow penalty coefficients are described in the subsequent sections (Experiment 2.2).

7.2.1 Propulsion System Truth Model

The propulsion system truth model was created using the Environmental Design Space (EDS) tool. The EDS was developed under the sponsorship of NASA and the US Federal Aviation Administration's Office of Environment and Energy (FAA/AEE) for the assessment of the environmental effects of aviation [158]. It is an integrated, physics-based, multi-disciplinary modeling and simulation environment whose engine design modules include CMPGEN for generation of compressor maps, the Numerical Propulsion System Simulation (NPSS) tool for analysis of the thermodynamic cycle, and WATE for engine flow path analysis and weight estimation [159]. In EDS, a number of different design points are used as part of the Multi Design Point (MDP) approach to define the cycle design space [160]:

1. Aerodynamic Design Point (ADP): Mach 0.80, 35,000 ft, ISA - This is considered to be the turbomachinery design point in EDS where design pressure ratio and component efficiencies are specified

2. Top of climb: Mach 0.85, 35,000 ft, ISA - At this point, thrust requirements must be met while allowing an amount of fan over-speed that corresponds to a given ratio of corrected mass flow (top of climb to ADP)

3. Takeoff: Mach 0.25, sea-level, ISA + 27°F - The takeoff thrust requirement has to be satisfied at a specified combustor exit temperature (T_4) which is the maximum for the design

4. Sea-level static, installed, ISA + 27°F - The sea-level static thrust requirement must be met at the flat rating temperature (+ 27°F)

For each of these points, the shaft-power extraction and customer bleed air extraction can also be specified. In order to factor the subsystem architecture secondary power requirements into the sizing of the engine, the shaft-power and bleed air

extraction corresponding to a One Engine Inoperative (OEI) scenario (assumed to occur anywhere in the mission profile) for a particular subsystem architecture are computed. The secondary power requirements corresponding to the MDP conditions stated above are then used to size three engines corresponding to the secondary power requirements of three different subsystem architectures:

1. Mixed Off-take (MO) Engine: Sized taking into account the mixed secondary power off-take requirements corresponding to SSA-00000 (conventional baseline with pneumatic ECS, and pneumatic evaporative anti-icing WIPS and CIPS)

2. Reduced Bleed (RB) Engine: Sized taking into account the secondary power off-take requirements corresponding to SSA-00010 (electrified ECS, pneumatic evaporative anti-icing WIPS and CIPS)

3. Zero Bleed (ZB) Engine: Sized taking into account the pure shaft-power requirements corresponding to SSA-02210 (electrified ECS, electrothermal running-wet anti-icing WIPS, and electrothermal evaporative anti-icing CIPS)

Since the bleed air requirements are lower for running-wet anti-icing compared to evaporative anti-icing, the MO engine automatically satisfies the bleed requirements of pneumatic running-wet WIPS and CIPS. Further, since the electrical power requirements are lower for running-wet anti-icing relative to evaporative anti-icing and lower still for de-icing, the ZB engine automatically satisfies the power requirements of electrothermal de-icing WIPS and electrothermal running-wet anti-icing CIPS.

The power requirements for electric ECS are highest at cruise conditions, while the bleed air requirements for ice protection reach their maximum at an intermediate altitude and become zero at cruise. As a result, the RB engine, sized assuming electric ECS and pneumatic evaporative IPS, has sufficient shaft-power and bleed capacity to meet the off-take requirement of all subsystem architectures where the
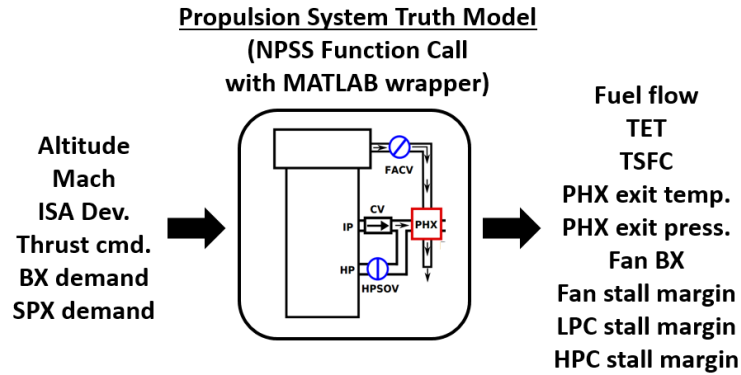
Figure 49: Inputs and outputs for truth model function call (executed as a function call to NPSS with a MATLAB wrapper)

ECS/WIPS/CIPS group has been only partially electrified (i.e., at least one member of the group is either pneumatic or electric).

The truth model contains a model of the precooler heat exchanger (PHX) in order to compute the mass flow rate of air that must be extracted from the fan in order to cool the bleed air to a target PHX exit temperature (set to a constant 200°C). The extraction of this mass flow rate also imposes a fuel consumption penalty on the engine. Thus, the TSFC degradation due to bleed air extraction computed using the truth model accounts for not only the direct penalty due to the extraction of the bleed air itself, but also the additional penalty due to the extraction of fan air in order to down-regulate the temperature of the bleed air. A simple bleed port selection logic is also implemented based on publicly available information so that at lower power settings, bleed air extraction from a higher pressure compressor stage is considered.

For each engine, the truth model is executed for combinations of altitude, Mach number, and power settings but with zero shaft-power and bleed air demand in order to generate a *basic* engine performance data-table (engine deck). This is used in order to evaluate the fuel consumption for the *basic* mission (§3.2.5) prior to accounting for the additional fuel consumption due to subsystem secondary power requirements and direct drag increments.

By wrapping a MATLAB script around the truth model, a truth model function call for each of the three engines is created with the inputs and outputs shown in Fig. 49. For the case of the ZB engine, the bleed air demand is always zero and the PHX model is not enabled (as the PHX would have been physically eliminated from bleedless architectures). The truth model is queried by means of this function call in order to obtain scheduled coefficients representing the degradation of engine TSFC due to shaft-power and bleed air off-takes, as described in the following section.

7.2.2 Determination of Fuel Flow Penalty Coefficients

The degradation in engine fuel consumption due to the extraction of shaft-power is known to increase approximately linearly with increase in the magnitude of the shaft-power extraction [63]. However, such a linear relationship for bleed air extraction is only true for relatively low mass flow rates of bleed air [63]. Off-line investigation of the impact of shaft-power and bleed air extraction on the predicted TSFC of the engine truth model confirmed these facts. Further, a sensitivity analysis performed on the TSFC revealed a slight interaction effect between the shaft-power and bleed air extraction. Based on these observations, a fuel flow rate penalty function of the following form is hypothesized:

$$\lambda_{sfc} = \frac{\Delta SFC}{SFC_0} = K_1 \ \dot{m}_{bx}^2 + K_2 \ \dot{m}_{bx} + K_3 \ \dot{m}_{bx} \ P_{spx} + K_4 \ P_{spx} \qquad (170)$$

For a given flight condition (altitude, Mach number, and thrust setting), the coefficients $K_1, \ldots K_4$ are determined by querying the truth model in order to solve the following linear system of the form $A \ K = B \implies K = A^{-1} \ B$:

$$
\begin{bmatrix}
\dot{m}_{bx,1}^2 & \dot{m}_{bx,1} & \dot{m}_{bx,1}^2 P_{spx,1} & P_{spx,1} \\
\dot{m}_{bx,2}^2 & \dot{m}_{bx,2} & \dot{m}_{bx,2}^2 P_{spx,2} & P_{spx,2} \\
\dot{m}_{bx,3}^2 & \dot{m}_{bx,3} & \dot{m}_{bx,3}^2 P_{spx,3} & P_{spx,3} \\
\dot{m}_{bx,4}^2 & \dot{m}_{bx,4} & \dot{m}_{bx,4}^2 P_{spx,4} & P_{spx,4}
\end{bmatrix}
\begin{bmatrix}
K_1 \\
K_2 \\
K_3 \\
K_4
\end{bmatrix}
= \frac{1}{SFC_0}
\begin{bmatrix}
SFC_1 - SFC_0 \\
SFC_2 - SFC_0 \\
SFC_3 - SFC_0 \\
SFC_4 - SFC_0
\end{bmatrix}
\qquad (171)
$$

It is clear that to solve $K = [K_1, \ldots, K_4]^T$ for a single flight condition, five evaluations of the truth model are required - a first evaluation to establish the basic TSFC (SFC_0) without any shaft-power or bleed off-takes, and four subsequent evaluations with off-take pairs $(\dot{m}_{bx,i}, P_{spx,i}), i = 1, \ldots, 4$, in order to populate the A and B matrices of Eq. 171. In literature, the TSFC degradation due to shaft-power and bleed air extraction is often expressed as percentage increase in TSFC due to 100 hp of shaft-power extraction or due to 1 lb/s of bleed extraction. Based on this, the four query points are set as (i) $P_{spx,1} = 100$ hp, $\dot{m}_{bx,1} = 0$ lb/s, (ii) $P_{spx,2} = 0$ hp, $\dot{m}_{bx,2} = 1$ lb/s, (iii) $P_{spx,3} = 100$ hp, $\dot{m}_{bx,3} = 1$ lb/s, and (iv) $P_{spx,4} = 40$ hp, $\dot{m}_{bx,4} = 0.6$ lb/s. This is done for all engines designed to provide mixed off-takes (i.e., both shaft-power and bleed). For the case of a bleedless engine, only the coefficient K_4 is evaluated, and by default $K_1 = K_2 = K_3 = 0$.

Since this evaluation is for a particular flight condition, the coefficients depend on altitude, Mach number, and thrust setting, i.e., $K_i = K_i(h, M, T), i = 1, \ldots, 4$. In this dissertation, the functional dependency is simplified through the following:

1. The mission performance analysis is set up such that the flight profile given by $t \in [0, t_f], h(t), M(t)$ is nearly invariant for all missions evaluated, regardless of the subsystem architecture

2. It is assumed that the variations in required thrust between different architectures at the same point in the mission profile (caused by variations in vehicle mass and drag increments) are not large enough to substantially alter the basic TSFC through the dependency of engine TSFC on thrust setting.[2]

Subject to the above, the coefficients $K = [K_1, \ldots, K_4]^T$, instead of being given as functions of h, M, and T, may instead be given as functions of the normalized mission

---

[2]It should be noted however that variations in fuel flow rate due to variations in thrust are captured directly through the terms of Eq. 20

time $\tau = \frac{t}{t_f} \in [0, 1]$, i.e., $K(\tau) = [K_1(\tau), \ldots, K_4(\tau)]^T$. Thus, for any mission being analyzed, the coefficient-set may be obtained from a 1-dimensional look-up.

7.2.3 Comparison of Penalty Coefficient Predictions Against Truth Model Predictions

The fuel consumption increment predicted using the penalty coefficients determined by the procedure outlined above was tested against that predicted by the truth model for the same flight condition and secondary power off-takes. To do this, the truth model is first queried with the altitude, Mach number, thrust, shaft-power off-take, and bleed air off-take corresponding to each instant of time within a selected mission profile. The fuel flow rates predicted by the truth model are integrated forward in time to obtain the truth (or reference) fuel consumption for that mission.

Next, using the normalized mission time, the coefficients $K(\tau) = [K_1(\tau), \ldots, K_4(\tau)]^T$ are obtained through 1-dimensional interpolation. Using the time histories of shaft-power and bleed air extraction, the degradation in TSFC (λ_{sfc}, Eq. 170) is computed for each instant of time. With the degraded TSFC given by $SFC = SFC_0 \, (1 + \lambda_{sfc})$ and the thrust from the mission profile, the fuel flow predicted by the interpolated penalty coefficients is computed for each time instant. These too are integrated forward in time to obtain the predicted fuel consumption for the mission. This is then compared to the truth (reference) fuel consumption obtained using the truth model directly.

When the comparison is carried out using the same mission profile that had been used to determine the coefficients, the error is negligibly small. Across the sized engines, for a constant $\pm 1,000$ ft perturbation to the altitude time history (i.e., a constant addition or subtraction of 1,000 ft to each altitude data point), the magnitude of the predicted fuel consumption error is limited to 0.57 %. Similarly, for a constant ± 0.01 perturbation in the Mach number time history, the magnitude of the error is limited to 0.68 %. For a ± 5 % perturbation to the thrust time history,

the magnitude of the predicted fuel consumption error is limited to 0.39 %. It should be noted that since the mission performance analysis is set up such that the flight profile given by $t \in [0, t_f], h(t), M(t)$ is nearly invariant for all missions evaluated, the actual deviations of altitude and Mach number time history during architecture evaluations are of a much smaller magnitude.

The conclusion from the above is that it is feasible to develop a truth model for gas turbine engines designed to provide different secondary power off-take combinations using a higher-fidelity propulsion tool. Fuel penalty coefficients computed by querying the truth model can be incorporated into the mission performance analysis without directly incorporating the computationally expensive truth model.

7.3 Decomposition of Net Subsystem Architecture Impact

In order to guide the focus of design refinement efforts for subsystems, the design characteristics of the subsystems must be linked to mission-level performance metrics. However, as discussed previously, merely evaluating the net impact of a subsystem architecture on a mission-level metric does not by itself provide information regarding the contributions of the individual subsystems to the total impact. This information must instead be derived by (i) decomposing the net impact of the subsystem architecture into the contributions from different subsystems and (ii) decomposing the contribution from each subsystem further into contributions arising from mass, secondary power requirements, and direct drag increments. The approach followed to obtain this decomposition is discussed in the following sections (as part of Experiment 2.3). The breakdown of the net architecture impact into the contributions from mass, secondary power requirements, and direct drag increments arising from individual subsystems is demonstrated for a selected subsystem architecture (§7.3.1). Discussions regarding how such a decomposition may be used to facilitate design efforts for ECS and WIPS solutions are presented in §7.3.2 and §7.3.3. Finally, a

feasibility assessment for an optional subsystem such as an Electric Taxiing System (ETS) for the SSA, LTA, and VLA baselines is presented in §7.3.4.

7.3.1 Decomposition of Total Fuel Impact of Subsystem Architectures

The approach to evaluating the total fuel impact of the overall subsystem architecture was discussed in §3.2.5, where a system of equations (Eq. 17) was developed to account for the time-varying effects of secondary power extraction and direct drag increments. It was mentioned that evaluating this equation system for individual subsystems allowed the determination of the contributions of their masses, secondary power off-takes, and drag increments to mission fuel consumption. In other words, it permitted the evaluation of all the components of a subsystem's Total Fuel Impact (TFI), which for subsystem 'i' was defined in §3.1 as

$$TFI^{(i)} = \Delta w_{f,w}^{(i)} + \Delta w_{f,spx}^{(i)} + \Delta w_{f,bx}^{(i)} + \Delta w_{f,d}^{(i)}. \tag{172}$$

The relative magnitudes of the four effects (shaft-power, bleed, drag increment, and weight) may be represented through the following four ratios:

$$\kappa_{spx}^{(i)} = \frac{\Delta w_{f,spx}^{(i)}}{TFI^{(i)}}, \qquad \kappa_{bx}^{(i)} = \frac{\Delta w_{f,bx}^{(i)}}{TFI^{(i)}}, \qquad \kappa_{d}^{(i)} = \frac{\Delta w_{f,d}^{(i)}}{TFI^{(i)}}, \qquad \kappa_{w}^{(i)} = \frac{\Delta w_{f,w}^{(i)}}{TFI^{(i)}} \tag{173}$$

The TFI itself may be expressed as a percentage of the block fuel (BF). The weight $W^{(i)}$ of each subsystem may be expressed as a percentage of the operating empty weight (OEW). Finally, the TWI of each subsystem may expressed as a percentage of the aircraft's Maximum Ramp Weight (MRW). This information may be represented in a tabular form as shown in Table 28, where the breakdown shown corresponds to architecture SSA-73310 (All Electric bleedless subsystems architecture without ETS installed). Within the integrated environment, the information within this table is re-computed once per iteration and stored in matrix form for each subsystem architecture evaluated. The tabular representation of Table 28 decomposes the subsystem architecture's impact on BF (a mission-level metric) in two levels:

1. *Level 1 - decomposition of net impact into contributions from each subsystem:* This information may be obtained by inspecting the normalized TFI column ($TFI^{(i)}/BF$) of Table 28. This shows which subsystems within the architecture have the most dominant effect on fuel consumption. For this architecture (SSA-73310), these are seen to be the ECS and the EPGDS.

2. *Level 2 - decomposition of each subsystem's impact into contributions from its mass, secondary power requirements, and drag increments:* For any subsystem, this information may be obtained by inspecting the relative magnitudes of $\kappa_w^{(i)}$, $\kappa_{spx}^{(i)}$, $\kappa_{bx}^{(i)}$, and $\kappa_d^{(i)}$. The relative magnitudes may be used to guide design refinement efforts for each subsystem. For instance, it is clear that the impact of the actuation subsystems is predominantly on account of their mass. Therefore, while designing these subsystems, the minimization of mass may be prioritized.

Table 28: Decomposition of net subsystem architecture fuel impact into contributions from mass, secondary power requirements, and drag increments of individual subsystems (Breakdown shown for SSA-73310, All Electric subsystems architecture, PPGDS and HPGDS completely eliminated, ETS not installed)

	Norm. fuel penalties				Norm. fuel & wt. impact		
Sub-system	$\kappa_w^{(i)}$ (%)	$\kappa_{spx}^{(i)}$ (%)	$\kappa_{bx}^{(i)}$ (%)	$\kappa_d^{(i)}$ (%)	$TFI^{(i)}/BF$ (%)	$W^{(i)}/OEW$ (%)	$TWI^{(i)}/MRW$ (%)
FCAS	99.79	0.21	0	0	1.09	1.89	1.24
LGAS	99.93	0.07	0	0	0.19	0.32	0.21
NWSS	99.88	0.12	0	0	0.09	0.15	0.10
WBS	99.90	0.10	0	0	0.72	1.26	0.82
ETS	-	-	-	-	-	-	-
TRAS	100.00	0.00	0	0	0.02	0.03	0.02
ECS	47.42	24.46	0	28.11	3.79	3.12	2.53
WIPS	62.75	3.08	0	34.17	0.09	0.10	0.07
CIPS	91.01	8.99	0	0	0.08	0.13	0.09
EPGDS	93.58	6.42	0	0	2.31	3.74	2.49
HPGDS	-	-	-	-	-	-	-
PPGDS	-	-	-	-	-	-	-
MPGDS	61.15	38.85	0	0	0.13	0.14	0.10

For other subsystems such as the ECS, there are significant contributions from weight, shaft-power requirement, and drag increment. In such cases, the design of the subsystem should not focus solely on the minimization of mass. This is discussed in greater detail in subsequent sections by considering design solutions for the ECS and WIPS.

7.3.2   Analysis of TFI Breakdown for Pneumatic and Electric ECS

The relative contributions of system mass, secondary power requirement (either shaft-power or bleed air), and direct drag increments on the Total Fuel Impact (TFI) of conventional (pneumatic) and electric ECS are shown in Fig. 50 for the SSA, LTA, and VLA baselines. It is seen that for all three baselines, the necessary pneumatic off-take (bleed air) accounts for a very significant percentage of the TFI of the pneumatic ECS. A much smaller percentage of the TFI is accounted for by the system mass, whose effect is seen to reduce with increase in the aircraft size (while the contribution of bleed air off-take increases). The remaining small percentage of
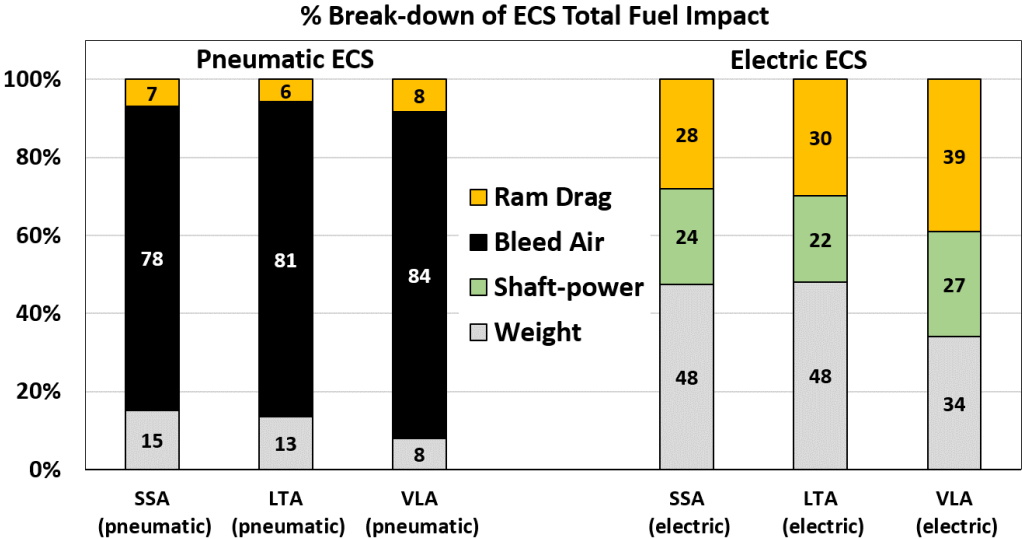
Figure 50: Decomposition of total fuel impact for pneumatic and electric ECS into contributions from mass, secondary power requirement, and direct drag penalty

244

the TFI is accounted for by ram drag caused by the cooling stream required for the ECS heat exchangers.

In attempting to minimize the TFI of the pneumatic ECS, it is clear that a proportionately high weighting factor would have to be associated with the reduction of bleed air penalty, with smaller weighting factors for the minimization of weight and ram air requirement. The magnitude of the penalty is proportional to the work done to compress the bleed air prior to extraction, which may be expressed as

$$W_{bleed} \propto \dot{m}_{bleed} \, h_{bleed} \, \Delta t, \tag{174}$$

where $\dot{m}_{bleed}$ is the mass flow rate of bleed air and h_{bleed} is the specific enthalpy of the bleed at its extraction point. Thus, the penalty may be reduced by

- Reducing the mass flow rate requirement: This is already seen in current pneumatic ECS designs, where recirculation is used to reduce the net mass flow rate of air that has to be extracted from the engines [13]. In fact, in modern ECS designs, the recirculation fraction is already up to 50 %

- Reducing the specific enthalpy: The bleed port selection logic employed in all modern commercial aircraft essentially attempts to achieve this through localized energy management. Bleed air is extracted from a lower pressure port whenever possible unless the temperature and pressure available at that port is insufficient (due to low power settings). However, even the air bled from the lower pressure port often has excessive temperature and pressure (as pointed out previously) and has to be down-regulated using a precooler heat exchanger (PHX) and a pressure reducing valve

Thus, while the bleed air penalty constitutes a very large percentage of the TFI of a pneumatic ECS design, it would appear that sufficient design freedom does not exist to substantially reduce this penalty. ECS design efforts could focus on reduction

of the impact of mass (mass optimization) or improvement of the overall effectiveness of heat exchange (pack performance optimization, which would reduce the ram air requirement). However, as evident from Fig. 50, these collectively account for a much smaller fraction of the TFI of the pneumatic ECS. Therefore, the gains arising out of such design refinement efforts would likely not be of very large magnitudes.

Figure 50 also shows that the scenario is quite different for the electric ECS solution, where mass, secondary power requirement, and drag increments have a more balanced contribution. The following observations may be made regarding the effects and the means available to reduce them:

- Mass: This has a far more substantial contribution to the TFI. As mentioned previously, for an electric ECS design, there is a significant addition of mass due to the incorporation of CACs, electric motors, and power electronics. Due to the higher percentage contribution of system mass, mass optimization of an electric ECS design will have a much more significant impact on the TFI

- Shaft-power: This can be reduced by reducing the power consumption of the CACs, which increases with increasing mass flow rate and higher discharge pressure requirements. Similar to the case of pneumatic ECS, the mass flow requirements can only be reduced up to a point (using recirculation). The required discharge pressure may be reduced by using ECS packs that are designed to operate at lower pressures [116]

- Ram drag: This has two sources, the first being the cabin supply air which is admitted through dedicated ram air inlets, and the second being the cooling stream for the pack heat exchangers. Since minimum cabin airflow requirements have to be met, the first source of drag can only be reduced up to a limit. The second source can be reduced through pack performance optimization (similar to the case for pneumatic ECS)

246

The conclusion from these observations is that greater design freedom exists for refining the design of an electric ECS solution, either through design improvements with a fixed component technology level, or through improvement in technological SOTA of components such as motors and power electronics. On the other hand, the design freedom for a conventional (pneumatic) ECS is more limited. The second level of the two-level decomposition of the subsystem architecture TFI permits the identification of the relative contributions of ECS mass, secondary power requirements, and direct drag penalties to the mission-level fuel consumption. These may be used as a rational means to determine the weights of an objective function for ECS design optimization. The focus of the optimization is seen to differ based on the ECS solution considered (pneumatic versus electric).

7.3.3 Analysis of TFI Break-down for Different WIPS Solutions

The contributions from mass, secondary power requirement, and direct drag penalty for the WIPS solutions that were considered in this dissertation are shown in Fig. 51 for the SSA baseline. The trends for the LTA and VLA baseline are similar, but in those cases the contribution of the WIPS mass to its TFI is higher since those aircraft cruise for longer durations at altitudes where the WIPS is inactive.

It is seen from Fig. 51 that the penalty due to bleed air off-take is the most significant for the pneumatic *evaporative* anti-icing system. In this case, higher bleed air mass flow rate is required in order to maintain the surface at the higher temperature required to completely evaporate all impinging water droplets. The contribution of bleed air off-take for a pneumatic *running-wet* anti-icing system is lower, since in this case, the surface only has to be maintained at a temperature sufficient to prevent impinging water from freezing. This reduces the bleed air requirement, and in this case, bleed air and system mass have roughly comparable contributions to the TFI of the WIPS.

% Break-down of Total Fuel Impact for Different WIPS Solutions
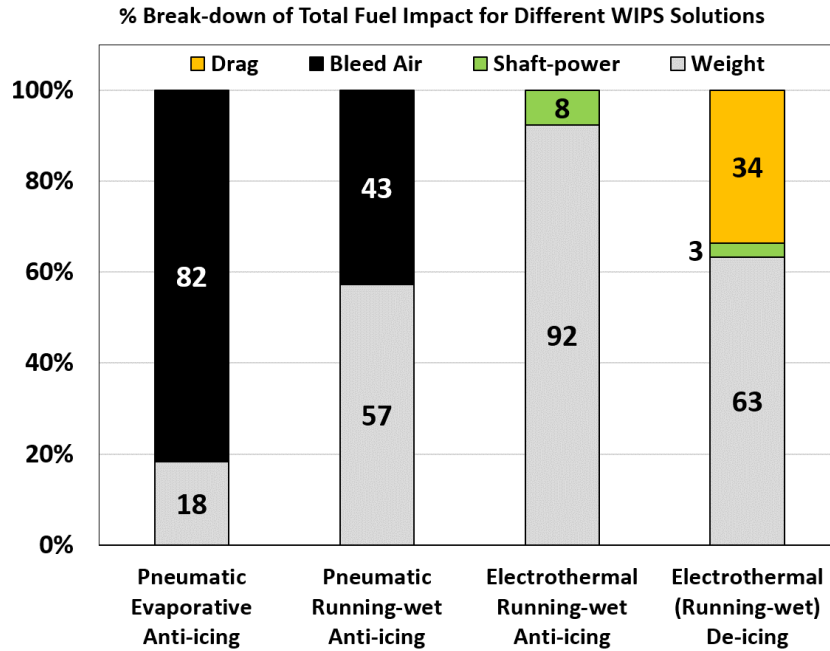
Figure 51: Decomposition of total fuel impact for different WIPS solutions into contributions from mass, secondary power requirement, and direct drag penalty

The contribution of system mass towards the WIPS TFI is much higher for the case of the electrothermal WIPS solutions. Based on the modeling approach followed in this dissertation, the masses of the heating elements themselves are identical for both an electrothermal running-wet anti-icing system and a de-icing system. However, the mass of the power control electronics, which are assumed to be proportional to the peak power requirement of the WIPS, are therefore higher for the case of the anti-icing system. For the same reason, the contribution from shaft-power off-take requirements is also higher for the electrothermal running-wet anti-icing system. For the de-icing system, there is also a direct drag contribution due to the buildup of ice during the heat-off period of the system's cycle. The drag due to ice buildup is a function of the heater-off time, which coincides with the ice buildup time. Thus, for a de-icing system, there is a tradeoff between the penalty from the electrical power requirement and the penalty from the drag increment due to ice buildup.

7.3.4 Feasibility Analysis for Electric Taxiing System (ETS)

As discussed in Chapter 4, the incorporation of an Electric Taxiing System (ETS) *always* requires addition of hardware to the aircraft and thus causes an increase in the OEW. The direct mass additions are due to the electric motors, gearboxes, and power electronics for the ETS, and due to higher-capacity APU generators and additional cabling within the EPGDS. Further, with the modeling approach followed in this dissertation, the LGAS actuators are re-sized if the incorporation of an ETS is detected, since the ETS changes the main landing gear actuating moment due to the addition of considerable mass at the lowest portion of the landing gear leg. As seen from Fig. 24 and Eq. 80, the mass addition and power requirement increase significantly with aircraft mass, leading to the general belief that ETS is suitable only for smaller aircraft flying short-haul routes. This belief was tested by analyzing the feasibility of an ETS for all three baselines - SSA, LTA, and VLA.

The intended purpose of the ETS is to save fuel, and the fuel savings (if any) depend on the relative magnitudes of fuel saved on the ground while taxiing and extra fuel consumed in-flight due to the added mass of the ETS. It was shown in §4.6.3 that the fuel savings directly depend on the time that the ETS is operational on the ground (which is the total taxiing time less the time for main engine warm-up and cool-down), and the flight distance (or duration). Since these vary significantly, the feasibility assessment of the ETS is not a single-point analysis. Therefore, for each baseline, the assessment is made for a range of trip distances and taxiing times. The results for the SSA, LTA, and VLA are summarized in Fig. 52 and Fig. 53. For each trip distance, the percentage variation in fuel consumption is computed with respect to the fuel consumption of a conventional baseline with no ETS flying the same distance.

For the SSA, it is seen from Fig. 52 that for total taxiing times in excess of 15 minutes, the ETS permits a net reduction in fuel consumption over a substantial
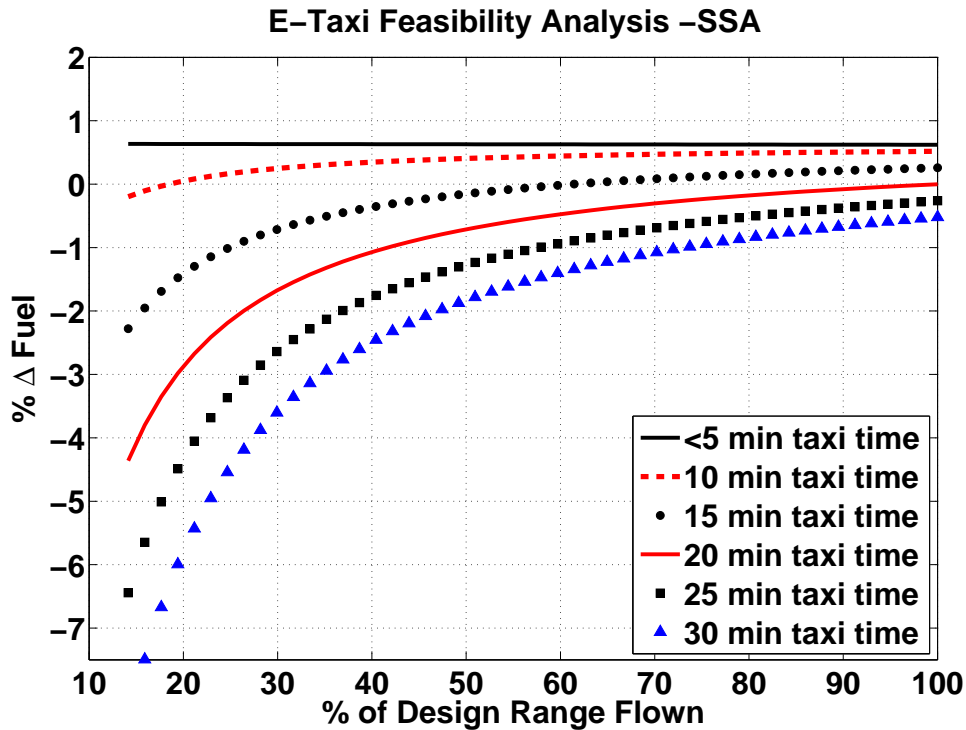
Figure 52: Electric taxiing feasibility analysis for SSA (SSA-00001)

portion of the range capability of the aircraft. Further, for total taxiing times in excess of 20 minutes, a fuel burn advantage is retained even at 100 % range. These predictions are in reasonable agreement with estimates provided by Airbus for the case of electric taxiing applied to the Airbus A320 aircraft [32]. The feasibility analysis suggests that ETS may be viable for smaller commercial aircraft that spend a significant amount of time taxiing, and which fly numerous short-haul flights at only a fraction of their maximum range capability.

On the other hand, the feasibility assessment for the LTA and VLA (Fig. 53) supports the claim that ETS is *not* suitable for aircraft of these sizes. In this case, the in-flight fuel penalty due to mass addition nullifies the fuel saved even for the longest taxiing times considered at only 45-60 % of the aircrafts' range capabilities (for shorter taxiing times, the cross-over point is even earlier). These aircraft are typically operated on long-haul trans-oceanic routes, where they are regularly flown
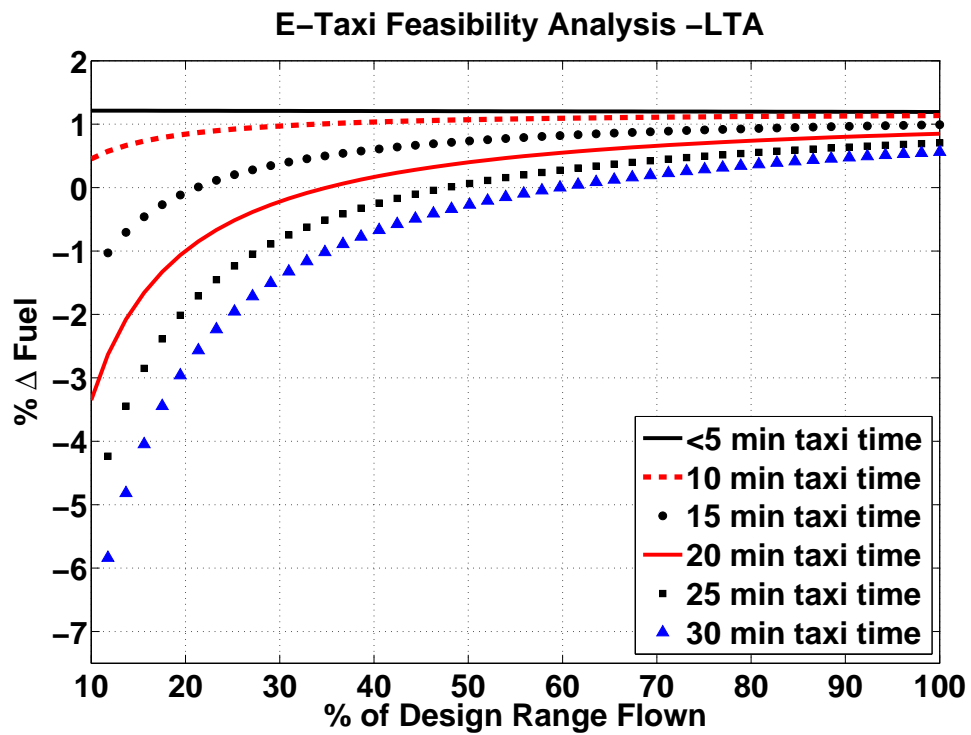
(a) Electric taxiing feasibility analysis for LTA (LTA-00001)
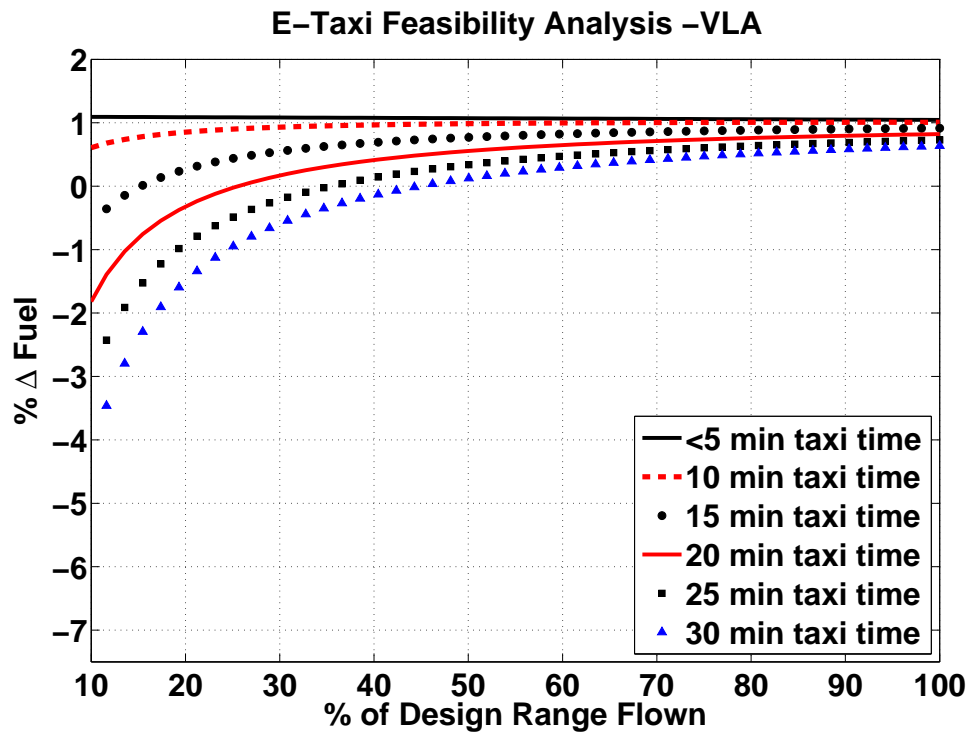
(b) Electric taxiing feasibility analysis for VLA (VLA-00001)

Figure 53: Feasibility assessment of electric taxiing for LTA and VLA

out to much larger percentages of their maximum range capability than the SSA typically is. The overall fuel penalty incurred for such operations would therefore make the incorporation of ETS on such aircraft impractical.

This assessment assumes that the incorporation of ETS is the only modification to the aircraft, i.e., all other subsystems remain conventional. If other subsystems are also electrified and have a larger favorable impact, then it is possible that the resulting architecture may in certain cases show some savings relative to the conventional baseline even in the operating areas of Fig. 53 where the sole inclusion of ETS results in increased fuel consumption. This in itself does not mean that ETS should necessarily be considered practical for larger aircraft (LTA and VLA) provided other subsystems are being electrified, since it could be counter-argued that incorporating ETS simply serves to negate some of the fuel saving potential of the other electrified subsystems. Nevertheless, since the stated goals of this dissertation include analyzing various combinatorial possibilities for subsystems and the effect of technological state-of-the-art (SOTA) on subsystem architecture performance, ETS is considered for all three baselines and not just for the SSA baseline alone.

7.4 Chapter Summary

This chapter presented experiments that verified certain capabilities of the integrated sizing and analysis environment such as (i) the automatic definition of subsystem architectures by a heuristics-based algorithm, (ii) the incorporation of information regarding engine performance characteristics into the analysis without direct integration of a higher-fidelity tool, and (iii) the decomposition of an architecture's overall impact into the contributions from individual subsystem masses, secondary power requirements, and drag increments in order to determine the focus of subsystem design efforts. The results presented and the observations made from them support the statements of Hypothesis 2.

CHAPTER VIII

SENSITIVITY OF SELECT ARCHITECTURES TO EPISTEMIC AND TECHNOLOGICAL UNCERTAINTY

It has been mentioned previously that to be suitable for a conceptual design stage analysis, the methods used to size and analyze the subsystems must allow for rapid evaluation and require only limited information regarding the design. As a result, a number of modeling simplifications or simplifying assumptions are required. In some other cases, models for novel subsystem architecture components were created and used even though there was not a large volume of reference data available with which to validate or calibrate these models. This uncertainty regarding the accuracy of the models or arising from simplifying assumptions in the modeling approach leads to a corresponding uncertainty in the predictions of subsystem architecture performance. Therefore, it is not sufficient to make conclusions regarding the predicted performance of subsystem architectures without assessing the extent to which model uncertainties influence those predictions. This assessment is presented in §8.1.

The predicted performance of a subsystem architecture is also influenced by assumptions regarding the technological state-of-the-art (SOTA). Starting with current technological SOTA, projections are typically made for the technological SOTA corresponding to a future time. However, other than basing such projections on certain historical trends (assuming such information is available), there is no way to project a future technological SOTA that is guaranteed to be accurate. The predicted performance of MEA architectures is particularly sensitive to technological SOTA, as (i) considerable challenges currently exist due to the additional electrical/electronic component mass that has to be incorporated into the aircraft, and (ii) the development

curve for these components is much steeper than those for components within a conventional architecture, which have already reached the point of technology saturation. In order to determine the variation in predicted subsystem architecture performance that is driven by assumptions regarding technological SOTA, separate sensitivity analyses are performed, and these are discussed in §8.2. For these analyses, the secondary power extraction penalties are computed using the higher-fidelity engine truth model (§7.2) and an architecture-to-engine association logic discussed subsequently in §9.2.

8.1 *Sensitivity to Epistemic Uncertainty*

A convenient way to capture the effect of model/modeling uncertainty is through the incorporation of variation factors commonly known as *K-factors*. These K-factors may be associated with model parameters that are known to be the sources of the uncertainty. The sensitivity is essentially indicated by variations in responses of interest caused by deliberate variations of the K-factors.

There are no hard-and-fast rules or guidelines regarding the number of K-factors that should be used to perform the sensitivity analysis or how they should be associated with the sources of uncertainty. In this dissertation, a selective approach is taken in which only a limited number of K-factors (identified in §8.1.1) is strategically chosen to represent major sources of uncertainty in the model. The overall sensitivities of top-level metrics such as block fuel (BF), maximum ramp weight (MRW), and operating empty weight (OEW) to all such K-factors collectively as well as to individual K-factors are then assessed.

8.1.1 Identification of Epistemic Uncertainty Parameters

Considerable uncertainty exists regarding the magnitude of the actuation loads for the actuation functions (FCAS, LGAS, NWSS, WBS, and TRAS). For the primary flight controls, the actuation loads are derived from an estimate of the hinge moments.

These depend on the definition of the control surface relative to the main lifting surface, however the control surface dimensions are finalized later in the design process. Similarly, the identification of the flight conditions yielding the maximum hinge moment for these control surfaces requires estimation of key speeds such as maneuver speed, design cruise speed, and design dive speed, and certain stability and control coefficients. These too are not known with complete certainty during early design. The magnitude of the actuating loads for the high-lift devices varies considerably depending on the flap mechanism kinematics [66], which are not finalized until later in the design process.

Similar uncertainty exists for the actuation loads for subsystems associated with the landing gear group. Landing gear actuation loads are affected by both the estimate of the landing gear leg mass (which is also affected by the estimates of the masses of the associated subsystems such as the brakes and the steering mechanism) and details regarding the mechanism kinematics. These affect the sizing and thus the mass of the LGAS actuators. The NWSS actuation load depends on several key geometric characteristics such as the rake angle and the tire trail, for which only estimates from preliminary design guidelines are available. A similar argument also applies for the case of brake actuation loads, which affect the flow requirements of hydraulic brakes and the mass and power requirements of electric brakes. TRAS actuation power requirements are inferred from a very limited set of data, and are also uncertain.

In general, it is impossible to say *a priori* whether the predicted actuation loads will be under-predictions or over-predictions. In fact, it is possible that some of the actuation loads described above are under-predicted, while others are over-predicted. While an exhaustive sensitivity analysis is possible in which a sensitivity factor or K-factor is associated with each and every actuation load, the overall sensitivity of the architecture's performance to actuation load predictions may also be assessed by the use of a single K-factor for all actuation loads. This K-factor $K_{act-loads}$, which is

255

of a multiplicative nature, is assumed to modify either actuation loads (when these are computed directly) or actuation power requirements.

While the activities for the LGAS, NWSS, WBS, TRAS, and the high-lift devices of the FCAS are reasonably well defined in terms of when in the flight they occur and for what duration, the same is not the case for the activities of the primary flight control surfaces and spoilers of the FCAS. The amplitudes of their excursions are dependent upon the required maneuvering authority, the magnitudes of atmospheric disturbances and the effectiveness of the individual control surfaces. The duration of such activity (as a function of total mission time) is also dependent upon atmospheric conditions. For example, while cruising under calm atmospheric conditions, there may be very little control surface movement, while considerable control surface movements may be required to stabilize the aircraft's trajectory and attitude under gusty or turbulent conditions. To account for these uncertainties, two additional K-factors are defined for the FCAS. The first factor $K_{fcas-amp}$ multiplies with the peak amplitude of assumed control surface excursions δ_{peak} (Eq. 44 of §4.1.9), while the second factor $K_{fcas-acti}$ multiples with the activity factor ϵ (Eqs. 47 and 48 of §4.1.9).

For the ECS analysis, the heat transfer rate through the fuselage walls is computed based on an estimate of the total heat transfer area and the effective thermal resistance across the fuselage skin. The trend seen in modern aircraft is towards the increased use of composite materials for the aircraft structure. The thermal conductivity of composites is typically less than that of metallic skin, which has the effect of reducing the rate of heat transfer across the fuselage wall for the same temperature gradient. At the same time, the contributors to the internal heat load, such as the galley and IFE loads, show an increasing trend in modern aircraft. Further, the effect of direct solar radiation incidence on the fuselage and solar radiation through transparencies are not accounted for in the current analysis. The net effect of each of the factors mentioned above is to increase the net heat load that the ECS has to *remove* from

the cabin in order to maintain it at the desired temperature, which is modeled using a single multiplicative K-factor $K_{ecs-load}$ to multiply the $\dot{Q}_{int}$ term of Eq. 94 (§4.7).

For the ice protection systems (WIPS and CIPS), there is uncertainty regarding (i) the estimate of the surface area for which ice protection is required, (ii) the estimate of the heat flux required to provide ice protection to a protected surface for a given set of flight and atmospheric conditions, and (iii) the assumed overall efficiency of the IPS layout for both pneumatic and electrothermal IPS setups. The ultimate consequence of (i)-(iii) is uncertainty regarding the net heat rate of the WIPS and CIPS, which affects the required bleed air mass flow rate for pneumatic IPS and the required electric power demand for electrothermal IPS. As with the actuation loads, it is not possible to say *a priori* whether the analysis approach employed will result in an under-prediction or an over-prediction of the required heat rate. Further, it is possible to under-predict the WIPS loads while over-predicting the CIPS loads, or vice versa. In order to analyze the variation of responses subjected to this uncertainty, a single multiplicative K-factor $K_{ips-load}$ is linked to the computed IPS bleed air and electric power requirement (Eqs. 125 and 127 of §4.8.6).

For the EPGDS, the total mass of electrical cables is computed by summing contributions from each electrical connection, which are of the form $M_{cbl}(P_{in}, L) = \kappa_{inst}\, \mathcal{K}_{cbl}\, P_{in}\, L$. Variations in the computed mass may occur due to (i) variations in mass properties and electrical properties of the conducting material (affecting $\mathcal{K}_{cbl}$), (ii) variations in cabling length L due to the need to avoid obstacles, (iii) variations in installation factor κ_{inst} caused by attachments and fittings. These are captured through a multiplicative K-factor K_{cbl-wt} which multiplies the computed mass of each cable. In an exactly similar manner, a multiplicative K-factor $K_{duct-wt}$ is used to multiply the computed mass of each duct within the PPGDS to account for mass variations due to the same causes.

The K-factors discussed above and their ranges are summarized in Table 29. The

Table 29: Summary of model sensitivity parameters

K-factor	Subsystem(s) affected	Range
$K_{act-loads}$	FCAS, LGAS, NWSS, WBS, TRAS	[0.75, 1.25]
$K_{fcas-amp}$	FCAS	[0.50, 2.00]
$K_{fcas-acti}$	FCAS	[0.50, 2.00]
$K_{ecs-load}$	ECS	[1.00, 2.00]
$K_{ips-load}$	WIPS, CIPS	[0.50, 2.00]
K_{cbl-wt}	EPGDS	[0.75, 1.25]
$K_{duct-wt}$	PPGDS	[0.75, 1.25]

ranges for each factor were determined through engineering discretion and based on the perceived accuracy of the modeling approaches that are utilized. Instead of performing the sensitivity analysis for all 512 subsystem architectures of Table 4, the following architectures are down-selected for the SSA, LTA, and VLA (Note: the numbering scheme is explained in Fig. 9):

1. Arch-00000 (SSA-00000, LTA-00000, VLA-00000): the baseline with conventional subsystems architecture

2. Arch-70000 (SSA-70000, LTA-70000, VLA-70000): fully-electrified actuation functions, but retaining pneumatics for ECS, WIPS, and CIPS

3. Arch-03310 (SSA-03310, LTA-03310, VLA-03310): electrified ECS, WIPS, and CIPS, but retaining conventional hydraulics for actuation functions

4. Arch-73310 (SSA-73310, LTA-73310, VLA-73310): AEA with electrification of all subsystems (all hydraulics and pneumatics removed)

For each of the subsystem architectures chosen for analysis, a full-factorial set of K-factor combinations is considered, with each K-factor permitted two levels corresponding to the upper and lower bounds shown in Table 29. This leads to $2^7 = 128$ case evaluations for each of the four subsystem architectures for each of the three aircraft sizes (a total of 128 x 4 x 3 = 1,536 architecture evaluations).

8.1.2 Assessment of Architecture Sensitivities

Regardless of the aircraft size (SSA, LTA, or VLA), many similarities were noted in the sensitivities exhibited by the four selected subsystem architectures. Therefore, only the results from the sensitivity analysis for the SSA are presented in the main text, while those for the LTA and VLA are presented in Appendix B.1.

The *overall* sensitivities of the four chosen subsystem architectures to the epistemic uncertainty parameters for the case of the SSA are shown in Fig. 54. The percentage changes in block fuel (BF), maximum ramp weight (MRW), and operating empty weight (OEW) are all computed relative to the conventional baseline with all K-factors set to unity. The dots represent the four architectures with all K-factors set to unity. For K-factor values other than unity, the position of the architecture on the plots shifts. The individual shifted positions corresponding to all the K-factor settings are not shown. Instead, the dotted lines represent the convex hull of the region occupied by the shifted architectures. It is clear that the most desirable location for any architecture on the BF-MRW and BF-OEW plots is in the lower-left quadrant (indicating lower BF, RW, and OEW relative to the baseline). However, as mentioned previously, it is possible for MEA architectures to be heavier than their conventional counterparts in terms of equipment weight. Therefore, it is possible to have architectures in which the RW and OEW are higher than those for the baseline, but the BF is less than that of the baseline. This situation corresponds to the upper-left quadrant of one or both plots. For architectures falling in the remaining two quadrants (lower-right and upper-right), the BF is higher than that of the baseline, and therefore, these are not competitive architectures.

Since the baseline itself is affected by the K-factors listed in Table 29, the movement of the baseline architecture SSA-00000 on the plots is first established in Fig. 54. The original position of the all-electric actuation architecture, SSA-70000, is seen to be in close proximity to that of SSA-00000. Therefore, the regions
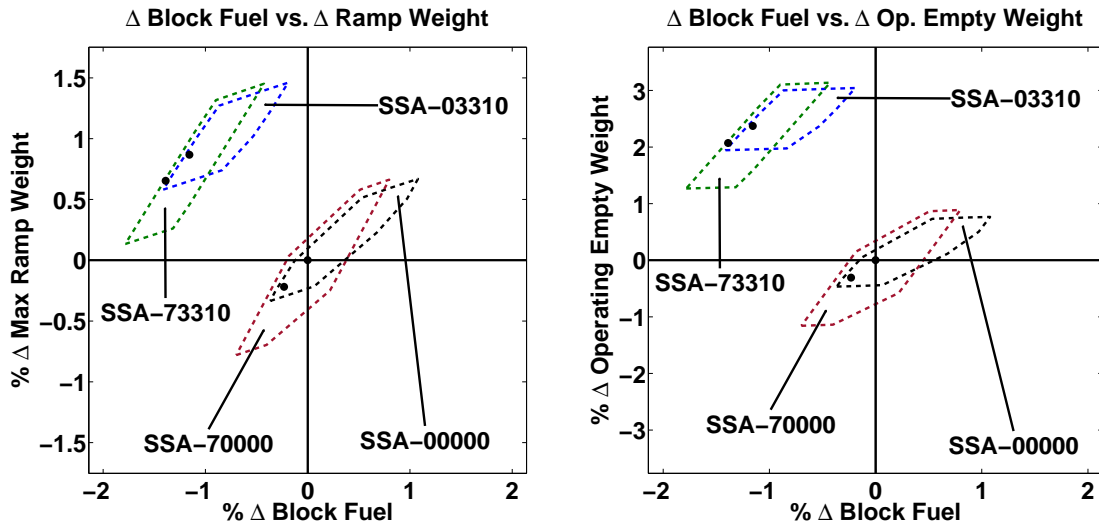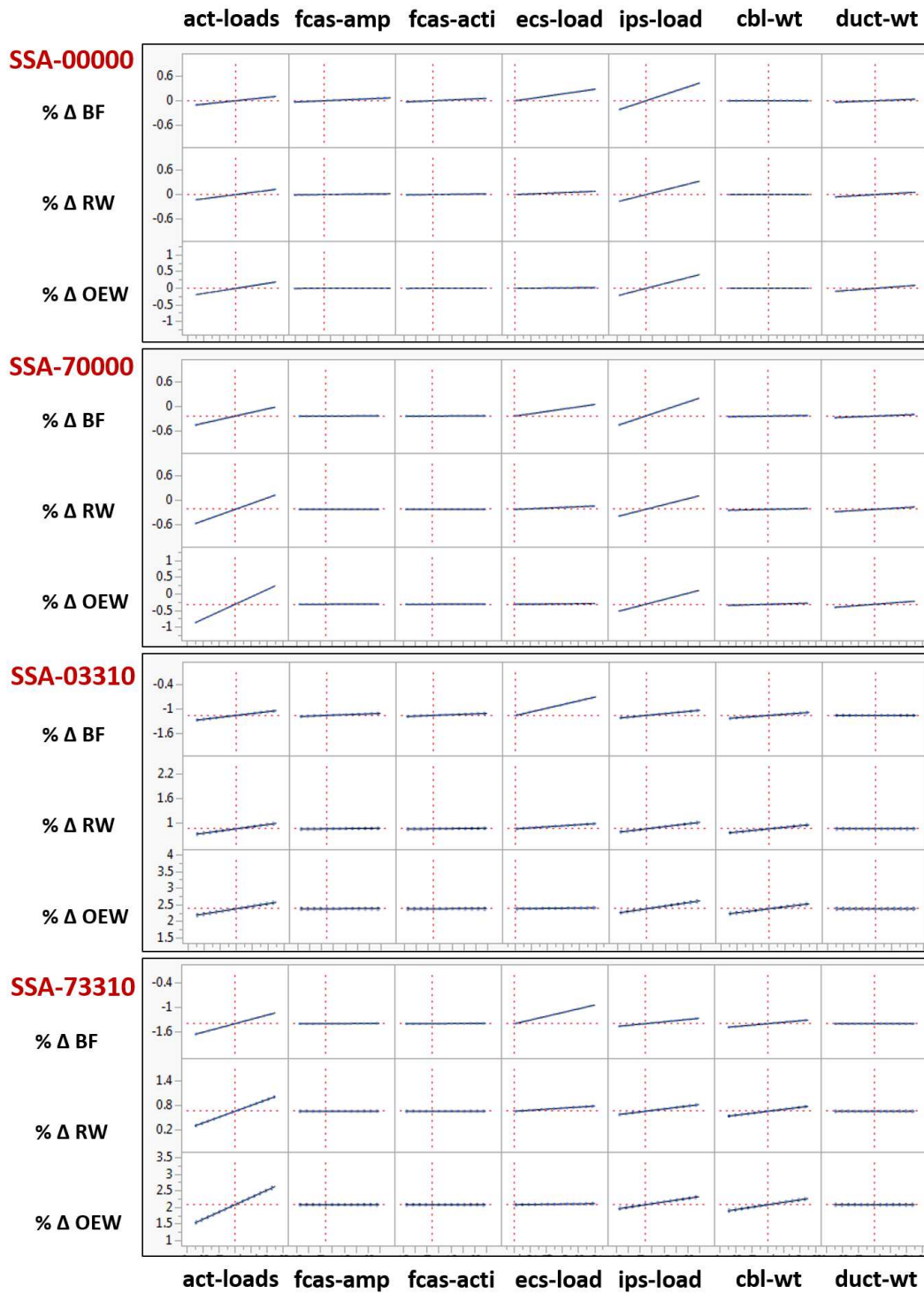
Figure 54: Gross sensitivity of SSA-00000, SSA-70000, SSA-03310, and SSA-73310 to epistemic uncertainty K-factors

corresponding to these two architectures naturally overlap. Inspecting the nature of the overlap, the only conclusion that can be drawn from these plots is that the degradation in performance of SSA-70000 in the worst-case scenario is less than that of SSA-00000 for its worst case scenario. Also, the improvement for SSA-70000 for the best-case scenario is more than that of SSA-00000 for its best-case scenario.

Inspection of the convex hulls for architectures SSA-03310 and SSA-73310 reveals that there are no quadrant-crossings for these two architectures due to the variation of the epistemic uncertainty K-factors. Thus, a fuel burn advantage is predicted for these two architectures (relative to the baseline SSA-00000 with all K-factors set to unity) over the entire range of variation of the K-factors. Between SSA-03310 and SSA-73310, the sensitivity of the OEW and RW of SSA-73310 to the variation of the K-factors is seen to be greater. Similar observations apply to the corresponding subsystem architectures for the LTA and VLA (Appendix B.1).

It is not possible to determine the impact of the individual K-factors listed in Table 29 on the BF, OEW, and MRW from inspection of Fig. 54 alone. For this. it is necessary to inspect Fig. 55, which shows the sensitivities of BF, OEW, and MRW

260

Figure 55: Impact of individual epistemic uncertainty K-factors on performance of SSA-00000, SSA-70000, SSA-03310, and SSA-73310

261

of the SSA architectures to the individual K-factors (corresponding sensitivities for the LTA and VLA are presented in Appendix B.1). In this plot, in which the plotting ranges for BF, OEW, and MRW are identical for all four architectures, the sensitivity of a response (BF, OEW, or MRW) to a particular K-factor is directly related to the slope of the corresponding line. The following observations may be made regarding the effects that the K-factors have on each of the architectures analyzed:

1. $K_{act-loads}$: The sensitivity of BF, RW, and OEW to this K-factor depends on whether the actuation functions are all-hydraulic or all-electric. It is seen that the sensitivity is greater in case of all-electric actuation. This is due to the fact that electric actuator power-to-mass and force-to-mass ratios are assumed to be inferior to those of their hydraulic counterparts for current technological SOTA. Therefore, the same variation in the magnitude of the actuation load causes larger variations in electric actuator mass than in hydraulic actuator mass. The sensitivity increases with aircraft size due to the larger number of control surfaces (thus larger number of actuators in total) and higher actuation loads per control surface

2. $K_{fcas-amp}$ and $K_{fcas-acti}$: The sensitivity of BF, RW, and OEW to these two K-factors is seen to be marginal for all three aircraft. The sensitivity of BF is only marginally higher for the case of hydraulic actuation. This is due to the fact that hydraulic actuation power requirements are proportional to the rates of the control surfaces (Eq. 48), whose mission-averaged value increases with both these K-factors. The electric actuation power requirement, as seen from Eq. 47, is a more complex function depending not only on excursion amplitude but also on the rate at which hinge moments change with unit control surface deflection. The conclusion that may be drawn is that while control surface duty cycles affect actuator design significantly (more so for electric actuators [161, 162]), the impact on top-level parameters (BF, OEW, and MRW) is not as significant

3. $K_{ecs-load}$: This K-factor has no effect on OEW for any of the SSA and LTA architectures. This indicates that for these two aircraft, even though the net ECS heat load increases significantly in magnitude, it is not sufficient to require an increase in the mass flow rate (in other words, the lower bound for cabin inlet temperature is not reached). Such an increase in mass flow rate would otherwise have resulted in an increase in electric ECS mass due to higher-rating CACs, motors, and power electronics being required. As the mass flow rate requirement does not change, neither do the secondary power requirements of both pneumatic ECS and electric ECS. Therefore, the change in BF is caused by an increase in *ram drag* due to increased ram air flow requirement across the ECS pack heat exchangers. The effect is seen to be slightly more pronounced for the case of electric ECS, indicating that the increase in cooling airflow requirement is higher in this case. However, since ECS pack optimization was not attempted for either the conventional or electric ECS, no further conclusion can be drawn from this observation. For the VLA, the increased ECS load *does* result in the lower bound for cabin inlet temperature being reached. As a result, the mass flow rate of supply air has to be increased, resulting in increased penalty from bleed air and shaft-power extraction for the VLA architectures with pneumatic and electric ECS respectively

4. $K_{ips-load}$: This K-factor has a more pronounced effect on conventional pneumatic IPS than on electrothermal IPS for all three aircraft sizes. Since the masses of the heater mats of the electrothermal IPS are computed on a mass-per-unit-area basis and those of the piccolo tubes of the pneumatic IPS on a mass-per-unit-length basis, the masses of the IPS do not change in either case due to the variation in $K_{ips-load}$. Variations in IPS heat load clearly affect the bleed air requirement of the pneumatic IPS and the electric power requirement of the electrothermal IPS. However, since the IPS operates for a reasonably small

fraction of the flight, the observed effect on block fuel is only partially due to the increased off-takes. The majority of the effect is due to the variations in OEW of the aircraft. For pneumatic IPS, this is due to the variations of PPGDS duct and precooler sizes based on the IPS bleed air requirements. For electrothermal IPS, this is due to variations in EPGDS cable and generator masses caused by variations in IPS power requirement

5. K_{cbl-wt} and $K_{duct-wt}$: These two K-factors represent variations in electrical cable and pneumatic duct masses caused by material properties or under/over-estimates of their lengths. Since the pneumatic system is invariant between SSA-00000 and SSA-70000, so is the sensitivity to $K_{duct-wt}$ for these two architectures. Since the pneumatic system is removed for SSA-03310 and SSA-73310, the effect of this K-factor is naturally nil. The effect of K_{cbl-wt} increases from SSA-0000 to SSA-73310 due to the incorporation of progressively more electrical cabling. The sensitivity to these two K-factors increases slightly with vehicle size, presumably due to the fact that the net ducting and cable mass increases with vehicle size

8.2   Sensitivity to Assumed Technological State-of-the-Art

A similar parsimonious approach is taken to identifying the technology K-factors with which to assess the effect of assumed or projected technological SOTA on the performance of subsystem architectures.

8.2.1   Identification of Technology Uncertainty Parameters

For the actuation functions (FCAS, LGAS, NWSS, WBS, TRAS), electric actuators are currently assessed as being heavier than their conventional hydraulic counterparts. With the progression of technology, the power-to-mass or force-to-mass ratios of the electric actuators will certainly increase. However, it would be improper to associate

a technology K-factor directly to such figures of merit. This is due to the fact that not all sub-components of an electric actuator are likely to see improvements of the same order of magnitude. For example, the main components of an EHA are the electric motor and power electronics, a hydraulic pump (and perhaps an accumulator), and a hydraulic piston/cylinder arrangement. The pump, accumulator, and piston/cylinder are traditional hydraulic components whose design has already reached a high degree of refinement. Therefore, it could be argued that mass reductions occurring for an EHA would *not* stem primarily from these components. Similarly, the major components of an EMA are the electric motor and power electronics, a gearbox, and a ballscrew. The gearbox and the ballscrew are traditional mechanical components which have been similarly refined over a long period. Thus, mass reductions for these actuators (and other electric actuators as well) would likely stem primarily from motors and power electronics with higher power-to-mass ratios. Therefore, it is more logical to associate the K-factors with the motor and power electronics power-to-mass ratios than with the overall figure of merit of the actuators themselves. It was this thought process, in fact, which motivated the generic electric actuator mass estimation relationship that was developed and discussed previously (Chapter 4, Eq. 31).

Motors are not merely limited to electrified actuation subsystems, but also to major subsystems like electric ECS, where the CACs are driven by electric motors. Many considerations go into the selection of the type of motor for a particular application (even different types of actuators may employ different types of motors), and increases in power-to-mass ratio due to technology improvements need not necessarily be of the same magnitude for each motor design. However, in the early design phases, there may be insufficient information available regarding the type of motor most suitable for a given application. The interest lies in determining or bounding the extent to which improvements in electric motor technology may affect the performance of electrified architectures in which they are present. As a result,

a single K-factor $K_{em-sota}$ is used "across-the-board" to represent the technology improvement for all electric motors for all subsystems.

A similar across-the-board approach is taken for characterizing improvements in power electronics technology. Power electronics will be pervasive within MEA architectures, especially if variable-frequency generation is used, since almost all individual loads will require power regulation prior to use [142]. Similar to electric motors, significant differences in design exist for power conversion equipment, and it is also unlikely that the improvements in power-to-mass ratio will be uniform for all such designs. However, for the same reason stated for electric motors, a single K-factor $K_{pe-sota}$ is used to represent improvements in technological SOTA for power electronics for all subsystems.

The electrification of the ECS requires the incorporation of significant hardware (thus significant mass), part of which comes from the mass of the CACs. Therefore, a K-factor $K_{cac-sota}$ is applied to assess the effect of improvements in technological SOTA for this component. It is not clear whether improvements in the power-to-mass ratio of CACs can be of the same magnitude as improvements for motors and power electronics. However, similar ranges were set for $K_{cac-sota}$ as for $K_{em-sota}$ and $K_{pe-sota}$.

As the required power generation capability increases with progressively greater electrification of the major aircraft subsystems, the mass of the generators (EDGs and APUGs) also increases significantly. Therefore, improvements in the technological SOTA (power-to-mass ratio) of generators would clearly have an effect on the net addition of mass to the EPGDS. This effect is modeled using the K-factor $K_{gen-sota}$.

A final K-factor $K_{apu-start}$ is used to model the effect of factoring in the power generation capacity of the APU generators into the sizing of the EDGs. Therefore, this is not a technology K-factor in the strict sense of the word, since no improvements in APU technology are being modeled using it. Instead, a setting of $K_{apu-start} = 0$ simply indicates that APU generator capacity *cannot* be factored into the sizing of the

Table 30: Summary of technological SOTA K-factors

| K-factor	Subsystem(s) affected	Settings
$K_{em-sota}$	actuation, ECS	{1,2,3}
$K_{pe-sota}$	actuation, ECS, EPGDS	{1,2,3}
$K_{cac-sota}$	ECS	{1,2,3}
$K_{gen-sota}$	EPGDS	{1,2,3}
$K_{apu-start}$	EPGDS	{0,1}

EPGDS, while $K_{apu-start} = 1$ assumes that the EDG ratings can be down-sized based on the availability of the APU generation capacity in contingency/failure scenarios.

Table 30 summarizes the technology K-factors discussed above along with the discrete settings of each for which the architectures were assessed. In all cases, the setting of $K_{(.)} = 1$ for the technology K-factors indicates current technological SOTA, while settings $K_{(.)} = 2$ and $K_{(.)} = 3$ indicate respectively a two-fold and three-fold improvement in the SOTA. The impacts of technology SOTA on the performance of the following SSA, LTA, and VLA subsystem architectures are assessed:

1. Arch-70000 (SSA-70000, LTA-70000, VLA-70000): fully-electrified actuation functions, but retaining pneumatics for ECS, WIPS, and CIPS

2. Arch-03310 (SSA-03310, LTA-03310, VLA-03310): electrified ECS, WIPS, and CIPS, but retaining conventional hydraulics for actuation functions

3. Arch-73310 (SSA-73310, LTA-73310, VLA-73310): AEA with all subsystems electrified (all hydraulics and pneumatics removed)

4. Arch-73311 (SSA-73311, LTA-73311, VLA-73311): AEA with all subsystems electrified (all hydraulics and pneumatics removed), with ETS installed

8.2.2 Assessment of Architecture Sensitivities

The overall sensitivity of each of the above architectures to variations in the technology K-factors is shown in Fig. 56. Similar figures for the LTA and VLA are
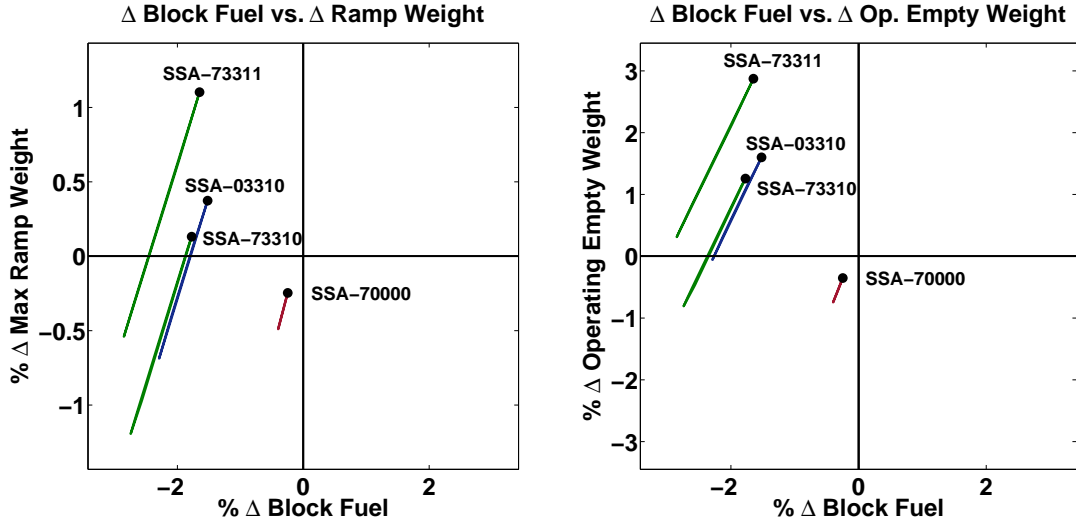
Figure 56: Gross sensitivity of SSA-70000, SSA-03310, SSA-73310 and SSA-73311 to technological SOTA

presented in Appendix B.2. For each architecture, the marker represents the location of the design with all technology K-factors set to unity, while the line emanating from each marker shows the direction of movement of the design when the technology K-factors are varied.

Since the variations in the technology K-factors lead to the reduction of masses of motors, power electronics, CACs and generators, the net impact is a reduction in vehicle mass. Thus, the lines seen in the plots are the sensitivities of the MRW and the BF to changes in the OEW. That the relationship is approximately linear can be established starting with a manipulation of the Breguet range equation (for cruise flight only) to yield the fuel burn penalty due to an increment in OEW:

$$\Delta BF = \Delta OEW \ \left\{ e^{c_t R/(V(L/D))} - 1 \right\} = \mathcal{E} \ \Delta OEW \tag{175}$$

From the above, it is easy to show that the three %-Δ quantities being plotted are related through the following:

$$\begin{aligned}
\left(\frac{\Delta BF}{BF} \right) &= \mathcal{E} \left(\frac{OEW}{BF} \right) \left(\frac{\Delta OEW}{OEW} \right), \\
\left(\frac{\Delta MRW}{MRW} \right) &= (\mathcal{E} + 1) \left(\frac{OEW}{MRW} \right) \left(\frac{\Delta OEW}{OEW} \right).
\end{aligned} \tag{176}$$

Thus, it is established that %-Δ BF and %-Δ MRW are linearly related to %-Δ OEW. The magnitude of %-Δ OEW is greater for the more heavily electrified architectures (in which motors, power electronics, CACs, and generators account for a higher percentage of the OEW), and therefore, it follows that %-Δ BF and %-Δ MRW magnitudes are greater for those architectures as well. As a result, for each aircraft size (SSA, LTA, and VLA), the net displacement of the architecture on the plot increases with increasing electrification of the subsystem architecture.

An interesting observation can be made by comparing architectures SSA-73310 and SSA-73311, between which the only difference is the inclusion of the Electric Taxiing System (ETS). With all technology K-factors set to unity, SSA-73311 has a slight fuel burn penalty relative to SSA-73310. This is due to the fact that the extra fuel consumed transporting the mass of the e-Taxi system over the mission exceeds the mass of fuel saved while taxiing on the ground with the ETS for the assumed taxiing duration. However, with $K_{em-sota} = K_{pe-sota} = 3$, there is a substantial reduction in the mass penalty associated with the ETS motors and power electronics. In that case, SSA-73311 has a slight fuel burn advantage relative to SSA-73310. However, this is not the case for the LTA and VLA (Appendix B.2), for which the installation of ETS continues to result in an overall degradation in fuel burn performance.

The individual impacts of the technology K-factors on the BF, OEW, and MRW may be analyzed by inspection of Fig. 57, which is for the SSA. Similar figures for the LTA and VLA are presented in Appendix B.2, since the significant trends are similar for all three aircraft sizes. In these plots, the plotting ranges for BF, OEW, and MRW are identical for all four architectures. Therefore, the sensitivity of a response (BF, OEW, or MRW) to a particular K-factor is directly indicated by the slope. The curvature indicates diminishing returns with continuing improvement in the technology SOTA. The following observations may be made regarding the effects that the technology K-factors have on each of the architectures analyzed:
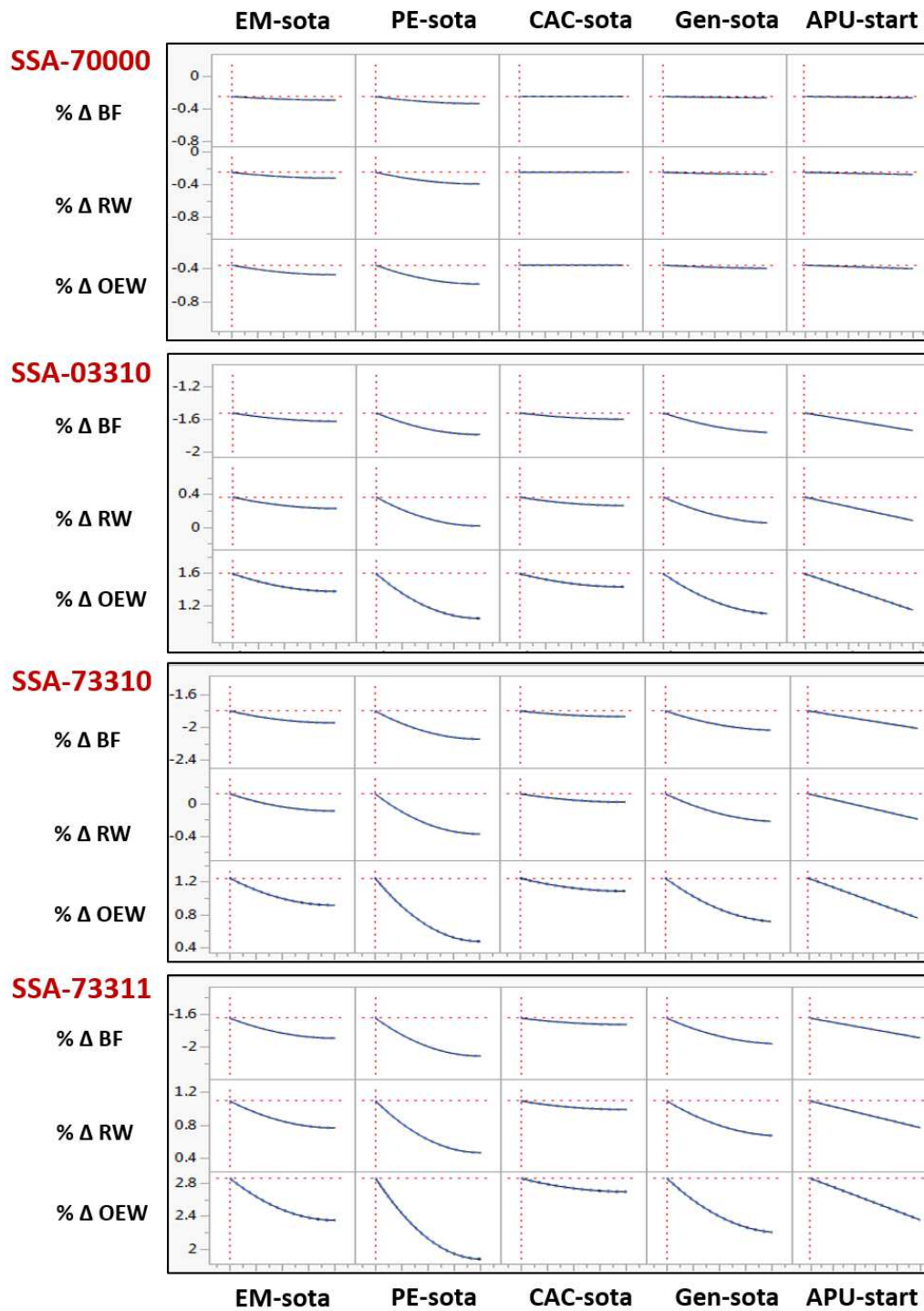
Figure 57: Impact of individual technological SOTA K-factors on performance of SSA-70000, SSA-03310, SSA-73310, and SSA-73311

1. $K_{em-sota}$: The impact of motor power-to-mass ratio (SOTA) increases as the total contribution of motors to OEW increases. Therefore, it is quite prominent for SSA-73310, which has electric motors for all actuation functions as well as to drive the ECS CACs. However, the effect on SSA-73311 is greater still, due to the presence of high power-rating electric motors for the ETS

2. $K_{pe-sota}$: The impact of power electronics power-to-mass ratio increases with the increasing proliferation of power electronic components into the subsystem architecture. Within the analysis volume for SSA-70000, these include the power converters for the actuators and also the ATRUs which convert AC power to DC power. However, the effect is greater for SSA-03310 due to the high rating of the CAC power electronics and the increased rating of the ATRUs. It is greater still for SSA-73310 which combines electric actuation with electric ECS. Finally, the impact on SSA-73311 is greatest due to the additional power electronics for the ETS. Similar trends are also seen for the LTA and VLA (Appendix B.2)

3. $K_{cac-sota}$: The impact of CAC power-to-mass ratio is seen to be less pronounced than that of motor and power electronics power-to-mass ratio. It should also be noted that it is uncertain whether a three-fold increase in the SOTA of a compressor is feasible

4. $K_{gen-sota}$: The impact of generator power-to-mass ratio naturally increases as the required total capacity of the EPGDS increases, and is thus highest for the All Electric subsystem architectures (SSA-73311, LTA-73311, and VLA-73311) due to the additional APU generator capacity required for the ETS and ground operation of the ECS, and additional EDG capacity to support all electrified subsystems in-flight

5. $K_{apu-start}$: Taking the power generation capability of the APU generators into account allows the main engine generators to be sized to a lower power rating,

thus saving weight. This has a direct effect on the OEW, which subsequently affects the BF and MRW. The magnitude of the weight savings is directly related to the power rating of the APU generators, and is greatest for architectures in which the ECS is electric and/or an ETS is installed. In these cases, the APU generator capacity has to be up-sized to be able to support these extra loads. However, it should be noted that there are other practical considerations that may also determine whether it is feasible to consider the APU generator capacity while sizing the main engine generators. First, this would require a guarantee that the APU can be re-started at any point in the flight envelope. Second, it may not be possible to dispatch the airplane with an inoperative APU generator

8.3   Chapter Summary

In this chapter, the sensitivities of certain select subsystem architectures to epistemic and technological uncertainties were evaluated in order to address Research Question 3. This was performed through the judicious association of a limited number of K-factors with internal model parameters to represent epistemic uncertainty (Expt. 3a) or with the assumed state-of-the-art for a particular technology (Expt. 3b). For architectures that had a reasonable performance advantage relative to the baseline, the variation of K-factors representing epistemic uncertainty affected the magnitude of the advantage but not its existence. This was not the case for architectures that had only a marginal advantage relative to the baseline, in which case the continued existence of such an advantage could not be guaranteed. When technology K-factors were used to simulate advancement in the SOTA of electric motors, power electronics, and generators, the greatest performance improvement was observed for subsystem architectures where these components were present in higher capacities. The fact that trends and sensitivities of this nature can be detected and analyzed using this approach confirms the sub-statements of Hypothesis 3.

CHAPTER IX

EVALUATION OF SUBSYSTEM ARCHITECTURES
# WITHIN MATRIX OF ALTERNATIVES

In preceding chapters, one-to-one comparisons between subsystem architectures were described and the sensitivities of selected subsystem architectures to epistemic and technological uncertainty were investigated. In this chapter, the relative performances of all architectures within the architectural design space defined in Table 4 (Chapter 3) are analyzed for the SSA, LTA, and VLA (§9.1). Additionally, the effect of factoring in the subsystem architecture secondary power requirements into the sizing and selection of the engine is shown as a special case for the SSA (§9.2). Finally, a case study is presented in which it is assumed that electric and hydraulic actuators sized for the same actuation requirements have identical mass (§9.3).

9.1 Assessment of Relative Performance of Architectures for SSA, LTA, and VLA

All 512 subsystem architecture combinations present within the Matrix of Alternatives presented in Table 4 (Chapter 3) are evaluated for the SSA, LTA, and VLA. For these evaluations, the impacts of secondary power off-takes are represented using the simplified method with constant penalty coefficients (as introduced in Chapter 6). In each case, the vehicles are re-sized to the same wing loading, thrust-to-weight ratio, and tail volume coefficients as the baseline (regardless of whether re-sizing improved or degraded performance). The results are summarized in Fig. 58, where the Block Fuel (BF), Operating Empty Weight (OEW), and Maximum Ramp Weight (MRW) of the architectures are shown as %-Δ quantities relative to the corresponding quantities for the baseline with conventional subsystem architecture.
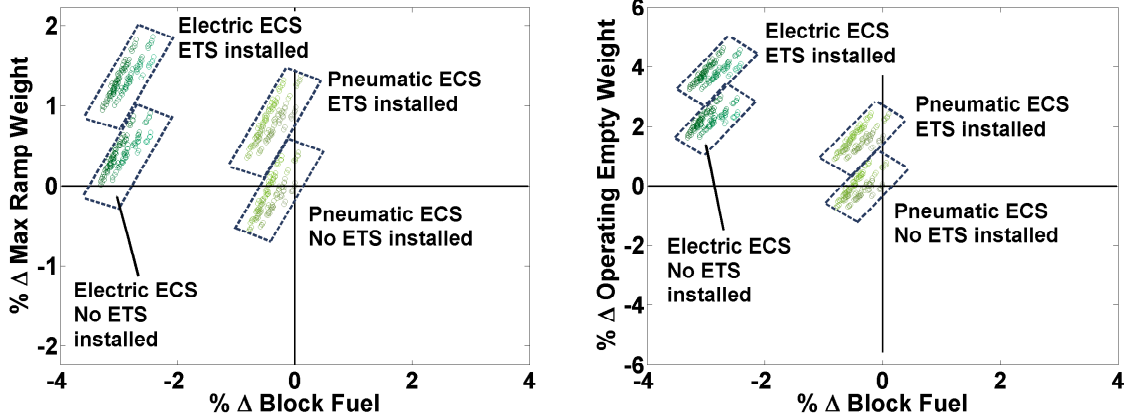
(a) Relative performance of 512 subsystem architectures for SSA
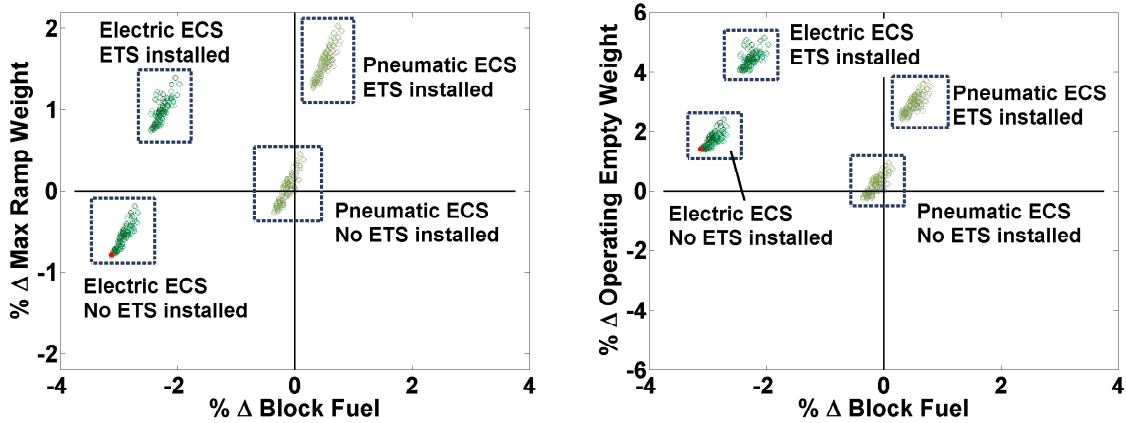
(b) Relative performance of 512 subsystem architectures for LTA
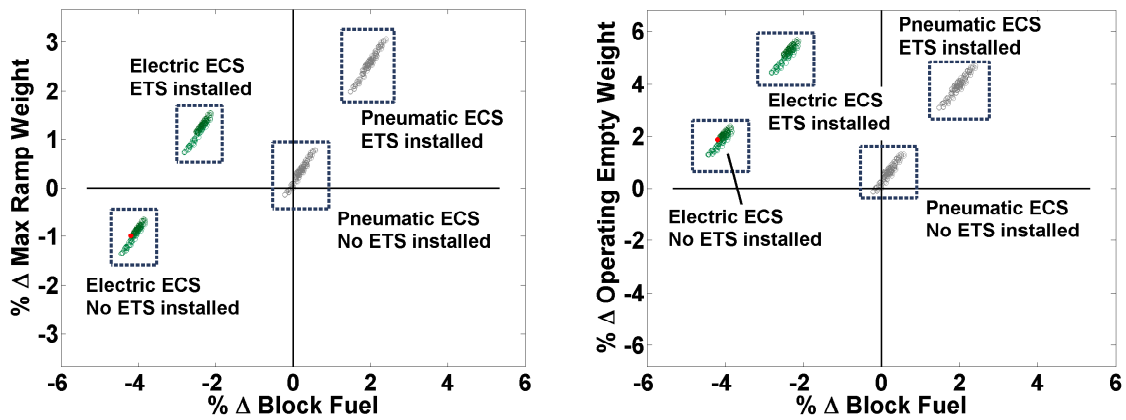
(c) Relative performance of 512 subsystem architectures for VLA

Figure 58: Comparison of 512 subsystem architectures for SSA, LTA, and VLA

274

As a result, these baselines (SSA-00000, LTA-00000, and VLA-00000) occupy the origins of the respective plots. Inspection of Fig. 58 shows that for all three vehicle sizes, the architecture combinations fall within one of four clusters. Inspection of the subsystem architectures of points within each cluster reveals that cluster affiliation is determined by the subsystem solution for the ECS (pneumatic or electric) and the presence/absence of the ETS. Each of the four clusters is described briefly:

1. Cluster 1 (Pneumatic ECS, no ETS installed): Designs within this cluster are in the vicinity of the origin. Some of the designs show improvements in fuel consumption relative to the baseline, while others show a degradation. For the SSA, the majority of the designs within this cluster show improvement in fuel consumption, while the reverse is true for the VLA

2. Cluster 2 (Electric ECS, no ETS installed): Designs within this cluster show the greatest improvement in fuel consumption, whose magnitude is the greatest for the VLA. For the LTA and the VLA, designs within this cluster also show reductions in MRW. For all three vehicles, architectures within this cluster have higher OEW than the baseline architecture

3. Cluster 3 (Electric ECS, ETS installed): Designs within this cluster show an increase in both OEW and MRW relative to the baseline. For the SSA, this cluster is offset almost directly upwards relative to Cluster 2. For the LTA and VLA however, the offset is upward and to the right. Therefore, for each point within Cluster 3 for the LTA and VLA, the fuel burn performance is worse compared to the corresponding point in Cluster 2 which lacks the ETS. Essentially, this indicates that regardless of the solutions employed for other subsystems, the inclusion of ETS for the LTA and VLA is impractical

4. Cluster 4 (Pneumatic ECS, ETS installed): All points within this cluster are heavier in terms of OEW and MRW. For the LTA and VLA, designs within this

cluster consume more fuel than the baseline. This is simply further proof that the incorporation of ETS is infeasible for vehicles of this size (this was also seen previously in §7.3, where the feasibility of ETS was addressed)

It is clear therefore that the nature of the ECS (pneumatic or electric) and the presence/absence of the ETS determines which of the four clusters a subsystem architecture lies in. Within a particular cluster, the variations in BF, OEW, and MRW occur due to variations in the designs of the actuation and ice protection subsystems. This is analyzed further for Clusters 1 and 2 (since Clusters 3 and 4 are infeasible/impractical for the LTA and VLA). The relative impacts of the actuation and IPS architectures within Clusters 1 and 2 for the SSA, LTA, and VLA are summarized in Table 31, 32, and 33 respectively. For each aircraft, a reference architecture is chosen for each cluster. For Cluster 1, the fully conventional architectures (SSA-00000, LTA-00000 and VLA-00000) are chosen as the reference. For Cluster 2, an architecture where electrification was limited to the ECS is chosen as the reference (SSA-00010, LTA-00010, and VLA-00010).

1. Impact of actuation architectures: For each aircraft, the change in actuation architecture from Package 0 to Package 7 (Table 3, §3.2.3) results in progressive removal of the hydraulic system, progressive addition of electrical cables, power electronics, and additional generator capacity, and a general increase in the actuator masses due to the assumed technological state-of-the-art (SOTA) of electric actuators relative to hydraulic ones. For the SSA, the net result of these counter-acting effects tends to be a reduction in the OEW of the aircraft. The trend is reversed for the LTA and the VLA, in which case there is an increase in the OEW. This is due to a combination of higher actuation loads leading to a greater surface controls mass penalty for electric actuators, longer and heavier electrical cables and feeders, and a larger increase in required generator capacity. A small improvement in BF is possible for the SSA. Due to mutual cancellation

of the counter-acting effects, the influence of actuation architecture on the BF performance of the LTA is negligible. For the VLA, the OEW increase results in a degradation in BF performance

2. Impact of IPS architectures: Regarding the effect of electrification of the IPS architecture, for most of the combinations of WIPS and CIPS solutions (Table 4), there is a reduction in BF due to the exchange of bleed air requirement for shaft-power requirement, which in certain cases is accompanied by a reduction of the OEW (the net result of the mass changes to the following:

Table 31: Architecture impacts within Clusters 1 and 2 for SSA (Note: All %-Δ quantities are with respect to the conventional architecture SSA-00000. All Δ(%-Δ) quantities are with respect to the reference architecture within each Cluster)

	Cluster 1	Cluster 2
Reference architecture	SSA-00000	SSA-00010
	(pneumatic ECS)	(electric ECS)
%-Δ BF	0.00	- 2.47
%-Δ MRW	0.00	+0.62
%-Δ OEW	0.00	+2.38
Impact intervals of actuation arch.		
Δ(%-Δ BF)	[- 0.19, + 0.00]	[- 0.21, + 0.01]
Δ(%-Δ MRW)	[- 0.23, + 0.04]	[- 0.20, + 0.05]
Δ(%-Δ OEW)	[- 0.34, + 0.08]	[- 0.29, + 0.10]
Impact intervals of IPS arch.		
Δ(%-Δ BF)	[- 0.60, + 0.06]	[- 0.68, + 0.00]
Δ(%-Δ MRW)	[- 0.34, + 0.38]	[- 0.39, + 0.24]
Δ(%-Δ OEW)	[- 0.36, + 0.74]	[- 0.42, + 0.53]
Cluster characterization		
%-Δ BF	$0.00^{+0.06}_{-0.79}$	$- 2.47^{+0.01}_{-0.84}$
%-Δ MRW	$0.00^{+0.43}_{-0.57}$	$+ 0.62^{+0.29}_{-0.61}$
%-Δ OEW	$0.00^{+0.83}_{-0.71}$	$+2.38^{+0.63}_{-0.75}$

WIPS, CIPS, PPGDS, and EPGDS). Slight degradations in BF performance occur for the electrothermal evaporative CIPS design. In this case, the high power requirement triggers mass additions from higher-rating generators, power control equipment, and higher gage electrical cabling. These mass additions collectively exceed mass deletions due to the elimination of pneumatic ducting from the CIPS and PPGDS. The magnitude of BF improvements reduces with aircraft size, being highest for the SSA and lowest for the VLA

The conclusion from this analysis is that the ECS design (pneumatic or electric) has a dominant influence on the performance of a subsystem architecture. The

Table 32: Architecture impacts within Clusters 1 and 2 for LTA (Note: All %-Δ quantities are with respect to the conventional architecture LTA-00000. All Δ(%-Δ) quantities are with respect to the reference architecture within each Cluster)

	Cluster 1	Cluster 2
Reference architecture	LTA-00000	LTA-00010
	(pneumatic ECS)	(electric ECS)
%-Δ BF	0.00	- 2.73
%-Δ MRW	0.00	- 0.50
%-Δ OEW	0.00	+1.67
Impact intervals of actuation arch.		
Δ(%-Δ BF)	[- 0.08, + 0.08]	[- 0.07, + 0.05]
Δ(%-Δ MRW)	[- 0.03, + 0.13]	[- 0.03, + 0.11]
Δ(%-Δ OEW)	[- 0.00, + 0.24]	[- 0.00, + 0.23]
Impact intervals of IPS arch.		
Δ(%-Δ BF)	[- 0.29, + 0.08]	[- 0.33, + 0.01]
Δ(%-Δ MRW)	[- 0.25, + 0.32]	[- 0.27, + 0.20]
Δ(%-Δ OEW)	[- 0.27, + 0.72]	[- 0.29, + 0.51]
Cluster characterization		
%-Δ BF	$0.00^{+0.15}_{-0.36}$	$- 2.73^{+0.06}_{-0.40}$
%-Δ MRW	$0.00^{+0.46}_{-0.28}$	$- 0.50^{+0.32}_{-0.30}$
%-Δ OEW	$0.00^{+0.97}_{-0.27}$	$+1.67^{+0.74}_{-0.29}$

solutions employed for the remaining subsystems have an impact that is of a smaller magnitude. This is evident from the clustering of subsystem architectures that is seen in Fig. 58. The impact of ECS electrification on the subsystem architecture performance is influenced not only by mass changes to multiple subsystems, but by the effect that the exchange of bleed air requirement for shaft-power requirement has on the TSFC degradation of the engine.

The ten best-performing subsystem architectures for the SSA, LTA, and VLA are listed in Table 34. For convenience, the architecture identification scheme is presented again in Fig. 59. For a given aircraft size, the ten best-performing architectures fall

Table 33: Architecture impacts within Clusters 1 and 2 for VLA (Note: All %-Δ quantities are with respect to the conventional architecture VLA-00000. All Δ(%-Δ) quantities are with respect to the reference architecture within each Cluster)

	Cluster 1	Cluster 2
Reference architecture	VLA-00000	VLA-00010
	(pneumatic ECS)	(electric ECS)
%-Δ BF	0.00	- 4.20
%-Δ MRW	0.00	- 1.18
%-Δ OEW	0.00	+1.44
Impact intervals of actuation arch.		
Δ(%-Δ BF)	[- 0.00, + 0.36]	[- 0.00, + 0.36]
Δ(%-Δ MRW)	[- 0.00, + 0.48]	[- 0.00, + 0.46]
Δ(%-Δ OEW)	[- 0.00, + 0.76]	[- 0.00, + 0.73]
Impact intervals of IPS arch.		
Δ(%-Δ BF)	[- 0.22, + 0.20]	[- 0.25, + 0.01]
Δ(%-Δ MRW)	[- 0.15, + 0.31]	[- 0.17, + 0.08]
Δ(%-Δ OEW)	[- 0.14, + 0.53]	[- 0.16, + 0.21]
Cluster characterization		
%-Δ BF	$0.00^{+0.57}_{-0.22}$	$- 4.20^{+0.36}_{-0.25}$
%-Δ MRW	$0.00^{+0.79}_{-0.15}$	$- 1.18^{+0.54}_{-0.17}$
%-Δ OEW	$0.00^{+1.31}_{-0.14}$	$+1.44^{+0.95}_{-0.16}$

Table 34: Best-performing SSA, LTA, and VLA subsystem architectures with respect to fuel consumption improvement relative to conventional subsystem architecture

	SSA		LTA		VLA	
Rank	Arch.	%-ΔBF	Arch.	%-ΔBF	Arch.	%-ΔBF
1	SSA-73310	-3.31	LTA-73310	-3.13	VLA-03310	-4.45
2	-73110	-3.31	-73110	-3.13	-01310	-4.43
3	-63310	-3.29	-63310	-3.11	-03110	-4.43
4	-63110	-3.29	-63110	-3.11	-01110	-4.41
5	-71310	-3.28	-71310	-3.10	-02110	-4.38
6	-73311	-3.28	-71110	-3.10	-02310	-4.36
7	-73111	-3.28	-61310	-3.08	-13310	-4.36
8	-61310	-3.26	-61110	-3.08	-11310	-4.34
9	-63311	-3.26	-53310	-3.07	-13110	-4.34
10	-63111	-3.26	-53110	-3.07	-03010	-4.33
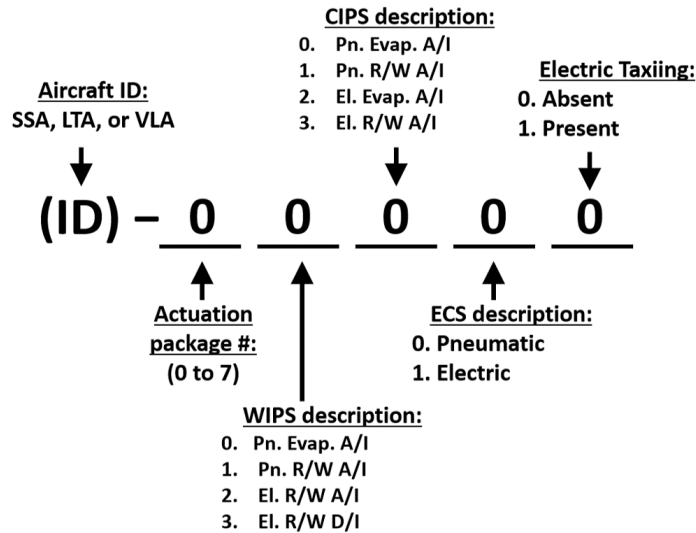
Figure 59: Definition of *Candidate Subsystem Architecture Descriptor* (repeated)

within a very narrow range of fuel consumption improvement. Thus, even though the architectures are ranked in descending order of fuel consumption improvement relative to the baseline conventional architecture, the intent of this tabulation is not to determine a "winner". Instead, the intent is to permit observations regarding subsystem architecture trends, such as the following:

1. Electric Taxiing System (ETS) - For reasons already stated previously, ETS does not feature in any of the top architectures for the LTA and the VLA. For the SSA however, architectures containing ETS do make appearances. For all such architectures, a counterpart not containing ETS is also present in the list

2. Environmental Control System (ECS) - All the best-performing architectures for the SSA, LTA, and VLA contain electric ECS. Referring to Fig. 58, all these architectures lie within Cluster 2 for the LTA and VLA, and within either Cluster 2 or Cluster 3 for the SSA. The dominant effect of ECS electrification on the performance of the subsystem architecture has been noted previously

3. Ice Protection Systems (WIPS & CIPS) - The best-performing architectures avoid the use of pneumatic evaporative ice protection due to the associated bleed air penalty (Fig. 51). There is only one exception: VLA-03010, which retains pneumatic evaporative CIPS, which is perhaps being compensated for by the presence of electrothermal de-icing WIPS. In general, the best-performing architectures show a gravitation either towards electrothermal IPS or towards pneumatic running-wet anti-icing systems. For the SSA and LTA, in which three slats on each wing are protected, running-wet electrothermal anti-icing is avoided (due to high electrical power requirement)

4. Actuation functions: For the SSA and LTA, the presence of actuation Packages 5, 6, and 7 (refer to Table 3) indicates substantial electrification of the actuation functions, including partial or complete electrification of primary control surface actuation. On the other hand, for the best-performing VLA architectures, actuation electrification never progresses beyond Package 1 (electrified brakes and thrust reversers). Due to the high actuation loads for the VLA and the assumed technological SOTA (whereby electric actuators are heavier than equivalent hydraulic actuators), the mass addition to the actuation subsystems

due to electrification is more significant for the VLA than for the LTA and SSA. At the same time, higher actuation loads result in higher power requirements, which increases the mass added to the electrical system (EPGDS) through electrical cabling, generator up-sizing, and power conversion equipment. For the VLA, these mass additions outweigh the progressive mass deletion due to removal of the hydraulic system (HPGDS) beyond actuation Package 1

Despite the differences in the extent of electrification of the actuation functions between the SSA and LTA on the one hand and the VLA on the other, the following commonalities exist: the top architectures for all three aircraft sizes are either bleedless architectures, or architectures with significantly reduced bleed requirements (through electrification of ECS, electrification of either the WIPS or the CIPS, and the use of a running-wet design for the remaining pneumatic ice protection function).

9.2 Assessment of Subsystem Architecture Performance with Architecture-to-Engine Association Logic

In this case the 512 architectures for the SSA are evaluated using the scheduled coefficients (§7.2) to represent the penalties due to shaft-power and bleed air extraction. Such coefficients were computed off-line for three engines sized for three different shaft-power and bleed air extraction limits, as shown in Table 35. Also shown in Table 35 are the criteria for associating the three engines with the 512 subsystem architectures. As per this association logic, the Mixed Off-take (MO) engine is used for all architectures where the ECS, WIPS, and CIPS are pneumatic (conventional). The Zero Bleed (ZB) engine is used for all bleedless architectures, in which the ECS, WIPS, and CIPS are electrified. As a result, the shaft-power capability of the ZB engine is significantly higher than that of the MO engine, while the customer bleed availability is eliminated. For all architectures where at least one or more from among the ECS, WIPS, and CIPS remain pneumatic, the Reduced Bleed

Table 35: Secondary power extraction limits for Mixed Off-take (MO), Reduced Bleed (RB), and Zero Bleed (ZB) engines for SSA thrust class and association rules between engines and ECS, WIPS, and CIPS architectures

Thrust class: 27,000 lbf (120 kN)	Mixed Off-take Engine (MO)	Reduced Bleed Engine (RB)	Zero Bleed Engine (ZB)
Sec. power capacity			
Shaft-power extraction	-	+ 204 %	+ 266 %
Bleed air extraction	-	− 34 %	− 100 %
ECS, WIPS,	all	at least one	all
& CIPS Arch.	pneumatic	pneumatic	electrified

(RB) engine is used. To be able to meet the shaft-power and bleed air requirements of all these architecture combinations, the RB engine requires an appreciable increase in shaft-power capability, but only a one-third reduction in bleed air capability is possible. The performance of the 511 MEA architectures relative to the conventional baseline (SSA-00000) with this architecture-to-engine association logic is shown in Fig. 60. Once more, the architectures are seen to appear in clusters. However, the cluster characteristics are somewhat different from and more complex than those seen previously (in Fig. 58). These new SSA clusters are described below in brief:

1. Cluster 1 (Pneumatic ECS, WIPS, and CIPS, MO Engine): As per the architecture-to-engine association logic, these designs use the conventional Mixed Off-take (MO) engine. The performance variations within this cluster are caused by the changes in actuation architecture and the effect of reduced bleed requirements of running-wet WIPS and CIPS relative to evaporative type. As such the fuel consumption benefits of designs within this cluster are limited

2. Cluster 2 (Electric ECS, pneumatic WIPS and/or CIPS, RB Engine): These designs use the Reduced Bleed (RB) engine. The fuel burn reduction of designs within this cluster is driven by the electrification of the ECS. As noted
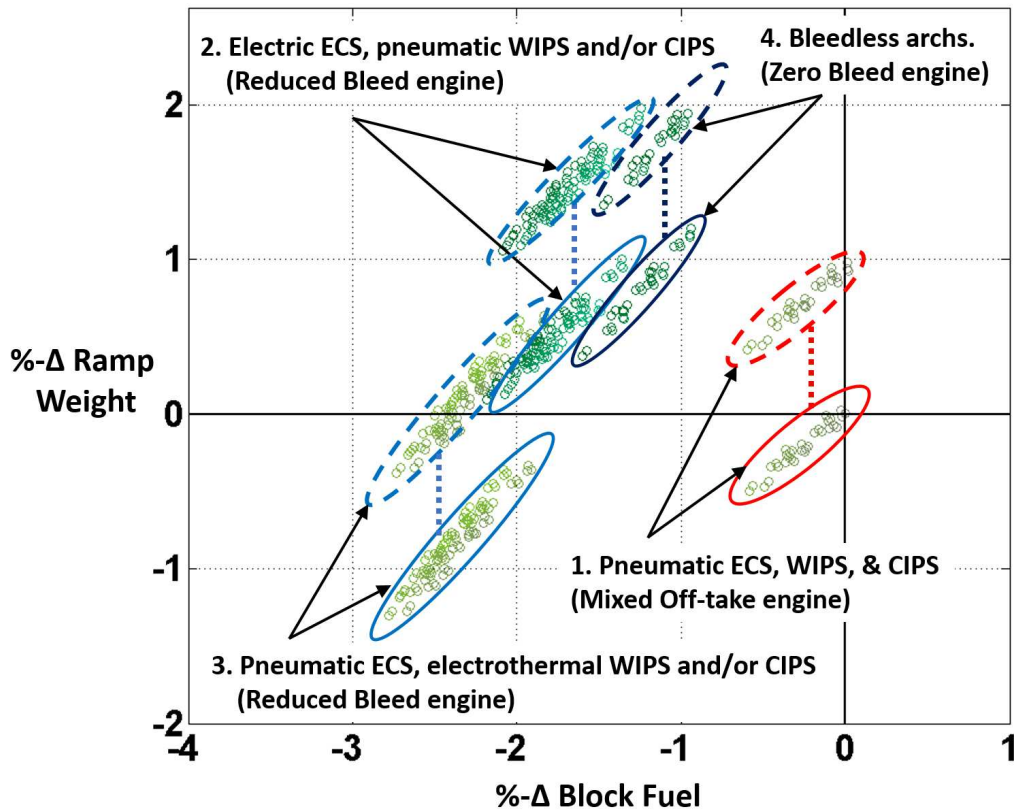
Figure 60: Performance comparison of SSA subsystem architectures using scheduled penalty coefficients for secondary power off-takes and the architecture-to-engine association logic of Table 35. Absence or presence of ETS from designs within clusters is indicated using solid and dotted bounding lines respectively
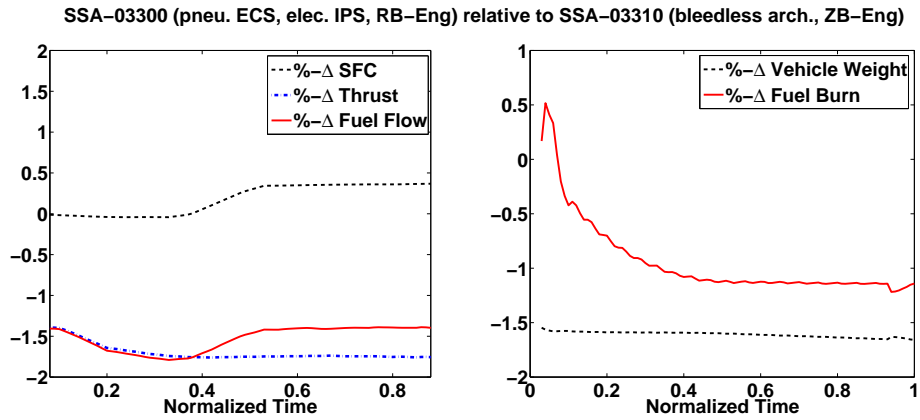
previously, ECS electrification adds significant mass to both the ECS and the EPGDS. Variations in performance within the cluster are caused by actuation, WIPS, and CIPS architecture

3. Cluster 3 (Pneumatic ECS, electrothermal WIPS and/or CIPS, RB Engine): These designs also use the Reduced Bleed (RB) engine. The fuel burn reduction for designs within this cluster are driven by the partial reduction or complete elimination of the IPS bleed air requirement and also by reduced OEW on account on mass deletions from the PPGDS due to WIPS and/or CIPS electrification. This cluster shows the greatest fuel burn reduction among all the clusters

4. Cluster 4 (Bleedless architecture, ZB Engine): These are bleedless architectures where the ECS, WIPS, and CIPS are all electrified. Designs within this cluster use the Zero Bleed (ZB) engine. These designs show a reasonable fuel burn reduction relative to the baseline, but not as large as those shown by designs within Clusters 2 and 3

Given the prior observations from Fig. 58 (for which the analysis did *not* consider any architecture-to-engine associations), the following observations were somewhat unexpected, and were therefore investigated further:

1. Performance advantage of Cluster 2 designs relative to Cluster 4 bleedless designs: it must be noted that the magnitudes of the secondary power off-takes were factored into the sizing of the RB and ZB engines, and therefore influences the determination of the engine cycle parameters. Inspection of the mission performance data for two architectures, SSA-00010 (only electrified ECS, belonging to Cluster 2, using the RB engine) and SSA-03310 (bleedless architecture, belonging to Cluster 4, using the ZB engine), reveals that the basic TSFC (accounting for only propulsive power requirements and not non-propulsive power requirements) of the former is lower than that of the latter.

2. Performance advantage of Cluster 3 designs relative to Cluster 4 designs, even though the former retain pneumatic ECS: This is analyzed by comparing mission performance data of SSA-03300 (electrified WIPS and CIPS, pneumatic ECS, using RB engine, Cluster 3) against that of SSA-03310 (bleedless architecture using ZB engine, Cluster 4), as shown in Fig. 61(a). Despite the basic TSFC observation made above, it is seen that the overall TSFC of SSA-03300 is higher for the majority of the flight (due to the pneumatic ECS bleed requirement). However, SSA-03310 is heavier than SSA-03300 owing to the mass additions

SSA–03300 (pneu. ECS, elec. IPS, RB–Eng) relative to SSA–03310 (bleedless arch., ZB–Eng)

(a) Mission performance comparison of SSA-03300 relative to SSA-03310

SSA–03300 (pneu. ECS, elec. IPS, RB–Eng) relative to SSA–00010 (elec ECS, RB–Eng)
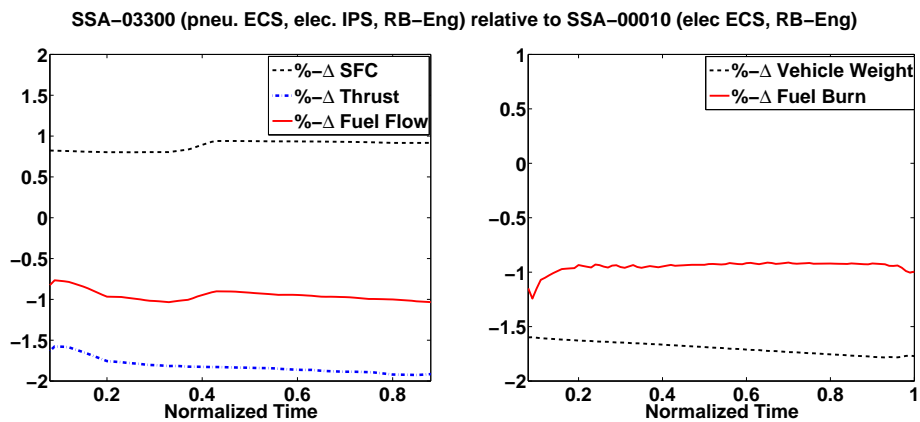
(b) Mission performance comparison of SSA-03300 relative to SSA-00010

Figure 61: Mission performance comparison of selected SSA architectures from Clusters 2 and 3 (RB engine) and Cluster 4 (ZB engine)

to the ECS and EPGDS due to ECS electrification and has additional ECS ram drag. Thus, SSA-03300 has a lower thrust requirement, and the two counter-acting effects of thrust and TSFC result in a lower fuel flow rate for SSA-03300, which ultimately leads to the fuel burn advantage

3. Performance advantage of Cluster 3 designs relative to Cluster 2 designs, even though the former retain pneumatic ECS: This is analyzed by comparing the mission performance of SSA-03300 (electrified WIPS and CIPS, pneumatic ECS, using RB engine, Cluster 3) against that of SSA-00010 (electric ECS

architecture also using RB engine, Cluster 2), as shown in Fig. 61(b). The observations and reasoning are identical to those above. SSA-03300 has a higher TSFC, but a lower thrust requirement that ultimately leads to lower fuel burn

This analysis demonstrates that logic for associating the subsystem architecture with one of several engines sized for different secondary power off-take limits can have a significant effect on the predicted performance of subsystem architectures. In the prior analysis (summarized in Fig. 58), the electrification of the ECS had a dominant effect on the performance of the subsystem architecture, with the design of the remaining subsystems generating perturbations of a smaller magnitude about a base point determined by the ECS solution.

However, in the current analysis, the predicted advantage for architectures containing electrified ECS is reduced due to a combination of factors. First, the penalty coefficients for bleed extraction identified for the MO and RB engines using the NPSS engine truth model are of a smaller magnitude than the constant coefficient obtained from the SAE AIR 1168/8 method [163] (Chapter 6). At the same time, the predicted penalty for shaft-power extraction is higher than that predicted by the k_p^* method of Scholz (Chapter 6). The net result is a reduction in the off-take fuel advantage enjoyed by electric ECS architectures over pneumatic ECS architectures in the previous analysis.

Since an engine optimized for pure shaft-power extraction will be at a disadvantage in providing bleed air [3], such an engine may be unsuitable for architectures that are not bleedless. On the other hand, an engine optimized for reduced (but non-zero) bleed extraction and higher shaft-power extraction may offer acceptable performance for a number of MEA subsystem architectures. Since cost and time constraints would make it infeasible to design a bespoke engine for each More Electric subsystem architecture, usability of a common engine for multiple subsystem architectures may be an important consideration in addition to fuel consumption.

## 9.3 Case Study: Equal Electric and Hydraulic Actuator Masses

As mentioned previously, with the current technological state-of-the-art (SOTA), it is generally assumed that electric actuators will weigh more than hydraulic actuators designed for the same actuation requirements [73]. This reduces the competitiveness of architectures featuring substantial electrification of actuation functions for higher actuation loads, as evident from the absence of such architectures for the VLA from Table 34. In Chapter 8, the impact of advancement in electric motor and power electronics SOTA on the performance of an All Electric actuation architecture was assessed. In this section, a special case study is presented in which it is assumed that the electric actuators (or actuation system) for the FCAS, LGAS, NWSS, and TRAS weigh *exactly* the same as the hydraulic actuators (or actuation systems) that they replace. This assumption however is not applied to the WBS, since electric brake actuation will require the incorporation of EMAs which will always add some mass to the WBS. With this assumption in place, the progressive electrification of the actuation architecture through actuation packages 0 to 7 (Table 3) involves the following two counter-acting effects:

1. Mass deletions from the 5,000 psi HPGDS due to elimination of progressively more piping and down-sizing of hydraulic pumps

2. Mass addition to the EPGDS due to additional electrical feeders/cabling, power conversion equipment, and increased generator capacity

The impacts of progressive electrification of the actuation architecture for the SSA, LTA, and VLA are presented in Fig. 62 in the form of %-Δ OEW, %-Δ BF, and %-Δ MRW relative to the conventional actuation architecture. The following observations are readily made:

1. For the SSA, the performance improvement is the most pronounced and is also
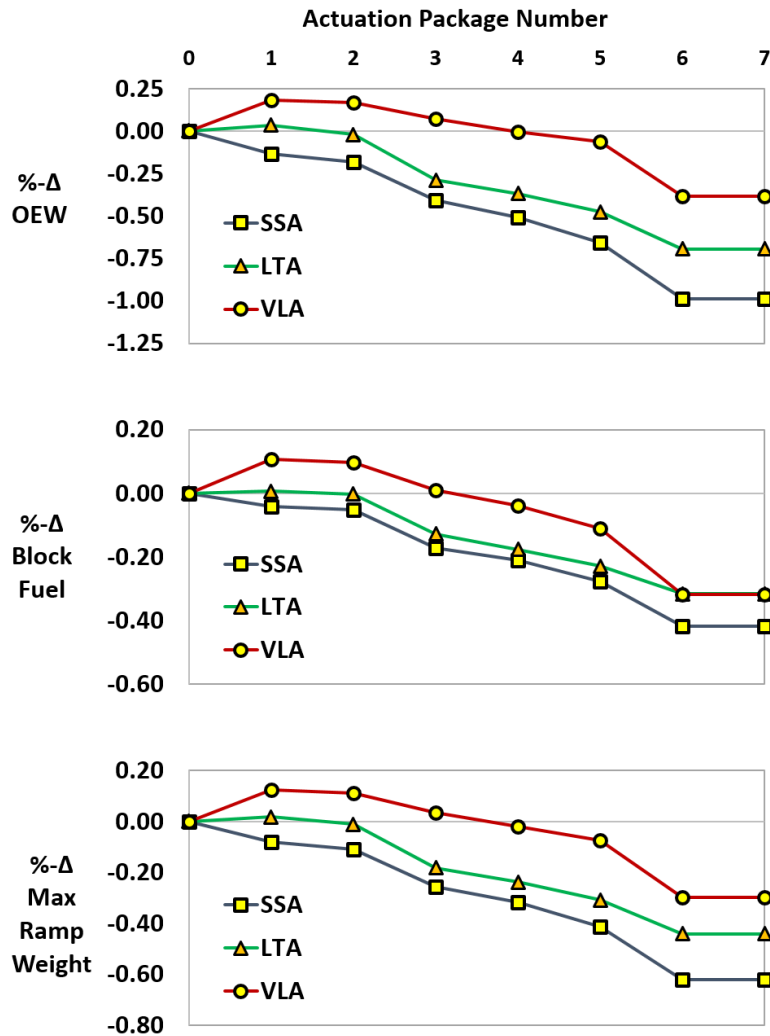
Figure 62: Effect of electrification of actuation functions for SSA, LTA, and VLA under the technology assumption that electric actuators for FCAS, LGAS, NWSS, and TRAS weigh exactly the same as the hydraulic actuators they replace

monotonic. Even though there is a mass addition to the WBS for Package 1 (electrification of WBS and TRAS), the mass deletion from the HPGDS is of sufficient magnitude to result in a net reduction of OEW

2. For the LTA, Package 1 results in a slight OEW penalty due to the mass addition caused by electrification of the WBS. However, subsequent actuation packages result in monotonic improvements in OEW, BF, and MRW

3. For the VLA, the mass addition due to the electrification of the WBS in Package 1 is more significant. Although subsequent packages see monotonic improvements in OEW, BF, and MRW, electrification must progress till Package 4 before any aircraft-level OEW or mission-level BF reduction appears

Thus, it is evident that even with this optimistic technology assumption, complete electrification of actuation functions yields a predicted fuel consumption reduction of approximately 0.42 % for the SSA, and approximately 0.32 % for the LTA and VLA. While these savings are not negligible, it must be noted that (i) they are subject to a very optimistic technology assumption (that electric actuators suffer no mass penalty relative to hydraulic ones), and (ii) the reduction in fuel consumption is almost an order of magnitude less than that predicted for ECS electrification.

9.4   Chapter Summary

In this chapter, Research Question 2 was addressed by evaluating a large number of subsystem architectures for three aircraft sizes. It was found that architectures fell into one of four distinct clusters depending on whether or not the ECS was electrified and whether or not an Electric Taxiing System (ETS) was installed on the aircraft. The presence of ETS within architectures on the two larger aircraft (LTA and VLA) resulted in substantial degradation in the performance of those architectures. This was also observed in a previous analysis (Experiment 2.3), and as such it is possible to rule out the practicality of such a system on larger aircraft.

The electrification of the ECS resulted in an increase in the Operating Empty Weight (OEW) but also a reduction in the fuel consumption. LTA and VLA (but not SSA) architectures in which the ECS was electrified (and which did not feature an ETS) showed a reduction in Maximum Ramp Weight (MRW), implying that these designs benefited from the down-sizing that occurred during the re-sizing iterations. ECS electrification was found to have a dominant effect on the performance of any

subsystem architecture featuring it. The solutions for all other subsystems were seen to have impacts of a significantly lower magnitude. When the SSA architecture space was evaluated employing scheduled penalty coefficients derived from querying a higher-fidelity truth model and an architecture-to-engine association logic, the nature of the architecture clusters was seen to change. While electric ECS architectures still showed an advantage, the magnitude was seen to be lower. Investigation of the time-history of mission performance parameters revealed that this was largely due to the significant mass addition associated with ECS electrification.

The best performing architectures for the SSA and LTA differed from those for the VLA in the extent of electrification of the actuation functions. The best-performing SSA and LTA architectures featured actuation packages with significant electrification of the actuation subsystems. This was not the case for the VLA, due to the significant mass additions to the actuation subsystems themselves and to the EPGDS due to the higher actuation loads and actuation power requirements. Even when electric actuators were assumed to have no mass penalty relative to hydraulic ones, it was found that the potential for performance improvement was still limited to a much smaller magnitude than that afforded by transition to bleedless architectures. Part of this reduced advantage is clearly attributable to the assumption of a 5,000 psi state-of-the-art (rather than 3,000 psi) for the conventional hydraulics. These observations are of course subject to the assumed characteristics of the actuation packages themselves, which were employed to reduce the dimension of the combinatorial sub-space for actuation architectures. The three aircraft sizes did however show a similarity in that the best-performing architectures were either bleedless ones or ones that had significantly reduced bleed air requirements. In the majority of cases, the best-performing architectures did not feature electrothermal running-wet anti-icing WIPS designs and electrothermal evaporative anti-icing CIPS designs, due to higher power requirements relative to other available options.

In conclusion, the developed integrated sizing and analysis environment allowed Research Question 2 to be addressed and yielded insight regarding the best-performing subsystem architectures and variations of architecture performance with variation in the aircraft size. Since the performance evaluation for all the subsystem architectures was facilitated by the automatic architecture definition algorithm, the first sub-statement of Hypothesis 2 was supported. Further, since a separate evaluation of architecture performance for the SSA was performed by incorporating knowledge regarding subsystem secondary power requirements into the sizing of three separate engines, the second sub-statement of Hypothesis 2 is also supported. The results presented in this chapter and the preceding ones allowed the major research questions to be addressed and the hypotheses to be tested. The final chapter of this dissertation summarizes the core contributions of this work, the major conclusions drawn, and the avenues identified for further extensions of the methodology.

CHAPTER X

CONTRIBUTIONS, CONCLUSIONS, AND RECOMMENDATIONS FOR FUTURE WORK

This chapter concludes the dissertation with a summary of the key contributions, a summary of conclusions from the investigations performed, and recommendations for future avenues of work to be performed to extend the research.

10.1 Contributions

The primary contribution of this dissertation is the creation and demonstration of an integrated and modular approach for the simultaneous sizing of an aircraft and its subsystems in the early design phase. In particular, it allows rapid assessments of the effect of novel subsystem architectures for which little or no historical data exists.

A core aim of the modeling approach was to ensure that the subsystem models developed for sizing and analysis were suitable for use during conceptual or early design phases. This aim was decomposed into two main requirements: (i) that the models be computationally inexpensive so as to permit the evaluation of a large number of subsystem architectures within a reasonable amount of time, and (ii) that the models require as input only information that would either be available or easily estimated during the early design phases. A salient feature of the demonstrated approach is that the required input from the analyst is limited to the following:

1. A minimal description of the aircraft being considered, in terms of the payload-range capabilities, number of engines, mission profile, etc.

2. A qualitative description of the subsystem architecture(s) of interest that, containing information on the solutions employed for particular subsystems

3. Settings for K-factors that modify internal model parameters to simulate epistemic uncertainty or advancement in technological state-of-the-art (only for performing sensitivity analyses)

Further, unlike some other tools and approaches, no input from the analyst is required for determining the connectivity existing among elements of the subsystem architecture. These connectivities are automatically determined by a heuristic algorithm that was developed based on inspection of the redundancy present in existing subsystems architectures. This automatic architecting capability is significant as (i) it permits any number of subsystem architectures of interest to be evaluated successively without any input from the analyst and (ii) it does not require that the analyst be a Subject Matter Expert (SME) in order to carry out meaningful subsystem architecture analyses and tradeoff studies.

The approach to the sizing and evaluation of the aircraft subsystems revolves around a generic representation of the subsystem architecture featuring (i) prime movers, (ii) power sources, (iii) power systems, (iv) power distribution elements, and (v) power consumers. Such a representation was developed as a basic framework for the distribution of secondary (non-propulsive) power through the aircraft. Subsystems responsible for the generation, distribution, and consumption of the three main types of secondary power (pneumatic, hydraulic, and electric) were viewed as special cases of this generic framework. The significance of this representation is the fact that it can accommodate all onboard subsystems, including those not directly addressed in this dissertation. Due to this modular representation of the subsystem architecture, additional subsystems can be modeled and integrated at a future time without affecting the core setup of the integrated capability.

To evaluate the impact of the subsystems on the aircraft-level and mission-level metrics of interest, the following standard information from each subsystem was propagated upward to the aircraft-level and mission-level: (i) subsystem mass,

(ii) shaft-power requirement, if any, (iii) bleed air requirement, if any, and (iv) direct drag increment, if any. The latter three are evaluated by the relevant subsystem modules and may be arbitrary functions of time. Unlike some other approaches, there is no requirement that the shaft-power, bleed, or direct drag increments be assumed constant over a flight phase or over any extended interval of time.

A salient feature of the presented approach is that in addition to computing the net impact of the subsystems architecture on a mission-level metric such as fuel burn, it decomposes the net impact though a two-level decomposition. The first level decomposes the net impact into the contributions from individual subsystems. The second level decomposes the contribution of each subsystem into component contributions stemming from the subsystem's mass, secondary power requirements, and drag increments. These constituent impacts may be used as rational weighting factors in an objective function developed in order to optimize each subsystem.

The developed approach is noteworthy in that a tight coupling is established between aircraft sizing and subsystem sizing. Once the impact of the subsystem architecture is reflected in the updated mission performance analysis, an iterative re-sizing of the aircraft and subsystems commences. In accordance with a set of re-sizing rules, the aircraft geometry and thrust are re-sized based on impacts originating from the subsystem-level, following which the subsystems are once more sized based on the updated aircraft-level information. Due to the parametric definitions of control surfaces and ice protection zones relative to a main lifting surface such as a wing (to give an example), the re-sizing at the aircraft level automatically triggers re-sizing at the subsystem level as well.

To study the impact of aircraft size on the performance of subsystem architectures, three aircraft of varying sizes were considered: a Small Single-aisle Aircraft (SSA), a Large Twin-aisle Aircraft (LTA), and a Very Large Aircraft (VLA). These were chosen since they collectively span a wide spectrum of gross weight. For each of

these aircraft, a subset of the subsystem architecture space was down-selected based on certain physical design constraints for subsystems and subject to an assumption regarding a possible staged or packaged approach to the electrification of the aircraft's actuation functions. All candidate architectures within the identified subset were evaluated exhaustively. Such an approach made the analyses tractable but at the same time permitted the evaluation of a sufficiently large number of More Electric Aircraft subsystem architectures. Most importantly, it provided insight into the effect of vehicle size on subsystem architecture performance. A further notable contribution arising out of the presented approach is the fact that it facilitates the investigation of the effect of epistemic and technological uncertainty on the predicted performance of subsystem architectures.

As part of the developed approach, a performance model of a gas turbine engine created using a higher-fidelity propulsion system analysis tool was used as a truth model. The truth model was queried to find penalty coefficients representing the effect of shaft-power and bleed air extraction on the engine fuel consumption. These coefficients were used in the integrated environment in lieu of directly integrating the more computationally expensive propulsion system tool directly. Coefficient sets were obtained by querying multiple engines that had been sized for different shaft-power and bleed air extraction requirements. An architecture-to-engine association logic (to allow an engine to be selected based on the architecture of the subsystems) was implemented and the effects of the engine association logic on the performance of subsystem architectures were assessed.

In summary, the demonstrated approach fills a hitherto existing gap by facilitating the automated investigation of a large number of subsystem architectures for multiple aircraft sizes, while accounting for subsystem-subsystem and aircraft-subsystem dependencies, the effect of simultaneous re-sizing of the aircraft and subsystems, and the effects of epistemic and technological uncertainties.

10.2 Conclusions

A series of experiments was performed in order to test and verify certain capabilities of the integrated subsystem sizing and analysis environment. These included the following (for each of three chosen baselines):

1. Ability to assess the effects of electrification of a single power consuming subsystem (Expt. 1.1)

2. Ability to assess the effects of electrification of the whole subsystem architecture (Expt. 1.2)

3. Ability to automatically determine connectivities among subsystem architecture elements that provide redundancy equivalent to that observed in existing conventional and MEA subsystem architectures (Expt. 2.1)

4. Ability to utilize information regarding the fuel consumption penalties due to secondary power off-takes generated using a higher-fidelity propulsion system analysis tool, but without directly integrating the tool (Expt. 2.2)

5. Ability to decompose the overall mission-level impact of a subsystem architecture into contributions originating from individual subsystems, and the decomposition of those contributions into component contributions from mass, secondary power off-takes, and drag (Expt. 2.3)

6. Ability to determine the sensitivity of select subsystem architectures to epistemic uncertainty (Expt. 3.1)

7. Ability to determine the sensitivity of select subsystem architectures to uncertainty and assumptions regarding current or projected technological state-of-the-art (Expt. 3.2)

8. Ability to assess the relative performance of a large number of subsystem architectures within an architectural design space relative to a conventional baseline for aircraft of varying sizes (Expt. 4.0)

As part of Expt. 1.1, the performance of an architecture with electric ECS was compared to that of a conventional subsystem architecture. As part of Expt 1.2, the performance of an All Electric subsystems architecture was compared to that of a conventional one. From these, it was observed that some of the MEA architectures permitted moderate to significant reduction in the mass of the Hydraulic Power Generation and Distribution System (HPGDS) and the Pneumatic Power Generation and Distribution System (PPGDS), and in certain cases the elimination of these subsystems altogether. However, significant mass was added back to the aircraft mainly due to one or more of the following factors:

1. significant expansion of the Electrical Power Generation and Distribution System (EPGDS) to include higher-rating generators, significantly more power conversion equipment, and additional electrical cabling

2. additional hardware and power conversion equipment required for electrification of a major subsystem such as the Environmental Control System

3. the fact that electric actuation solutions were in general heavier than the hydraulic solutions that they replaced with the assumed technological state-of-the-art

In most cases, the net consequence of these counter-acting effects was an increase in the Operating Empty Weight (OEW) of the MEA architectures. Despite this, the MEA architectures in many cases showed a reduction in fuel consumption relative to the conventional architecture. This was largely driven by the elimination of pneumatic off-takes (bleed air) from the engines through electrification of major subsystems such as the ECS and the Ice Protection Systems (IPS).

As part of Expt. 2.1, the heuristic architecting algorithm was tested with inputs corresponding to existing aircraft with conventional and MEA subsystem architectures. In each case the algorithm generated subsystem architecture connectivities that were either identical to or equivalent to those found in these existing architectures in terms of redundancy of power consumers, power systems, and power sources. Further, when provided inputs corresponding to two existing MEA, the Airbus A380 and the Boeing 787, the algorithm was able to capture the elimination of one hydraulic system from the former and the significant expansion of the electrical system of the latter.

As part of Expt. 2.2, a higher-fidelity engine model that had been developed using the Numerical Propulsion System Simulation (NPSS) tool was used as the truth model. For multiple engines sized to different combinations of shaft-power and bleed off-takes, the truth model was queried in order to determine coefficients that represented the degradation in engine TSFC on account of secondary power off-takes. Rather than determining the penalty coefficients as functions of altitude and Mach number, they were instead scheduled with respect to normalized mission time, under the assumption of an invariant mission profile and insignificant variation of engine TSFC with thrust for the range of variations in thrust between different subsystem architectures. Penalty coefficients obtained in this manner were used to evaluate SSA subsystem architecture performance subsequently as part of Expt 4.0.

As part of Expt. 2.3, the net subsystem architecture impact was decomposed into contributions from individual subsystems and further decomposed into the contributions arising from mass, secondary power, and drag increments. From the first level of decomposition, it was found that the ECS (whether pneumatic or electric) had a dominant effect on the fuel burn performance of architectures. The contributions of the remaining power consuming subsystems were seen to be of a much smaller magnitude. From the second level of decomposition, it was found that the Total

299

Fuel Impact (TFI) of the actuation functions originated almost completely from the masses of these subsystems. For pneumatic ECS, bleed air off-takes accounted for the majority of the subsystem's TFI, whereas for electric ECS, the TFI was more evenly contributed to by the subsystem mass, shaft-power off-takes, and ram drag. An assessment of the feasibility of an optional subsystem such as the Electric Taxiing System (ETS) revealed that such a system would only be feasible for the SSA (flying short-haul flights) but impractical for the LTA and the VLA (flying long-haul flights).

As part of Expt. 3.1, when strategically chosen model parameters were varied to represent the effect of epistemic uncertainty, architectures that featured electrified ECS and IPS (i.e., bleedless architectures) were seen to maintain a fuel consumption advantage. On the other hand, for architectures that featured All Electric actuation but retained pneumatics, no advantage could be guaranteed in the presence of the epistemic uncertainty.

As part of Expt. 3.2, when an advancement of the technological state-of-the-art of electric motors, power electronics, and electric generator technology was simulated, all MEA architectures showed improvement in performance. These gains were much more significant for architectures where these components were more pervasive or where their rated capacities were higher. MEA architectures featuring higher levels of electrification were also seen to benefit if the available capacity of the Auxiliary Power Unit (APU) generators was factored into the sizing of the capacities of the Engine Driven Generators (EDGs). However, in reality, the feasibility of this would be determined and perhaps limited by operational and dispatch reliability requirements.

As part of Expt 4.0, the performances of 511 MEA architectures were compared relative to a conventional subsystem architecture for the SSA, LTA, and VLA baselines. In general, the magnitude of the predicted benefits of the MEA architectures was seen to increase with increasing vehicle size, which is in line with similar observations from several previous research studies and programs. An

exception to this trend was observed for the Electric Taxiing System (ETS), which was established to be practical only for the SSA but not for the LTA or the VLA. In case of the LTA and the VLA, the cross-over range, beyond which the in-flight fuel penalty due to the ETS mass exceeded the fuel saved during taxiing, was seen to be less than the trip distances that aircraft of such sizes are typically operated on. When the architectures were evaluated using a constant coefficient penalty for secondary power off-takes, they were found to appear in four clusters characterized by whether the ECS was electrified and whether the ETS was installed. However, when the SSA architectures were evaluated using the scheduled penalty coefficients and an architecture-to-engine association logic, the clustering of the architectures was found to be somewhat more complex. An explanation for this observed behavior was obtained by comparison of the time histories of mission performance parameters for representative architectures present within each cluster.

In summary, these experiments revealed that the developed methodology was capable of assessing the performance of different subsystem architectures for differing aircraft sizes with a level of resolution deemed acceptable for the early design phases, and thus partially or completely supported all hypotheses associated with the three major research questions.

10.3   Recommendations for Future Work

In order to size and evaluate the performance of the different subsystem solutions considered within the scope of this dissertation, a number of models were developed that were computationally inexpensive and required only information that is either available or easily estimable during the early design phases. Further refinement and validation of these models will serve to reduce the effect of epistemic uncertainty on the predicted performance of the various subsystem architectures. This therefore is a general recommendation that applies to the overall modeling approach. In addition

to the above, some specific avenues for further research are identified as follows:

1. The current investigation assumed identical pack configuration for conventional (pneumatic) and electric ECS solutions. This is not necessarily the optimal choice for an electric ECS solution. Given the observed impact of ECS electrification on the performance of MEA architectures, the development of an ECS pack model customized for the MEA architecture is warranted

2. With progressively more architecture electrification, the heat rejection from power electronics equipment becomes significant and increases the ECS heat load. While the effect of this was implicitly evaluated through a sensitivity study, the development of a more detailed thermal model of the vehicle and a model of a dedicated power electronics cooling system are warranted

3. The incorporation of knowledge regarding subsystem secondary power requirements into the determination of the engine cycle parameters, which was analyzed to a limited extent in this dissertation, must be investigated further

4. The dimensionality of a large combinatorial space of architectural possibilities was reduced through the imposition of logic such as packaged electrification of actuation functions, and the down-selected subset of architectures was evaluated exhaustively. However, an expanded investigation that includes a much larger set of architectures may be attempted, perhaps utilizing a Genetic Algorithm to populate and propagate generations of high-performing architectures

The above areas form potential avenues for future research and further extension of the capabilities of the integrated subsystem sizing and analysis tool. However, the integrated environment in its current form was sufficient to address the identified research questions and meet the stated research objective.

APPENDIX A

IMPACT OF SUBSYSTEM ARCHITECTURE

ELECTRIFICATION FOR LTA AND VLA (EXPT. 1.2)

**Table 36:** Impact of All Electric subsystem architecture for LTA

Sub -system	%Δ Fuel due to				%Δ Total Fuel Imp.	%Δ Weight	%Δ Total Wt. Imp.
	Weight	SPX	BX	Drag			
FCAS	18.3	-2.8	0.0	0.0	15.4	20.5	18.3
LGAS	58.6	0.0	0.0	0.0	58.6	60.9	60.0
NWSS	12.2	0.0	0.0	0.0	12.2	13.8	13.1
WBS	4.7	0.0	0.0	0.0	4.7	6.1	5.5
TRAS	76.0	0.0	0.0	0.0	76.0	79.4	78.0
ECS	8.4	10.2	-80.8	7.9	-54.2	65.1	-35.8
WIPS	8.5	0.4	-79.9	3.0	-68.0	44.3	-43.9
CIPS	9.2	1.1	-76.5	0.0	-66.3	41.1	-40.3
EPGDS	138.0	0.0	0.0	0.0	138.0	141.4	139.9
HPGDS	-93.9	-6.1	0.0	0.0	-100.0	-100.0	-100.0
PPGDS	-100.0	0.0	0.0	0.0	-100.0	-100.0	-100.0
Aircraft/Mission-level impact					BF: -3.10	EW: 1.72	RW: -0.65

Table 37: Impact of All Electric subsystem architecture for VLA

Sub -system	%Δ Fuel due to				%Δ Total Fuel Imp.	%Δ Weight	%Δ Total Wt. Imp.
	Weight	SPX	BX	Drag			
FCAS	23.5	-4.0	0.0	0.0	19.5	23.0	21.7
LGAS	64.8	0.0	0.0	0.0	64.8	62.5	63.3
NWSS	29.4	0.0	0.0	0.0	29.4	27.7	28.3
WBS	10.7	0.0	0.0	0.0	10.7	9.2	9.7
TRAS	82.1	0.0	0.0	0.0	82.1	80.0	80.8
ECS	7.4	12.1	-83.8	9.1	-55.2	91.3	-37.4
WIPS	10.9	0.5	-85.1	3.2	-70.5	71.4	-41.1
CIPS	1.1	1.6	-71.3	0.0	-68.6	2.5	-44.7
EPGDS	121.1	0.0	0.0	0.0	121.1	118.2	119.3
HPGDS	-88.9	-11.1	0.0	0.0	-100.0	-100.0	-100.0
PPGDS	-100.0	0.0	0.0	0.0	-100.0	-100.0	-100.0
Aircraft/Mission-level impact					BF: -3.96	EW: 2.55	RW: -0.61
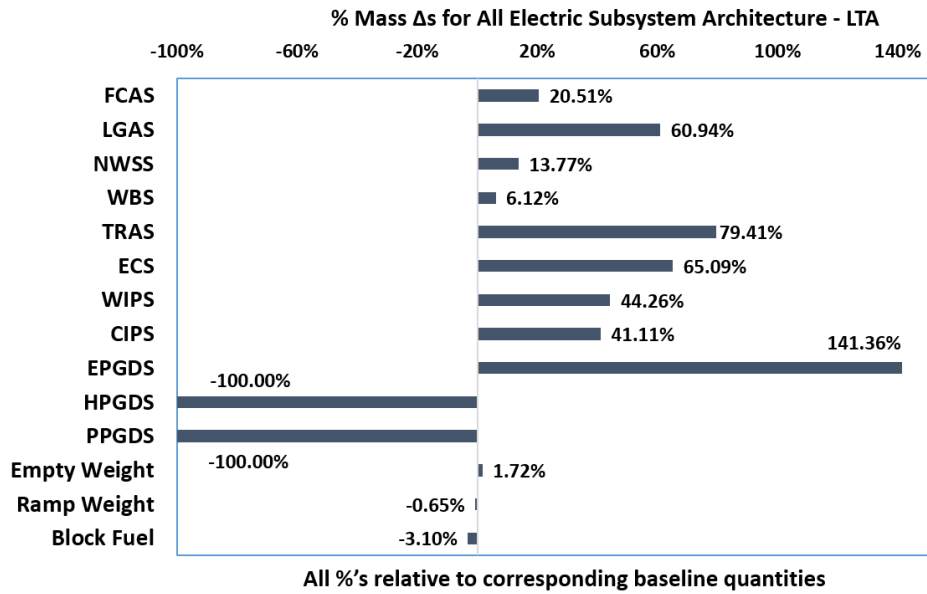
Figure 63: Summary of effects of conventional to All Electric subsystem architecture transition for LTA (LTA-73310 relative to LTA-00000)
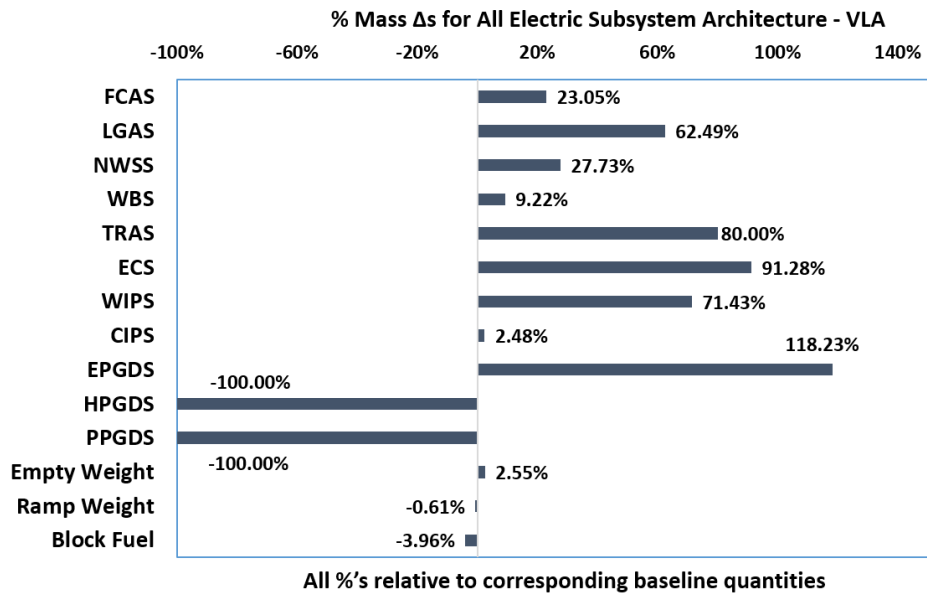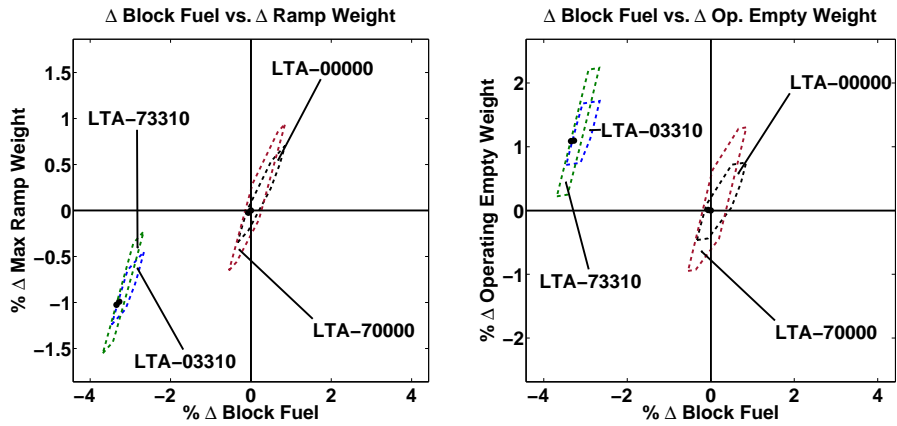

Figure 64: Summary of effects of conventional to All Electric subsystem architecture transition for VLA (VLA-73310 relative to VLA-00000)
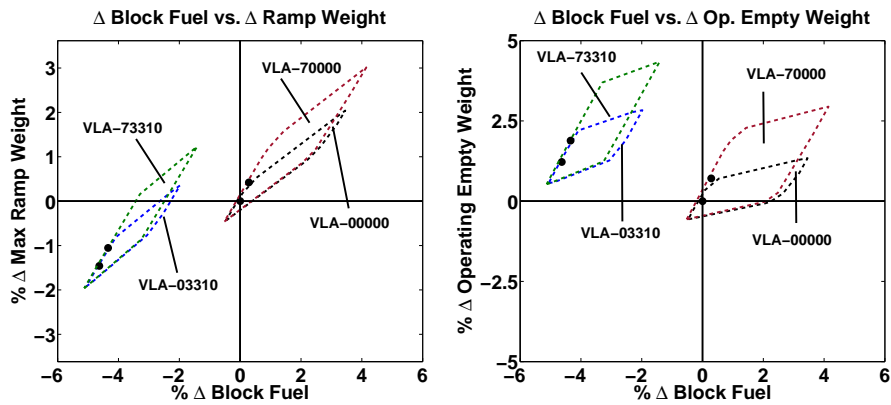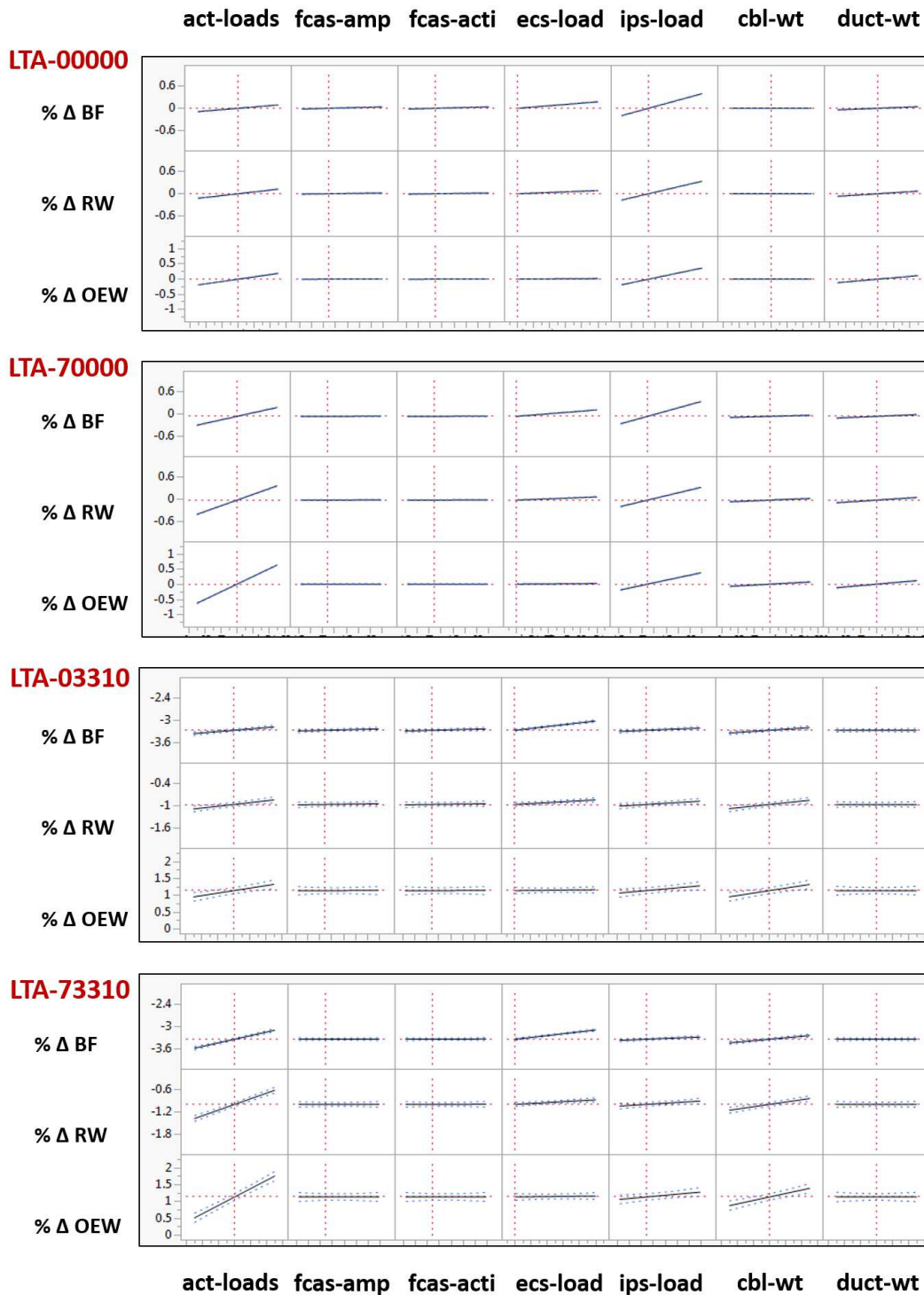
APPENDIX B

SENSITIVITY ANALYSIS FOR LTA & VLA

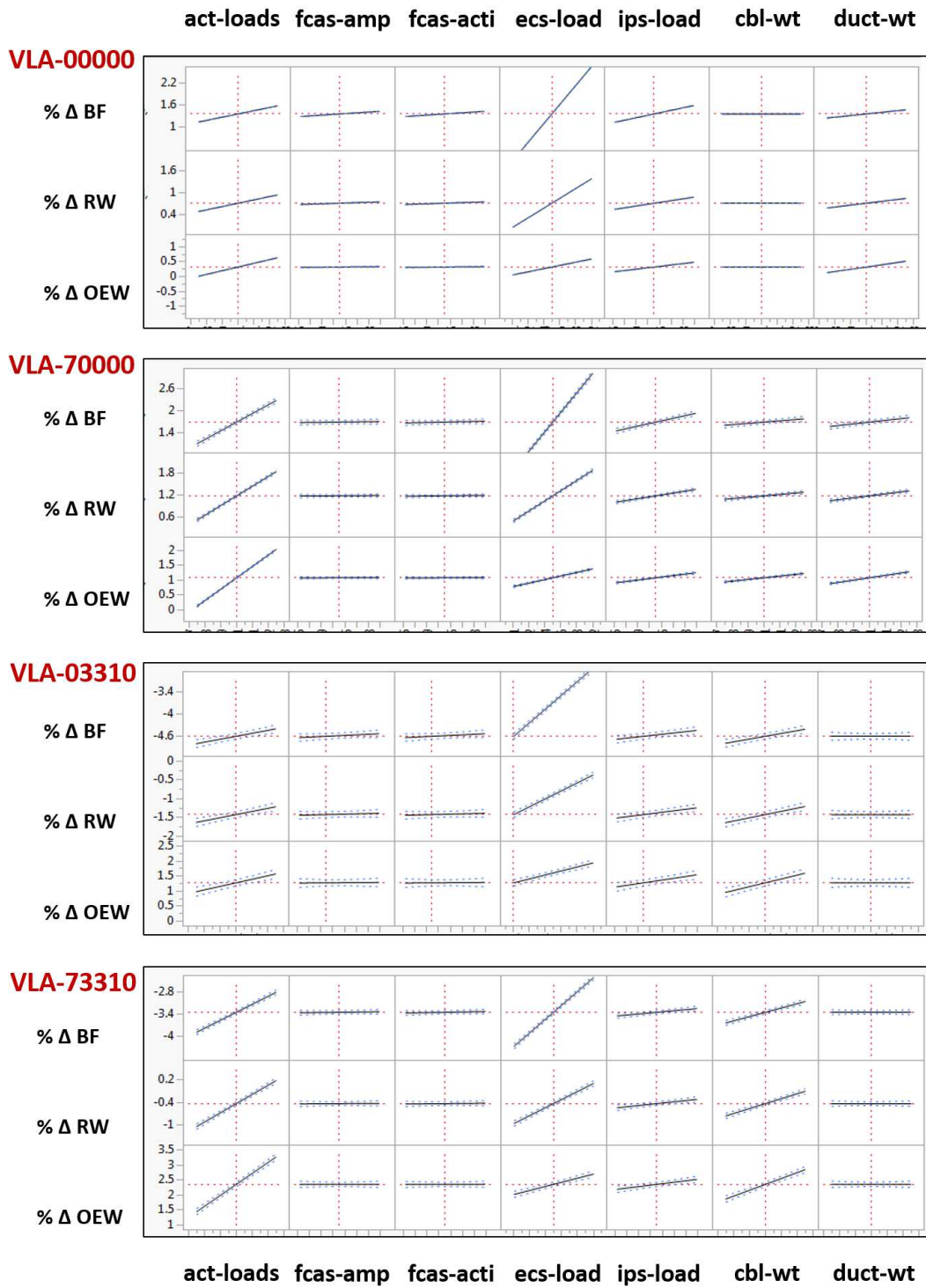## B.1 Sensitivity to Epistemic Uncertainty (Expt. 3.1)

Figure 65: Gross sensitivity of LTA-00000, LTA-70000, LTA-03310, and LTA-73310 to epistemic uncertainty K-factors

Figure 66: Gross sensitivity of VLA-00000, VLA-70000, VLA-03310, and VLA-73310 to epistemic uncertainty K-factors
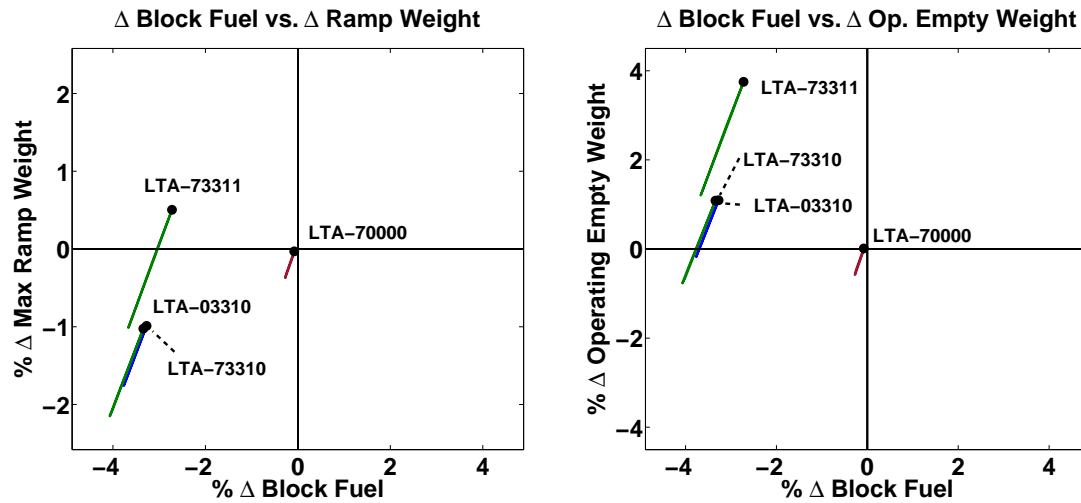
Figure 67: Impact of individual epistemic uncertainty K-factors on performance of LTA-00000, LTA-70000, LTA-03310, and LTA-73310
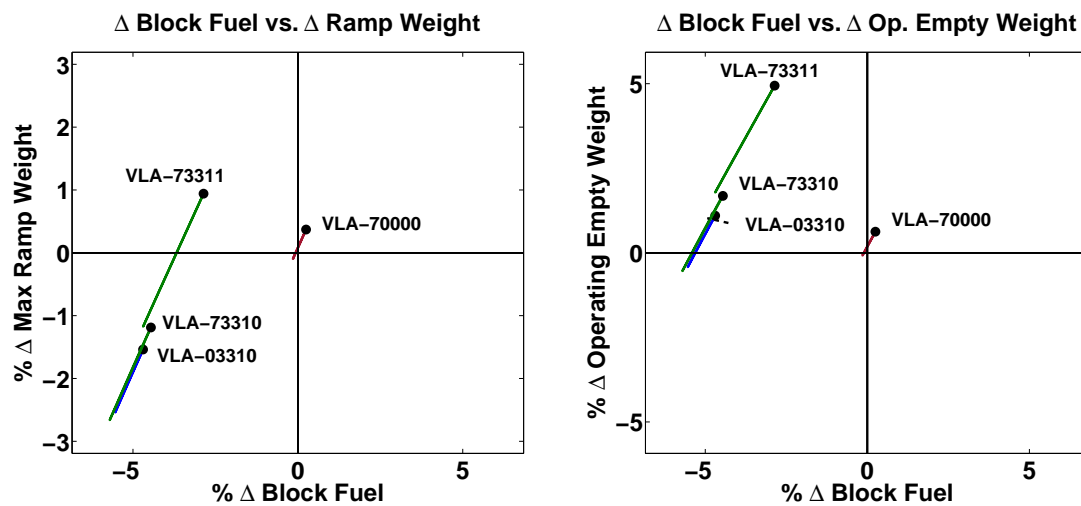
Figure 68: Impact of individual epistemic uncertainty K-factors on performance of VLA-00000, VLA-70000, VLA-03310, and VLA-73310
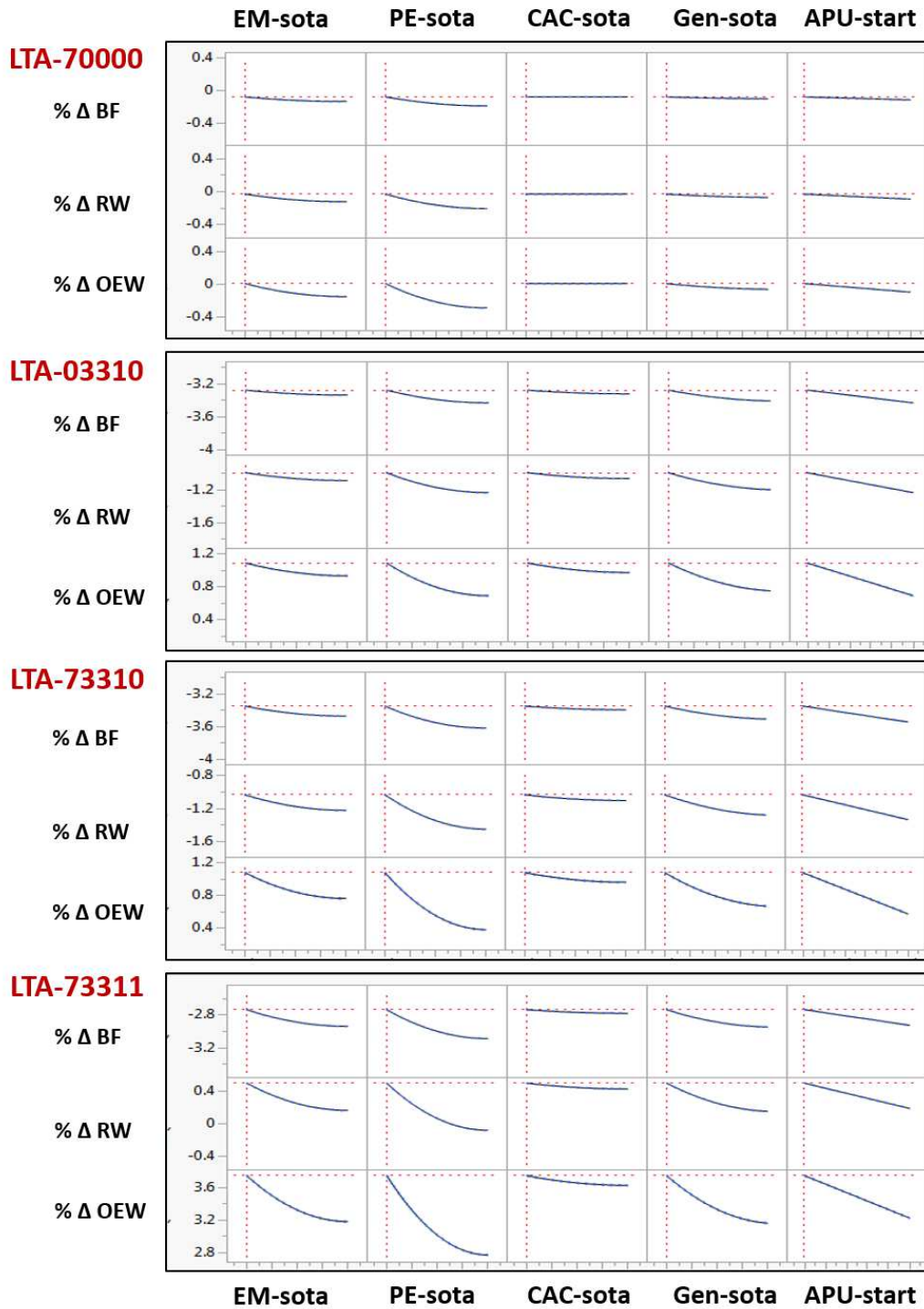
## B.2 Sensitivity to Technological State-of-the-Art (Expt. 3.2)

Figure 69: Gross sensitivity of LTA-70000, LTA-03310, LTA-73310 and LTA-73311 to technological SOTA

Figure 70: Gross sensitivity of VLA-70000, VLA-03310, VLA-73310 and VLA-73311 to technological SOTA

Figure 71: Impact of individual technological SOTA K-factors on performance of LTA-70000, LTA-03310, LTA-73310, and LTA-73311
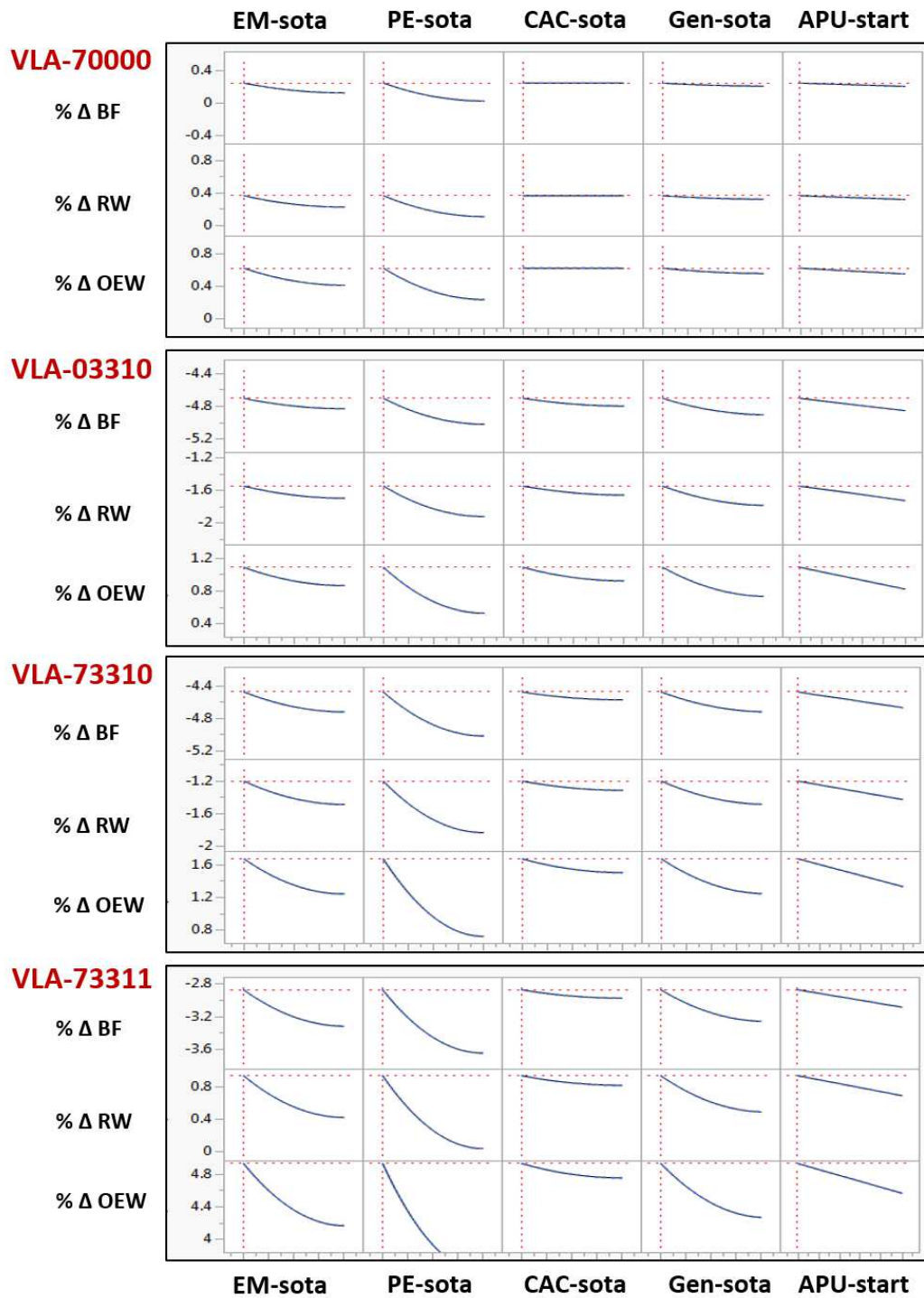
Figure 72: Impact of individual technological SOTA K-factors on performance of VLA-70000, VLA-03310, VLA-73310, and VLA-73311

REFERENCES

[1] Faleiro, L., "Beyond the More Electric Aircraft," *AIAA Aerospace America, September, 2005*, September 2005, pp. 35–40.

[2] "Energy Optimized Aircraft and Equipment Systems Program (EOASys)," American Institute of Aeronautics and Astronautics (AIAA).

[3] Jones, R., "The More Electric Aircraft - Assessing the Benefits," *Proceedings of the Institution of Mechanical Engineers, Part G, Journal of Aerospace Engineering*, Vol. 216, 2002, pp. 259–270.

[4] Cutts, S., "A collaborative approach to the More Electric Aircraft," *International Conference on Power Electronics, Machines and Drives*, No. 487, 2002, pp. 223–228.

[5] Woodford, C., "Electrics for Aircraft," *Journal of the Royal Aeronautical Society*, Vol. 49, 1945, pp. 518–565.

[6] Jones, R., "The More Electric Aircraft: the past and the future?" *IEE Colloquium on Electrical Machines and Systems for the More Electric Aircraft*, 1999, pp. 1/1–1/4.

[7] Rosero, J., Ortega, J., Aldabas, E., and Romeral, L., "Moving Towards a More Electric Aircraft," *Aerospace and Electronic Systems Magazine, IEEE*, Vol. 22, No. 3, March 2007, pp. 3–9.

[8] Cronin, M., "The all-electric aircraft," *IEE Review*, Vol. 36, No. 8, sep 1990, pp. 309 –311.

[9] Cloyd, J., "Status of the United States Air Force's More Electric Aircraft initiative," *Aerospace and Electronic Systems Magazine, IEEE*, Vol. 13, No. 4, April 1998, pp. 17–22.

[10] Engelland, J., "The evolving revolutionary all-electric airplane," *IEEE Transactions on Aerospace and Electronic Systems*, Vol. AES-20, No. 2, 1984, pp. 217–220.

[11] Rubertus, D., Hunter, L., and Cecere, G., "Electromechanical Actuation Technology for the All-Electric Aircraft," *IEEE Transactions on Aerospace and Electronic Systems*, Vol. AES-20, No. 3, 1984, pp. 243–249.

[12] Treacy, J., "Flight Safety Issues of an All-Electric Aircraft," *IEEE Transactions on Aerospace and Electronic Systems*, Vol. AES-20, No. 3, 1984, pp. 227–233.

[13] Hunt, E., Reid, D., Space, D., and Tilton, F., "Commercial Airliner Environmental Control System - Engineering Aspects of Air Quality," *Aerospace Medical Association Annual Meeting*, Anaheim, California, 1995.

[14] Sinnett, M., "Boeing 787 No-Bleed Systems: Saving Fuel and Enhancing Operational Efficiencies," Boeing Aero Magazine, Quarter 4, Online: `http://www.boeing.com/commercial/aeromagazine/`, 2007.

[15] Cronin, M., "All-Electric vs. Conventional Aircraft: The Production/Operational Aspects," *Journal of Aircraft*, Vol. 20, No. 6, 1983, pp. 481–486.

[16] National Transportation Safety Board (NTSB), "Aircraft Accident Report - United Airlines Flight 232, McDonnell Douglas DC-10-10, Sioux Gateway Airport, Sioux City, Iowa, July 19, 1989," Aircraft Accident Report NTSB/AAR-90/06, November 1, 1990.

[17] Biedermann, O. and Geerling, G., "Power Control Units with Secondary Control Hydraulic Motor - A New Concept for Application in Aircraft High Lift Systems," *Proceedings of the Conference on Recent Advances in Aerospace Hydraulics*, Toulouse, France, 1998.

[18] Churn, P., Maxwell, C., Schofield, N., Howe, D., and Powell, D., "Electro-hydraulic actuation of primary flight control surfaces," *IEE Colloquium on All Electric Aircraft*, 1998.

[19] Thompson, K., "Notes on 'The electric control of large aeroplanes'," *Aerospace and Electronic Systems Magazine, IEEE*, Vol. 3, No. 12, December 1988, pp. 19 –24.

[20] Navarro, R., "Performance of an Electro-Hydrostatic Actuator on the F-18 Systems Research Aircraft," *16th Digital Avionics Systems Conference*, Irvine, California, October 1997.

[21] Jensen, S., Jenney, G., and Dawson, D., "Flight test experience with an electromechanical actuator on the F-18 Systems Research Aircraft," *19th Digital Avionics Systems Conference, 2000*, Vol. 1, 2000, pp. 2E3/1 – 2E310.

[22] Burkhard, A. and Dietrich, R., "Joint Strike Fighter Integrated Subsystems Technology, A Demonstration for Industry, by Industry," *Journal of Aircraft*, Vol. 40, 2003, pp. 906–913.

[23] Vohnout, S., Bodden, D., Kim, B., Wagoner, R., Kunst, N., Edwards, P., Gleeson, B., Cascio, D., Brzuszkiewicz, S., Wagemans, R., Rounds, M., and Clements, N., "Prognostic-Enabling of an Electrohydrostatic Actuator (EHA) System," *Annual Conference of Prognostics and Health Management Society*, Minneapolis, MN, 2012.

[24] Van den Bossche, D., "The A380 Flight Control Electrohydrostatic Actuators, Achievements and Lessons Learnt," *25th International Congress of the Aeronautical Sciences, ICAS 2006*, Hamburg, Germany, 2006.

[25] Kulshreshtha, A. and Charrier, J., "Electric Actuation for Flight and Engine Control: Evolution and Challenges," *SAE-ACGSC Meeting 99*, SAE, Feb 28 - Mar 2, 2007.

[26] Atallah, K., Caparrelli, F., Bingham, C., Schofield, N., Howe, D., Mellor, P., Maxwell, C., Moorhouse, D., and Whitley, C., "Permanent magnet brushless drives for aircraft flight control surface actuation," *Electrical Machines and Systems for the More Electric Aircraft (Ref. No. 1999/180), IEE Colloquium on*, London, U.K., 1999, pp. 8/1 –8/5.

[27] Fronista, G. and Bradbury, G., "An electromechanical actuator for a transport aircraft spoiler surface," *Energy Conversion Engineering Conference, 1997. IECEC-97., Proceedings of the 32nd Intersociety*, Vol. 1, 1997, pp. 694–698.

[28] Recksiek, M., "Advanced High Lift System Architecture with Distributed Electrical Flap Actuation," *Aviation System Technology Workshop*, Hamburg, Germany, 2009.

[29] Bennett, J., Mecrow, B., Jack, A., Atkinson, D., Sheldon, S., Cooper, B., Mason, G., Sewell, C., and Cudley, D., "A prototype electrical actuator for aircraft flaps and slats," *Electric Machines and Drives, 2005 IEEE International Conference on*, San Antonio, TX, 2005, pp. 41–47.

[30] "Goodrich 787 Electro-Mechanical Brake," UTC Aerospace Systems - capabilities, `http://utcaerospacesystems.com/cap/Documents`, accessed: November 4, 2015.

[31] Bennett, J., Mecrow, B., Atkinson, D., and Atkinson, G., "Safety-critical design of electromechanical actuation systems in commercial aircraft," *Electric Power Applications, IET*, Vol. 5, No. 1, 2011, pp. 37–47.

[32] Nicolas, Y., "eTaxi - Taxiing aircraft with engines stopped," Flight Airworthiness Support Technology (FAST) 51, Airbus Technical Magazine, `http://www.airbus.com/support/publications/`, January 2013.

[33] Secunde, R., Macosko, R., and Repas, D., "Integrated Engine-Generator Concept for Aircraft Electric Secondary Power," Technical Memorandum NASA-TM-X-2579, NASA Lewis Research Center, Cleveland, OH, USA, June 1972.

[34] Cao, W., Mecrow, B., G.J., A., Bennet, J., and Atkinson, D., "Overview of Electric Motor Technologies Used for More Electric Aircraft (MEA)," *IEEE Transactions on Industrial Electronics*, Vol. 59, September 2012, pp. 3523–3531.

[35] Atkinson, G., Mecrow, B., Jack, D., Atkinson, D., Sangha, P., and Benarous, M., "The analysis of losses in high-power fault-tolerant machines for aerospace applications," *IEEE Trans. Ind. Appl.*, Vol. 42, No. 5, 2006, pp. 1162–1170.

[36] Nam, T., *A Generalized Sizing Method for Revolutionary Concepts under Probabilistic Design Constraints*, Ph.D. thesis, School of Aerospace Engineering, Georgia Institute of Technology, 2007.

[37] Raymer, D., *Aircraft Design: A Conceptual Approach*, AIAA Education Series, 4th ed., 2006.

[38] Roskam, J., *Airplane Design Part V - Component Weight Estimation*, Design Analysis & Research, 1999.

[39] Lammering, T., *Integration of Aircraft Systems into Conceptual Design Synthesis*, Ph.D. thesis, Institute of Aeronautics and Astronautics (ILR), RWTH Aachen University, 2014.

[40] Heimbold, R., Cronin, M., and Howison, W., "Application of Advanced Electric/Electronic Technology to Conventional Aircraft," NASA Contractor Report NASA-CR-163576, Lockheed-California Co., Burbank, CA, Lockheed-Georgia Co., AiResearch Manufacturing Co., Honeywell Inc., July 1980.

[41] Howison, W. and Cronin, M., "Electronic/Electric Technology Benefits Study," NASA Contractor Report NASA-CR-165890, Lockheed-California Company, Burbank, California, May 1982.

[42] Tagge, G., Irish, L., and Bailey, A. R., "Systems Study for an Integrated Digital/Electric Aircraft (IDEA)." NASA Contractor Report 3840, January 1985.

[43] Cronin, M., Hays, A., Green, F., Radovcich, N., Helsley, C., and Rutchik, W., "Integrated Digital/Electric Aircraft Concepts Study," NASA Contractor Report 3841, 1985.

[44] Hoffman, A., Hansen, I., Beach, R., Plencher, R., Dengler, R., Jefferies, K., and Frye, R., "Advanced Secondary Power System for Transport Aircraft," NASA Technical Paper 2463, National Aeronautics and Space Administration (NASA), 1985.

[45] Crowder, R. and Jones, R., "Collaborative Research Initiative into Secondary Power Systems - Final Summary Report," CoA CIT and University of Southampton, October 1992.

[46] Jones, R., "Collaborative Research Initiative into Secondary Power Systems - Executive Summary Final Report," CoA CIT, January 1993.

[47] TEOS Forum Organization Committee, "Technology for Energy Optimized Aircraft Equipment Systems - Technical Summary," Power Optimized Aircraft (POA) project consortium, 2006.

[48] Dodds, G. and Faleiro, L., "Technology for Energy Optimized Aircraft Equipment Systems - The Way Forward," Power Optimized Aircraft (POA) project consortium, 2006.

[49] Jomier, T., "More Open Electric Technologies (MOET)," MOET-FP6-030861, Airbus Operations S.A.S. and MOET Consortium Partners, 2009.

[50] Bodie, M., Russell, G., McCarthy, K., Lucuc, E., Zumberge, J., and Wolff, M., "Thermal Analysis of an Integrated Aircraft Model," *48th AIAA Aerospace Sciences Meeting Including the New Horizons Forum and Aerospace Exposition*, 2010.

[51] Walters, E.A. and Iden, S. et al., "INVENT Modeling, Simulation, Analysis and Optimization," *48th AIAA Aerospace Sciences Meeting Including the New Horizons Forum and Aerospace Exposition*, 2010.

[52] Jackson, D., *Robust Aircraft Subsystem Conceptual Architecting*, Ph.D. thesis, Georgia Institute of Technology, 2013.

[53] de Tenorio, C., *Method for Collaborative Conceptual Design of Aircraft Power Architectures*, Ph.D. thesis, Georgia Institute of Technology, Atlanta, GA, USA, 2010.

[54] Armstrong, M., *Identification of Emergent Off-Nominal Operational Requirements During Conceptual Architecting of the More Electric Aircraft*, Ph.D. thesis, Georgia Institute of Technology, 2011.

[55] Armstrong, M., *A Process for Function Based Architecture Definition and Modeling*, Master's thesis, Georgia Institute of Technology, 2008.

[56] Liscouet-Hanke, S., *A Model-Based Methodology for Integrated Preliminary Sizing and Analysis of Aircraft Power System Architectures*, Ph.D. thesis, Universite' de Toulouse, 2008.

[57] Liscouet-Hanke, S., Mare, J.-C., and Pufe, S., "Simulation Framework for Aircraft Power System Architecting," *Journal of Aircraft*, Vol. 46, No. 4, 2009, pp. 1375–1380.

[58] Liscouet-Hanke, S., Pufe, S., and Mare, J.-C., "A Simulation Framework for Aircraft Power Management," *Proceedings of the Institution of Mechanical Engineers, Part G: Journal of Aerospace Engineering*, Vol. 222, No. 6, June 2008, pp. 749–756.

[59] Seresinhe, R. and Lawson, C., "Electrical load-sizing methodology to aid conceptual and preliminary design of large commercial aircraft," *Proceedings of the Institution of Mechanical Engineers, Part G, Journal of Aerospace Engineering*, May 2014, pp. 1–22.

[60] Seresinhe, R., *Impact of aircraft systems within aircraft operation: A MEA trajectory optimization study*, Ph.D. thesis, Centre for Aeronautics, School of Aerospace, Transport, and Manufacturing, Cranfield University, September 2014.

[61] Leonard, J., "The All-Electric Fighter Airplane Flight Control Issues, Capabilities, and Projections," *IEEE Transactions on Aerospace and Electronic Systems*, Vol. AES-20, 3, May 1984, pp. 234–242.

[62] Hlavacek, I., Chleboun, J., and Babuska, I., *Uncertain Input Data Problems and the Worst Scenario Method*, North-Holland Series in Applied Mathematics and Mechanics, Elsevier B.V., 2004.

[63] Moir, I. and Seabridge, A., *Design and Development of Aircraft Systems*, No. ISBN: 978-1-119-94119-4, Wiley Aerospace Series, 2013.

[64] Mattingly, J. D., *Aircraft Engine Design*, American Institute of Aeronautics and Astronautics Education Series, 2002.

[65] McCullers, L., *Flight Optimization System, Release 8.11, User's Guide*, NASA Langley Research Center, Hampton, VA 23681-0001, October 9 2009.

[66] Rudolph, P., "High Lift Systems on Subsonic Commercial Airliners," NASA Contractor Report 4746 CONTRACT A46374D(LAS), National Aeronautics and Space Administration, September 1996 1996.

[67] Bennett, J., *Fault Tolerant Electromechanical Actuators for Aircraft*, Ph.D. thesis, Newcastle University, School of Electrical, Electronic and Computer Engineering, 2010.

[68] Bennett, J., Mecrow, B., Atkinson, D., Maxwell, C., and Benarous, M., "Fault-tolerant electric drive for an aircraft nose wheel steering actuator," *IET Electrical Systems in Transportation*, Vol. 1, No. 3, 2011, pp. 117–125.

[69] Bennett, J., Mecrow, B., Jack, A., and Atkinson, D., "A Prototype Electrical Actuator for Aircraft Flaps," *Industry Applications, IEEE Transactions on*, Vol. 46, No. 3, 2010, pp. 915–921.

[70] Botten, S., Whitley, C., and King, A., "Flight Control Actuation Technology for Next-Generation All-Electric Aircraft," *Technology Review Journal - Millenium Issue*, 2000, pp. 55–68.

[71] Heinrich, A., Ross, R., Zumwalt, G., Provorse, J., Padmanabhan, V., Thompson, J., and Riley, J., "Aircraft Icing Handbook - Volume 2 of 3," DOT/FAA/CT-88/8- I, Department of Transporation, Federal Aviation Administration Technical Center, 1991.

[72] Scholz, D., "Fuel Costs due to Aircraft Systems - Calculated from Small Time Intervals," Memo, Aircraft Design and Systems Group, Hamburg University of Applied Sciences, 2007.

[73] Blanding, D., "Subsystem Design and Integration for the More Electric Aircraft," *25th International Congress of the Aeronautical Sciences (ICAS 2006)*, Hamburg, Germany, September 3-8, 2006.

[74] Nelson, T., "787 Systems and Performance," Flight Operations Engineering, Boeing Commercial Airplanes, March 2009, online: `http://myhres.com/Boeing-787-Systems-and-Performance.pdf`, accessed November 4, 2015.

[75] Roskam, J., *Airplane Design Part VI - Preliminary Calculation of Aerodynamic, Thrust and Power Characteristics*, Design Analysis & Research, 1999.

[76] Chakraborty, I., Trawick, D., Hegde, C., Choi, H., Mendez-Ramos, E., and Mavris, D. N., "Development of a Modeling and Simulation Environment for Real-time Performance Analysis of Electric Actuators in Maneuvering Flight," *51st AIAA Aerospace Sciences Meeting Including The New Horizons Forum and Aerospace Exposition*, No. AIAA-2013-0471, Grapevine, TX, January 2013.

[77] "Federal Aviation Regulations (FAR) Part 25 - Airworthiness Standards: Transport Category Airplanes," Federal Aviation Administration (FAA), online: `http://www.ecfr.gov/`, accessed November 4, 2015.

[78] Scholz, D., "Development of a CAE-Tool for the Design of Flight Control and Hydraulic Systems," *AeroTech '95*, Birmingham, U.K., 1995.

[79] Scholz, D., "Equations for a Preliminary Actuator Design," Technical Note TN-EV52-360/91, Deutsche Airbus, 1991.

[80] Scholz, D., "Computer Aided Engineering for the Design of Flight Control and Hydraulic Systems," *ICAS Proccedings 1996 (20th Congress of the International Council of the Aeronautical Sciences)*, 1996.

[81] Airbus Training, "Airbus A330 Flight Crew Operating Manual - Flight Controls," online: `http://www.smartcockpit.com/aircraft-ressources/A330-Flight_Controls.html`, accessed November 4, 2015.

[82] *Boeing 777 Aircraft Maintenance Manual, Chapter 27 - Flight Controls*, 2006.

[83] *Boeing 737-600/700/800 System Schematic Manual, Chapter 27 - Flight Controls*, 2012.

[84] Society of Automotive Engineers, "SAE Aerospace Information Report (AIR) 5005A - Commercial Aircraft Hydraulic Systems," 2010.

[85] Socheleau, J., Mare, J.-C., and Baudu, P., "Actuation Technologies and Application - Flight Controls and Thrust Reverser Actuation," *Technologies for Energy Optimized Aircraft Equipment Systems (TEOS forum)*, Paris, France, 2006.

[86] Chakraborty, I., Mavris, D., Emeneth, M., and Schneegans, A., "A Methodology for Vehicle and Mission Level Comparison of More Electric Aircraft Subsystem Solutions - Application to the Flight Control Actuation System," *Proceedings of the Institution of Mechanical Engineers, Part G: Journal of Aerospace Engineering*, Vol. 229, No. 6, July 28 2014, pp. 1088–1102.

[87] Chakraborty, I., Mavris, D., Emeneth, M., and Schneegans, A., "An Integrated Approach to Vehicle and Subsystem Sizing and Analysis for Novel Subsystem Architectures," *Proceedings of the Institution of Mechanical Engineers, Part G: Journal of Aerospace Engineering*, DOI: 10.1177/0954410015594399, accepted for publication July 20, 2015.

[88] Garmendia, D., Chakraborty, I., and Mavris, D., "A Method for Evaluating Electrically Actuated Redundant Control Surface Layouts for the Hybrid Wing Body," *AIAA Journal of Aircraft*, DOI: 10.2514/1.C033061, accepted for publication Feb 18, 2015.

[89] Garmendia, D., Chakraborty, I., and Mavris, D., "A Multidisciplinary Approach to Assessing Actuation Power of a Hybrid Wing Body," *AIAA Journal of Aircraft*, accepted for publication Sep 8, 2015.

[90] Chakraborty, I., Trawick, D., Jackson, D., and Mavris, D., "Electric Control surface Actuator Design Optimization and Allocation for the More Electric Aircraft," *AIAA Aviation 2013 Conference*, No. AIAA 2013-4283, Los Angeles, California, August 12-14, 2013.

[91] Rea, J., "Boeing 777 High Lift Control System," *IEEE Aerospace and Electronic Systems Magazine*, Vol. 8, No. 8, August 1993, pp. 15–21.

[92] Eaton Aerospace Group, "Aerospace Capabilities - Boeing 777," online: `http://www.eaton.com/ecm/groups/public/@pub/@eaton/@aero/documents/content/ct_194202.pdf`, accessed November 4, 2015.

[93] Martinez, M., Sawata, T., Rouge-Carrassat, T., and Blineau, J.-M., "Electrical Power Sources and Aircraft Power Networks," *Technologies for Energy Optimized Aircraft Equipment Systems (TEOS forum)*, Paris, France, 2006.

[94] Slingerland, R., Zandstra, S., Scholz, D., and Seeckt, K., "Green Freighter Systems," *46th AIAA Aerospace Sciences Meeting and Exhibit*, No. AIAA-2008-146, American Institute of Aeronautics and Astronautics, 7-10 January 2008.

[95] Li, W. and Fielding, J., "Preliminary Study of EMA Landing Gear Actuation," *28th International Congress of the Aeronautical Sciences (ICAS 2012)*, Brisbane, Australia, 2012.

[96] Jenkins, S., "Landing Gear Design and Development," *Proceedings of the Institution of Mechanical Engineers, Part G: Journal of Aerospace Engineering*, Vol. 203, No. 1, 1989, pp. 67–73.

[97] Currey, N., *Aircraft Landing Gear Design: Principles and Practices*, No. ISBN: 978-0-930403-41-6, AIAA Education Series, American Institute of Aeronautics and Astronautics, 1988.

[98] Young, D., "Aircraft landing gears - the past, present and future," *Proceedings of the Institution of Mechanical Engineers, Part D: Journal of Automobile Engineering*, Vol. 200, No. 2, 1986, pp. 75–92.

[99] Roskam, J., *Airplane Design Part IV - Layout of Landing Gear and Systems*, Design Analysis & Research, 1999.

[100] Grac, S., "Distributed and Redundant Electro-mechanical Nose Wheel Steering System (DRESS) - Publishable Executive Summary," Messier-Bugatti (Safran Group), 2010.

[101] Cameron-Johnson, A., "Some Aspects of the Design of Aircraft Steering Systems," *Aircraft Engineering and Aerospace Technology*, Vol. 43, No. 6, 1971, pp. 7–10.

[102] Hendricks, E. and Tong, M., "Performance and Weight Estimates for an Advanced Open Rotor Engine," NASA/TM2012-217710, National Aeronautics and Space Administration, Glenn Research Center, Cleveland, OH, September 2012.

[103] Nevoret, P., "Recent Advances and Future Electrical Landing Gear Systems," *ICAS Biennial Workshop - "The More Electrical Aircraft: Achievements & perspectives for the future"*, Cape Town, South Africa, September 2013.

[104] Wahi, M., Warren, S., and Straub, H., "An Extended Prediction Model for Airplane Braking Distance and a Specification for a Total Braking Prediction System," Technical Report ASD-TR-77-6, Boeing Commercial Airplane Company, Aeronautical Systems Division, Air Force Systems Command, Wright-Patterson Air Force Base, OH 45433, 1977.

[105] The Goodyear Tire and Rubber Company, "Aircraft Tire Data Book," 1144 East Market Street, Akron, OH 44316-0001, 2002.

[106] Collins, A., "EABSYS: Electrically Actuated Braking System," *IEE Colloquium on Electrical Machines and Systems for the More Electric Aircraft*, London, U.K., 1999, p. 4.

[107] Root, R., "Brake Energy Considerations in Flight Operations," Flight Operations Engineering, Boeing Commercial Airplanes, September, 2003, online: `www.smartcockpit.com`, accessed: November 4, 2015.

[108] Allen, T., Miller, T., and Preston, E., "Operational Advantages of Carbon Brakes," Boeing Aero Magazine, Quarter 3, Online: `http://www.boeing.com/commercial/aeromagazine/`, 2009.

[109] Bernery, Y. and Minehan, J., "Actuation Technologies and Application - Braking and Landing Gear Actuation," *Technologies for Energy Optimized Aircraft Equipment Systems (TEOS forum)*, Paris, France, 2006.

[110] Chai, S. and Mason, W., "Landing Gear Integration in Aircraft Conceptual Design," *6th AIAA/NASA/ISSMO Symposium on Multidisciplinary Analysis and Optimization*, No. AIAA 96-4038, Bellevue, WA, September 4-6 1996.

[111] Linke-Diesinger, A., *Systems of Commercial Turbofan Engine - An Introduction to Systems Functions*, Springer, 2007.

[112] Honeywell Aerospace, "Thrust Reverser Actuation Systems: Hydraulic (HTRAS)," Online: `https://aerospace.honeywell.com/en/products/actuation/thrust-reverser-actuation-systems-hydraulic-htras`, Accessed November 4, 2015.

[113] Scholz, D., "MPC 75 Hydraulic Load Analysis," Technical Note TN-EV52-362/91, Deutsche Airbus, Hamburg, July 1991.

[114] Chakraborty, I., LeVine, M., and Hassan, M., "Assessing Taxiing Trade Spaces from Aircraft, Airport, and Airline Perspectives," *AIAA AVIATION 2015 Conference*, No. AIAA-2015-2386, American Institute of Aeronautics and Astronautics, Dallas, TX, June 22-26 2015.

[115] Morris, K., "Results from a number of surveys of power settings used during taxi operations," Technical Report EJT/KMM/1126/14.8, British Airways, October 2005.

[116] Sinnett, M., "787 Program - Electrical System and Batteries," Online: www.boeing.com/787-media-resource/docs/Sinnett-TOS-Deck.pdf, February 2013.

[117] Herzog, J., "Electrification of the Environmental Control System," *25th International Congress of the Aeronautical Sciences (ICAS)*, No. ICAS 2006-7.7.1, Hamburg, Germany, 3 - 8 September 2006.

[118] Colin, A., Herzog, J., Dodds, G., and Larue, F., "Environmental Control System and Wing Ice Protection (ECS & WIPS)," *Technologies for Energy Optimized Aircraft Equipment Systems (TEOS forum)*, Paris, France, 2006.

[119] Muller, C., Scholz, D., and Giese, T., "Dynamic Simulation of Innovative Aircraft Air Conditioning," *First CEAS European Air and Space Conference*, Berlin, September 10-13 2007.

[120] Pratt, J., Klebanoff, L., Munoz-Ramos, K., Akhil, A., Curgus, D., and Schenkman, B., "Proton Exchange Membrane Fuel Cells for Electrical Power Generation On-Board Commercial Airplanes," Sandia Report SAND2011-3119, Sandia National Laboratories, Albuquerque, New Mexico 87185 and Livermore, California 94550, May 2011.

[121] Airbus Industrie, "Airbus A320 Simulator Flight Crew Operating Manual - Air Conditioning, Pressurization, and Ventilation," online: `http://www.smartcockpit.com/aircraft-ressources/A320-Air_Conditioning_and_Pressurization.html`, accessed November 4, 2015.

[122] Airbus Industrie, "A319/A320/A321 Technical Training Manual, 21 Air Conditioning," 2000.

[123] Airbus Industrie, "Airbus A330 Simulator Flight Crew Operating Manual - Air Conditioning, Pressurization, and Ventilation," online: `http://www.smartcockpit.com/aircraft-ressources/A330-Aircond-Press-Vent.html`, accessed November 4, 2015.

[124] Airbus Industrie, "Airbus A340 Simulator Flight Crew Operating Manual - Air Conditioning, Pressurization, and Ventilation," online: `http://www.smartcockpit.com/aircraft-ressources/FCOM_A340-Air_Cond-Press-Vent.html`, accessed November 4, 2015.

[125] Boeing, "Boeing 737NG - Systems Summary, Air Systems," online: `http://www.smartcockpit.com/aircraft-ressources/B_NG-Air_Systems.html`, accessed November 4, 2015.

[126] Brasseur, A., Leppert, W., and Pradille, A., "Inside the 747-8 New Environmental Control System," Boeing Aero Magazine, Issue 45, Quarter 1, 2012. Online: `http://www.boeing.com/commercial/aeromagazine/articles/2012_q1/pdfs/AERO_2012q1_article4.pdf`.

[127] Hodal, P. and Liu, G., "Bleed Air Temperature Regulation System: Modeling, Control, and Simulation," *Proceedings of the 2005 IEEE Conference on Control Applications*, Toronto, Canada, August 28-31, 2005.

[128] Heinrich, A., Ross, R., Zumwalt, G., Provorse, J., Padmanabhan, V., Thompson, J., and Riley, J., "Aircraft Icing Handbook - Volume 1 of 3," DOT/FAA/CT-88/8- I, Department of Transporation, Federal Aviation Administration Technical Center, 1991.

[129] Thomas, S. K., Cassoni, R. P., and MacArthur, C. D., "Aircraft anti-icing and de-icing techniques and modeling," *Journal of Aircraft*, Vol. 33, No. 5, 1996, pp. 841–854.

[130] Bu, X., Lin, G., Yu, J., Shen, X., and Hou, P., "Numerical analysis of a swept wing hot air ice protection system," *Proceedings of the Institution of Mechanical Engineers, Part G: Journal of Aerospace Engineering*, Vol. 227, No. 10, 2013, pp. 1608–1622.

[131] Al-Khalil, K., Keith, T., DeWitt, K., Nathman, J., and Dietrich, D., "Thermal Analysis of Engine Inlet Anti-Icing Systems," *Journal of Propulsion*, Vol. 6, No. 5, 1990, pp. 628–634.

[132] Patricelli, L., *Innovative Solutions for the Thermal Control of Aeronautic Vehicles*, Ph.D. thesis, Dipartimento di Ingegneria Industriale, Universit degli Studi di Padova (University of Padua), 2014.

[133] Krammer, P. and Scholz, D., "Estimation of Electrical Power Required for Deicing Systems," Technical Note, Aircraft Design and Systems Group, Department of Automotive and Aeronautical Engineering, Hamburg University of Applied Sciences (HAW), 2009.

[134] European Aviation Safety Agency (EASA), "Certification Specifications and Acceptable Means of Compliance for Large Aeroplanes: CS-25, Amendment 16," 2013.

[135] Jeck, R., "Icing Design Envelopes (14 CFR Parts 25 and 29, Appendix C) Converted to a Distance-Based Format," Final Report DOT/FAA/AR-00/30, Federal Aviation Administration, Airport and Aircraft Safety Research and Development, William J. Hughes Technical Center, 2002.

[136] Society of Automotive Engineers, "SAE Aerospace Applied Thermodynamics Manual - SAE AIR 1168," 1989.

[137] Bowden, D., Gensemer, A., and Skeen, C., "Engineering Summary of Aircraft Icing Technical Data," Technical Report ADS-4, Federal Aviation Agency, Washington D.C., 1964.

[138] Wright, W., "An Evaluation of Jet Impingement Heat Transfer Correlations for Piccolo Tube Application," *42nd Aerospace Sciences Meeting and Exhibit*, No. AIAA-2004-0062, 2004.

[139] Al-Khalil, K., Horvath, C., Miller, D., and Wright, W., "Validation of Thermal Ice Protection Computer Codes: Part 3 - The Validation of ANTICE," *35th Aerospace Sciences Meeting and Exhibit*, No. AIAA-97-0051, Reno, Nevada, 1997.

[140] Gray, V., "Correlations Among Ice Measurements, Impingement Rates, Icing Conditions, and Drag Coefficients for Unswept NACA 65A004 Airfoil," NACA Technical Note 4151, National Advisory Committee for Aeronautics, Washington, February 1958.

[141] Sadeghi, T. and Lyons, A., "Fault Tolerant EHA Architectures," *IEEE AES Systems Magazine*, Vol. 7, No. 3, March 1992, pp. 32–42.

[142] Wheeler, P. W., Clare, J. C., Trentin, A., and Bozhko, S., "An overview of the more electrical aircraft," *Proceedings of the Institution of Mechanical Engineers, Part G: Journal of Aerospace Engineering*, Vol. 227, No. 4, 2012, pp. 578–585.

[143] Giraud, X., Piquet, H., Budinger, M., Roboam, X., Sartor, M., and Vial, S., "Knowledge-based system for aircraft electrical power system reconfiguration," *Electrical Systems for Aircraft, Railway and Ship Propulsion (ESARS), 2012*, Oct 2012, pp. 1–6.

[144] Banel-Caule, I., "Systems Weight Estimation Enhanced Method for Early Project Phases," *66th Annual Conference of Society of Allied Weight Engineers, Inc.*, No. SAWE Paper No. 3430, Society of Allied Weight Engineers, Inc., Madrid, Spain, May 26-31 2007.

[145] Airbus Industrie, "Airbus A320 Aircraft Maintenance Manual, ATA29," 2006.

[146] Xia, X., *Dynamic Power Distribution Management for All Electric Aircraft*, Master's thesis, School of Engineering, Cranfield University, 2011.

[147] Whyatt, G. and Chick, L., "Electrical Generation for More-Electric Aircraft using Solid Oxide Fuel Cells," Report PNNL-21382, Pacific Northwest National Laboratory, Richland, WA 99352, April 2012.

[148] Christou, I., Nelms, A., Cotton, I., and Husband, M., "Choice of Optimal Voltage for More Electric Aircraft Wiring Systems," *IET Electrical Systems in Transportation*, Vol. 1, No. 1, 2010, pp. 24–30.

[149] U.S. Department of Transporation, Federal Aviation Administration, "Acceptable Methods, Techniques, and Practices - Aircraft Inspection and Repair," Advisory Circular AC 43.13-1B, September, 1998.

[150] Airbus Training, "Airbus A319/A320/A321 Pneumatics," online: `http://www.smartcockpit.com/aircraft-ressources/A319-320-321-Pneumatics.html`, accessed November 4, 2015.

[151] Airbus Training, "Airbus A330 Flight Crew Operating Manual - Pneumatic," online: `http://www.smartcockpit.com/aircraft-ressources/A330-Pneumatic.html`, November 4, 2015.

[152] *Boeing 777 Aircraft Maintenance Manual, Chapter 36 - Pneumatic*, 2006.

[153] Peacock, D., "Effective Design using Titanium," *Intl. Conf. Titanium in Practical Applications, Norwegian Association of Corrosion Engineers*, 1990.

[154] Australian Transport Safety Bureau, "Air/pressurization involving a Boeing Company 767-277. VH-RMF, near Canberra Aerodrome, ACT on 21 October 1993," Investigation number: 199303375, 1993, online: `https://www.atsb.gov.au/publications/investigation_reports/1993/aair/199303375.aspx`, accessed November 4, 2015.

[155] Ramgopal, M., "Refrigeration and Air Conditioning - Design of Air Conditioning Ducts," Indian Institute of Technology Kharagpur, through National Programme on Technology Enhanced Learning (NPTEL), online: `http://nptel.ac.in/courses/112105129/pdf/R&AC%20Lecture%2038.pdf`, accessed November 4, 2015.

[156] European Aviation Safety Agency (EASA), *EASA Type Certification Data Sheet - CFM International S.A. - CFM56-7B series engines*, December 17 2012.

[157] Scholz, D., Seresinhe, R., Staack, I., and Lawson, C., "Fuel Consumption due to Shaft Power Off-takes from the Engine," *4th International Workshop on Aircraft System Technologies, AST 2013*, Shaker, Hamburg,, April 23-24 2013, pp. 169–179.

[158] Kirby, M. and Mavris, D., "The Environmental Design Space," *26th International Congress of the Aeronautical Sciences (ICAS)*, No. ICAS-2008-4.7.3, Anchorage, Alaska, September 14-19 2008.

[159] Schutte, J., Tai, J., and Mavris, D., "Multi-Design Point Cycle Design Incorporation into the Environmental Design Space," *48th AIAA/ASME/SAE/ASEE Joint Propulsion Conference & Exhibit*, Atlanta, GA, July 30 - Aug 1 2012.

[160] Schutte, J., Tai, J., Sands, J., and Mavris, D., "Cycle Design Exploration using Multi-Design Point Approach," *Proceedings of ASME Turbo Expo 2012*, Copenhagen, Denmark, June 11-15 2012.

[161] Simsic, C., "Electric actuation system duty cycles," *Aerospace and Electronics Conference, 1991. NAECON 1991., Proceedings of the IEEE 1991 National*, 1991, pp. 540–545 vol.2.

[162] Blanding, D., Sexton, M., Segal, M., and Grow, J., "The Application of Confidence Interval in the Evaluation of Electric Actuation Duty Cycle," *27th Congress of International Council of the Aeronautical Sciences (ICAS)*, No. ICAS 2010-7.3.3, Nice, France, 19 - 24 September 2010.

[163] Society of Automotive Engineers, "Aircraft Fuel Weight Penalty Due to Air Conditioning, SAE Aerospace Applied Thermodynamics Manual - SAE AIR 1168/8," 1989.

VITA

Imon Chakraborty hails from Kolkata, West Bengal, India. He enrolled in the undergraduate program at the National Institute of Technology, Tiruchirappalli in 2005 and received his Bachelor of Technology (B.Tech) degree in Mechanical Engineering in May 2009. He joined the Daniel Guggenheim School of Aerospace Engineering at the Georgia Institute of Technology in August 2009, and earned his Master of Science in Aerospace Engineering (MSAE) degree in August 2011. Thereafter, he transferred to the Aerospace Systems Design Laboratory (ASDL) at the School of Aerospace Engineering to pursue his doctoral studies. He earned his Doctor of Philosophy (Ph.D.) degree in December 2015. During the course of his graduate studies at Georgia Tech, he authored/co-authored 6 peer-reviewed articles and 18 papers in conference proceedings. He holds a Private Pilot (Airplane Single-Engine Land) certification, and at the time of writing is checked out on the Cessna 172 and Diamond DA20 aircraft. He is the recipient of the 2015 William T. Piper, Sr. General Aviation Systems Graduate Award. He is a member of the American Institute of Aeronautics and Astronautics (AIAA) and the Aircraft Owners and Pilots Association (AOPA).